Polarizable Particles and their Two-Dimensional Arrays: Advances in Small Antenna and Metasurface Technologies

by

Carl R. Pfeiffer

A dissertation submitted in partial fulfillment
of the requirements for the degree of
Doctor of Philosophy
(Electrical Engineering)
in The University of Michigan
2015

Doctoral Committee:

Associate Professor Anthony Grbic, Chair
Professor Roberto D. Merlin
Professor Amir Mortazawi
Professor Kamal Sarabandi

To my mother and father

ACKNOWLEDGEMENTS

I am most grateful to my research advisor and friend, Professor Anthony Grbic. Tony, your passion for research and positive attitude are extremely contagious. I am thankful that you are always there when I need guidance, while also providing plenty of opportunities for me to explore my own ideas. I am also indebted to you for teaching me how to independently pursue my own research ideas.

I would also like to thank my other committee members. Professor Amir Mortazawi and Professor Kamal Sarabandi, your classes provided my foundation in electromagnetics that made this thesis possible. Professor Roberto Merlin, I would like to thank you for our stimulating conversations. I can always count on you to make me question the scientific principles I take for granted.

I would also like to thank my fiancée, Kelsey, for her unconditional love and support. I love you and I look forward to spending the rest of my life with you. In addition, I would like to thank my family for always being there for me. Mom, your unwavering warmth and compassion have made me a better person. Dad, you instilled in me a love of engineering that I carry with me today. My brother Dave, your wonderful sense of humor and contagious laugh make me look forward to your visits.

Thank you to my friends for the all great times. Whenever we get together, we pick up right where we left off. To all current and previous RADLAB members, thank you for making my time at the office very enjoyable. I would also like to personally thank the previous members of our research group, Scott Rudolph, Mohammadreza Imani, Amit Patel, and Gurkan Gok for being great mentors and friends.

TABLE OF CONTENTS

LIST OF FIGURES

Figure

LIST OF TABLES

Table

ABSTRACT

Polarizable Particles and their Two-Dimensional Arrays: Advances in Small Antenna and Metasurface Technologies

by

Carl Pfeiffer

Chair: Anthony Grbic

Metamaterials are subwavelength-structured materials designed to exhibit tailored electromagnetic properties. Metamaterials have allowed extreme control over constituent material parameters (i.e. permittivity, permeability, and chirality), which has enabled a myriad of counterintuitive physical phenomena. However, metamaterials typically suffer from high losses, difficulties in fabrication, and are bulky. This has led to the development of metasurfaces, which are the two dimensional equivalent of metamaterials. Metasurfaces can impart abrupt discontinuities on electromagnetic wavefronts, allowing electromagnetic fields to be tailored across subwavelength length scales.

The building blocks of metasurfaces are subwavelength textured, polarizable particles. Near resonance, these particles support strong currents, which makes them excellent small antennas. In this thesis, a circuit model is developed that can model an arbitrary small antenna based on its frequency dependent polarizability. In addition, a direct transfer patterning process is developed that allows metallic patterns to be printed onto arbitrarily contoured substrates. This work will find immediate

applications in a number of emerging technologies resulting from the rapid expansion of the mobile electronics industry.

Next, extreme control of the polarization and profile of a wavefront is demonstrated using two-dimensional arrays of polarizable particles (i.e. metasurfaces). A new class of metasurfaces, referred to as metamaterial Huygens' surfaces, is shown to have a significantly improved efficiency over the state of the art. Metamaterial Huygens' surfaces utilize polarizable particles that exhibit both an electric and magnetic response, which allows for reflectionless wavefront control. Next, it is shown that simply cascading patterned metallic sheets can also provide high transmission and complete phase control. To demonstrate the design methodology, several different metasurfaces are developed that deflect incident Gaussian beams to a stipulated angle or convert an incident Gaussian beam into a vector Bessel beam. Further, utilizing sheets with anisotropic patterns provides additional magneto-electric coupling, which enables complete control of a wavefront (i.e. amplitude, phase, and polarization control). The experimental verification at frequencies ranging from microwaves to optics highlights the versatility of this work.

CHAPTER I

Introduction

1.1 Background

Metamaterials are materials with subwavelength granularity that can be designed to exhibit tailor electromagnetic properties. They are typically realized by arranging metal and/or dielectric inclusions in a specified manner to achieve their novel properties. When the periodicity of these inclusions is much less than the wavelength of the electromagnetic field, they can be characterized as an effective medium [1]. To date, extreme control over constituent material parameters (i.e. permittivity, permeability, and chirality) has been achieved. With this control, a myriad of counterintuitive physical phenomena has resulted. Perfect lenses [2], invisibility cloaks [3], and tailoring of the photonic density of states [4] are just a few of the exciting applications enabled by these structures.

However, There are some limitations to these materials. Most notably, they typically suffer from narrow bandwidths, high losses, and difficulties in fabrication [5, 6]. This has led to the development of metasurfaces which are the two dimensional analog of metamaterials [7, 8]. Just as metamaterials provide complete control of an electromagnetic field within a volume, metasurfaces provide control of an electromagnetic wavefront at a surface. For example, consider Fig. 1.1 where both a homogeneous negative-index metamaterial and an inhomogeneous near-field plate metasurface realize subwavelength focal spots. The metamaterial achieves a subwavelength focus by resonant restoration of the evanescent spectrum within the material [2, 9]. In contrast, the metasurface imparts discontinuities onto the field to generate highly oscillatory fields whose interference results in a subwavelength focal spot [10, 11]. Metasurfaces have the advantage of being very thin, which results in reduced weight and a lower profile compared metamaterials. In addition, electromagnetic fields decay exponentially as they propagate through a material, which means a reduced thickness

generally leads to lower losses. Metasurfaces are also much easier to fabricate. They typically consist of patterned metal/dielectric on a dielectric substrate, which can be fabricated with standard fabrication processes from centimeter to nanometer length scales [12].

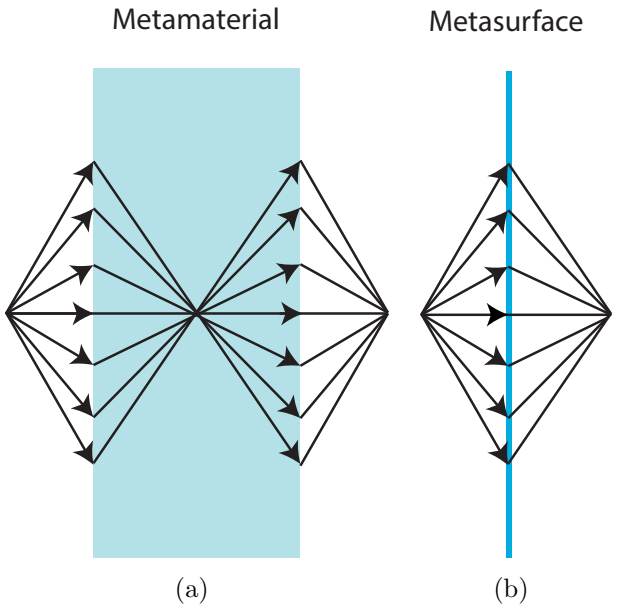

Figure 1.1: Comparison of metamaterials and metasurfaces. **(a)** Negative index metamaterial lens for subdiffractive focusing. **(b)** Near-field plate metasurface for subdiffractive focusing.

Metamaterials and metasurfaces are realized by distributing individually designed unit cells in a three-dimensional or two-dimensional lattice, respectively. Thus the cell's design is of utmost importance since it determines the properties of the overall structure. Each unit cell is realized with a subwavelength textured geometry. When the unit cell is near resonance, it can act as an open, short, resistor, inductor, or capacitor with slight variations in the cell geometry. In an analogous way that lumped components (i.e. inductors, capacitors, and resistors) control electric signals in electronic devices, metamaterial unit cells can control electromagnetic fields throughout a region of space [13].

Next, let us consider removing a unit cell from a metasurface and illuminating it with a plane wave. Near the resonant frequency of the cell, it supports a strong current, and becomes an excellent radiator. Therefore, each unit cell of a metasurface can be viewed as a small antenna. These antennas act as building blocks of the metasurface. In fact, the size, bandwidth, resonant frequency, as well as loss are important design considerations that are common to both small antennas and

metasurfaces [14, 15].

Aside from providing insight into the design of metasurfaces, small antennas are also important for a number of emerging wireless technologies. The rapid expansion of the mobile electronics industry has created a glaring need for devices that are both small and able to communicate wirelessly. The largest component of wireless devices today is typically the antenna. This fact alone has driven numerous antenna miniaturization studies and research efforts into the design and fabrication of small antennas.

First, this thesis presents novel methods to both analyze and fabricate small antennas. This work is immediately relevant for small antennas that are currently being developed for portable, vehicular, and aeronautical applications. Furthermore, since small antennas can be though of as building blocks for metasurfaces, this work also introduces many important concepts that are needed for the design of metasurfaces. Next, metasurfaces that tailor the wavefront and polarization of electromagnetic fields are developed. The majority of the presented metasurfaces achieve a similar functionality as previously reported structures, but with a significantly improved performance. Thus, this work provides a link between basic research in physics and practical commercial applications.

1.2 Motivation

1.2.1 Electrically Small Antennas

The microelectronics industry has enabled a wide range of devices that provide high computing power within a small size. This has led to a dramatic increase in the number of portable electronic devices such as cellular phones and sensor networks. Virtually all of these devices need low-profile antennas for communication. Additionally vehicles and aircraft often require low-profile antennas for aerodynamic reasons. This has generated a large research effort into antennas that are physically small.

There is also a desire to operate these antennas at large wavelengths because the distance over which antennas can communicate is directly proportional to the square of the operating wavelength, in accordance with the Friis Transmission Equation [16]. Longer wavelengths also are useful because the radiated signal will easily bend around obstacles, so that it is not necessary for the transmitter to be within the line of sight of the receiver. Thus there is a strong desire to realize antennas that are much smaller than the operating wavelength, which are known as electrically small antennas.

The most significant issues related to designing electrically small antennas is

achieving a good impedance match, high radiation efficiency, and maximal operating bandwidth. However, the input impedance of a small antenna generally presents a large reactance in addition to a low resistance, which makes matching to 50 Ω port impedances difficult. Furthermore, attempts to utilize conventional matching networks typically suffer from narrow operating bandwidths, and are inherently lossy. In addition, the matching network itself can occupy a significant size, thus reducing the benefits provided by the small antenna size. This has motivated the design of self-resonant electrically small antennas.

The highest performance self-resonant small antennas are typically realized by arranging metal in a volumetric geometry such as a hemisphere [14,17–19]. The most common method to fabricate these complex designs is by manually bending a wire. However, this method is imprecise, time consuming, and expensive. More recently, a method was introduced to print conductive ink onto a volumetric surface [20]. In that case, the ink used had a conductivity approximately 30% that of copper, which ultimately limited the antenna efficiency. In addition, since it was a direct write process, every trace was individually drawn, making the process relatively slow. Another method that is used to fabricate volumetric antennas is to first print the antenna onto a flexible printed circuit board using conventional photolithography, and then deform the circuit board into a desired shape [21]. However, this method is limited to fabricating relatively flat shapes, since substantial substrate deformation can cause the metallic lines to crack.

When designing small antennas, it is important to note that an antenna of any size can theoretically be made self-resonant at an arbitrary frequency. Thus, there are no fundamental limitations on achieving a good impedance match and high radiation efficiency. However, there exist fundamental limitations for the maximum achievable bandwidth. Therefore, the goal is to design an antenna that maximizes its bandwidth for a given electrical size. Of utmost importance to analyzing these limitations is the radiation quality factor (Q) of the antenna [22]. At the resonant frequency ($\omega_\circ$) of the antenna, Q is defined as,

$$Q(\omega_\circ) = \frac{\omega_\circ W(\omega_\circ)}{P_{rad}(\omega_\circ)}, \tag{1.1}$$

where $W(\omega_\circ)$ is the time-averaged stored electric and magnetic energy and $P_{rad}(\omega_\circ)$ is the radiated power [22].

The Q of an arbitrary resonator can then be related to its maximum achievable

bandwidth as demonstrated by Bode and Fano, [23, 24],

$$BQ \leq \frac{\pi}{\ln(\frac{1}{\Gamma_m})} \tag{1.2}$$

where B is the 3 dB fractional bandwidth and Γ_m is the maximum allowable reflection coefficient within the passband. Thus, the goal when designing small antennas is to minimize the antenna Q, so that the bandwidth can be maximized. However, it should be mentioned that the Bode-Fano limit does assume that all elements are passive. If active elements are utilized, the Bode-Fano limits no longer apply, and there is no limit on the achievable bandwidth [25–28]. Although promising, addressing the oscillation and noise of active components remains an ongoing area of research.

In the 1940's, Chu and Wheeler analytically solved for the minimum quality factor of an electrically small antenna [29, 30]. In Wheeler's work [30], he modeled a small antenna as a lumped capacitor or inductor in combination with a radiation resistance. Using well-known formulas for the inductance, capacitance, and resistance of various geometries, he showed that the Q of an antenna is inversely proportional to its volume. In particular, by analyzing the Q of a spherical coil surrounding a high permeability sphere, he derived the minimum Q for a single mode electrically small antenna,

$$Q_{\text{Wheeler}} = \frac{1}{(ka)^3} \tag{1.3}$$

where $k = \omega\sqrt{\mu_\circ \epsilon_\circ} = 2\pi/\lambda$ is the free space wave number, λ is the wavelength in free space, and a is the minimum radius of a sphere that circumscribes the antenna (see Fig. 1.2). Wheeler used circuit models to derive the first fundamental bounds relating the antenna size to a minimum Q. Although this approach was physically insightful, it was not entirely rigorous since a full-wave analysis was not performed. This caused the model to break down as the antenna size increased.

Chu performed a more rigorous full wave analysis of small antennas [29]. Chu used the recurrence relations of the spherical Bessel functions to develop an equivalent circuit to model the radiation of transverse electric (TE) and transverse magnetic (TM) spherical modes. By analyzing the Q of this circuit, the minimum Q of electrically small antennas was established, and is often referred to as the Chu limit,

$$Q_{\text{Chu}} = \frac{1}{(ka)^3} + \frac{1}{ka} \tag{1.4}$$

Chu rigorously showed that the bandwidth of an antenna is directly proportional

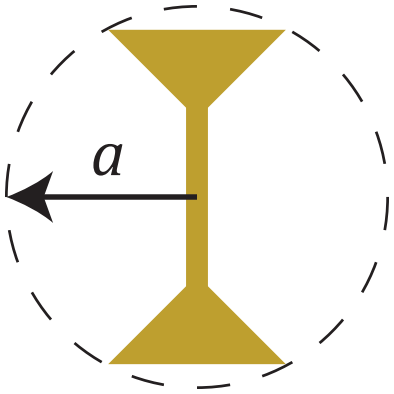

Figure 1.2: Arbitrary antenna that fits inside a sphere of radius a.

to its volume. Although the circuit model developed by Chu provides useful metrics for determining the performance of an optimal antenna, it provides little physical intuition. It is based only on the recurrence relations of the spherical Bessel functions rather than physical intuition.

Since then, fundamental limitations that relate bandwidth, size, loss, and directivity, while making additional assumptions that are more relevant for a given antenna implementation, have been derived [31]. These analyses have shed light on the limitations of various antenna designs. To date, many antenna designs have been reported that approach these fundamental limitations. However, generalized methods to analyze these antennas have been complex, making it difficult to gain physical intuition.

Furthermore, the vast majority of small antennas radiate as either an electric dipole or magnetic dipole. These radiation patterns are relatively omni-directional with a directivity of 1.5. However, for many applications a low directivity is undesirable since radiation in directions other than toward the receiver hurts the signal-to-noise ratio of the system. Therefore, it is desirable to develop a small antenna that exhibits a high directivity. This motivated the development of Huygens' sources which have a directivity of 3 [32]. These antennas radiate the electric and magnetic dipole modes simultaneously, so that the fields add constructively in one direction and destructively in the opposite direction. Huygens' sources are so named because they can generate the outgoing spherical wavefronts envisaged by the well-known Huygens' principle [33].

1.2.2 Metasurfaces for wavefront and polarization control

The second part of this thesis focuses on electromagnetic wavefront manipulation with two-dimensional metasurfaces. Electromagnetic wavefronts are typically con-

trolled using dielectric lenses, spatial light modulators, and waveplates. However, these devices rely on phase shifts that are gradual. This leads to bulky devices that are many wavelengths in thickness. This is especially problematic at microwave frequencies since dielectric lenses are required to be centimeters in thickness. This leads to a much larger volume and weight than most systems can afford. In addition, methods to fabricate these complex, three-dimensional geometries are expensive.

This has motivated wavefront control by an electrically thin surface (metasurface). This concept was first demonstrated in the 1960's to focus microwave radiation and realize high gain antennas [34]. These metasurfaces were generally referred to as reflectarrays and transmitarrays for the manipulation of wavefronts upon reflection and transmission, respectively. Transmitarrays are also commonly referred to as frequency selective surfaces [35], phase shifting surfaces [36], and antenna-filter-antennas [37]. Reflectarrays with high efficiency and broad bandwidth have been demonstrated at mm-wave frequencies [38, 39]. However, a feed placed in front of the antenna can degrade radiation patterns and significantly adds to the antenna size. Conversely, transmitarrays do not suffer from feed blockage. In addition, their configuration is more favorable for integrating the radiating element with the transceiver, which provides a more compact system [40]. The inclusion of active elements has also enabled beam scanning [41–44]. Although transmitarrays worked well at low GHz frequencies, scaling them to higher frequencies is not straightforward [36, 45–49]. For example, transmitarrays commonly employ receive antennas, connected to a phase shifter, and then connected to a transmitting antenna [37,50]. However, these structures are lossy and complex to fabricate at high frequencies. This is important because there is a desire to increase the operating frequency for many applications [51–53].

A particularly attractive method of providing wavefront control at wavelengths ranging from millimeter to nanometer was recently proposed in [54]. An inhomogeneous, two-dimensional array of V-antennas imparted abrupt phase discontinuities onto light passing through the surface. The surface can be designed to transform an incident wavefront into an arbitrary transmitted wavefront. However, there are some limitations to this work. First, the structure only employs electric dipoles, which are bidirectional radiators. Therefore, the power scattered into the forward direction is equal to the power scattered in the backward direction. This leads to high reflection losses. In addition, only the cross-polarized component of the transmitted field can be extensively controlled. From symmetry and reciprocity arguments this fundamentally limits the maximum achievable efficiency. Accounting for the reflection and polarization losses, the maximum achievable efficiency of these structures is 25% [55].

In fact, the limitations of V-antennas become clear by considering the work of Shelkunoff in 1936 [56]. Shelkunoff developed the surface equivalence principle, which demonstrated that both electric and magnetic surface currents are necessary to realize complete control of an electromagnetic wavefront. Generating the electric response is relatively easy, and a vast literature of work has been published [57]. However, generating a magnetic response is more challenging. The first metamaterials realized magnetic responses with split-ring-resonators consisting of capacitively loaded loops [58]. A magnetic flux through the middle of the loop excites currents which resonate with the capacitance. By operating throughout the resonance, the effective permeability can take on nearly arbitrary values. In addition, controlling the response is simple and intuitive. This effect was employed to realize collocated electric and magnetic dipole moments in some of the first reported metamaterials [2]. Even today, split-ring-resonators are commonly used to realize a magnetic response in metamaterials. Although utilizing collocated electric and magnetic responses is common when designing metamaterials, this concept has not been applied to the design of metasurfaces.

Split-ring-resonators do have some significant limitations. Split-ring-resonators suffer from excessive loss and complex fabrication at higher frequencies. Creating isotropic split-ring-resonators is also challenging. To address these limitations an alternative method of realizing a magnetic response was proposed in [59]. It was shown that a magnetic response is achievable by cascading patterned metallic sheets. This led to the well known fishnet structure for achieving a negative index of refraction at optical frequencies [60]. Realizing a magnetic response with cascaded metallic sheets has several advantages over the split-ring-resonator. It is easier to fabricate cascaded metallic sheets since they adhere to the standard 2.5 dimensional fabrication processes commonly employed in the microelectronics industry. They have also demonstrated a much lower loss than split-ring-resonators [5].

In addition to beam shaping, polarization control is also desirable for numerous applications [61]. Most often, polarization control is achieved with waveplates such as a quarter-wave plate [62, 63]. For a quarter-wave plate, the transmitted phase difference between two orthogonal electric field components is a quarter of the wavelength (90°). When an incident field is linearly polarized at 45° relative to its crystal axes, the quarter-wave plate converts the transmitted field to circular polarization, which has applications in satellite communication and rain clutter suppression [62]. Although quarter-wave plates have been realized with metasurfaces since the 1960s [62], there are few examples of metasurfaces that efficiently incorporate both wavefront and po-

larization control [40, 64]. For example, focusing transmitarrays that receive linear polarization and transmit circular polarization were reported at 60 GHz by Hamza Kaouach *et al.* [40]. However, the vias connecting the transmit and receive antennas presented increased fabrication costs, and the coarse phase quantization led to an additional 4 dB of loss. Although a method to address these limitations was proposed, no design was reported [40].

While wave plates provide some polarization control, complete control of the polarization requires a bianisotropic response (i.e. electric, magnetic, and chiral responses). To date there are many structures that exhibit novel polarization effects such as asymmetric transmission [65], and giant optical activity [66]. However, the performance of most devices is far from optimal because there is no systematic design methodology for realizing these low symmetry structures. In most cases, the design procedure is to use a resonant geometry that exhibits the necessary mirror and rotational symmetry so that a desired bianisotropic response is simply possible. But there is no guarantee that the performance will be near optimal [67]. Additionally, the description of the physics involved is often device specific, and its generalization to future designs is not straightforward. Alternatively, it is possible to achieve novel polarization effects by simply cascading dielectric wave-plates and linear polarizers [68]. However, this approach leads to bulky structures that do not easily lend themselves to system integration.

1.3 Thesis Outline

This thesis addresses many of the current limitations of electrically small antennas and metamaterials. Chapters 2-4 present new methods to fabricate and analyze electrically small antennas that achieve near optimal bandwidths and improved directivities. Chapters 5-9 detail metasurfaces that provide extreme control over a wavefront and its polarization, which significantly advances the state-of-the-art.

In Chapter II, a direct transfer patterning process is presented. This process allows arbitrary metallic patterns to be stamped onto a contoured substrate, such as a sphere. This process can be used to accurately and rapidly fabricate volumetric electrically small antennas on a variety of shaped substrates. In addition, this technology allows components with small features, (e.g., interdigitated capacitors or densely packed metallic conductors) to be placed onto arbitrarily contoured substrates. This has potential applications in diverse areas such as high gain antennas, conformal antenna arrays, RFIDs, metamaterials, and transformation optics. Here, this process is used to

make some of the most efficient electrically small antennas to date, while maintaining bandwidths approaching the physical limit.

In Chapter III, a circuit model for electrically small antennas is introduced that is based on their frequency-dependent polarizabilities. This model is useful for straightforwardly analyzing several different small antenna geometries. A negative permittivity sphere, shell, and spheroid are all analyzed. An inductively loaded dipole, a top-hat loaded dipole, and a spherical sheet impedance are also analyzed. The circuit model provides the antenna's radiation quality factor (Q), radiation efficiency (η_{rad}), and bandwidth. Unlike the circuit model developed by Chu, the circuit model developed here provides physical intuition, which can aid and simplify design.

Chapter IV discusses how to increase the directivity of small antennas using Huygens' sources. An electrically-small Huygens' source is introduced that is realized as two concentric spherical sheet impedances. Closed-form expressions for the electric and magnetic polarizabilities, the directivity, and the scattering bandwidth of the Huygens' source are found. A trade-off between scattering bandwidth and directivity is explicitly shown. Design methodologies and practical implementations are introduced. An impedance-matched, electrically-small antenna (ESA) of the same topology with a directivity of 7.6 dB is presented. The antenna is simply fed with a coaxial connector. In addition to its usefulness as an electrically small antenna, the analysis also provides great insight into the design of impedance-matched metasurfaces, which are discussed in the following chapters.

In Chapter V, Huygens principle is applied to develop designer surfaces that provide extreme control of electromagnetic wavefronts across electrically thin layers. These reflectionless surfaces, referred to as metamaterial Huygens surfaces, provide new beam shaping, steering, and focusing capabilities. The metamaterial Huygens surfaces are realized with two-dimensional arrays of polarizable particles that provide both electric and magnetic polarization currents to generate prescribed wave fronts. This structure can be envisaged as a nonperiodic distribution of Huygens' sources. A straightforward design methodology is demonstrated and applied to develop a beam-refracting surface and a Gaussian-to-Bessel beam transformer. This metasurface demonstrates a dramatic improvement in efficiency over previous metasurfaces that only use electric currents for wavefront control.

In Chapter VI, it is shown that metasurfaces can deflect a normally incident wavefront off to a specified angle, while simultaneously converting the polarization from linear to circular. In this chapter, two separate metasurfaces that operate at 77 GHz are designed and fabricated. The first metasurface acts as a quarter-wave

plate that transforms a linearly polarized incident wave into a circularly polarized transmitted wave. The second metasurface acts as both a quarter-wave plate and a beam refracting surface to provide polarization and wavefront control. When the second metasurface is illuminated with a normally incident, linearly polarized beam, the transmitted field is efficiently refracted to 45°, and the polarization is converted to circular. The half-power bandwidth was measured to be 17%, and the axial ratio of the transmitted field remained below 2.5 dB over the entire bandwidth. Both designs have a subwavelength thickness of 0.4 mm ($\lambda_\circ/9.7$). The developed structures are fabricated with low cost printed-circuit-board processes on flexible substrates. The metasurfaces are realized by cascading three patterned metallic surfaces (sheet admittances) to achieve complete phase control, while maintaining high transmission. Polarization conversion is accomplished with anisotropic sheets that independently control the field polarized along the two orthogonal axes. The structures are analyzed using circuit-based and fields-based approaches.

Chapter VII demonstrates that the design methodology presented in the previous chapter can be used to achieve unprecedented control of electromagnetic wavefronts. Specifically, reflectionless metasurfaces are developed that can manipulate vector Bessel beams: cylindrical vector beams with a Bessel profile. First, two metasurfaces are developed to convert linearly and circularly polarized Gaussian beams into vector Bessel beams. Each unit cell of the metasurfaces provides polarization and phase control with high efficiency. Next, the reciprocal process is demonstrated: an incident radially-polarized Bessel beam is transformed into collimated, linearly and circularly polarized beams. In this configuration, a planar Bessel beam launcher is integrated with a collimating metasurface lens to realize a low profile lens-antenna. This is the first lens-antenna with a subwavelength overall thickness that achieves a high gain (exceeding 20 dB). This work experimentally demonstrates that metasurfaces can be used to generate arbitrary combinations of radial and azimuthal polarizations for applications such as focus shaping or generating tractor beams.

Chapter VIII demonstrates that Huygens' surfaces composed of cascaded sheet admittances can be realized even at optical wavelengths. In this chapter, a metasurface lens that focuses light and controls its polarization at a wavelength of 2 μm is presented. This lens demonstrates high transmission and complete phase control within a subwavelength thickness at near-infrared frequencies. By cascading four patterned sheets, the efficiency is dramatically improved over more common single sheet designs. In addition, by utilizing anisotropic sheets, arbitrary birefringence can be achieved. A planar lens that both focuses light and converts its polarization from

linear to circular is analyzed. Next, a broadband Huygens surface that efficiently refracts normally incident light at the telecommunication wavelength of 1.5 μm is reported. The cascaded sheets have a subwavelength overall thickness of 430 nm. The metasurface is experimentally characterized, and measured to have a peak efficiency and extinction ratio that are 3 and 4 times larger than the state of the art V-antenna geometries, respectively [69].

In Chapter IX, more exotic forms of polarization control are demonstrated with metasurfaces exhibiting bianisotropic responses (i.e. electric, magnetic, and chiral responses). This work represents the most general description of the interaction between metasurfaces and electromagnetic fields to date. In this section, an arbitrary bianisotropic metasurface is analyzed using closed-form expressions that relate the reflection and transmission coefficients to its constituent surface parameters. Next, a systematic method to synthesize bianisotropic metasurfaces is outlined. It is analytically shown that bianisotropic metasurfaces can be realized by cascading anisotropic, patterned metallic sheets (electric sheet admittances). This geometry allows for straightforward design and fabrication from microwave to optical wavelengths. To demonstrate the utility of the proposed method, four devices exhibiting novel polarization transformations are presented: a polarization rotator, an asymmetric circular polarizer, an asymmetric linear polarizer, and a symmetric circular polarizer. The optimal performance at centimeter, millimeter, and micrometer wavelengths highlights the versatility of the design process.

CHAPTER II

Direct Transfer Patterning of Electrically Small Antennas

2.1 Chapter Introduction

The most basic electrically small antenna (ESA) consists of a small dipole antenna with an external matching circuit. However, this antenna generally exhibits a narrow bandwidth and relatively low efficiency [14]. Other miniaturized antenna designs include resonant, magnetically-coupled antenna elements packed into a small volume [70], space-filling curve antennas, and fractal curve antennas [71]. ESAs can be categorized as either volumetric or planar. Volumetric ESAs offer excellent performance, whereas planar designs exhibit limited performance: relatively low bandwidths and low radiation efficiencies [14]. Planar designs, on the other hand, are popular since their fabrication is simple and inexpensive. Here, the advantages of these two technologies are combined by developing a simple method to fabricate high performance, volumetric, printed ESAs.

In this chapter, a direct transfer patterning process that allows printing by direct stamping of arbitrary patterns onto a contoured substrate is presented. This process can be used to accurately and rapidly fabricate volumetric ESAs on a variety of shaped substrates. In addition to the fabrication of electrically small antennas, this process can also be applied to other wireless technologies such as high gain antennas, antenna arrays, radio-frequency identification devices (RFIDs), metamaterials and transformation optics [3, 72]. To demonstrate the value of this process, we designed, fabricated, and measured ESAs of various electrically small sizes that operate over several frequency ranges. We show that the antennas fabricated using this direct transfer patterning process have significantly higher performance and are potentially easier to mass produce than with previously reported methods on non-planar surfaces.

A common metric used to analyze the performance of an ESA is the ratio Q/Q_{lb}, where Q is the quality factor of the antenna under consideration and Q_{lb} is the lower bound given by $Q_{lb} = 1/(ka)^3 + 1/(ka)$. To date, there are several examples of antennas that closely approach the fundamental limit [14, 18–20, 30, 70]. We chose to fabricate the spherical helix antenna because it closely approaches this limit, and its design is relatively simple [18]. The spherical helix antenna inductively loads a dipole antenna by winding metallic arms around the surface of a hemisphere. By varying the number of arms and the number of turns each arm makes around the sphere, it can be impedance-matched to 50 Ω.

2.2 Direct Transfer Patterning

Direct transfer patterning has been previously used to fabricate photodetector arrays on a hemispherical surface [73]. To realize ESAs, the process is modified to dramatically (by a factor of 500) increase the thickness of the metallic patterns, allowing very low resistance, conductive antenna arms to be fabricated. This process can also be used to pattern metal onto extreme curvatures, such as the entire surface of a hemisphere down to its equator. The process involves stamping metallic patterns onto a contoured substrate, and then electroplating the patterns to a thickness of 5-10 μm. A summary of the process is shown in Figure 2.1.

The substrate used to fabricate the antenna is 0.5 mm thick, glycol-modified polyethylene terephthalate (PETg), which has a relative dielectric constant $\epsilon_r = 3.1$ and loss tangent tan δ=0.015 [74]. To begin, a flat sheet of PETg is deformed into the desired shape by heating to 150°C (above its softening temperature), and then drawing it into a vacuum mold where it is cooled. Next, 30 nm thick SiO_2 and 3 nm thick Cu layers are sputtered onto the contoured substrate followed by deposition of an 8 nm Au strike layer. The SiO_2 and Cu serve to improve the adhesion of Au to the substrate. Then, a Si pattern master is prepared by etching 40 μm trenches using standard lithography and deep reactive ion etching. The location of the trenches corresponds to the final location of the metal patterns to be printed onto the substrate. A liquid polydimethyl-siloxane (PDMS) pre-polymer and hardening agent are then poured onto the Si pattern master at a 10:1 mass ratio. The PDMS is cured at 100°C for 2 hrs, after which it is peeled from the pattern master to form a stamp. The PDMS stamp is approximately 0.5 mm thick, with 40 μm high ridges corresponding to the pattern that is to be printed on the contoured substrate. Next, a 17 nm Au seed layer is added to the stamp using electron beam evaporation (Figure 2.1(a), Step

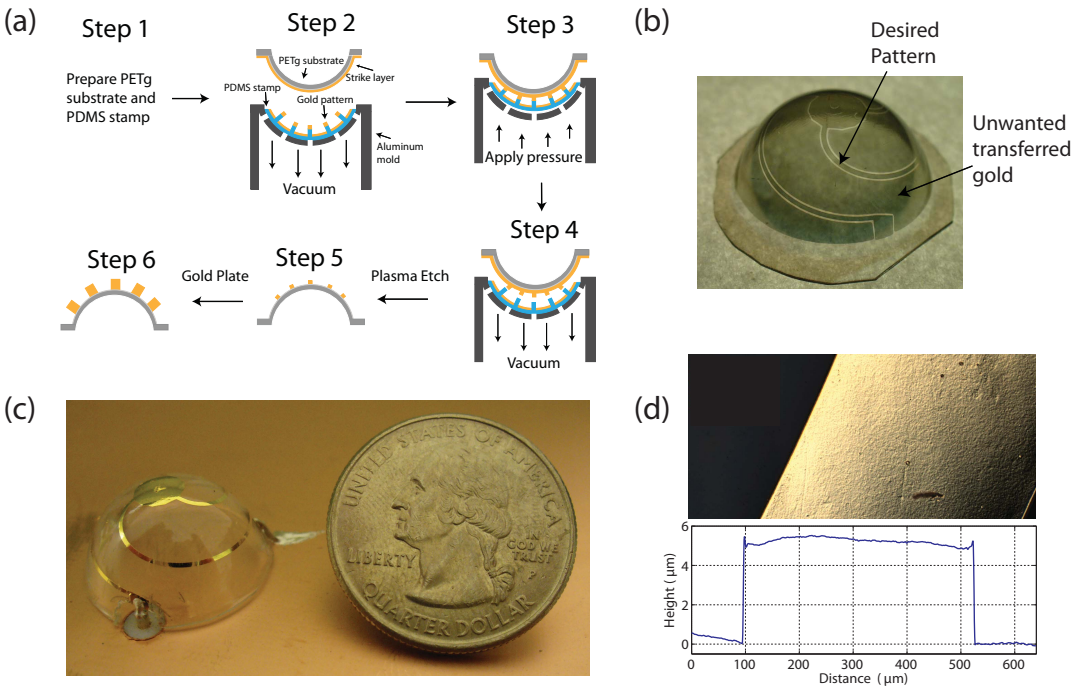

Figure 2.1: **(a)** Outline of the direct transfer patterning process that is used to stamp metallic patterns onto a contoured substrate. **(b)** Patterned Au on a hemispherical substrate prior to electroplating (between Step 5 and 6). Note that there are areas where unwanted Au is stamped onto the substrate, which are later removed. **(c)** The fabricated spherical helix antenna after connection to a ground plane. **(d)** Optical micrograph and profilometry scan of a metal conductor. The surface roughness is 0.5 μm.

1).

To pattern the substrate, the stamp is drawn into the same vacuum mold used to deform the substrate (Step 2). The substrate is subsequently placed in close proximity to the deformed stamp. When the vacuum is released and a small amount of pressure ($\sim$1 atm) is applied to the back of the stamp, the ridges contact the surface of the substrate, resulting in a cold-welded metallic bond formed between the Au on the stamp and that on the substrate (Step 3). Then the vacuum is reapplied to separate the stamp from the substrate, transferring the 17 nm thick Au patterns to the surface of the contoured substrate (Step 4). Next, the substrate is etched in an Ar plasma at 30 mTorr and 150 W for 70 s to remove the strike layer that electrically connects all of the transferred patterns (Step 5). Exposure to the Ar plasma substantially heats the substrate, which is problematic since PETg has a relatively low softening temperature. To minimizing heating, the plasma is pulsed (10 s on, 60 s off). Figure 2.1(b) shows the patterned substrate after the plasma etch. Finally, the patterns are electroplated to a thickness of 5-10 μm (Step 6). This process allows one to print arbitrary patterns onto contoured substrates, such as the spherical helix antenna shown in Figure 2.1(c).

It can be seen in Figure 2.1(b) that there is additional Au, between the helical conductors. When pressure is applied to the back of the stamp, its ridges contact the substrate to form a cold-welded metallic bond. When these ridges are spaced sufficiently far apart, additional areas of the flexible PDMS stamp also contact the substrate, thereby creating transfer of Au in between the conductive traces. The interstitial Au can be removed using a wet Au etch (Transene TFA Au Etch). Following the plasma etch, there is a gap between the unwanted Au and the desired pattern. This gap creates electrical isolation such that only the desired pattern is electroplated. After electroplating, a wet Au etch is used to remove the 17 nm thick, unwanted Au with minimal effect on the electroplated pattern.

The direct transfer patterning process relies on forming a cold-welded bond between the stamp and substrate (Figure 2.1(a), Step 3). For cold-welding to occur, the two surfaces must be coated with identical metal layers and brought into intimate contact so that they adhere [75–78]. The surfaces must be clean and smooth since small dust particles or surface nonplanarity will inhibit intimate contact. Elastomers such as PDMS can mold themselves around surface defects, thereby limiting their adverse effects [75, 76]. In direct transfer patterning, it is desirable to transfer metal thicknesses that are significantly thicker than the strike layer to provide a high contrast for the plasma etch (Figure 2.1(a), Step 5). It has been shown that thicknesses

up to 20 nm can be transferred using this process [73]. However, greater thicknesses were difficult to obtain, possibly due to wrinkling of the PDMS during the metal deposition [73, 79].

To maximize antenna efficiency, the conductor thickness should be at least 3δ, where δ is the skin depth (2 μm at L-band) at the operating frequency. Several factors influence the optimal metal plating thickness. When the metal is plated too thick, it becomes overly stressed, forcing it to peel off the substrate. Rougher substrates can employ thicker metal films due to increased mechanical anchoring [80]. The surface roughness of the PETg substrate is 14 nm, measured using atomic force microscopy (AFM). For Cu and Au plating, we achieved a thickness of 12 μm and 7 μm, respectively, without the metal peeling. In addition, the use of adhesion layers can significantly increase the maximum thickness of the metal. We found that SiO2 and Cu adhesion layers work well because they offer sufficient adhesion to electroplate to the desired thickness, while Cu is easy to remove during the Ar plasma etch [81].

The minimum achievable feature size is limited by the lithography techniques used to pattern the Si pattern master, and the thickness of the electroplated conductors. Typically, feature sizes of <10 μm can be achieved using this process for 10 μm thick patterns. Figure 2.1(d) shows an optical micrograph and profilometry scan of an antennas conductive arm. The surface roughness is 0.5 μm. We chose to use a PETg substrate because of its low cost, tolerance to the electroplating process, and vacuum forming properties. In general, any other substrate that can be shaped into the desired contour could also be utilized, but attention should be paid to its electroplating properties.

2.3 Antenna Measurements

We fabricated and measured three spherical helix antennas whose performance is provided in Figure 2.4. Figure 2.2 shows the dimensions of a spherical helix antenna that operates at 1.12 GHz. Each arm was designed to have 1.5 turns using [18](Eqs. (1-5)), except that the arms begin spiraling 2 mm above the surface of the ground plane rather than at the ground plane. All but one of the arms was connected to a 200 mm x 200 mm ground plane using Ag-loaded epoxy, while the remaining arm was connected to the inner conductor of a coaxial transmission line acting as an antenna feed. The radius of the hemisphere is 10 mm. A 2 mm radius cap was placed at the top of the antenna to allow for an easy electrical connection while electroplating. Since the current near the top of the antenna is small, the cap does not affect the

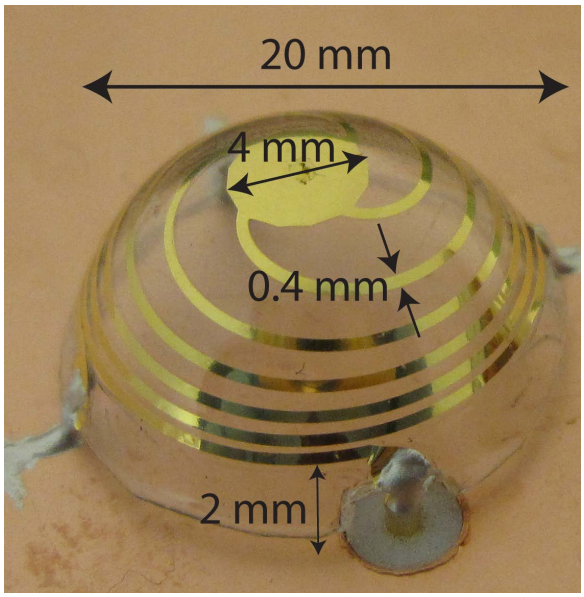

Figure 2.2: Dimensions of a spherical helix antenna that operates at 1.12 GHz.

performance. The width of the conducting paths is 0.4 mm, and their thickness is 5 μm. All antennas are impedance-matched to 50 Ω with a return loss greater than 15 dB, as shown in Figure 2.3(a). The antennas that operate at 1.52 GHz and 2.7 GHz are identical to that in Figure 2.2 except they each have 3 arms with 1.0 and 0.5 turns per arm respectively. The input impedance was used to calculate the Q of the antenna [22]. The radiation patterns of the antennas were also measured (see Figures 2.3(b)-(d)), and all antennas exhibit the expected electric dipole radiation patterns. Simulations also show that as the size of the ground plane increases, the dipole radiation patterns approach those of a monopole, as expected.

The radiation efficiency of the antennas was measured using both the Wheeler cap method and the gain comparison method [16, 30]. In the Wheeler cap method, the input impedance of the antenna is measured in free space. Next, a Wheeler cap is placed over the antenna and secured to the ground plane, and the input impedance is remeasured. These two measurements are used to find the radiation and loss resistances, and therefore the radiation efficiency. The accuracy of this method can be improved when postprocessing the data by adding an ideal transmission line to rotate the input impedance around the Smith chart, such that it resembles a constant resistance or conductance circle [82].

The radiation patterns were measured using the University of Michigans 18 m anechoic chamber. The antenna under test (AUT) is placed on a rotating styrofoam platform in the quiet zone of the chamber. The AUT is then connected to a signal

generator (Agilent N5183A). At the other end of the chamber is a recieving, standard gain horn antenna connected to a spectrum analyzer (Hewlett Packard 8592L) to measure the recieved power. By rotating the AUT and measuring the power recieved by the horn antenna, the radiation patterns are measured. Then the radiation efficiency is found using the gain comparison method [16]. For this, the AUT is replaced by a reference horn antenna with a known gain. By comparing the recieved power of the AUT to the reference, the gain and radiation efficiency are determined. The radiation efficiency measured using the gain comparison method agreed to within 2% of the efficiency found using the Wheeler cap method.

Finally, the radiation quality factor (Q) was found using the measured input impedance of the antenna. It can be shown that for single resonant antennas, the Q is related to the input impedance through the following relation [22],

$$Q(\omega_\circ) = \frac{\omega_\circ}{2R_\circ(\omega_\circ)} \left| \frac{dZ(\omega)}{d\omega} \right|_{\omega_\circ} \tag{2.1}$$

Here, $\omega_\circ$ is the resonant frequency of the antenna, $R_\circ$ is the input resistance, and $dZ(\omega)/d\omega$ is the frequency derivative of the input impedance evaluated at the resonant frequency.

Using the stamping process, three different spherical helix antennas were designed and fabricated to operate at three different frequencies. These results allow for the direct comparison of the antennas with previously published data of similar electrical sizes. To highlight the effect of the fabrication method on antenna performance, Table 1 summarizes the results of some competing fabrication methods such as manually bending wires [18], silver ink printing [20], and conventional 2D printed circuit board (PCB) techniques [15].

Manually fabricated spherical helix antennas provide the best performance since they have a very low Q and high efficiency. The increased Q of the direct transfer patterning technique primarily results from the presence of a substrate [83]. The reasons for the decreased efficiency of the antenna fabricated using direct transfer patterning is the additional substrate loss, and the lower skin depth due to the higher frequency of operation [84]. Although manual fabrication offers improved performance, manually bending wires is a time consuming and potentially expensive process. Silver ink printing achieves comparable Q's, but significantly lower efficiency than direct transfer patterned devices since the conductivity of the ink is only 30% that of copper [20]. This lower efficiency leads to an increased bandwidth of the silver ink printed antennas. In addition, the ink printing process is relatively slow since every conductive

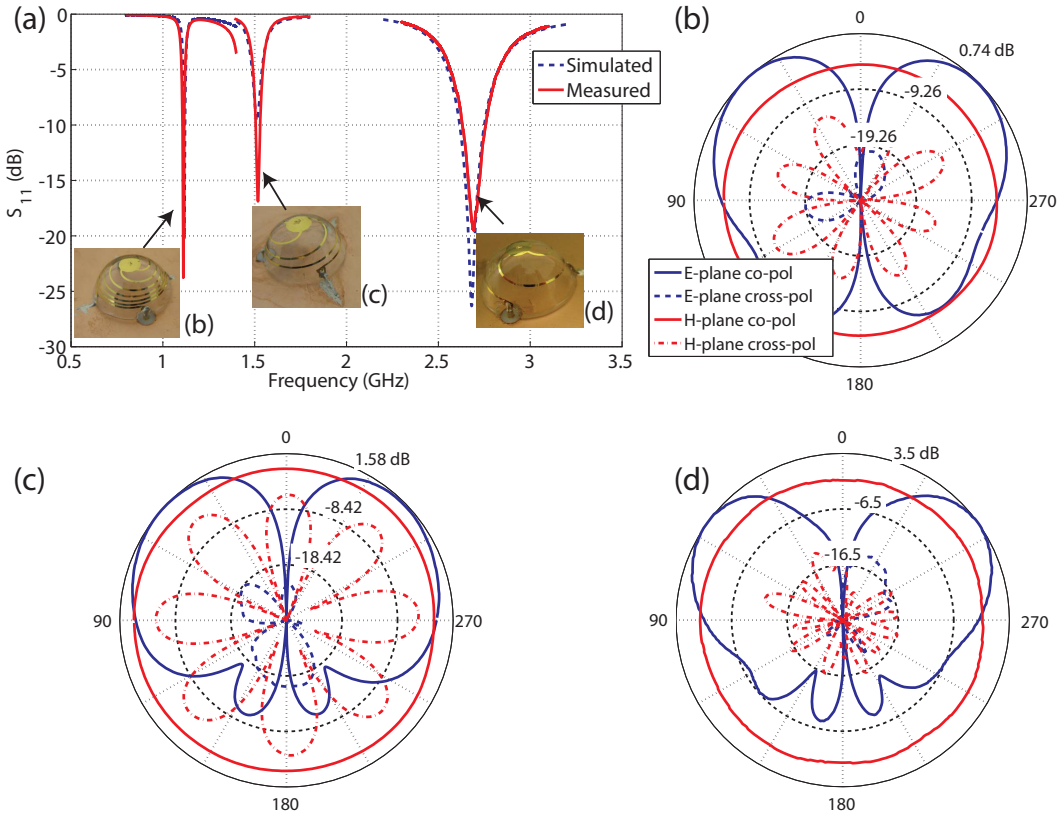

Figure 2.3: **(a)** Reflection coefficient of the antennas compared with simulation. **(b)-(d)** Co-polarization and cross-polarization gain patterns along the electric (E) and magnetic (H) field planes of the spherical helix antennas operating at 1.12 GHz, 1.52 GHz, and 2.7 GHz, respectively.

Fabrication Method	Frequency (GHz)	ka	Q/Q_{lb}	η_{eff}	Half Power Bandwidth
Direct transfer patterning	1.12	0.23	2.1	52%	2.0%
	1.52	0.31	1.8	69%	5.3%
	2.70	0.56	2.2	88%	14.2%
Manually bending wires	0.30	0.38	1.5	98%	7.6%
	0.30	0.45	1.8	99%	6.7%
Silver ink printing	0.79	0.21	2.0	14%	6.3%
	1.70	0.46	1.5	71%	15.2%
Printed-circuit-board	0.43	0.35	5.8	58%	2.3%
	1.40	0.50	5.4	89%	4.1%

Figure 2.4: The performance of electrically small, spherical helix antennas fabricated using the direct transfer patterning process. For comparison, the performances of several alternative fabrication techniques are also provided. The direct transfer process has a slightly lower efficiency than manualy bending wires, but otherwise outperforms the other fabrication techniques. Several different electrical sizes (ka) are shown to demonstrate their scaling properties.

trace needs to be individually drawn. Finally, conventional two-dimensional printed circuit board fabrication offers a significantly higher Q and lower efficiency since the antennas do not take advantage of the volume provided by a spherical geometry.

2.4 Chapter Summary

In summary, a process to rapidly stamp antennas onto arbitrarily contoured substrates was presented. In addition, the ability to fabricate antennas whose bandwidths approach the maximum achievable limit for a given electrical size was demonstrated. It was shown that direct transfer patterning can produce electrically small antennas that are significantly more efficient than previously published methods and potentially less expensive to fabricate. In addition, this technology allows components with small features, (e.g. interdigitated capacitors or densely packed metallic conductors) to be placed onto arbitrarily contoured substrates. This has potential applications in diverse areas such as high gain antennas, conformal metasurfaces and antenna arrays, RFIDs, metamaterials, and transformation optics [3, 72].

CHAPTER III

A Circuit Model for Electrically Small Antennas

3.1 Chapter Introduction

In [29], Chu developed an equivalent circuit to model the radiation of transverse electric (TE) and transverse magnetic (TM) spherical modes. By analyzing the Q of this circuit, the minimum Q of ESAs was established. The minimum achievable Q for an ESA is known as the Chu limit, $Q_{\text{Chu}} = 1/(ka)^3 + 1/(ka)$. The results of Chu did not consider the energy stored within the antenna, and they were later revisited to obtain more accurate bounds for realistic small antennas [85–87].

The vast majority of ESAs radiate either the TE_{10} or TM_{10} modes, and can therefore be characterized by an electric or magnetic polarizability [88, 89]. The polarizability relates the radiated fields to those of a small electric or magnetic dipole, and indicates how well an antenna scatters the fields of an incident plane wave. It will be shown that using the polarizability of an arbitrary ESA for a polarization of interest, an equivalent circuit can be found to model its performance: bandwidth, Q, and efficiency. The analysis reported here allows one to analyze the fundamental operation of the antenna, independent of the effects of a particular feed.

In this chapter, circuit models are presented for electrically small antennas including a negative permittivity sphere, shell and spheroid, based on their frequency-dependent polarizabilities. The Q of the equivalent circuits is analyzed and compared to previously reported values. The advantage of the proposed technique for evaluating antenna Q is that it can be applied to many different types of small antennas. The equivalent circuit for the inductively loaded dipole and top-hat loaded dipole is also found using the same approach. In addition, inductive and capacitive spherical sheet impedances are analyzed. The inductive sheet, which radiates the TM_{10} mode, is shown to have the same circuit as the negative permittivity sphere. Finally, it is shown how the feed of a small antenna can be modeled by analyzing the negative

permittivity hemisphere antenna design reported in [90], as well as a conventional inductively loaded dipole and top-hat loaded dipole.

3.2 Concept

Consider the case where an ESA scatters the field of an incident plane wave. For the time being, let's assume the antenna is not loaded by a particular feed, and is thus acting as a scatterer. When the antenna is small compared to the wavelength, the scattered fields are predominately those of a small electric and/or magnetic dipole [88]. We will first investigate the electric dipole (TM_{10}) mode. The incident electric field of the plane wave will be denoted as $\vec{E}_\circ$, and assumed to be polarized along the dipole moment of the antenna. In the near field, reactive components of the electric field dominate. These fields can be compared to those of a short dipole with polarizability (α). The dipole moment of the ESA is equal to $\vec{P} = \epsilon_\circ \alpha \vec{E}_\circ$, which can in turn be related to that of a dipole: $\vec{P} = q\vec{dl}$. If these fields are time harmonic and assumed to be quasi-static, then $j\omega q\vec{dl} = I\vec{dl} = j\omega\epsilon_\circ\alpha\vec{E}_\circ$. As a result $I = j\omega\epsilon_\circ\alpha V/dl^2$. Thus, an equivalent impedance Z_{electric} can be defined for the electric dipole,

$$Z_{\text{electric}} = \frac{dl^2}{j\omega\epsilon_\circ\alpha}. \tag{3.1}$$

An equivalent circuit representing Z_{electric} can provide physical insight into the operation of the small antenna. The ESA is not loaded by a feed since it is excited by a plane wave instead. This allows one to investigate the fundamental operation of the small antenna independent of its feed. In addition, feeding the antenna with a plane wave offers insight into the minimum Q, and also provides the equivalent circuit for the antenna when it is operated in the receiving mode [88]. Fortunately, near the operating (resonant) frequency of ESAs, the current distribution is the same for both the transmitting and receiving modes [91]. Therefore, (3.1) is also valid for transmitting antennas. When the effects of the feed are desired, it is relatively straightforward to include in the circuit, as will be shown in Section 3.7.

Since the radiated fields are of interest, an accurate model of the polarizability must take into account radiative damping [90, 92]. At resonance (when α approaches infinity), the magnitude of a radiation reaction field $\vec{E}_r = -j(2/3)k^3\vec{P}/(4\pi\epsilon_\circ)$ becomes non-negligible. Adding $\vec{E}_r$ to the excitation $\vec{E}_\circ$, results in the following dipole

moment [92]:

$$\vec{P} = \epsilon_\circ \alpha \left[\vec{E_\circ} - \frac{jk^3 \vec{P}}{6\pi\epsilon_\circ} \right] \tag{3.2}$$

By solving for $\vec{P}$, the effective polarizability α_{eff} is given by,

$$\alpha_{\text{eff}} = \frac{\alpha}{1 + j\frac{\alpha k^3}{6\pi}}. \tag{3.3}$$

For lossless ESAs, α is purely real. By substituting α_{eff} for α in (3.1), Z_{electric} can be written as

$$Z_{\text{electric}} = \frac{dl^2}{j\omega\epsilon_\circ\alpha} + \frac{dl^2 k^3}{6\pi\epsilon_\circ\omega}. \tag{3.4}$$

The term $dl^2/(j\omega\epsilon_\circ\alpha)$ represents a reactive element in series with a resistor of value $dl^2k^3/(6\pi\epsilon_\circ\omega)$. Energy stored in the reactive component is proportional to the energy stored in the reactive field of the ESA, while the energy dissipated by the resistor is proportional to the radiated energy. Note that the resistance is independent of the ESA and is equal to that of a small dipole of height dl, consistent with the results of [93].

Since the impedance in (3.4) is of the form $R(\omega) + jX(\omega)$, the Q of the circuit at resonance can be easily found using the result of [94],

$$Q(\omega_\circ) = \frac{\omega_\circ}{2R(\omega_\circ)} X'(\omega_\circ), \tag{3.5}$$

where $X'(\omega_\circ)$ is the derivative of $X(\omega)$ evaluated at the resonant frequency $\omega_\circ$. Inserting (3.4) into (3.5) results in the Q at resonance of an arbitrary ESA based on its frequency-dependant polarizability,

$$Q(\omega_\circ) = \frac{-3\pi\omega_\circ}{k^3} \frac{d(\frac{1}{\alpha})}{d\omega}. \tag{3.6}$$

Electrically small antennas are often required to fit within an overall geometry that is stipulated by the application (e.g. cell phones and laptops require planar antennas). Therefore, a practical case is to consider the equivalent circuit of a perfect electrically conducting (PEC) object with a frequency-independent polarizability given by α_{pec}. No assumption is made about the object's shape. This case is useful for understanding the physical limitations of arbitrarily shaped small antennas since a PEC object exhibits the lowest achievable Q that is excited by electric currents only [88]. If we assume that this object is somehow tuned to a resonant frequency $\omega_\circ$ with an ideal

inductor, Z_{electric} simplifies to,

$$Z_{\text{electric}} = \frac{dl^2}{j\omega\epsilon_\circ\alpha_{\text{pec}}} + \frac{j\omega dl^2}{\omega_\circ^2\epsilon_\circ\alpha_{\text{pec}}} + \frac{dl^2k^3}{6\pi\epsilon_\circ\omega}. \tag{3.7}$$

When (3.7) is inserted into (3.5), the Q of this circuit simplifies to,

$$Q(\omega_\circ) = \frac{6\pi}{k^3\alpha_{\text{pec}}}, \tag{3.8}$$

which is identical to the minimum achievable Q for an electric dipole mode excited by electric currents only [88] .

It is also important to examine the effects of material absorption on the circuit model. Absorption causes the polarizability to become complex: $\alpha_c = \text{Re}(\alpha_c) - j\text{Im}(\alpha_c)$. Inserting α_c into (3.4) results in a circuit impedance,

$$Z_{\text{electric}} = \frac{dl^2\text{Re}(\alpha_c)}{j\omega\epsilon_\circ|\alpha_c|^2} + \frac{dl^2\text{Im}(\alpha_c)}{\omega\epsilon_\circ|\alpha_c|^2} + \frac{dl^2k^3}{6\pi\epsilon_\circ\omega}. \tag{3.9}$$

From the expression above, it is evident that there are two resistors in series with a reactive component, where $R_{\text{loss}} \propto \text{Im}(\alpha_c)$ accounts for material absorption, and $R_{\text{rad}} \propto k^3$ accounts for the radiated power. To find the radiation efficiency (η_{rad}), one can simply divide the energy radiated by the total energy dissipated,

$$\eta_{\text{rad}} = \frac{R_{\text{rad}}}{R_{\text{rad}} + R_{\text{loss}}} = \frac{1}{1 + \frac{6\pi\text{Im}(\alpha_c)}{k^3|\alpha_c|^2}}. \tag{3.10}$$

3.3 Negative Permittivity Sphere

The first small antenna to be considered is a negative permittivity sphere. Let's consider scattering from such an electrically small sphere by a plane wave. The polarizability of an electrically-small sphere with relative dielectric constant ϵ_s is [92],

$$\alpha = \frac{4\pi a^3(\epsilon_s - 1)}{(\epsilon_s + 2)}. \tag{3.11}$$

A negative permittivity material must be dispersive to obey the well-known causality relationships. A Drude model will be assumed for the permittivity dispersion, since this model has the lowest frequency derivative (lowest Q) that satisfies the Landau-Lifshitz criteria for the frequency derivative of the permittivity [95,96]. The frequency-

dependant permittivity $\epsilon_s(\omega)$ has the form,

$$\epsilon_s(\omega) = 1 - \frac{\omega_p^2}{\omega(\omega - j\gamma)}. \tag{3.12}$$

Here ω_p is the plasma frequency and γ represents material absorption, which at first will be assumed to be zero.

When the permittivity of the sphere is $\epsilon_s = -2$, the sphere resonates since α becomes infinite and Z_{electric} from (3.4) becomes purely resistive. From (3.12), it is clear that the frequency necessary for resonance is $\omega_\circ = \omega_p/\sqrt{3}$. Combining (3.4), (3.11) and (3.12), the circuit impedance simplifies to

$$Z_{\text{electric}} = \frac{dl^2}{j4\pi\omega a^3\epsilon_\circ} + \frac{j3dl^2\omega}{4\pi\omega_p^2 a^3} + \frac{dl^2k^3}{6\pi\epsilon_\circ\omega}. \tag{3.13}$$

This impedance is the same as that formed by a series RLC resonator with equivalent circuit values given in Fig. 3.1. The Q of this circuit is found from the ratio of the energy stored in the reactive circuit elements ($\sum |1/2Li^2| + |1/2Cv^2|$) to the energy dissipated by the resistor (i^2R) and is equal to,

$$Q_{\text{sphere}} = \frac{1.5}{(ka)^3}, \tag{3.14}$$

consistent with [90].

Comparing the results of [97] with (3.13), it can be seen that the negative permittivity material provides a distributed inductance (L_{sph}) which cancels the capacitance of the fringing electric fields (C_{fringe}) and the internal electric fields (C_{in}). Since the fields outside the sphere are identical to the fields of the TM_{10} spherical wave, the fact that $Q_{\text{sphere}} = 1.5\ Q_{\text{Chu}}$ implies that the electric energy internal to the sphere is half of the fringing electric energy. This fact allows the determination of a unique ratio of C_{fringe} to C_{in} in the equivalent circuit of Fig. 3.1, and provides physical insight into where exactly energy is stored.

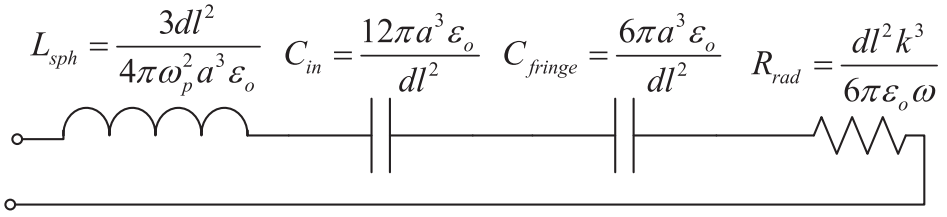

Figure 3.1: Equivalent circuit for the negative permittivity sphere.

Let's consider absorption by a negative permittivity sphere. To arrive at an equivalent circuit and radiation efficiency, the complex polarizability (α_c) is first found by substituting (3.12) into (3.11). Assuming a nonzero γ, α_c is given by,

$$\alpha_c = \frac{4\pi a^3 \omega_p^2}{3j\omega\gamma - 3\omega^2 + \omega_p^2}. \tag{3.15}$$

Then α_c is inserted into (3.9) and (3.10) to provide the impedance and the radiation efficiency, respectively. As expected, the equivalent circuit is identical to Fig. 3.1 except with an added resistor of value,

$$R_{\text{loss}} = \frac{3dl^2\gamma}{4\pi\epsilon_\circ\omega_p^2 a^3}. \tag{3.16}$$

Inserting α_c into (3.10), the efficiency at resonance ($\omega_\circ = \omega_p/\sqrt{3}$) is found to be,

$$\eta_{\text{rad}} = \frac{1}{1 + \frac{3\sqrt{3}\gamma}{2(ka)^3\omega_p}}, \tag{3.17}$$

identical to the results of [90].

3.4 Comparison to Other Small Antenna Circuit Models

In the previous sections, it was shown that knowledge of the frequency-dependent polarizability of an ESA can be used to easily develop an equivalent circuit model, which can in turn be used to calculate the antenna's Q and efficiency. Note that these equivalent circuits are valid for all frequencies for which the antenna is considered to be electrically small, and not just simply around the resonance. An antenna's Q can also be calculated by directly integrating the stored internal and external energies, as well as the power radiated [86]. However, the use of a circuit model provides further intuition into the antenna's operation, which can aid in design.

Others have also developed circuit models for ESAs. The circuit models developed in [87, 97, 98] are very useful for analyzing particular designs, but they are not applicable to as broad of a range of antennas as the Z_{electric} circuit model presented in this chapter. In [98], it is shown that a negative index material can be used to match an ESA to free space. However, some of the reactive circuit elements have negative values, which has limited physical meaning if the antenna is a passive device. In [97], it is demonstrated that nanocapacitors, nanoinductors and nanoresistors can be made

by simply distributing different plasmonic and dielectric materials into various geometries. However, no mention is made of radiative damping, which is necessary to model an ESA's Q and efficiency. In [97, 98], the values of the reactive components are frequency-dependent, whereas here they are only functions of the geometry and materials used to make the antenna. Also, there was no attempt in these papers to predict a small antenna's Q using a circuit model. A practical circuit model for the design of an ESA is shown in [87]. It provides a circuit model that can be used to analyze all the spherical modes, but is only valid for spherical wire antennas.

In [90], the use of a negative permittivity material to match an ESA is introduced, and the Q of the negative permittivity sphere is calculated from the scattering cross section (C_{sca}). However, this method involves using a Lorentzian approximation, which only models the behavior of the antenna near resonance.

3.5 Other Useful Geometries

One advantage of the technique presented here is that it can be applied to find the Q of several different electrically small antennas. All that needs to be known is the frequency response of the polarizability. In this section, the negative permittivity shell and spheroid are considered.

3.5.1 Negative Permittivity Shell

The negative permittivity shell, shown in Fig. 3.2(a), will be analyzed first. In [99], the polarizability was found to be

$$\alpha = 4\pi r_2^3 [\frac{\epsilon_n \epsilon_a - \epsilon_b}{\epsilon_n \epsilon_a + 2\epsilon_b}], \tag{3.18}$$

where,

$$\begin{aligned} \epsilon_a &= \epsilon_{in}(3-2T) + 2\epsilon_n T \\ \epsilon_b &= \epsilon_{in} T + \epsilon_n (3-T) \\ T &= 1 - (\frac{r_1}{r_2})^3. \end{aligned} \tag{3.19}$$

Combining (3.4), (3.12), and (3.18), the impedance $Z_{electric}$ can be found. This impedance can be represented by the circuit shown in Fig. 3.2(b). The values of the

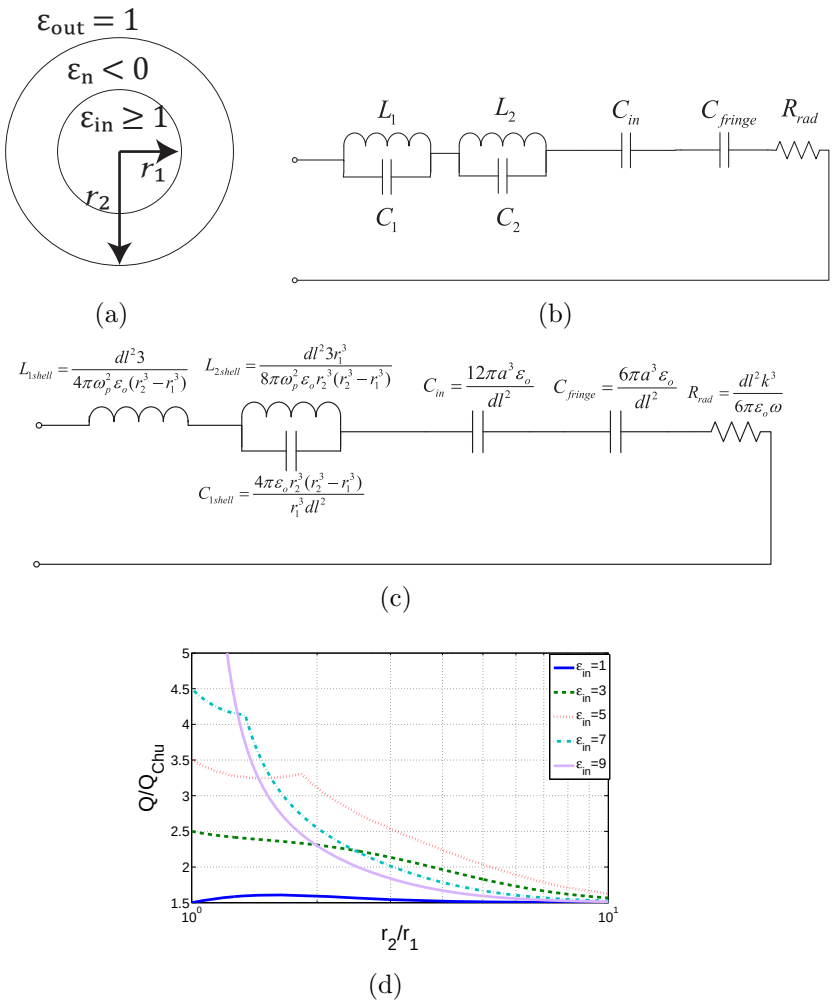

Figure 3.2: (a) Negative permittivity shell geometry. (b) Circuit model for a negative permittivity shell. (c) Simplified circuit model for a negative permittivity shell when $\epsilon_{\text{in}} = 1$. (d) Q at resonance for the circuit shown in Fig. 3.2(b) for various ratios of r_2/r_1 and ϵ_{in}.

circuit elements are:

$$\begin{aligned} L_1 &= \frac{3dl^2}{16}(2\epsilon_{\text{in}}r_1^6 + 2\epsilon_{\text{in}}r_2^6 - 13\epsilon_{\text{in}}r_1^3r_2^3 + 2xr_2^3 + r_1^3x \\ &\quad + r_1^6 + 4r_2^6 + 4r_2^3r_1^3)/(\pi\epsilon_\circ x\omega_p^2 r_2^3(r_2^3 - r_1^3)) \end{aligned}$$

$$\begin{aligned} L_2 &= \frac{3dl^2}{16}(-2\epsilon_{\text{in}}r_1^6 - 2\epsilon_{\text{in}}r_2^6 + 13\epsilon_{\text{in}}r_1^3r_2^3 + 2xr_2^3 + r_1^3x \\ &\quad - r_1^6 - 4r_2^6 - 4r_2^3r_1^3)/(\pi\epsilon_\circ x\omega_p^2 r_2^3(r_2^3 - r_1^3)) \end{aligned}$$

$$\begin{aligned} C_1 &= \frac{1}{dl^2}(8\pi\epsilon_\circ x r_2^3 r_1^3(\epsilon_{\text{in}} - 1))/(-6\epsilon_{\text{in}}^2 r_1^6 - 3\epsilon_{\text{in}}^2 r_2^3 r_1^3 \\ &\quad + r_2^3\epsilon_{\text{in}}x - r_1^3 x\epsilon_{\text{in}} + 12r_2^3 r_1^3\epsilon_{\text{in}} + 2xr_2^3 + r_1^3 x \\ &\quad - 3\epsilon_{\text{in}}r_1^6 + x^2) \end{aligned}$$

$$C_2 = \frac{1}{}(8\pi\epsilon_\circ x r_2^3 r_1^3(\epsilon_{\text{in}} - 1))/(-6\epsilon_{\text{in}}^2 r_1^6 - 3\epsilon_{\text{in}}^2 r_2^3 r_1^3$$

$$
\begin{aligned}
C_{in} &= \frac{12\pi r_2^3 \epsilon_\circ}{dl^2} \\
C_{fringe} &= \frac{6\pi r_2^3 \epsilon_\circ}{dl^2} \\
R_{rad} &= \frac{dl^2 k^3}{6\pi \epsilon_\circ \omega} \\
x &= (\epsilon_{\text{in}}^2 r_2^6 + 4\epsilon_{\text{in}}^2 r_2^3 r_1^3 + 4r_2^6 \epsilon_{\text{in}} - 26 r_2^3 \epsilon_{\text{in}} r_1^3 \\
&\quad + 4\epsilon_{\text{in}}^2 r_1^6 + 4\epsilon_{\text{in}} r_1^6 + 4r_2^6 + 4r_2^3 r_1^3 + r_1^6)^{1/2}.
\end{aligned}
$$

However, if the permittivity within the shell is equal to free space ($\epsilon_{\text{in}} = 1$), the circuit simplifies to that in Fig. 3.2(c). Similar to the negative permittivity sphere, the negative permittivity material acts as a distributed inductance to cancel the capacitance resulting from the fringing and internal electric field. However, within this distributed inductance, there is an additional positive internal permittivity (ϵ_{in}). This contributes an added capacitance C_{1shell}, which raises the stored energy and therefore the Q. The circuit model shows that the Q of the negative permittivity shell is always greater than the $Q_{\text{sphere}} = 1.5/(ka)^3$ of the negative permittivity sphere, since the shell's circuit contains added reactive components that store energy. For the circuit shown in Fig. 3.2(b), the minimum Q/Q_{Chu} at resonance vs. the ratio r_2/r_1 for various values of ϵ_{in} is plotted in Fig. 3.2(d). Since there are two inductors in the circuit, there exist two values of ω (or equivalently ϵ_{n}) that cause this structure to resonate. However, one of the resonances will provide a lower Q than the other. This physically means that there exists two possible modes which can radiate. Depending on the ratio r_2/r_1 and ϵ_{in}, either one of these modes may have the minimum Q. In Fig. 3.2(d), the locations where the traces are not smooth for $\epsilon_{\text{in}} = 5$ and $\epsilon_{\text{in}} = 7$, indicate points where two modes have the same Q.

The electric field profiles for the modes where the $\epsilon_{\text{in}} = 5$ trace is not smooth are plotted in Fig. 3.3. The incident electric field is polarized along the vertical axis, and the modes are azimuthally symmetric. Although the modes have different electric field profiles near the negative permittivity shell, they both have the far field radiation pattern of a small electric dipole.

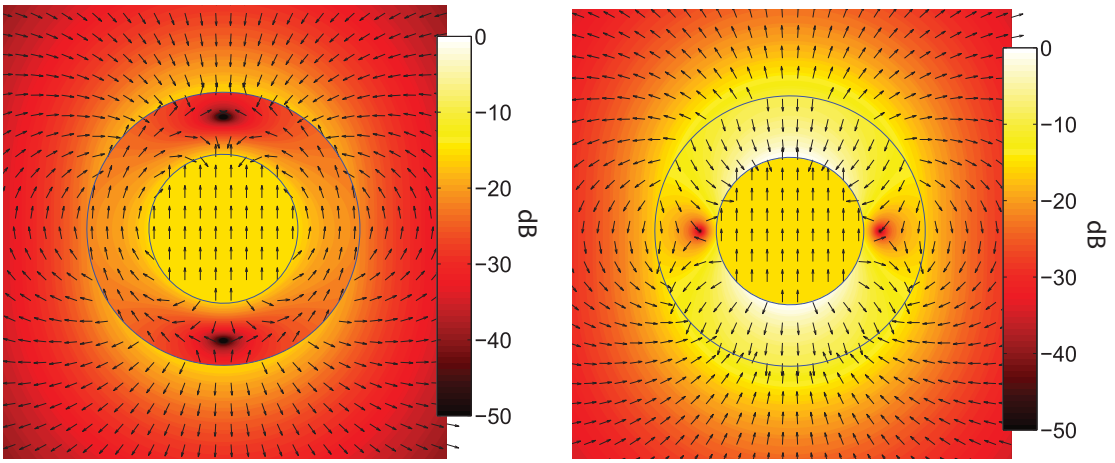

(a) (b)

Figure 3.3: Comparison of the normalized electric field of two different modes with the same Q. (a) $\omega = 0.388\omega_p$. (b) $\omega = 0.728\omega_p$. For both modes $r_2/r_1 = 1.83$, $\epsilon_{\text{in}} = 5$, and $Q = 3.3/(ka)^3$.

3.5.2 Negative Permittivity Spheroid

Another structure that will be investigated is the negative permittivity spheroid depicted in Fig. 3.4(a) [100–103]. The spheroid in Fig. 3.4(a) is rotationally invariant around the vertical axis. A spheroid is considered to be prolate (pencil-shaped) if $b > a$ and oblate (pancake-shaped) if $a > b$ (see Fig. 3.4(a)). The eccentricity of the spheroid is $e_p = \sqrt{1-(a/b)^2}$ if it is prolate, and $e_o = \sqrt{1-(b/a)^2}$ if it is oblate. If $\vec{E}_\circ$ is polarized along the vertical axis, the polarizability of a spheroid is [102]

$$\alpha = \frac{4\pi a^2 b(\epsilon_s - 1)}{3f(\epsilon_s + (1/f - 1))}, \tag{3.20}$$

where,

$$f = \frac{1-e_p^2}{e_p^2}\left(-1 + \frac{1}{2e_p}\ln\frac{1+e_p}{1-e_p}\right) \tag{3.21}$$

for a prolate spheroid and,

$$f = \frac{1}{e_o^2} - \frac{\sqrt{1-e_o^2}}{e_o^3}\left[\frac{\pi}{2} - \tan^{-1}\frac{\sqrt{1-e_o^2}}{e_o}\right] \tag{3.22}$$

for an oblate spheroid. The parameter f is dimensionless and depends only on the ratio b/a. It ranges between 0 (prolate) and 1 (oblate).

From (3.20), it can be seen that if $\epsilon_s = 1 - 1/f$, α becomes infinite causing the spheroid to resonate. Again combining (3.4), (3.12), and (3.20), the circuit impedance

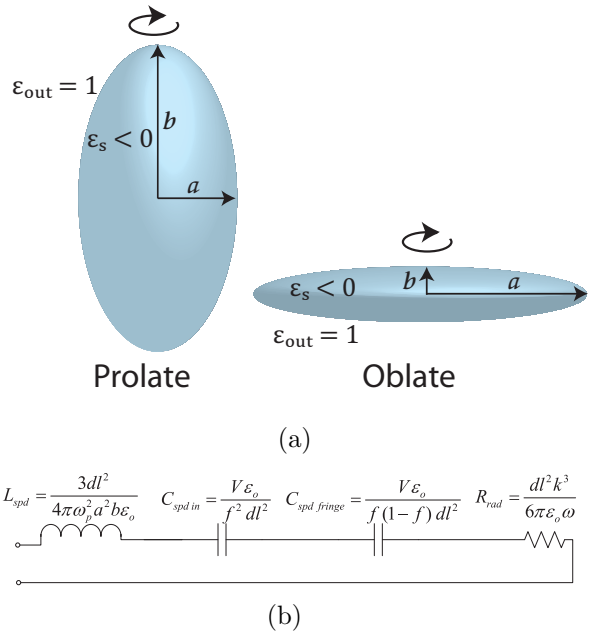

Figure 3.4: (a) Negative permittivity spheroid geometry. (b) The circuit model for the negative permittivity spheroid.

Z_{electric} can be found. Similar to the negative permittivity sphere, the impedance is equivalent to that of a series RLC circuit, but with the values given in Fig. 3.4(b). The stored energy in the fringing and internal electric fields can be found from [88], which provides the values of $C_{spd\ in}$ and $C_{spd\ fringe}$. When $a = b$, f reduces to 1/3, and the circuit simplifies to that for a negative permittivity sphere. The Q of the circuit in Fig. 3.4(b) at resonance is,

$$Q_{\text{spheroid}} = \frac{6\pi f}{Vk^3}, \tag{3.23}$$

where V is the volume of the spheroid. This is identical to the result in [96] and is also equal to the minimum Q for a spheroidal geometry that is fed with electric currents only [88]. It should be noted that f is defined differently here than in [96]. The value of Q normalized to the Chu limit is plotted for various ratios of b/a in Fig. 3.5. The fact that Q varies much less rapidly for prolate spheroids than for oblate spheroids as the ratio b/a changes, suggests that pencil-shaped geometries are preferable to pancake-shaped geometries. Also note that Fig. 3.5 differs from that in [100], since the analysis presented in this chapter considers stored energy internal to the spheroid in addition to the energy external to it.

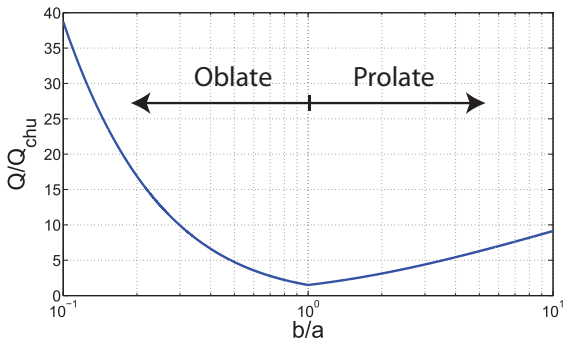

Figure 3.5: Q/Q_{Chu} of a negative permittivity spheroid for various ratios of b/a

3.5.3 Inductively Loaded Dipole

In the previous examples, a negative permittivity material was used to provide a distributed inductance. This inductance cancelled the capacitance of the fringing electric fields which are inherent to electrically small antennas that radiate the TM_{10} mode. However, the use of a negative permittivity material requires a bulk medium. Either the antenna must operate at very high frequencies (typically above 30 THz) where negative permittivity occurs naturally, or it can be achieved using plasmas [104, 105] or metamaterials [106, 107], which can be challenging.

Next, some more conventional ESAs are considered. First, let's consider a short wire dipole, loaded with a 240 nH inductor at its center, as shown in Fig. 3.6(a). The wire is perfect electrically conducting (PEC), with a 0.2 mm radius and a 20 mm length. The antenna was designed to resonate near 1 GHz ($ka = 0.210$).

To arrive at an equivalent circuit, we first need to find the frequency-dependent polarizability of this antenna. This example differs from all the previous examples in that a closed-form expression for the polarizability of a short conducting cylinder does not exist [89]. Therefore the polarizability must be solved numerically. Here, we used a commercial finite element electromagnetic solver, Ansoft's HFSS, to numerically solve for the polarizability.

To begin, the antenna is excited with a plane wave traveling in the $\hat{y}$ direction with a $\hat{z}$ polarized incident electric field. The scattered far field is found and can be represented as the sum of a $\hat{z}$ directed electric dipole and a $\hat{x}$ directed magnetic dipole whose amplitudes are proportional to the polarizabilities α_e and α_m respectively. The

radar cross section $\sigma(\theta, \phi)$ can be easily related to the polarizabilities [108],

$$\sigma(\theta,\phi) = \frac{k^4 \left|\alpha_m^{\text{eff}} \sin(\phi) + \alpha_e^{\text{eff}} \sin(\theta)\right|^2}{4\pi} + \frac{k^4 \left|\alpha_m^{\text{eff}} \cos(\phi)\cos(\theta)\right|^2}{4\pi}, \tag{3.24}$$

where

$$\alpha_{e,m}^{\text{eff}} = \frac{\alpha_{e,m}}{1 + j\frac{\alpha_{e,m} k^3}{6\pi}}. \tag{3.25}$$

Here, $\alpha_{e,m}^{\text{eff}}$ is the effective electric or magnetic polarizability that accounts for radiative damping (see Section 3.2).

Now there are several ways in which $\alpha_{e,m}$ can be solved for. The simplest method would be to simply find $\sigma(\theta, \phi)$ along two different directions which results in two equations and two unknowns to be solved. However, a more accurate approach would be to take advantage of the fact that a single simulation provides $\sigma(\theta, \phi)$ in all directions. In this case, the system of equations is overdetermined, and a least squares method can be used to find a solution that is robust against small simulation errors. However, there is no closed form solution to finding the values of α_e and α_m that minimize the squares of the residuals, since the equations are nonlinear. MATLAB's optimization toolbox was used to find a numerical solution by utilizing an active-set algorithm [109]. To verify the accuracy of this method, the extracted polarizability was compared to theory by simulating a PEC sphere, which has an analytical solution. The error was less than 0.1% between the numerically found polarizability and the analytical solution to the polarizability.

The frequency-dependent polarizability extracted from simulation is then inserted into (3.4), which is used to find the input impedance in the circuit model. Next, the actual circuit elements that model this impedance are found. These reactive circuit elements are found by first noting the form of the impedance, and then using MATLAB's non-linear curve fitting tool to find their values. For example, the reactance of the circuit model based on the extracted polarizability is plotted in Fig. 3.6(b). We note that the form of the reactance is identical to that of a series LC resonator which is in parallel with a capacitor, as shown in Fig. 3.6(c). We then used MATLAB's non-linear curve fitting tool to numerically solve for the values of the circuit elements. Fig. 3.6(b) illustrates the accuracy of the circuit model based on the numerically extracted polarizability and (3.4). It can be seen that there is excellent agreement over all frequencies less than 5 GHz ($ka < 1$). This general procedure can be used to find

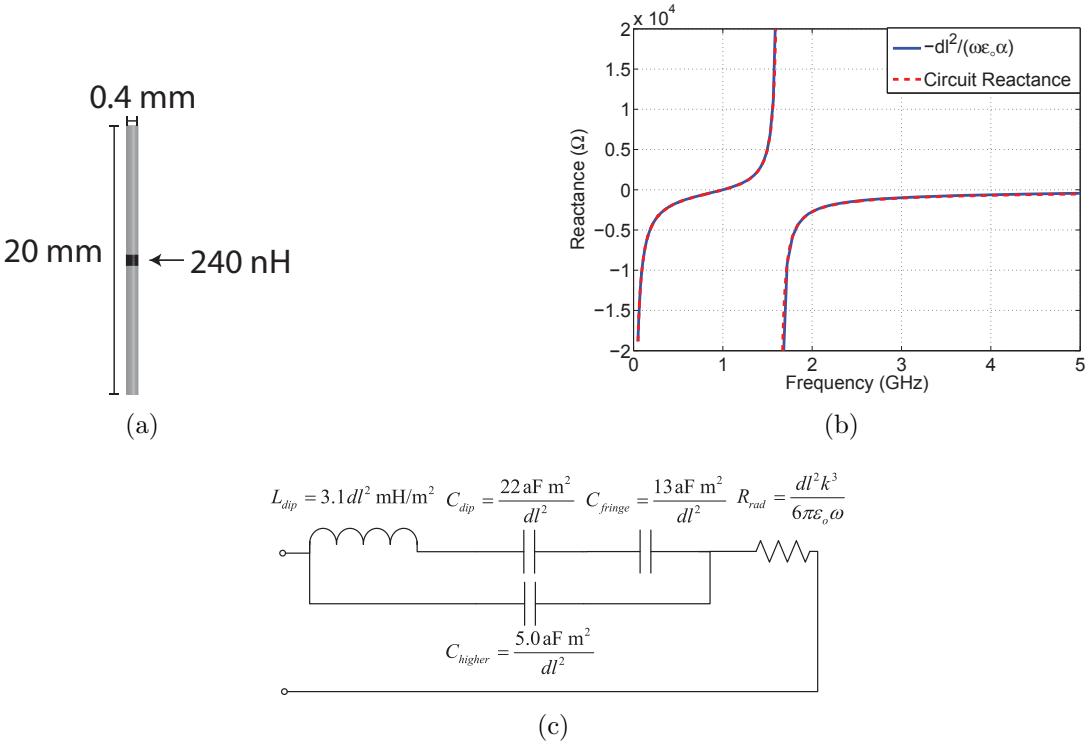

Figure 3.6: (a) Inductively loaded dipole geometry. (b) Comparison of the reactance of the circuit model and the reactance from (3.4). (c) Circuit model for the inductively loaded dipole.

the equivalent circuit of an arbitrary small antenna that does not have a closed-form polarizability.

The equivalent circuit that models this antenna is shown in Fig. 3.6(c). Again we can gain insight into where exactly energy is stored by extracting the capacitance due to the fringing electric field (C_{fringe}) that is inherent to the geometry of the antenna [88]. However, the fringing electric energy inherent to this geometry accounts for only 60% of the actual stored electric energy. In the previous examples, the additional electric energy was stored in the electric field that is internal to the antenna. However, the internal energy here accounts for less than 1% of the total amount due to the small volume of the antenna. The remaining energy is due to the non-ideal current distribution along the dipole. An inductively loaded, short dipole antenna exhibits a triangular current distribution whereas the current distribution of an unloaded short dipole is parabolic [91]. We know that the parabolic current distribution of the unloaded short dipole exhibits the lowest possible stored energy [88]. Therefore, the added energy due to the triangular current distribution must be modelled by an additional capacitor (C_{dip}). A similar result was obtained in [110], where it was

shown that as the current distribution becomes more uniform, the Q decreases. By separating C_{fringe} from C_{dip} it can be easily seen that a single inductive loading placed in the center of a short wire dipole does not provide the optimal Q for the given geometry.

In addition, there is a capacitance C_{higher}, which models the electric energy that results from higher order modes [111]. This capacitance does not affect the Q at resonance, but is necessary if the equivalent circuit is to model the antenna at all frequencies in which the antenna is electrically small. It is responsible for the diverging reactance near 1.6 GHz in Fig. 3.6(b).

The circuit has a Q that is 1.6 times the fundamental limit for the minimum cylinder that circumscribes the antenna and is excited with electric currents only [88]. This also corresponds to $Q = 20.5Q_{\text{Chu}}$, which illustrates the advantage that spherical geometries have over cylindrical ones.

One common approximation that is made is that the minimum Q of the wire dipole is the same as that of the prolate spheroid whose major and minor axes are the height and width respectively [88, 103]. As the ratio of the height to width approaches infinity, this assumption becomes accurate. However, for more realistic antennas, this assumption results in a significant error. For a height to width ratio of 50 as shown here, the minimum Q of the cylinder is 25% lower than that of the spheroid. This suggests the polarizability must be solved numerically for practical wire antennas, which are not extremely thin.

3.5.4 Top-Hat Loaded Dipole

Another common ESA is the top-hat loaded dipole, as depicted in Fig. 3.7(a). The top-hat of the antenna significantly increases the capacitance at the dipole ends so that a much smaller lumped inductor is needed to achieve resonance at a given frequency. The antenna was designed to have roughly the same size ($ka = 0.211$) and frequency as the inductively loaded dipole in Fig. 3.6(a). The exact dimensions of the antenna are shown in Fig. 3.7(a). In addition to a top-hat, it is also loaded with a 18.8 nH inductor to further miniaturize its size.

Again there is no analytical expression for the polarizability of this antenna. We therefore followed the same approach as in the previous subsection to find the polarizability, and thus the equivalent circuit. A comparison of the reactive impedance from (3.4) and the reactance of the equivalent circuit over all frequencies for which $ka < 1$ is shown in Fig. 3.7(b). It can be seen that the two curves begin to diverge near 3.5 GHz ($ka = 0.75$). The reason for this is that as the antenna becomes electrically

large ($ka > 0.5$), additional circuit elements may be required to correctly represent the stored energy in the higher order modes. The equivalent circuit is shown in Fig. 3.7(c). In the circuit model, C_{fringe} and C_{in} account for the electric energy that is stored in the fringing and internal electric fields, respectively. Again, there is an additional C_{hat} that models the energy that is due to the non-ideal current distribution. It should be noted though, that C_{hat} is very large, and stores roughly only 8% of the total electric energy. This suggests that the top-hat loaded dipole makes fairly efficient use of its volume. The circuit has a Q that is 1.08 times the fundamental limit for the minimum cylinder that circumscribes the antenna and is excited with electric currents only [88]. This corresponds to a $Q = 9.4Q_{\text{Chu}}$.

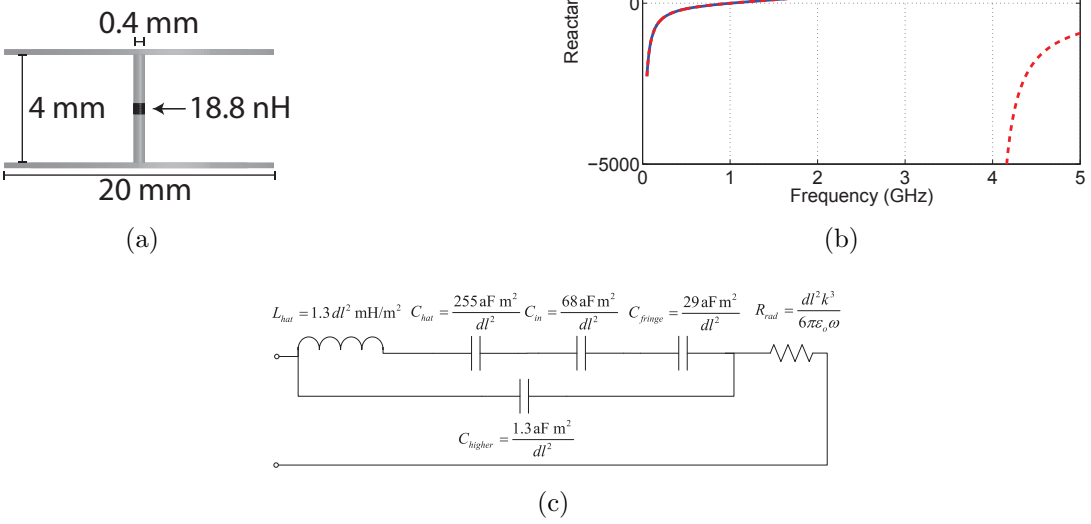

Figure 3.7: (a) Top-hat loaded dipole geometry. (b) Comparison of the reactance of the circuit model and the reactance from (3.4). (c) Circuit model for the top-hat loaded dipole.

3.6 Spherical Impedance Sheet

In the previous section, it was shown how a negative permittivity material can provide a distributed inductance which allows the Q to approach the Chu limit. Another way to provide a distributed inductance is through the use of an inductive sheet impedance. If a dielectric sphere is covered with an inductive sheet impedance, the

sheet impedance can resonate with the (capacitive) fringing electric fields. Furthermore, an inductive sheet impedance is easier to fabricate than a negative permittivity medium. Once the desired sheet impedance is determined, it can be realized using techniques from frequency selective surface (FSS) design [112]. For example, a metallic grid could be printed onto the surface of the dielectric sphere. In contrast, the use of a capacitive sheet impedance can be used to create an ESA that radiates the TE_{10} mode, similar to a magnetic dipole.

The use of a sheet impedance has been recently used to achieve cloaking [113]. The goal in cloaking applications is exactly opposite to the goal here. For a cloak, the desired sheet impedance causes the polarizability to approach zero in order to provide minimal scattering, while in antenna applications the polarizability approaches infinity.

A design approach similar to that in [113] will be followed. A plane wave illuminates a sphere covered by an infinitesimally thin sheet impedance. The sphere is assumed to have a radius a, relative permittivity ϵ_s, relative permeability μ_s, and wavenumber $k_s = \omega\sqrt{\mu_s\mu_\circ\epsilon_s\epsilon_\circ}$ within it. The fields inside and outside the dielectric are expressed as spherical waves. They are related to each other by Ampere's law at the surface of the sphere. The sheet impedance η_s obeys the following relation,

$$\vec{E}_{\tan} = \eta_s \vec{J}_{\mathrm{surf}}, \tag{3.26}$$

where $\vec{E}_{\tan}$ is the tangential electric field and $\vec{J}_{\mathrm{surf}}$ is the electric surface current. By choosing the correct sheet impedance η_s, the surface currents will resonate, forcing the scattered fields to become much larger than those of the incident plane wave. For example, if one desires to force the nth TM mode to radiate, the necessary sheet impedance is,

$$\eta_s = \frac{jk\sqrt{\mu_s}\widehat{H}_n'(ka)\widehat{J}_n'(k_s a)}{\omega\epsilon_\circ(\sqrt{\epsilon_s}\widehat{H}_n'(ka)\widehat{J}_n(k_s a) - \sqrt{\mu_s}\widehat{H}_n(ka)\widehat{J}_n'(k_s a))}, \tag{3.27}$$

where $\widehat{H}_n(\cdot)$ and $\widehat{J}_n(\cdot)$ are the spherical Bessel-Schelkunoff functions such that $\widehat{B}_n(\cdot) = \sqrt{\pi kr/2}B_{n+1/2}(\cdot)$, with $B_n(\cdot)$ being the ordinary Bessel functions of the first, second, and third kind [108].

For electrically small antennas, it is usually desired to only radiate the lowest order TM_{10} or TE_{10} modes, since they have the lowest Qs. Assuming $ka \ll 1$ and taking only the small argument expressions for the Bessel-Schelkunoff functions, the necessary sheet impedances for radiation of the TM_{10} and TE_{10} modes are found to

be:

$$\text{TM}_{10}\text{: } \eta_s = \frac{2j}{\omega a \epsilon_\circ (\epsilon_s + 2)} \tag{3.28}$$

$$\text{TE}_{10}\text{: } \eta_s = \frac{\omega a \mu_s \mu_\circ}{j(2 + \mu_s)}. \tag{3.29}$$

3.6.1 TM radiation

When only the TM_{10} mode is excited, the necessary sheet impedance is imaginary and positive (inductive). It is assumed to obey Foster's reactance theorem, and have a frequency response $\eta_s = j\omega L_s$, where $L_s = 2/(\omega_\circ^2 a \epsilon_\circ (\epsilon_s + 2))$ is found from (3.28) for a given frequency of operation $\omega_\circ$. By relating the field strength of the scattered TM_{10} fields to those of an electric dipole, the electric polarizability is found to be,

$$\alpha = \frac{4\pi a^3 (2 + j\omega \eta_s a \epsilon_\circ (\epsilon_s - 1))}{2 + j\omega \eta_s a \epsilon_\circ (\epsilon_s + 2)}. \tag{3.30}$$

By inserting (3.30) into (3.4) the equivalent circuit shown in Fig. 3.8 can be found. In general the Q at resonance is given by,

$$Q_{\text{TMsheet}} = \frac{1 + \epsilon_s/2}{(ka)^3}. \tag{3.31}$$

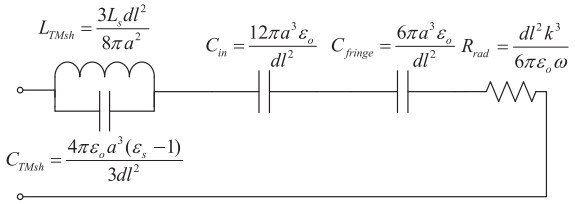

Figure 3.8: Equivalent circuit for the inductive sheet impedance radiating the TM_{10} mode

When the dielectric inside is equal to free space, C_{TMsh} becomes 0 and the circuit simplifies to that of the series RLC circuit with a Q equal to $1.5/(ka)^3$. When the dielectric inside is free space, the circuit elements for the inductive sheet impedance are identical to those for the negative permittivity sphere. Although the negative permittivity sphere and inductive sheet impedance may seem to operate under different principles, they are identical with respect to their frequency response and Q.

One method of achieving an inductive sheet impedance is through winding wires around a sphere such as in spherical helix antennas [114]. To demonstrate the similar-

ities between an ideal inductive sheet impedance and the spherical helix antenna, the scattering cross section (C_{sca}) vs. frequency for both were simulated using Ansoft's HFSS (see Fig. 3.9). The C_{sca} was found for two spherical helix antennas similar to those presented in [114], with their terminals short circuited. Both antennas have a radiation resistance of 50 Ω when fed at their terminals. The spherical helix in Fig. 3.9(a) has a radius of 58.9 mm ($ka = 0.38$), 4 arms with 1 turn per arm, and the width of each arm is 2.64 mm. The spherical helix in Fig. 3.9(b) has the same radius of 58.9 mm ($ka = 0.12$), 8 arms with 3.5 turns per arm, and the width of each arm is 1 mm. Next, C_{sca} was found for the ideal inductive spherical sheet impedances. The inductive sheet impedances ($\eta_s = j\omega L_s$) were designed to have the same resonant frequencies as the spherical helix antennas, and L_s was found using the imaginary part of the result obtained from (3.27). Eqn. (3.27) was used instead of (3.28) in order to account for the finite electrical size of the sphere. The resulting impedance found from the two equations differs by 10% when $ka = 0.38$ and 1% when $ka = 0.12$.

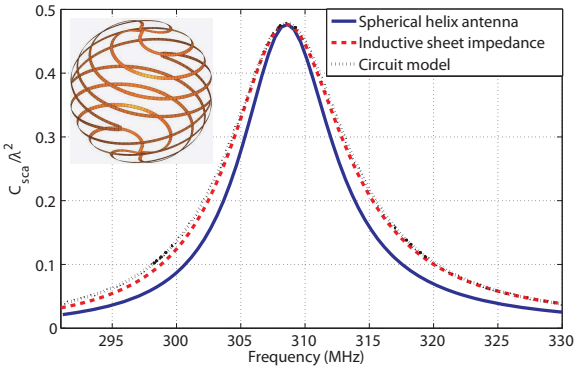

(a)

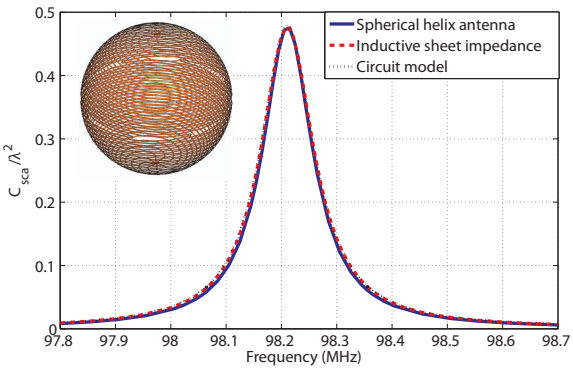

(b)

Figure 3.9: Comparison of the spherical helix antenna with an inductive spherical sheet impedance. C_{sca} vs frequency for the 4 armed (a) and 8 armed (b) spherical helix antennas and their equivalent inductive sheet impedances.

The simulated resonant frequency for the inductive sheet impedance was about 0.3% greater than the designed value. The slight frequency shift is attributed to numerical errors in the finite element (HFSS) simulation of the inductive sheet impedance. Therefore, to provide a better comparison between the spherical helix antenna and the inductive sheet antenna, a frequency-shifted version of C_{sca} for the inductive sheet impedance is plotted in Fig. 3.9. The frequency response of the spherical helix antenna is very similar to that of the ideal inductive sheet impedance. In [114], it was stated that as the length of each metal arm increased, the antenna's Q more closely approached the Chu limit. This is consistent with the assumption that it is well approximated by an inductive sheet impedance. As the metal on the spherical helix covers more area, it more closely approximates a sheet impedance that covers the entire surface area. This is evidenced by the results shown in Fig. 3.9. The scattering bandwidth for the 8 armed spherical helix antenna is very similar to the scattering bandwidth of its equivalent inductive sheet impedance. This is in contrast to the 4 armed spherical helix antenna, which has a noticeably smaller scattering bandwidth. Since the entire surface of the inductive sheet impedance is covered with currents, its radiation resistance and bandwidth are larger.

It is also possible to predict C_{sca} using the circuit model in Fig. 3.8. A plane wave excitation corresponds to simply exciting the circuit model with a voltage source of amplitude $E_\circ dl$. The power scattered by the antenna (P_{rad}) is identical to the power dissipated across R_{rad}, which can in turn be used to predict C_{sca},

$$C_{sca} = \frac{P_{\text{rad}}}{\frac{1}{2}\sqrt{\frac{\epsilon_\circ}{\mu_\circ}}|E_\circ|^2} = \frac{8\pi}{3}k^4a^6\frac{\omega_\circ^4}{\left(\omega^2-\omega_\circ^2\right)^2+\left(\omega_\circ^2\frac{2k^3a^3}{3}\right)^2}. \tag{3.32}$$

The scattering cross section predicted using the circuit model is also plotted in Fig. 3.9 and agrees well with the simulations. By comparing 3.9(a) with 3.9(b), it can be seen that as the electrical size of the antenna decreases, the circuit model more accurately predicts C_{sca} for the inductive sheet impedance. It is also not surprising to note that the expression for C_{sca} in (3.32) is identical to that of the negative permittivity sphere in [90] since the equivalent circuits are the same for these two structures.

3.6.2 TE radiation

The TE_{10} mode is also of interest since the Q of this mode can closely approaches the Chu limit if high permeability materials are used [87, 115]. For the case of TE

modes, much of the analysis is as before except that quantities are replaced by their duals. For example, a small magnetic dipole radiates the TE_{10} mode, while a small electric dipole radiates the TM_{10} mode. Since the analysis in Section 3.2 dealt with a small electric dipole, some changes needed to be made to analyze the magnetic dipole.

To begin, a magnetic polarizability given by $\vec{P}_m = \alpha_m \vec{H}_\circ$ must be defined, which relates the scattered fields of the antenna to those of a magnetic dipole. Assuming the fields are quasi-static in the near field of the antenna, it is found that $I_m = j\omega\alpha_m\mu_\circ \vec{H}_\circ \cdot \vec{dl}/dl^2$ where I_m is magnetic current. Therefore, $I_m/(\vec{H}_\circ \cdot \vec{dl}) = j\omega\alpha_m\mu_\circ/dl^2$ represents Z_{magnetic} for small antennas that radiate as magnetic dipoles. After considering the effects of radiative damping, (3.3) is again arrived at for the effective magnetic polarizability. Assuming α_m is purely real (lossless), the equivalent circuit impedance is,

$$Z_{\text{magnetic}} = \frac{1}{\frac{dl^2}{j\omega\mu_\circ\alpha_m} + \frac{dl^2k^3}{6\pi\mu_\circ\omega}}. \tag{3.33}$$

The term $j\omega\alpha_m\mu_\circ/dl^2$ represents the impedance of a reactive circuit element in parallel with a resistor of value $6\pi\mu_\circ\omega/(dl^2k^3)$. When considering an antenna that scatters the TE_{10} mode, an analysis similar to that used in the previous sections can be performed. The most significant difference is that α is replaced with α_m, and (3.4) is replaced with (3.33).

Let's now consider scattering by a magnetic sphere surrounded by a sheet impedance. The sheet impedance, η_s, is given by (3.29) to ensure that the antenna radiates the TE_{10} mode. We will assume that only electric currents can be supported by the sheet. The sheet impedance is negative and imaginary (capacitive), so it is assumed to be of the form $\eta_s = 1/(j\omega C_s)$, where $C_s = (2+\mu_s)/(\omega_\circ^2 a\mu_s\mu_\circ)$ is found from (3.29) for a given frequency of operation $\omega_\circ$. Then comparing these fields with those of a magnetic dipole, α_m is given by,

$$\alpha_m = \frac{2\pi a^3 j((2\mu_s - 2)\eta_s - ja\mu_s\mu_\circ\omega)}{(\mu_s + 2)j\eta_s - a\mu_s\mu_\circ\omega}. \tag{3.34}$$

Inserting (3.34) into (3.33) and assuming that $\mu_s \geq 1$ provides the impedance (Z_{magnetic}) of the equivalent circuit, shown in Fig. 3.10. At the operating frequency, C_{TEsh} resonates with the internal and fringing magnetic fields (L_{in} and L_{fringe}). As the permeability increases, the magnetic energy stored within the sphere (L_{in}) decreases thereby lowering the Q. If we ignore the self inductance of the feed (L_{Feed}), and the presence of the sheet impedance ($\eta_s \to \infty$), the circuit simplifies to an inductor (L_{TEpol}) in parallel with a resistor (R_{rad}). Therefore the energy stored in L_{TEpol} is

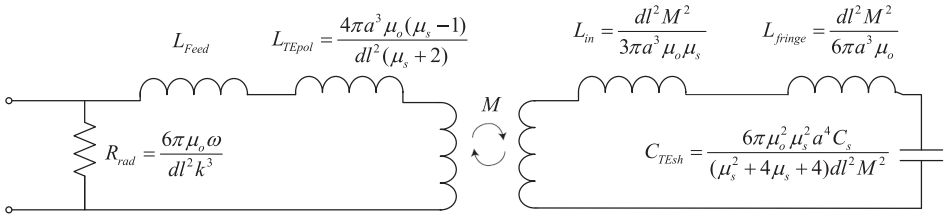

Figure 3.10: Equivalent circuit near resonance for the capacitive sheet impedance radiating the TE_{10} mode

proportional to the energy stored in the polarization currents of the magnetic sphere.

The variable M represents the mutual inductance between the feed and the antenna. In the circuit model, $M^2 > (L_{in} + L_{fringe})L_{TEpol}$. This means that without modelling the self inductance of the feed, (L_{Feed}), the total, stored energy can be negative which is unphysical. Therefore L_{Feed} and M must satisfy the relation, $M^2 < (L_{in} + L_{fringe})(L_{TEpol} + L_{Feed})$. This suggests that the value of M is determined by the geometry of the feed. It is also interesting to note that M has no effect on the Q for any frequency, and that L_{Feed} and L_{TEpol} have no effect on the Q at resonance. At resonance,

$$Q_{\mathrm{TEsheet}} = \frac{1 + 2/\mu_s}{(ka)^3}, \tag{3.35}$$

consistent with the results of [87,115]. From (3.35), it can be seen that increasing the permeability of the sphere lowers the Q. This is in contrast to the case of the electric dipole, where increasing the permittivity of the sphere increases the Q.

3.7 Feeding

Thus far, it was assumed that the analyzed ESAs were excited by a plane wave. This provided insight into how they operate independent of their feed. A realistic antenna however, requires a feed. The plane wave excitation allows the determination of an unloaded Q of the structure, which is the quality factor of the antenna assuming the feed can perfectly couple energy to the structure, without affecting its operation. The overall quality factor that includes the feed is known as the loaded Q, and if designed properly, can closely approach the unloaded Q. The feed also increases or decreases the radiation resistance of the antenna so that it can be impedance matched.

Fortunately the effects of a feed can be obtained straightforwardly from the circuit model. For example, let's first revisit the negative permittivity sphere which has the series RLC equivalent circuit shown in Fig. 3.1. An antenna design previously

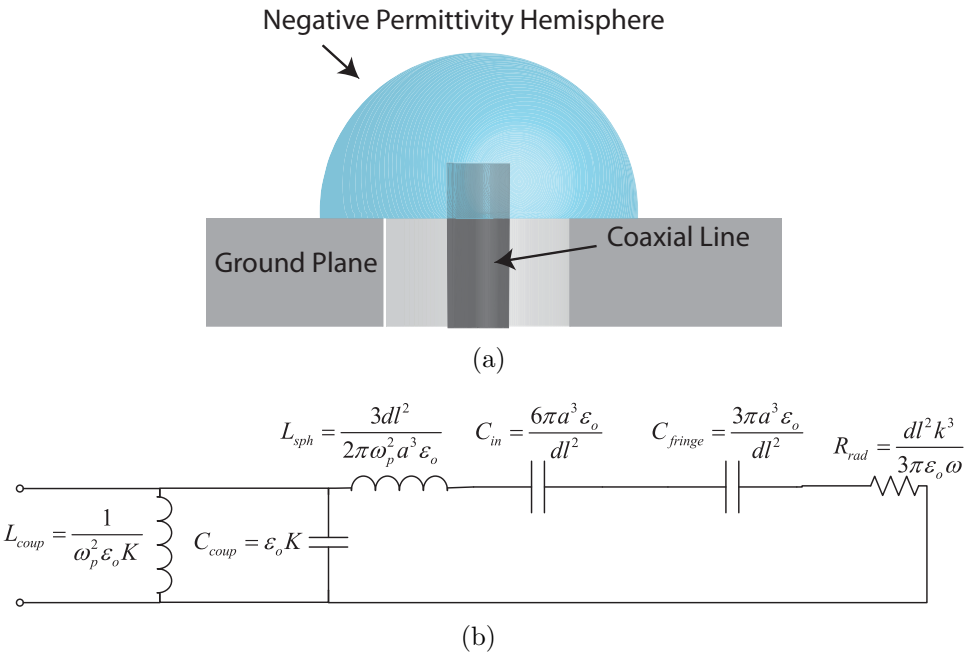

Figure 3.11: (a) Negative permittivity hemisphere fed by a coaxial cable. (b) Circuit model for a negative permittivity hemisphere including the coaxial feed.

considered in [90] consisted of a negative permittivity hemisphere over a ground plane. It was fed by a short monopole stub connected to a coaxial transmission line, as shown in Fig. 3.11(a) [90]. The negative permittivity hemisphere is assumed to have a plasma frequency $f_p = 3.54$ GHz and radius $a = 8$ mm, which corresponds to an electrical size of $ka = 0.34$. The coaxial cable has an inner conductor radius of 1.5 mm and an outer conductor radius of 3.5 mm. The vertical electric field of the feed couples to the resonant mode of the negative permittivity sphere to provide a return loss greater than 35 dB at 2.026 GHz, and a loaded Q equal to 1.47 times the Chu limit.

Essentially the coaxial transmission line is capacitively coupled to the negative permittivity sphere. In the circuit model, this corresponds to a coupling capacitor that is in parallel with the impedance of the negative permittivity sphere, Z_{electric}. However, this coupling capacitor is filled with a negative permittivity dielectric that has a Drude frequency response. The dispersion of the dielectric affects the equivalent circuit of the coupling capacitor. The capacitance will be of the form $C = \epsilon_\circ \epsilon_s K$, where K is a constant that depends on the geometry of the capacitor. If ϵ_s has a Drude response given by (3.12), the impedance of the coupling capacitor filled with

a negative permittivity becomes,

$$Z_{\text{cap}} = \frac{1}{j\omega\epsilon_\circ K + \frac{\omega_p^2 \epsilon_\circ K}{j\omega}}. \tag{3.36}$$

Z_{cap} has the same form as an inductor and capacitor in parallel with values $C_{coup} = \epsilon_\circ K$ and $L_{coup} = 1/(\omega_p^2 \epsilon_\circ K)$. By adjusting the height of the monopole stub, the value of K can be tuned to provide an impedance match to 50 Ω. For this design, the optimum stub height was found to be 3 mm. The overall equivalent circuit which combines Z_{electric} of the sphere with Z_{cap} of the feed is shown in Fig. 3.11(b). Note that the impedance of a monopole antenna over a ground plane is twice that of its dipole equivalent. Therefore the impedance in (3.4) was doubled to arrive at the circuit in Fig. 3.11(b). However, the exact values of dl and K are still unknown. Although their exact values do not affect the Q significantly, they are important because they determine the impedance match of the antenna. To determine their values, the antenna was simulated at three different frequencies near resonance. If a slight frequency shift Δf is also allowed between the simulated antenna and the circuit model due to the fact that the simulated antenna has a notable electrical size, there are now three unknown variables, (dl, K, Δf). By requiring the input impedance of the circuit model to be equal to that of the simulated antenna at three separate frequencies, we arrive at three equations and three unknowns which can be solved. For the antenna shown here, dl = 26.2 mm, K = 19.7 mm, and Δf = 10.4 MHz.

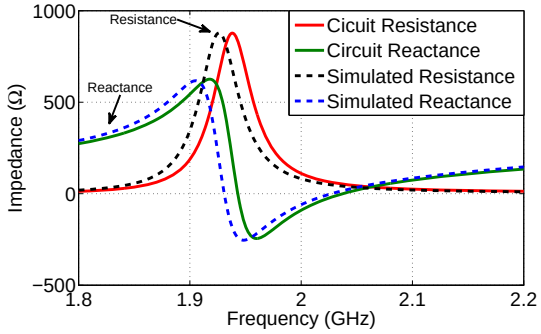

Figure 3.12: Comparison of the input impedance of the equivalent circuit shown in Fig. 3.11(b) with the simulated design shown in Fig. 3.11(a).

To demonstrate the accuracy of this model, Fig. 3.12 shows the input impedance of the circuit shown in Fig. 3.11(b) compared with the simulated input impedance. The impedance and quality factor of the equivalent circuit indeed matches the simulated

antenna very well. The circuit has a loaded $Q = 1.50/(ka)^3$. Finally, it should be noted that the inductor and capacitor L_{coup} and C_{coup} in 3.11(b) provide an impedance transformation that dramatically increases the radiation resistance to 50 Ω while at the same time negligibly affects the Q. This result is consistent with the various matching techniques demonstrated in [116].

In addition to the negative permittivity sphere, the feed of the inductively loaded dipole and the top-hat loaded dipole were also analyzed. These antennas are often cut in half and placed over a large (assumed to be infinite) ground plane to form a monopole since a monopole can be directly fed with a coaxial transmission line, as shown in Figs. 3.13(a) and 3.14(a). Since both of these antennas have very small radiation resistances, small inductive stubs need to be added in parallel with the feed to provide an impedance match to 50 Ω [116]. For the inductively loaded dipole and top-hat loaded dipole, the necessary inductances were found to be $L_{shunt} = 0.7$ nH and $L_{shunt} = 0.28$ nH, respectively. For both structures the return loss from simulation and the circuit model is greater than 20 dB. Again, the shunt inductors have little effect on the Q.

To find the effective height (dl), we could employ the same method used for the negative permittivity hemisphere. However, a simpler approach is to find dl by requiring that the inductances in the circuit model are equal to the actual ones used in simulation. We were unable to use this approach when analyzing the negative permittivity hemisphere because the negative permittivity provided a distributed inductive loading, whose equivalent lumped element value was unknown. Using this approach, the effective height of the inductively loaded and top-hat loaded monopoles were found to be 4.42 mm and 1.90 mm, respectively.

The equivalent circuit for the inductively loaded monopole is shown in Fig. 3.13(b). It has a $Q = 20.4Q_{\text{Chu}}$, which is within 1% of the quality factors of the simulated antenna and the unloaded structure analyzed in Section 3.5.3. Fig. 3.13(c) shows a comparison of the simulated input impedance and input impedance of the circuit model near resonance. The results agree very well and there is only a minimal frequency shift due to the notable electrical size.

The equivalent circuit for the top-hat loaded monopole is shown in Fig. 3.14(b). The Q of the circuit model and the simulated structure are both $Q = 9.4Q_{\text{Chu}}$, agreeing with the earlier result of Section 3.5.4. A comparison of the input impedances for the circuit model and simulated structure can be seen in Figs. 3.14(c), and there is very good agreement.

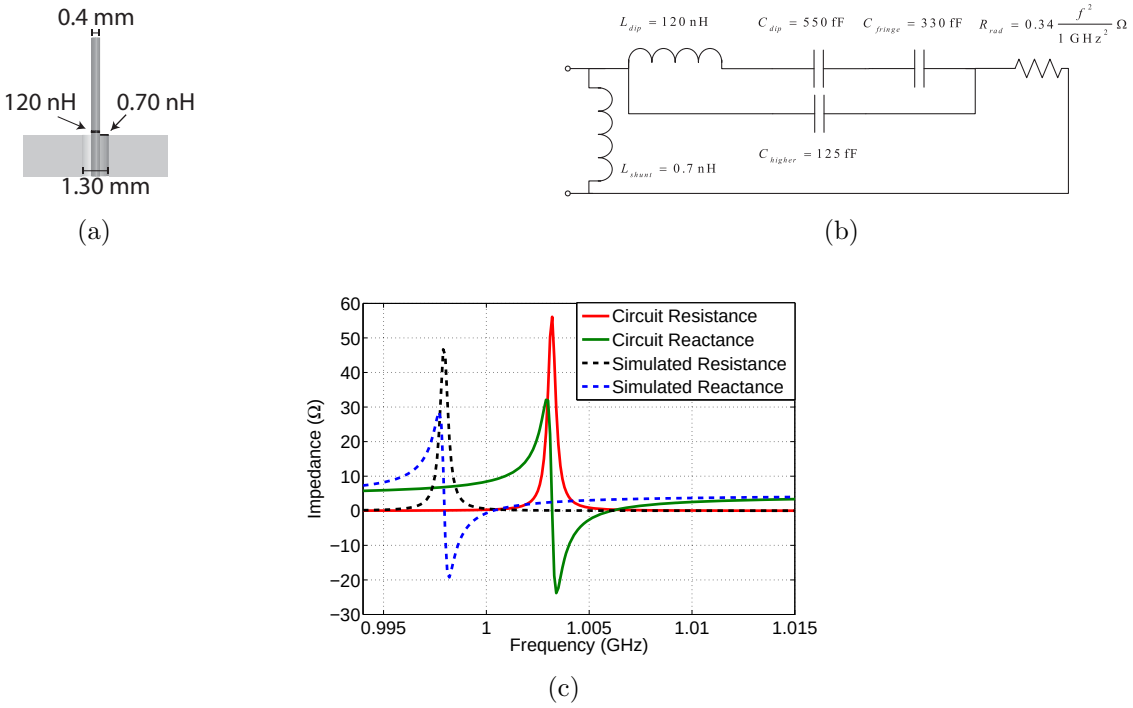

Figure 3.13: (a) Inductively loaded monopole geometry. (b) Circuit model for the inductively loaded monopole. (c) Comparison of the input impedance of the simulated inductively loaded monopole and the circuit model.

3.8 Chapter Summary

It was shown that the frequency-dependent polarizability of an electrically small antenna can be used to find an equivalent circuit that models its behavior. Specifically, for antennas radiating in the TM_{10} mode, the polarizability (α) is inserted into (3.4) to find its impedance, and subsequently an equivalent circuit. A similar approach is used for analyzing antennas that radiate the TE_{10} mode. An equivalent circuit is useful since it provides physical insight into the antenna operation. An equivalent circuit also allows one to easily find the Q of a small antenna. This is in contrast to directly integrating the near field of the antenna, or considering the time-averaged stored energy in dispersive media. This chapter also showed that loss can be incorporated into the circuit approach. It should be noted that the equivalent circuits shown here do not account for coupling between electric and/or magnetic dipole modes. Future work should account for this coupling if one wishes to model electrically small, circularly polarized or unidirectional antennas [32, 117–120].

Several different antennas were analyzed using their equivalent circuits. It was shown that a spherical inductive sheet impedance and negative permittivity sphere

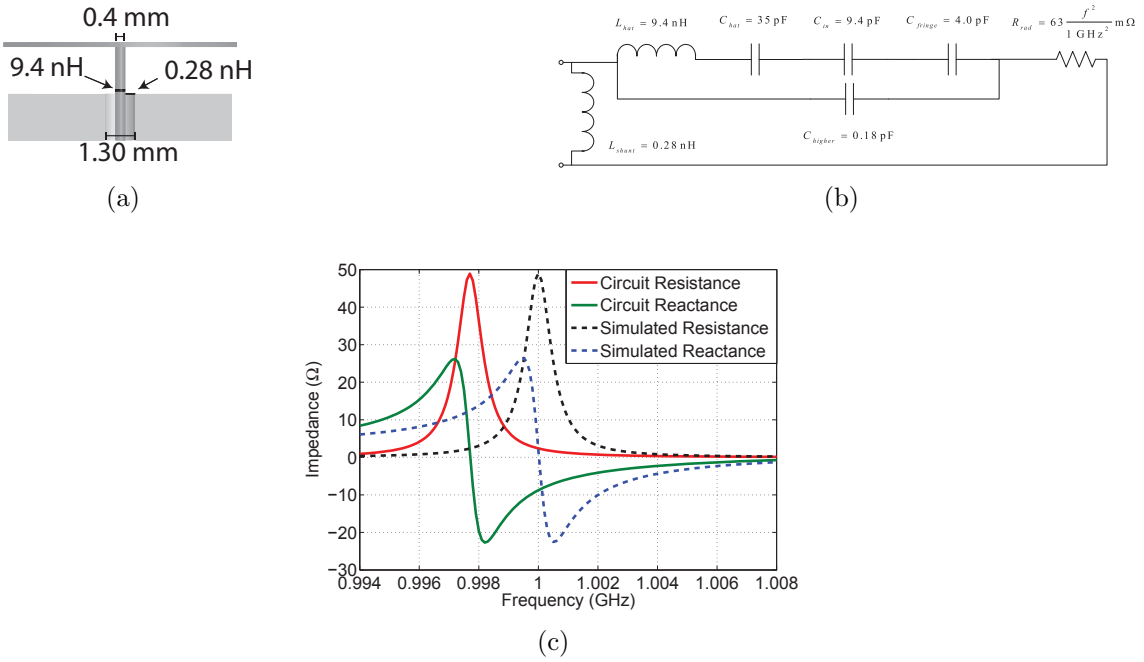

Figure 3.14: (a) Top-hat loaded monopole geometry. (b) Circuit model for the top-hat loaded monopole. (c) Comparison of the input impedance of the simulated top-hat loaded monopole and the circuit model.

can have a $Q = 1.5\ Q_{\text{Chu}}$, consistent with previously reported results [87, 90, 114]. Also, it was demonstrated that the the negative permittivity shell and spheroid must have a larger Q than the negative permittivity sphere because their equivalent circuits have added reactive elements. In addition, the equivalent circuits for the inductively loaded dipole and top-hat loaded dipole were found by numerically solving for the frequency-dependent polarizability. As new and innovative electrically small antennas are developed, it will be useful to analyze and compare their equivalent circuits using the techniques described here. For example, the fact that the negative permittivity sphere and the inductive sheet impedance have the same circuit suggests that their operation is fundamentally the same. Circuit models may also guide the design of multiband or multiresonant small antennas.

CHAPTER IV

Huygens' Sources Consisting of Concentric Spherical Sheet Impedances

4.1 Chapter Introduction

ESAs generally radiate as either electric or magnetic dipole modes because these modes have the lowest Q and therefore largest bandwidth [19, 114, 121–126]. However, if these two modes are both radiated in-phase, with equal amplitude, and with orthogonal orientations, a Huygens' source is created with twice the directivity of the electric or magnetic dipole alone ($D = 3 = 4.77$ dB). Further, if two of these Huygens' sources are combined, a directivity of 12 dB is possible in the presence of a ground plane [117]. Fundamental limitations on the gain and bandwidth of spherical modes have been extensively studied, but few antenna designs have been reported [127–135]. These electrically small, directive antennas would find wide application.

Huygens' sources are designed by placing an electric dipole orthogonal to a magnetic dipole [32, 136, 137]. However, optimizing the design of these antennas has not been straightforward. The design and analysis of the structures thus far has been simulation based, which can be time consuming and computationally intensive. Analytic models of the radiation patterns have been presented for infinitesimal electric and magnetic dipole sources, but these models are unable to predict the overall bandwidth, since they neglect mutual coupling between the two dipoles [132–134, 138].

Here, closed-form expressions for the performance of a Huygens' source, realized as two concentric spherical sheet impedances, are presented [139]. Previously, a negative permittivity sphere was analyzed in closed-form [90], and proved valuable in the design and analysis of many electric dipole ESAs [121, 125, 140–142]. Similarly, the spherical symmetry here allows for the electric and magnetic polarizabilities to be solved for in closed form using a Mie scattering approach. The sheet impedances necessary

to create a Huygens' source, as well as the Q, bandwidth, and directivity are all determined. The value of these expressions is that they provide intuition that can aid the design of future Huygens' sources. Next, a straightforward design process as well as some practical realizations of a spherical sheet impedance are presented. Finally, an antenna based on a Huygens' source, with a simple coaxial feed, is described. The performance of the described antenna offers an increased bandwidth and directivity compared to previously reported, electrically small Huygens' source antennas [32,136].

4.2 Single Sheet Impedance

The Huygens' source, consisting of two spherical sheet impedances, is designed based on its scattering properties when illuminated by an incident plane wave. Therefore, it is instructional to briefly review the Mie scattering solution to the problem at hand. First, let us review the simplified problem discussed in the previous chapter: a single sheet impedance. Without loss of generality, consider an $\hat{x}$-polarized plane wave traveling in the $\hat{z}$ direction with electric field magnitude $E_\circ$, incident upon a dielectric sphere covered by a sheet impedance. The sphere has radius, a, permittivity, ϵ_s, and permeability, μ_s. The sheet impedance is defined as the ratio of the tangential electric field to the surface current,

$$\vec{E}_{\tan} = \eta_s \vec{J}_{\text{surf}}, \tag{4.1}$$

where $\vec{E}_{\tan}$ is the tangential electric field and $\vec{J}_{\text{surf}}$ is the electric surface current.

The goal here is to solve for the electric and magnetic polarizabilities as a function of the sheet impedance. The fields are expressed in terms of spherical waves, and by equating the electric field within and outside the sheet impedance, as well as applying Ampere's law at the boundary, the scattered field can be found. Since the sphere is electrically small, the scattered field can be expressed in terms of the TM_{11} and TE_{11} modes. The field, in turn, can be related to electric (α_e) and magnetic (α_m) polarizabilities by comparing it with the field radiated by orthogonal electric and magnetic dipoles:

$$\alpha_e = \frac{4\pi a^3(2 + j\omega\eta_s a\epsilon_\circ(\epsilon_s - 1))}{2 + j\omega\eta_s a\epsilon_\circ(\epsilon_s + 2)} \tag{4.2}$$

$$\alpha_m = \frac{2\pi a^3 j((2\mu_s - 2)\eta_s - ja\mu_s\mu_\circ\omega)}{(\mu_s + 2)j\eta_s - a\mu_s\mu_\circ\omega}. \tag{4.3}$$

The sheet impedance needed for either the electric or magnetic polarizability to

diverge can then be found:

$$\text{TM}_{11}\text{: } \eta_s = \frac{2j}{\omega_\circ a \epsilon_\circ (\epsilon_s + 2)} \tag{4.4}$$

$$\text{TE}_{11}\text{: } \eta_s = \frac{\omega_\circ a \mu_s \mu_\circ}{j(2 + \mu_s)}. \tag{4.5}$$

Near resonance, the polarizabilities become singular, and therefore radiative damping cannot be neglected. This leads to an effective polarizability of [92],

$$\alpha_{\mathit{eff}} = \frac{\alpha}{1 + j\frac{\alpha k^3}{6\pi}}, \tag{4.6}$$

where α is either an electric or magnetic polarizability. Now, the Q of this resonant structure can be found. First, it is assumed that the sheet impedances are frequency dispersive to satisfy Fosters' reactance theorem. Therefore, the sheet impedance for the electric dipole resonance is given by, $\eta_s = j\omega L_s$, and the sheet impedance for the magnetic dipole resonance is given by, $\eta_s = 1/(j\omega C_s)$. By inserting (4.4) into (4.2), and the result into (4.6), the Q of the electric dipole resonance can be found, as shown in the previous chapter [143, 144]. Similarly, the Q of the magnetic dipole resonance can also be derived. The resulting Q's for the electric and magnetic dipole modes are given by,

$$Q_e = \frac{1 + \epsilon_s/2}{(ka)^3} \tag{4.7}$$

$$Q_m = \frac{1 + 2/\mu_s}{(ka)^3} \tag{4.8}$$

4.3 Double Sheet Impedance

In the previous section, it was shown that a single isotropic sheet impedance covering a magneto-dielectric sphere can be designed to resonate as either an electric or magnetic dipole. In this section, we will show that an internal, capacitive sheet impedance enclosed by an external, inductive sheet impedance can resonate both the magnetic and electric dipole modes simultaneously. Again, let us consider an $\hat{x}$-polarized plane wave traveling in the $\hat{z}$ direction with electric field magnitude $E_\circ$, incident upon two concentric spherical sheet impedances, as shown in Fig. 4.1. The scattered, radially directed electric and magnetic vector potentials in the three regions

are given by [108],

Region III

$$A_{r3} = \frac{E_\circ \alpha_e k^3}{4\pi\omega\mu_\circ}\cos(\phi)\sin(\theta)\widehat{H}_1^{(2)}(kr) \tag{4.9}$$

$$F_{r3} = \frac{E_\circ \alpha_m k^3}{4\pi k}\sin(\phi)\sin(\theta)\widehat{H}_1^{(2)}(kr) \tag{4.10}$$

Region II

$$A_{r2} = \frac{E_\circ}{\omega\mu_\circ}\cos(\phi)\sin(\theta)\left(A_2\widehat{J}_1(\sqrt{\epsilon_{s2}\mu_{s2}}kr) + B_2\widehat{Y}_1(\sqrt{\epsilon_{s2}\mu_{s2}}kr)\right) \tag{4.11}$$

$$F_{r2} = \frac{E_\circ}{k}\sin(\phi)\sin(\theta)\left(C_2\widehat{J}_1(\sqrt{\epsilon_{s2}\mu_{s2}}kr) + D_2\widehat{Y}_1(\sqrt{\epsilon_{s2}\mu_{s2}}kr)\right) \tag{4.12}$$

Region I

$$A_{r1} = \frac{E_\circ}{\omega\mu_\circ}\cos(\phi)\sin(\theta)A_1\widehat{J}_1(\sqrt{\epsilon_{s1}\mu_{s1}}kr) \tag{4.13}$$

$$F_{r1} = \frac{E_\circ}{k}\sin(\phi)\sin(\theta)C_1\widehat{J}_1(\sqrt{\epsilon_{s1}\mu_{s1}}kr) \tag{4.14}$$

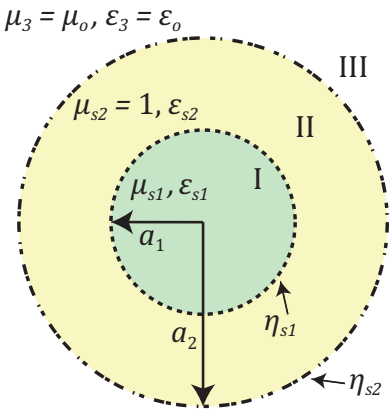

Figure 4.1: Geometry of two concentric spherical sheet impedances.

The coefficients α_e, α_m, $A_{1,2}$, B_2, $C_{1,2}$, and D_2 must all be solved simultaneously by applying (4.1) and Ampere's law at the spherical boundaries located at $r = a_1$ and $r = a_2$. Specifically, the boundary conditions separating any two regions is given

by,

$$\begin{aligned} \vec{J}_s &= \hat{r} \times \left(\vec{H}_2 - \vec{H}_1 \right) \\ 0 &= \hat{r} \times \left(\vec{E}_2 - \vec{E}_1 \right) \end{aligned} \tag{4.15}$$

The electric and magnetic fields can be related to the vector potentials of Eqns. (4.9)-(4.14) as demonstrated in [108]. Both the θ and ϕ components of the electric and magnetic fields are related at the two boundaries, thus providing eight equations for the eight unknowns. For example, E_θ can be related on the surface between regions I and II by,

$$\begin{aligned} 0 &= -E_{\theta 1} + E_{\theta 2} \\ 0 &= \frac{1}{a_1 \sin(\theta)} \frac{dF_{r1}}{d\phi} - \frac{1}{j a_1 \omega \epsilon_\circ \epsilon_{s1}} \frac{dA_{r1}}{d\phi} \\ &\quad + \frac{-1}{a_1 \sin(\theta)} \frac{dF_{r2}}{d\phi} + \frac{1}{j a_1 \omega \epsilon_\circ \epsilon_{s1}} \frac{dA_{r2}}{d\phi} \\ 0 &= \frac{C_1 \widehat{J}_1(\sqrt{\epsilon_{s1}\mu_{s1}} k a_1)}{k a_1} - \frac{D_1 \cos(\theta) \frac{d\widehat{J}_1(\sqrt{\epsilon_{s1}\mu_{s1}} kr)}{dr}|_{r=a_1}}{jk\epsilon_{s1}} \\ &\quad - \frac{C_2 \widehat{J}_1(\sqrt{\epsilon_{s2}} k a_1)}{k a_1} + \frac{A_2 \cos(\theta) \frac{d\widehat{J}_1(\sqrt{\epsilon_{s2}} kr)}{dr}|_{r=a_1}}{jk\epsilon_{s2}} \\ &\quad + \frac{-D_2 \widehat{Y}_1(\sqrt{\epsilon_{s2}} k a_1)}{k a_1} + \frac{B_2 \cos(\theta) \frac{d\widehat{Y}_1(\sqrt{\epsilon_{s2}} kr)}{dr}|_{r=a_1}}{jk\epsilon_{s2}} \end{aligned} \tag{4.16}$$

It is then assumed that $ka \ll 1$, and only the leading order terms of the Taylor series expansion of the spherical bessel functions are kept,

$$\begin{aligned} 0 &= \frac{C_1 k a_1 \epsilon_{s1}}{3} - \frac{j2 D_1 \cos(\theta)}{3} \\ &\quad + \frac{-C_2 k a_1 \epsilon_{s2}}{3} + \frac{D_2}{k^2 a_1^2 \epsilon_{s2}} \\ &\quad + \frac{A_2 2 \cos(\theta)}{3j} + \frac{B_2 \cos(\theta)}{jk^3 a_1^3 (\epsilon_{s2})^{3/2}} \end{aligned} \tag{4.17}$$

This is just one of the eight equations that must be solved simultaneously to calculate α_e and α_m. The other equations can be solved for straightforwardly by appropriately applying the boundary conditions between each surface. Let's assume

$\mu_{s2} = 1$, since it has a relatively small effect on the structure's Q. In addition, let's also assume the internal sheet is capacitive where $\lim_{ka\to 0}[\eta_{s1} = 0]$, in accordance with (4.5), and the external sheet is inductive where $\lim_{ka\to 0}[\eta_{s2} = \infty]$, in accordance with (4.4). In other words, for $ka \ll 1$ the inductive sheet is absent when finding the magnetic polarizability. Similarly, the capacitive sheet is a short when finding the electric polarizability. Once the eight coefficients are solved for, the polarizabilities become,

$$\alpha_e = \frac{4\pi a_2^3(2 + j\omega\eta_{s2}a_2\epsilon_\circ(\left(\epsilon_{s2}\frac{a_2^3+2a_1^3}{a_2^3-a_1^3}\right) - 1))}{2 + j\omega\eta_{s2}a_2\epsilon_\circ(\left(\epsilon_{s2}\frac{a_2^3+2a_1^3}{a_2^3-a_1^3}\right) + 2)} \tag{4.18}$$

$$\alpha_m = \frac{2\pi a_1^3 j((2\mu_{s1} - 2)\eta_{s1} - ja_1\mu_{s1}\mu_\circ\omega)}{(\mu_{s1} + 2)j\eta_{s1} - a_1\mu_{s1}\mu_\circ\omega}. \tag{4.19}$$

The resulting electric and magnetic polarizabilities are both functions of a_1, but are otherwise completely independent of each other. This analysis inherently takes into account the mutual coupling between the two surfaces.

The magnetic polarizability of the geometry shown in Fig. 4.1 is identical to (4.3) except that a is replaced by a_1, and μ_s is replaced by μ_{s1}. The electric polarizability is equal to (4.2) except that a is replaced by a_2, and ϵ_s is replaced by ϵ_{eff}, where ϵ_{eff} is the effective relative permittivity resulting from the presence of the capacitive sheet,

$$\epsilon_{\mathit{eff}} = \epsilon_{s2}\frac{a_2^3 + 2a_1^3}{a_2^3 - a_1^3}. \tag{4.20}$$

The necessary impedances for resonance and Q's are given by the expressions in Section 4.2, with the above mentioned substitutions. Mutual coupling between the two sheet impedances results in the increased effective relative permittivity given by (4.20). All additional mutual coupling effects are second order in nature ($\mathcal{O}((ka)^2)$), and have been neglected here. The inner (capacitive) sheet impedance creates a magnetic dipole resonance that radiates the TE_{11} mode, and the outer (inductive) sheet impedance creates an electric dipole resonance that radiates the TM_{11} mode. It should be noted that if the sheet impedances were reversed (outer is capacitive, and inner is inductive) the electric dipole mode cannot resonate when ($ka \ll 1$). This scenario would be similar to placing an electric dipole within a metallic sphere because of the low reactance of the capacitive sheet. Clearly, the electric dipole would not be able to radiate effectively if this were the case.

Let's first consider the electric dipole mode. The Q of this mode is minimized

when ϵ_{eff} is minimized. The minimum ϵ_{eff} appears when $a_1/a_2 \to 0$. However, this forces Q_m to diverge, which is undesirable for a Huygens' source. Therefore, one approach to designing a Huygens' source is to force the Q's of both the electric and magnetic dipole to be equal, so that the directivity remains constant over the entire operating bandwidth. This amounts to enforcing

$$\frac{Q_m}{Q_e} = \frac{2a_2^3(2+\mu_{s1})}{a_1^3\mu_{s1}(2+\epsilon_{\mathit{eff}})} = 1. \tag{4.21}$$

This condition stipulates a unique a_1/a_2 ratio and Q for a given material loading. It is informative to consider some limiting cases of this expression. The quality factors in Figure 4.2 are obtained by inserting the effective permittivity (4.20) into the expression for the electric dipole quality factor (4.7), and enforcing (4.21). The minimum Q results from minimizing the dielectric loading and maximizing the magnetic loading.

	$\mu_{s1}=1$	$\mu_{s1}>1$
$\epsilon_{s2}=1$	$\frac{9}{2(ka_2)^3}$	$\frac{4+5\,\mu_{s1}}{2\mu_{s1}(ka_2)^3}$
$\epsilon_{s2}>1$	$\frac{12\,(\epsilon_{s2}-1)}{\left(-8-\epsilon_{s2}+\sqrt{16+64\,\epsilon_{s2}+\epsilon_{s2}^2}\right)(ka_2)^3}$	$\frac{4\,(\epsilon_{s2}-1)(\,\mu_{s1}+2)}{\left(-4-\epsilon_{s2}\mu_{s1}-4\mu_{s1}+\sqrt{16+40\,\epsilon_{s2}\mu_{s1}+24\,\epsilon_{s2}\mu_{s1}^2+\epsilon_{s2}^2\mu_{s1}^2}\right)(ka_2)^3}$

Figure 4.2: $Q_e = Q_m$ of a Huygens' source realized through two concentric, spherical, sheet impedances under various material loading conditions.

Further, tradeoffs between directivity and bandwidth can be made. If one of the resonances is slightly shifted in frequency with respect to the other, the structure has two closely-spaced resonances that can be used to increase the overall bandwidth. If the sheet impedance (4.5) is again assumed to be frequency dispersive and inserted into the polarizability expression (4.3), and the result inserted into (4.6), the effective magnetic polarizability simplifies to,

$$\alpha_m^{\mathit{eff}} = \frac{6\pi\left(3\omega_\circ^2 + (\omega^2-\omega_\circ^2)\,Q_m k^3 a_1^3\right)}{k^3\left(3Q_m\,(\omega_\circ^2-\omega^2) + j3\omega_\circ^2 + jQ_m a_1^3 k^3\,(\omega^2-\omega_\circ^2)\right)}. \tag{4.22}$$

where $\omega_\circ$ is the resonant frequency. The same procedure can be applied to obtain the electric polarizability,

$$\alpha_e^{\mathit{eff}} = \frac{6\pi\left(3\omega^2 + (\omega_\circ^2-\omega^2)\,2Q_e k^3 a_2^3\right)}{k^3\left(3Q_e\,(\omega_\circ^2-\omega^2) + j3\omega^2 + j2Q_e a_2^3 k^3\,(\omega_\circ^2-\omega^2)\right)}. \tag{4.23}$$

Enforcing (4.21), causes the electric and magnetic dipole modes to have identical Q's

($Q = Q_e = Q_m$). If an additional assumption is made that the Huygens' source operates near resonance ($\omega \approx \omega_\circ$), the effective electric and magnetic polarizabilities simplify to,

$$\alpha_e^{res} = \alpha_m^{res} = \frac{6\pi\omega_\circ}{k^3(2Q(\omega_\circ - \omega) + j\omega_\circ)}, \tag{4.24}$$

Note that (4.24) is valid for both the electric and magnetic polarizabilities because (4.21) enforces that their Q's are identical. To increase the bandwidth of the scattered power, the resonant frequency of the electric and magnetic dipoles can be offset by a frequency shift $\Delta\omega$,

$$\alpha_\pm = \frac{6\pi\omega_\circ}{k^3(2Q(\omega_\circ \mp \Delta\omega/2 - \omega) + j\omega_\circ)}. \tag{4.25}$$

Here $\alpha_\pm$ denotes the polarizabilities at the resonant frequencies $\omega_\circ \pm \Delta\omega/2$.

The directivity and bandwidth can now be found as a function of $\Delta\omega$. The directive gain of a Huygens' source is given by [138],

$$\begin{aligned} D(\theta,\phi) &= \frac{3/2}{|\alpha_e|^2 + |\alpha_m|^2}\left[|\alpha_e \sin(\phi) + \alpha_m \sin(\phi)\cos(\theta)|^2 \right. \\ &\quad \left. + \, |\alpha_e \cos(\phi)\cos(\theta) + \alpha_m \cos(\phi)|^2\right] \end{aligned} \tag{4.26}$$

In the $\hat{z}$ direction ($\theta = 0$), (4.26) simplifies to,

$$D = \frac{3/2\,|\alpha_+ + \alpha_-|^2}{|\alpha_+|^2 + |\alpha_-|^2}, \tag{4.27}$$

and is equal to,

$$D(\omega_\circ) = \frac{3}{\left(\frac{Q\Delta\omega}{\omega_\circ}\right)^2 + 1}, \tag{4.28}$$

at the center frequency ($\omega_\circ$). As expected, the directivity at $\omega_\circ$ decreases with increasing $\Delta\omega$. When $Q\Delta\omega/\omega_\circ < 1$, the electric and magnetic dipole modes are in phase, and the maximum directive gain is in the $+\hat{z}$ (forward-scattered) direction. However, when $Q\Delta\omega/\omega_\circ > 1$ the two modes become out of phase. This causes the directive gain in the $-\hat{z}$ (back-scattered) direction to become largest, and the maximum directivity is no longer given by (4.27) and (4.28).

To find the bandwidth, we first note that the scattering cross section is given by,

$$\mathrm{C_{sca}} = \frac{P_{\mathrm{rad}}}{\frac{1}{2}\sqrt{\frac{\epsilon_\circ}{\mu_\circ}}|E_\circ|^2} = \frac{k^4}{6\pi}\left(|\alpha_+|^2 + |\alpha_-|^2\right), \tag{4.29}$$

which is simply a superposition of two frequency shifted Lorentzians. The fractional bandwidth (FBW_ν) is defined as,

$$FBW_\nu = \frac{\omega_u - \omega_l}{\omega_\circ}, \tag{4.30}$$

where $\omega_{u,l}$ are the upper and lower frequencies at which the scattering cross section is $(1-\nu)$ of the scattering cross section at $\omega_\circ$ ($\nu = 1/2$ for the -3 dB bandwidth). From (4.29) and (4.30), the FBW_ν can be found,

$$\begin{aligned} FBW_\nu = \Big[&\sqrt{1 - 6\delta^2 + 24\nu\delta^2 + 9\delta^4 - 8\nu\delta^4 - 16\nu^2\delta^2} \\ &- 1 + 3\delta^2 - 2\nu\delta^2 + 2\nu\Big]^{1/2} \frac{1}{Q\sqrt{2(1-\nu)}}, \end{aligned} \tag{4.31}$$

where

$$\delta = \frac{Q\Delta\omega}{\omega_\circ}. \tag{4.32}$$

As $\Delta\omega$ increases so does FBW_ν. When $\Delta\omega = 0$, the bandwidth is identical to that of a single resonant antenna [94, Eqn. 34]. Note that connecting a matched load to the antenna doubles the FBW_ν [111]. Since a nonzero $\Delta\omega$ creates two offset resonances, we can no longer apply the well known relationships between bandwidth and Q that are valid for single resonant antennas [145]. It should also be noted that the Q that appears in (4.31) and (4.32) is not the overall antenna Q, but is the Q of the individual electric and magnetic dipole modes. Eqns. (4.28) and (4.31) are particularly valuable because they provide closed-form expressions for the tradeoff between D and FBW_ν.

To verify the above analysis, two concentric sheet impedances with $a_1 = 10.0$ mm and $a_2 = 11.18$ mm were simulated using a commercial finite-element full wave solver, Ansoft's HFSS. The necessary sheet impedances to achieve a directivity of 3 at 1 GHz ($ka = 0.23$) are $\eta_{s2} = 311j\ \Omega$ and $\eta_{s1} = -25.1j\ \Omega$. It was assumed the inductive and capacitive sheets again obeyed Foster's reactance theorem. By slightly detuning the sheet impedances from the values necessary for maximum directivity, D and $\mathrm{C_{sca}}$ were found at 1 GHz for various values of $\Delta\omega$, as shown in Fig. 4.3.

D and $\mathrm{C_{sca}}$ were obtained semi-analytically. From the directivity (4.28) and assuming $Q = 4.5Q_{lb}$ for no material loading (see Figure 4.2), $\Delta\omega$ was found by noting the simulated directivity at 1 GHz. The polarizabilities α_+ and α_- were then found from (4.25), and inserted into (4.27) and (4.29) to arrive at the frequency response for D and $\mathrm{C_{sca}}$. A comparison of the semi-analytic formulation and the simulated results

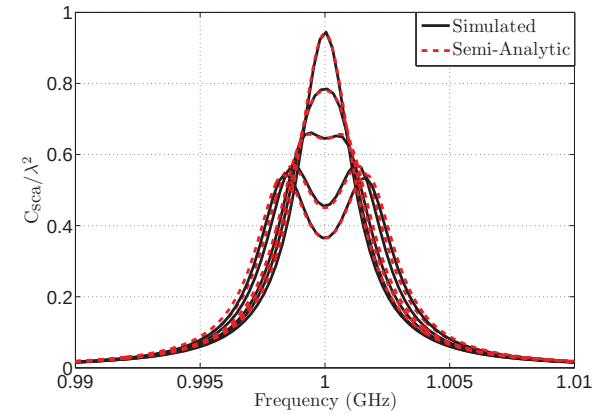

(a)

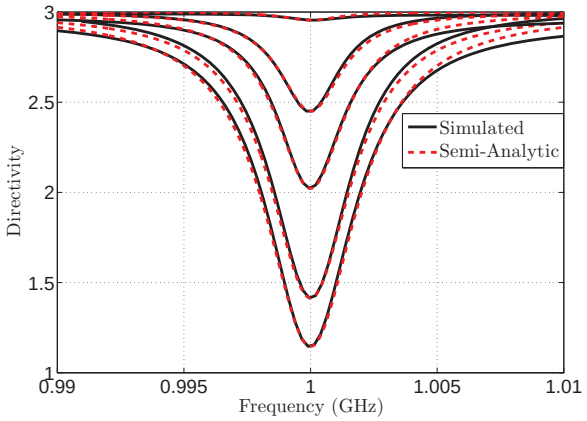

(b)

Figure 4.3: Scattering cross section (C_{sca}) (a) and directivity (D) (b) in the $\hat{z}$ direction vs. frequency for various values of $\Delta\omega$. As $\Delta\omega$ increases both C_{sca} and the D at 1 GHz decrease. The values of $\Delta\omega/(2\pi)$ considered here are 0.33 MHz, 1.28 MHz, 1.88 MHz, 2.86 MHz, and 3.44 MHz.

are shown in Fig. 4.3, which demonstrates the accuracy of the derived expressions.

It should be noted that due to the spherical symmetry of this problem, it is possible to exactly solve for the scattered field, and thereby obtain D and C_{sca} in closed-form without any information from simulation. This can be done if the exact expressions for the spherical bessel functions and the higher order terms ($\mathcal{O}((ka)^2)$) are retained, but this significantly lengthens the necessary algebra. In the presented analysis, many terms were eliminated by assuming $ka_2 \ll 1$, but this creates a slight frequency shift between the simulated and analytic response [144]. This is problematic since a frequency shift as small as 0.1% would be significant because it is on the order of the fractional bandwidth, as well as the numerical error of the finite element simulations. This error does not detract from the utility of the derived results though, since the

simple expressions developed provide valuable insight into the design of Huygens' sources.

4.4 Practical Antennas

The inductive and capacitive sheet impedances are necessary to radiate electric and magnetic dipole modes. However, such ideal sheet impedances do not exist in nature, and therefore must be approximated using metallic patterns. To realize an inductive sheet impedance, a grid of wires loaded with inductors at the equator can be used, as shown in Fig. 4.4. The conductor distribution supports the necessary currents to radiate the TM_{11} mode, and the lumped inductors force the currents to resonate at a desired frequency. To achieve a capacitive sheet impedance, loops of wires loaded with capacitors (see Fig. 4.4) can be used. This structure is similar to that introduced by Kim and Wheeler [19, 146]. It should be noted that realizing the sheet impedances with wire distributions does couple energy into higher order spherical modes that are not considered here. These higher order modes store additional energy that increase Q.

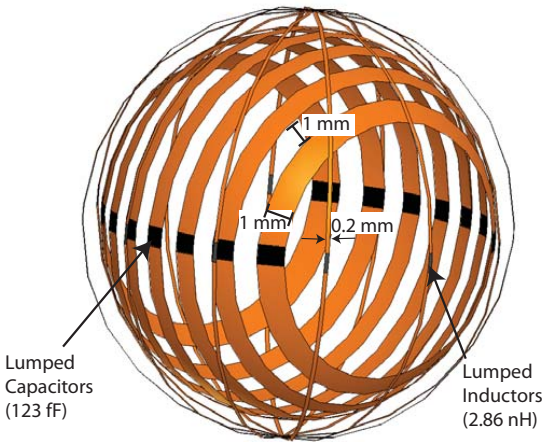

Figure 4.4: Anisotropic Huygens' source realized through capacitively-loaded loops (capacitive sheet) and an inductively-loaded grid (inductive sheet).

The metallic grids in Fig. 4.4 are equivalent to anisotropic sheet impedances since they are not rotationally symmetric. Such anisotropic sheet impedances were chosen because they are easier to design and fabricate. Therefore, the structure shown in Fig. 4.4 only works for a single polarization. Since the earlier expressions are valid for isotropic sheet impedances, we expect some inaccuracy in their ability to predict the behavior of these structures. However, the analysis is still useful for developing

an iterative design methodology.

Let's design a Huygens' source with an electrical size near $ka = 0.42$ to operate at 1.84 GHz without any material loading. We will use the structure shown in Fig. 4.4, and tune the lumped inductors and capacitors until the directivity is maximized. Internal and external radii were chosen to be $a_1 = 10$ mm and $a_2 = 11$ mm. Initially, the sheet impedances were simulated independently of each other. They were excited with an incident plane wave in two separate simulations. To first order, the capacitive sheet resonates at the same frequency as the Huygens' source and the inductive sheet impedance resonates at a higher frequency because of the increased effective relative permittivity (ϵ_{eff}) due to mutual coupling. Therefore, the lumped elements were tuned such that the scattered power of the capacitive and inductive sheets peaked near 1.8 GHz, and and 2.2 GHz, respectively. Then, the two sheets were combined and simulated again. By noting the differential scattering cross section ($\mathrm{C_{sca}}(\theta, \phi)$) vs. frequency, $\Delta\omega$ and the Q's of the two modes can be approximated. Then the lumped elements and a_1 are adjusted to bring the electric and magnetic dipole resonances closer, and the structure is re-simulated. Using this iterative design process, the two modes can be made to resonate at the same frequency, and thereby obtain a Huygens' source.

The structure shown in Fig. 4.4 has an inductive grid at an 11 mm radius made up of 0.2 mm wide perfect electrically conducting (PEC) traces. The grid consists of 12 arms connected at the top and bottom. Each arm is loaded with a 2.86 nH inductor at the equator. At the internal radius ($a_1 = 10$ mm), there are 8 loops that each have a 1 mm width, and are spaced 1 mm apart from each other. Each loop is loaded with two 123 fF capacitors at the equator. This Huygens' source achieves a directivity of 3 at 1.84 GHz. By detuning the lumped capacitors and inductors, it is also possible to increase the bandwidth by increasing $\Delta\omega$, while maintaining a center frequency of 1.84 GHz.

Eqns. (4.28) and (4.31) allow one to find the directivity and bandwidth for all values of $\Delta\omega$, given the Q of the $\mathrm{TM_{11}}$ and $\mathrm{TE_{11}}$ modes (see Fig. 4.5). Simulated values of the directivity and bandwidth for the ideal sheet impedance and the realized Huygens' source are shown in Fig. 4.5. The electric and magnetic dipole modes of the ideal sheet impedance were assumed to have $Q = 4.5Q_{lb}$. The Q's of the realized Huygens' source were estimated from (4.31) to be $Q = 6.7Q_{lb}$ from the simulated scattering bandwidth when $D(\omega_\circ) = 3$. Under such conditions, $\Delta\omega \approx 0$. Here, the bandwidth obeys well known relationships for single resonant antennas ($FBW_{\nu=1/2} = 3FBW_{\nu=1/10}$) [94].

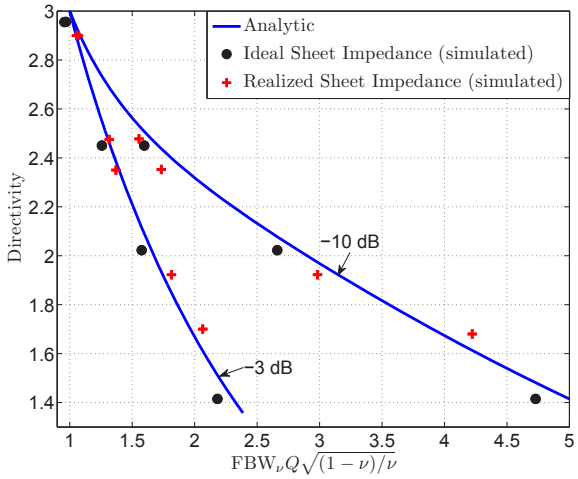

Figure 4.5: Directivity in the $\hat{z}$ direction vs. the normalized bandwidth ($FBW_\nu Q\sqrt{(1-\nu)/\nu}$) from Eqns. (4.28) and (4.31), from simulating ideal sheet impedances, and from simulating the structure shown in Fig. 4.4 (realized sheet impedances). For single resonant structures, $FBW_\nu Q\sqrt{(1-\nu)/\nu} = 1$ for all values of ν. Both the -3 dB bandwidth ($\nu = 1/2$) and -10 dB bandwidth ($\nu = 1/10$) are plotted.

Thus far, the scattering properties of spherical Huygens' sources have been analyzed. This allowed closed-formed expressions to be developed that model the behavior of these resonant structures. However, a realistic antenna cannot be fed with a plane wave. Therefore, a coaxially-fed monopole version of a Huygens' source was designed, as shown in Fig. 4.6. The coaxial cable was connected to the capacitive sheet. The lumped inductors present in Fig. 4.4 were removed, and the metallic traces were instead spiraled to achieve the necessary inductive loading. The helical arms were designed using [114, Eqns. 1-5], except here the spiraling began 7.3 mm above the surface of the ground plane, rather than at the ground plane itself. This increased the coupling between the inductive and capacitive sheets, which was necessary for the antenna to be fed with a single coaxial line. There are 4 arms with 0.55 turns per arm. The internal capacitive loops are identical to the previous design shown in Fig. 4.4, except that an additional loop was added so that the structure could be symmetrically fed. The input resistance of this antenna was initially greater than 500 Ω, so a L-section matching network was added at the feed. The matching network consisted of a series 410 fF capacitor and a shunt 18 nH inductor, to transform the input resistance to 50 Ω. It should be noted that the feed was not optimized, and it may be possible to realize an impedance match without the use of a L-section matching network by employing some of the techniques used in the design

of near-field resonant parasitic antennas [120, 121].

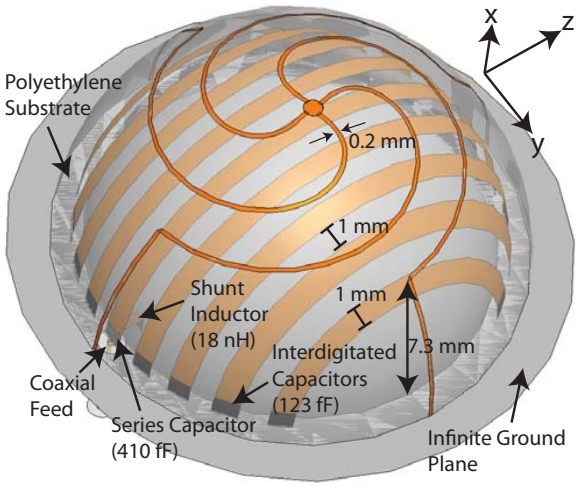

Figure 4.6: Huygens' source realized through capacitively-loaded loops (capacitive sheet) and a spherical helix (inductive sheet).

It is not possible to construct this antenna through traditional printed-circuit-board (PCB) techniques because of its spherical geometry. However, chapter 2 described recent advances in fabrication that allow for the printing of arbitrary metallic patterns onto three dimensionally contoured substrates [20, 143, 147]. A polyethylene substrate was chosen here ($\epsilon_r = 2.25$, $\tan(\delta)$=0.001) because of its low loss and vacuum forming properties. A capacitive sheet can be printed onto a 10 mm radius, 0.5 mm thick, polyethylene substrate, and an inductive sheet printed onto an 11 mm radius, 1 mm thick, polyethylene substrate. The 123 fF capacitors on the capacitive sheet can be realized by printing interdigitated traces to eliminate the lumped elements. The inductive sheet can then be placed on top of the capacitive sheet, and both structures secured to the ground plane. It was assumed that all metallic traces were made from copper. Metal and substrate losses were included in the simulation, and the shunt inductor in the L-section matching network had a $Q = 75$.

The simulated realized gain, directivity, reflection coefficient, and radiation patterns are shown in Fig. 4.7. The center frequency of the antenna is 1.93 GHz ($ka = 0.44$). At the center frequency the radiation efficiency, directivity, and realized gain are 52%, 7.6 dB, and 4.6 dB, respectively. The -10 dB bandwidth is 70 MHz ($FBW_{1/10} = 0.036$). The directivity in Fig. 4.7(a) is not constant over the entire operating frequency because of the simple feeding method. Below the operating frequency, more energy is coupled from the coaxial feed into the magnetic monopole mode, whereas above the resonant frequency, more energy is coupled into the elec-

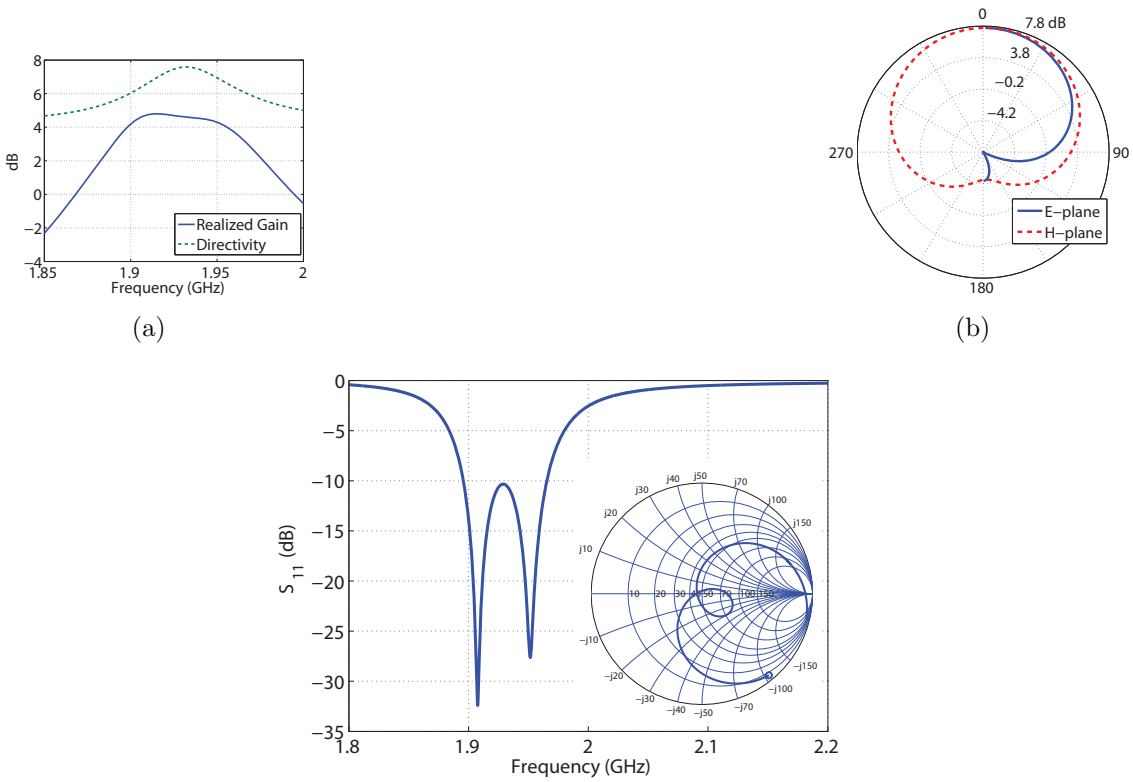

Figure 4.7: (a) Directivity and realized gain vs. frequency. (b) Directivity pattern at 1.93 GHz in the E-plane and H-plane. (c) Reflection coefficient (dB) and input impedance (inset).

tric monopole mode. However, an advantage of this feed is that the directivity is maximized, rather than minimized, at the center frequency when the bandwidth is maximized. It can be seen in Fig. 4.7(c) that there are two closely spaced resonances. The distance between these resonances was optimized to maximize the -10 dB bandwidth by tuning the capacitors on the capacitive sheet. The -10 dB bandwidth of this antenna is 1/2.6 times that of a single resonant antenna with a $Q = Q_{lb}$. The defined lower bound, Q_{lb}, is equal to both the single mode minimum Q, as well as the Huygens' source minimum Q [135].

4.5 Chapter Summary

A method to design a Huygens' source based on the electric and magnetic polarizabilities of two concentric, spherical sheet impedances was presented. Such a Huygens' source is particularly interesting because it can be analyzed analytically, and the di-

rectivity and bandwidth can be found in closed-form. The physical intuition gained here can aid the design of other Huygens' sources that are not realized through sheet impedances, but instead through alternate resonant structures that are described in the following chapters. Practical implementations of the concentric, spherical, sheet impedance have also been described, which is relevant to current antenna design. These implementations were looked at first from a scattering perspective, and then fed directly to develop a directional, electrically small antenna.

In the remainder of this thesis, we no longer consider the radiation properties of individual polarizable particles (i.e. small antennas). Instead, we distribute polarizable particles along two-dimensional arrays to realize metasurfaces that can arbitrarily control electromagnetic wavefronts.

CHAPTER V

Metamaterial Huygens' Surface

5.1 Chapter Introduction

The previous chapters analyzed individual polarizable particles. Next, we consider two-dimensional arrays of polarizable particles, which are commonly referred to as metasurfaces. Until recently, most metasurfaces have been periodic, which generally limited their application to filters, waveguides, and absorbers [1,7,148–151]. Here, we introduce non-periodic metasurfaces that react to both electric and magnetic fields. We will refer to these surfaces as metamaterial Huygens' surfaces, since their design is based on a rigorous formulation of Huygens' principle.

Huygens' principle qualitatively states that each point on a wavefront acts as a secondary source of outgoing waves [33]. In 1901, Love developed a rigorous form of Huygens' principle, which specified the secondary sources in terms of well defined, fictitious electric and magnetic currents [152]. Schelkunoff later extended Love's Equivalence Principle to allow for arbitrary field distributions on either side of a surface [56]. Schelkunoff's formulation is known today as simply the Surface Equivalence Principle, and is readily employed in the analysis of aperture antennas, diffraction problems, and computational electromagnetics formulations [16].

The contribution of this work is twofold. First, it is shown how the Surface Equivalence Principle can be employed to design electrically-thin layers (sheets) capable of establishing arbitrary field patters for a given illumination. The previously fictitious currents introduced by Schelkunoff are replaced with physical, polarization currents produced by a nonperiodic distribution of polarizable particles exhibiting both electric and magnetic responses. Secondly, it is detailed how to realize these arbitrary electric and magnetic polarization currents with metamaterial (subwavelength textured) surfaces. To outline the design methodology, a reflectionless Huygens' surface that provides a spatially varying phase response is experimentally demonstrated at

microwave frequencies. This structure can be envisaged as a non-periodic distribution of Huygens' sources [153, 154].

5.2 Huygens Surface Design

In the Surface Equivalence Principle, independent field distributions are stipulated in two regions of space (Regions I and II of Fig. 5.1). Since the fields are generally discontinuous at the surface S, fictitious electric and magnetic surface currents are needed on the surface to satisfy the boundary conditions,

$$\vec{J}_s = \hat{n} \times \left(\vec{H}_2 - \vec{H}_1\right), \qquad \vec{M}_s = -\hat{n} \times \left(\vec{E}_2 - \vec{E}_1\right) \tag{5.1}$$

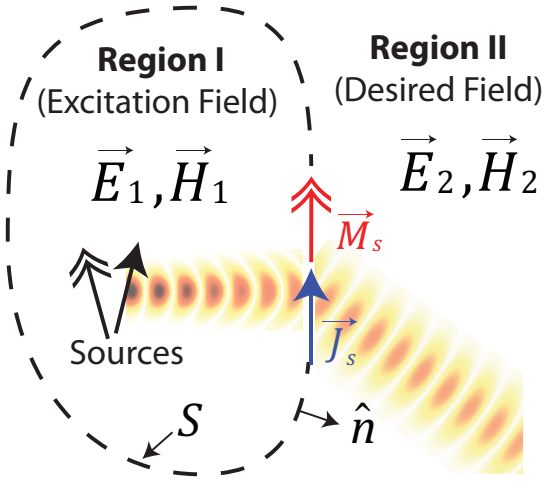

Figure 5.1: Arbitrary fields in two regions separated by a closed surface S that provides electric and magnetic surface currents. The fields in Region I and Region II are defined independently of each other, and the Surface Equivalence Principle is employed to find the fictitious electric and magnetic surface currents that satisfy the boundary conditions.

Here, we replace Schelkunoff's fictitious surface currents with physical, polarization currents. The polarization currents are generated by exciting a prescribed two-dimensional array of polarizable particles with an incident field. Each polarizable particle can be characterized by its quasi-static electric and magnetic polarizabilities ($\alpha_{e,m}$), defined as the ratio of the dipole moment to the local field. When these particles are closely spaced across a two-dimensional surface, a surface polarizability ($\alpha_{e,m}^{eff}$) that accounts for coupling between particles can be defined. By averaging the fields of the electric and magnetic dipole moments over S, the surface polarizability

can be related to the equivalent electric and magnetic surface currents [155],

$$\vec{J}_s = j\omega\overline{\overline{\alpha}}_e^{eff} \cdot \vec{E}_{t,av}\Big|_S, \qquad \vec{M}_s = j\omega\overline{\overline{\alpha}}_m^{eff} \cdot \vec{H}_{t,av}\Big|_S \tag{5.2}$$

A time-harmonic progression of $e^{j\omega t}$ is assumed, where ω is the radial frequency and t is the time. The expressions $\vec{E}_{t,av}|_S$ and $\vec{H}_{t,av}|_S$ represent the average, electric and magnetic fields tangential to the surface S.

The Surface Equivalence Principle is generally formulated in terms of fields and surface currents at a boundary. Therefore it may be more appropriate to define an impedance boundary condition. This can be done by defining an electric sheet admittance ($\overline{\overline{Y}}_{es} = j\omega\overline{\overline{\alpha}}_e^{eff}$) and magnetic sheet impedance ($\overline{\overline{Z}}_{ms} = j\omega\overline{\overline{\alpha}}_m^{eff}$) in terms of the surface polarizabilities. In general, $\overline{\overline{Y}}_{es}$ and $\overline{\overline{Z}}_{ms}$ are tensorial quantities. For illustration purposes, we will assume that the sheet impedance is isotropic: Y_{es}=Y_{es}^{yy}=Y_{es}^{zz} and Z_{ms}=Z_{ms}^{yy}=Z_{ms}^{zz} for a sheet in the $x = 0$ plane.

Once the necessary values of Y_{es} and Z_{ms} are known, the surface is discretized into unit cells. The sheet impedance of each cell is then realized through subwavelength texturing of a metallic cladding on a dielectric substrate. Field averaging techniques could be employed to find $\alpha_{e,m}^{eff}$ for a designed metallic pattern [155], but a more straightforward method is used here. The impedance is directly extracted from the complex reflection (R) and transmission (T) coefficients. As demonstrated in [156], R and T can be related to the sheet impedances of a periodic metasurface for a normally incident plane wave,

$$Y_{es} = \frac{2\,(1 - T - R)}{\eta\,(1 + T + R)}, \qquad Z_{ms} = \frac{2\eta\,(1 - T + R)}{(1 + T - R)} \tag{5.3}$$

where $\eta = \sqrt{\mu/\epsilon}$ is the wave impedance of free space. From Eq. (5.3), it can be easily shown that if the normalized electric sheet admittance and magnetic sheet impedance are equal and purely imaginary ($Y_{es}\eta = Z_{ms}/\eta$), the amplitude of the unit cell's transmission coefficient becomes unity. In addition, the transmitted phase can be varied anywhere between $-180°$ and $+180°$ to provide complete phase coverage by adjusting the magnitude of the impedance.

5.3 Relation to Previous Work

Metamaterial Huygens' surfaces introduce abrupt field discontinuities across electrically-thin layers. They are distinct from the work of Nanfang Yu *et al.* [54,157] and Xingjie

Ni *et al.* [158], which also allow field discontinuities. Unlike the metamaterial interfaces reported by these two groups, Huygens' surfaces do not incur reflection losses, and are not restricted to solely manipulating the phase of cross-polarized radiation. Huygen's surfaces can manipulate both co-polarized and cross-polarized radiation. This polarization control can be used to generate linear, circular, or elliptical polarization from a given excitation without reflection. Finally, Huygens' surfaces can redirect an incident beam with nearly 100% efficiency into a refracted beam. This is in contrast to the metamaterial interfaces reported earlier, which necessarily incurred reflection due to their exclusively electric response, and produced two refracted beams: an ordinary beam in addition to the anomalous beam. An alternative method that efficiently manipulates a wavefront involves stacking multiple layers of frequency selective surfaces [47, 159–162]. This approach is considered in the following chapters.

5.4 Beam Refraction

To demonstrate the proposed design methodology, a metamaterial Huygens' surface was developed to efficiently refract a normally incident plane wave to an angle $\phi = 45°$ from normal, as shown in Fig. 5.2(a). The fields are TM-polarized (magnetic field is $\hat{z}$-polarized), and an operating frequency of 10 GHz was chosen. Once the fields in Regions I and II are stipulated, the necessary sheet impedances can be solved. The fields in Region I are those of a plane wave traveling in the $\hat{x}$ direction, and the fields in Region II are those of a plane wave traveling at an angle of $\phi = 45°$ relative to $\hat{x}$,

$$\begin{aligned} \vec{E}_1 &= -\hat{y}e^{-jkx} \\ \vec{H}_1 &= -\hat{z}/\eta e^{-jkx} \\ \\ \vec{E}_2 &= 2^{1/4}\left(\hat{x}\,\sin(\phi) - \hat{y}\,\cos(\phi)\right) e^{-jk(y\sin(\phi)+x\cos(\phi))} \\ \vec{H}_2 &= -\hat{z}2^{1/4}/\eta e^{-jk(y\sin(\phi)+x\cos(\phi))} \end{aligned} \tag{5.4}$$

Here, $k = \omega\sqrt{\epsilon\mu} = 2\pi/\lambda$ is the propagation constant of free space and $\eta = \sqrt{\mu/\epsilon}$ is the wave impedance of free space. For $\phi = 45°$, the magnitude of the field in Region II is $2^{1/4}$ times that of Region I to ensure that power flow normal to the surface is conserved.

The Surface Equivalence Principle is then invoked to determine the necessary currents on the Huygens' surface. The resulting sheet impedance is calculated by

taking the ratio of the current to the tangential fields,

$$\begin{aligned} Y_{es} &= \frac{2\left(H_1^z - H_2^z\right)}{E_1^y + E_2^y} = \frac{2 - 2^{5/4}e^{-jky\sin(\phi)}}{\eta + 2^{1/4}\eta\cos(\phi)e^{-jky\sin(\phi)}} \\ Z_{ms} &= \frac{2\left(E_1^y - E_2^y\right)}{H_1^z + H_2^z} = \frac{2\eta - 2^{5/4}\eta\cos(\phi)e^{-jky\sin(\phi)}}{1 + 2^{1/4}e^{-jky\sin(\phi)}} \end{aligned} \tag{5.5}$$

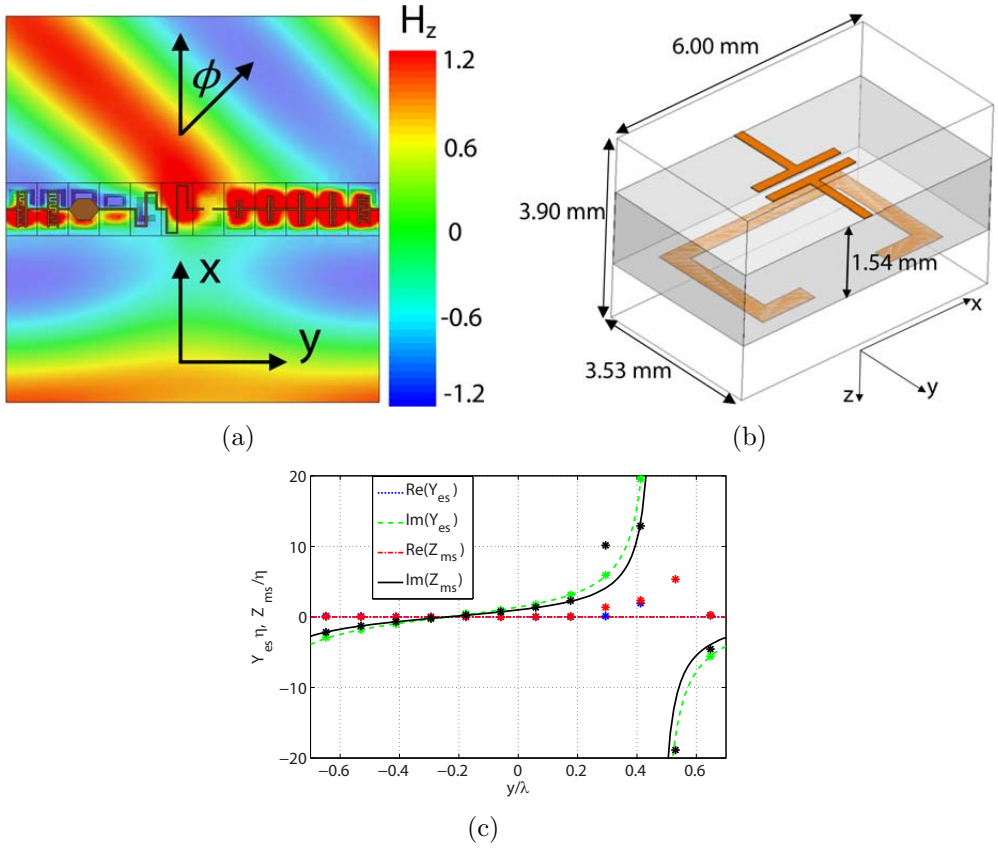

Figure 5.2: **(a)** Simulated time snapshot of the magnetic field (H_z) of a $\hat{y}$-polarized plane wave, normally incident upon the designed Huygens' surface. **(b)** Dimensions of the unit cells comprising the metamaterial Huygens' surface. The particular unit cell shown has $Y_{es} = (0.02 + 3.14j)/\eta$ and $Z_{ms} = (0.07 + 2.3j)\eta$. **(c)** One period of the real and imaginary sheet impedances to refract a normally incident electromagnetic wave to an angle of 45°. Lines are the computed values, and asterisks are the simulated values.

Since the incident and refracted waves are plane waves, the sheet impedances exhibit periodicity in the $\hat{y}$ direction with a period of $\lambda/\sin(\phi)$. Each period is discretized into 12 unit cells, consisting of patterned copper traces on a low loss, Roger's RO4003

substrate ($\epsilon_r = 3.55$, $\tan(\delta) = 0.0027$). The top layer of the substrate presents capacitively and inductively loaded traces to realize both positive and negative electric sheet reactances. The bottom layer presents capacitively loaded loops (split-ring-resonators) to realize the magnetic sheet reactances [58]. The sheet impedances extracted from simulation along with the desired values are plotted in Fig. 5.2(c). In Fig. 5.2(b), a unit cell with $Y_{es} = (0.02 + 3.14j)/\eta$ and $Z_{ms} = (0.07 + 2.3j)\eta$ is shown. The designed Huygens' surface was then simulated using a commercial, full-wave electromagnetics solver (Ansoft HFSS). Fig 5.2(a) shows a steady-state time snapshot of the simulated, $\hat{z}$ directed magnetic field. The plane wave normally incident from the bottom is steered to $\phi = 45°$ by the metamaterial Huygens' surface. From simulation, 4.7% of the incident power is absorbed by the Huygens' surface and 3.9% is scattered into undesired directions.

Since the sheet impedances are periodic, Floquet theory is employed to analyze the structure [1]. This discretizes the fields such that only well specified Floquet harmonics are allowed to propagate. When steering a wavefront to an angle $\phi = 45°$, the impedances have a periodicity of $\sqrt{2}\lambda$. In this case, the allowed propagating Floquet harmonics are simply plane waves traveling at angles $\pm 45°$ and $0°$, as shown in Fig. 5.3(a). From simulation, the fraction of the incident power that is scattered into the various propagating Floquet harmonics can be found. Fig. 5.3(b) shows this fraction for the simulated beam-refracting Huygens' surface. It can be seen that the Huygens' surface couples nearly all the incident power into the transmitted:n=1 harmonic, with minimal excitation of the other harmonics. We also note that Floquet theory dictates that this Huygens' surface exhibits frequency scanning, which is advantageous in many radar applications. For example, the direction of the n=1 harmonic changes from 51.8° to 36.1° as the frequency is scanned from 9 GHz to 12 GHz.

In general, the necessary sheet impedances can be complex for arbitrary fields on either side of the Huygens' surface. Imaginary components correspond to reactive sheets, while positive real components represent loss and negative real components represent gain. To simplify fabrication and minimize loss, the sheet impedances are approximated as being purely reactive ($\mathrm{Re}(Y_{es}) = \mathrm{Re}(Z_{ms}) = 0$). There are several methods by which this can be done, and they are compared in Fig. 5.4. In [10], the real part of the sheet impedance was simply set to zero (Method 1 of Fig. 5.4). Another method would be to analyze the reflection and transmission coefficients of a plane wave that is normally incident upon a periodic metasurface. To have a unidirectional scattered field, each unit cell of the approximated Huygens' surface could have a transmission coefficient with magnitude equal to unity and phase equal to that

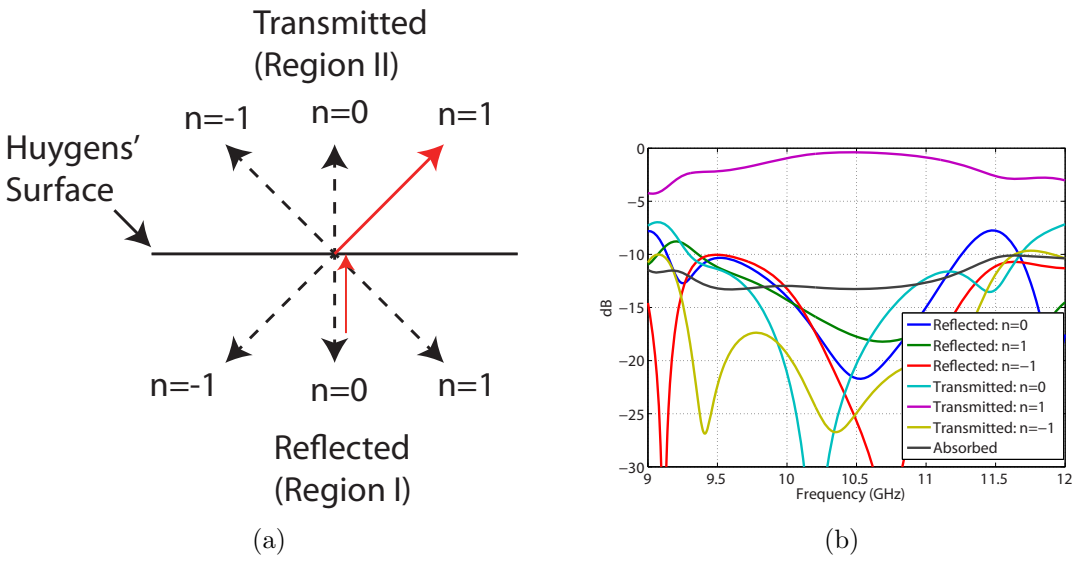

(a) (b)

Figure 5.3: **(a)** Plane wave Floquet harmonics for a Huygens' surface with $\sqrt{2}\lambda$ periodicity. The red lines correspond to the desired harmonics. **(b)** Fraction of the incident power that is coupled into the various Floquet harmonics. The Huygens' surface demonstrates high efficiency with -0.4 dB of the incident power coupled into the n=1 harmonic at 10.5 GHz, as well as a broad bandwidth of 26.1%

of the computed sheet impedance (Method 2 of Fig. 5.4). Here, we chose an alternate method. We chose the reactive sheet impedances such that they most closely approach the reflection and transmission coefficients of the computed complex sheet impedances. This was done using Matlab's nonlinear optimization toolbox to minimize the cost function, $(|R_{comp} - R_{approx}|^2 + |T_{comp} - T_{approx}|^2)$, where $(R, T)_{comp,approx}$ are the complex reflection and transmission coefficients of the computed and approximated sheet impedances respectively (Method 3 of Fig. 5.4). In general these three methods produce similar results. Approximating the sheet impedances as being purely reactive does lead to slight scattering into undesired directions. However, if the arbitrary phase difference between the fields in Regions I and II is judiciously chosen, its effect can be minimized.

Finally, it is well known from frequency selective surfaces that subwavelength unit cells exhibit minimal spatial dispersion [161, 163]. Small cell sizes ensure that the surface maintains the desired, gradient phase shift when excited at oblique angles of incidence. The angle of the refracted wave (ϕ_r) can be related to the incident angle (ϕ_i) using the generalized law of refraction that accounts for the phase discontinuity

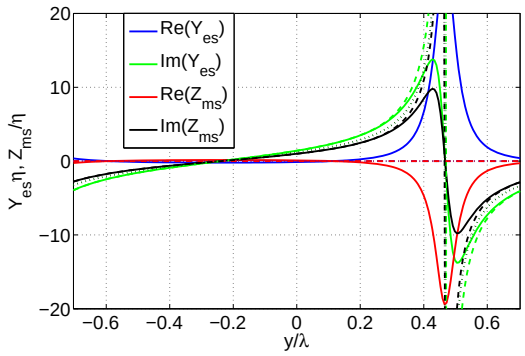

Figure 5.4: Three methods of approximating the computed, complex sheet impedance for the beam-refracting surface with purely reactive sheet impedances. Solid lines (—) correspond to the computed, complex sheet impedances. In Method 1, the real parts are simply set to zero. The dotted lines (·····) correspond to Method 2, where the sheet impedances have a transmission coefficient with unity amplitude and phase equal to the computed sheet impedance. The dashed lines (- - -) correspond to Method 3, where the sheet impedances are approximated as those minimizing the cost function $(|R_{comp} - R_{approx}|^2 + |T_{comp} - T_{approx}|^2)$.

between Regions I and II [54],

$$\sin(\phi_r) = \sin(\phi_i) + \sin(45^\circ) \tag{5.6}$$

Figs. 5.5(a) and 5.5(b) show simulated contour plots of the $\hat{z}$-polarized magnetic field values at 10.5 GHz for incident angles $\phi_i = 15^\circ$ and $\phi_i = -45^\circ$, respectively. It can be seen that the plane wave, incident from the bottom, is efficiently refracted by the surface. Fig. 5.5(c) shows the percentage of power that is refracted into the direction ϕ_r vs. the angle of incidence. The Huygens' surface performs as designed for angles of incidence from $\phi_i = -65^\circ$ to $\phi_i = 15^\circ$. As ϕ_i approaches 19°, ϕ_r approaches 90° and the performance begins to deteriorate since the refracted wave becomes a surface wave.

5.5 Measured Performance

To experimentally measure the performance of the metamaterial Huygens' surface, the normally incident plane wave was approximated with a Gaussian beam with a 57 mm beam waist. This required the fabricated surface to be 226 mm x 226 mm to capture 99.9% of the incident power [164]. A section of the fabricated Huygens' surface is shown in Fig. 5.6(a). It is composed of a vertical stack of 58 identical

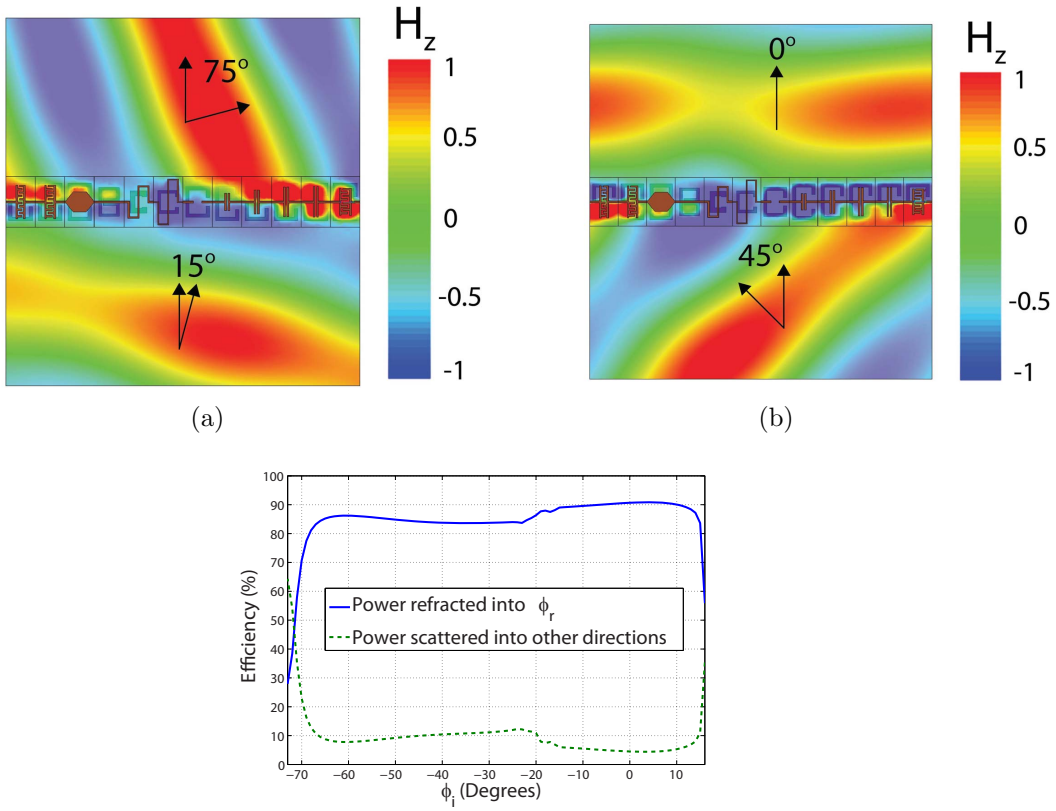

Figure 5.5: **(a)-(b)** Simulated time snapshot of the magnetic field of a TM-polarized plane wave, incident upon the designed Huygens' surface at angles $\phi = 15°$, and $-45°$, respectively. **(c)** Percentage of power that is refracted into the ϕ_r direction for various angles of incidence.

circuit board strips, with 2.35 mm air gaps between each of the boards. The top and bottom sides of the boards are shown in Figs. 5.6(b), and 5.6(c), which provide the required electric and magnetic polarization currents, respectively.

The Huygens' surface was measured using a near field scanning system [165, 166], and the performance is summarized in Fig. 5.7(a)-(e). All the contour plots of Figs. 5.7(a)-(d) are normalized by the magnitude of the incident Gaussian beam. The ratio of power transmitted in the refracted direction to the incident power, over the operating frequencies, is plotted in Fig. 5.7(e). The half-powered bandwidth and peak efficiency of the structure were measured to be 24.2% and 86%, respectively.

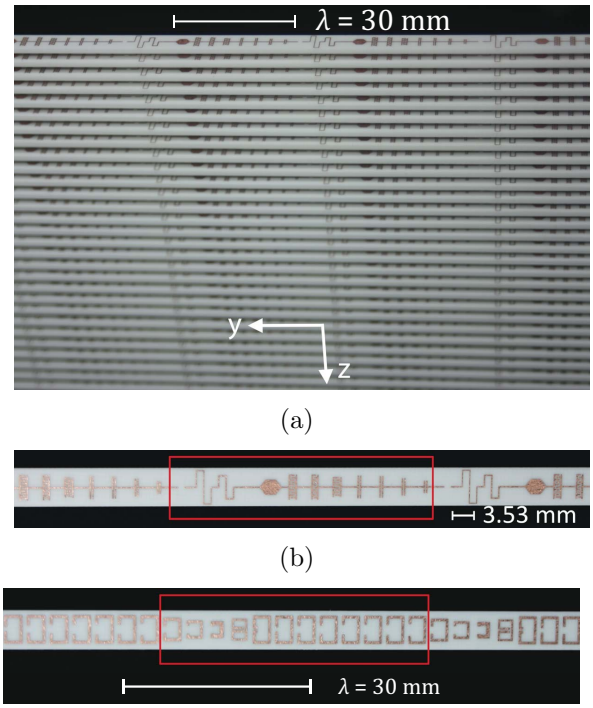

Figure 5.6: **(a)** Photograph of the fabricated Huygens' surface. **(b)** Copper traces on the top side of each substrate provide the necessary electric polarization currents. The pattern inside the red box repeats itself every 12 unit cells. **(c)** Split-ring resonators on the bottom side of each substrate provide the necessary magnetic polarization currents.

5.6 Theoretical Gaussian-to-Bessel Beam Transformer

Next, a metamaterial Huygens' surface that provides beam shaping capabilities is demonstrated with a Gaussian-to-Bessel beam transformer [157]. This example is particularly interesting because Bessel beams confine their energy to a narrow beamwidth, which has applications in fields such as near field probing, medical imaging, and radiometry [167,168]. For simplicity, we assume the fields are invariant along $\hat{z}$, and the electric field is $\hat{z}$-polarized. Since ideal Bessel beams carry infinite energy they must be truncated with a windowing function (a Gaussian was chosen), which causes them to diffract. To compensate for this, the field just behind the Huygens' surface in Region II, is stipulated to be the phase conjugated wavefront of a diffracted Bessel beam. This causes the wavefront to refocus to the desired Bessel beam profile at the designed focal plane ($x = 8.33\lambda$). Once the fields at the Huygens' surface are specified, the necessary reactive sheet impedances are determined. The incident

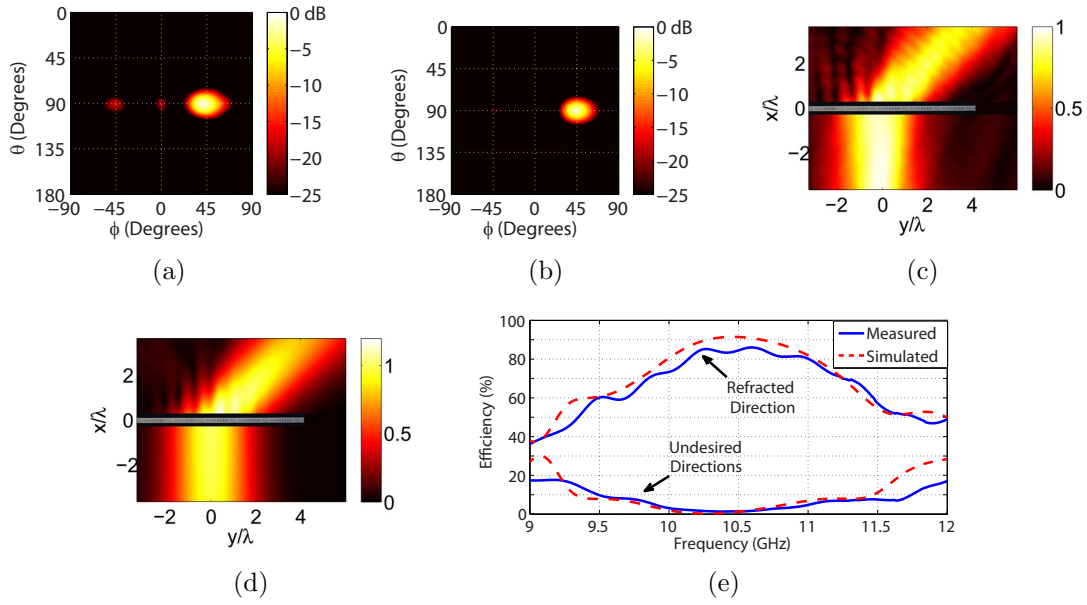

Figure 5.7: **(a** and **b)** Measured and simulated far field radiation patterns, respectively. **(c** and **d)** Measured and simulated magnetic field magnitudes in the xy plane, respectively. The incident field is shown for $x < 0$, and the transmitted field is shown for $x > 0$. **(e)** Measured and simulated efficiency of the Huygens' surface. The efficiency is defined as the ratio of the power in the refracted beam to the incident power.

electric field just in front of the Huygens' surface ($x = 0^-$) is given by,

$$E_z = \exp\left(\frac{-y^2}{(5.33\lambda)^2}\right), \tag{5.7}$$

while a Bessel beam is desired in Region II ($x > 0$). In this case, we stipulate the field at the focal plane ($x = 8.33\lambda$) to be a Gaussian truncated Bessel function,

$$E_z = 2.04 J_0(0.3ky) \exp\left(\frac{-y^2}{(8.33\lambda)^2}\right) \tag{5.8}$$

The amplitude of the Bessel function was chosen such that power was conserved between the incident and transmitted wavefronts. To apply the surface equivalence principle, the field just behind the lens ($x = 0^+$) is found by back propagating the field at the focal plane ($x = 8.33\lambda$) to the Huygens' surface. This causes the transmitted wavefront just behind the lens to refocus into the desired Bessel profile of Eq. (5.8) at the focal plane. Once the field at $x = 0$ is specified, the Huygens' surface can be realized with the reactive sheet impedances shown in Fig. 5.8.

In simulation, the computed impedances are realized with electrically thin (in

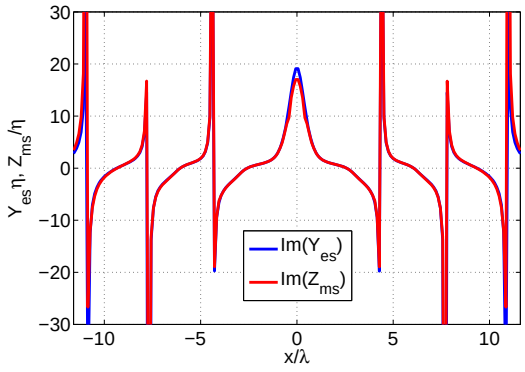

Figure 5.8: Sheet impedances that comprise the Gaussian-to-Bessel beam transformer. The real parts are zero.

terms of free space wavelengths) material slabs with identical reflection and transmission coefficients as the desired sheet impedance. This permits the use of commercial electromagnetic solvers for simulation, while maintaining virtually identical performance. Fig. 5.9(a) shows the magnitude of the simulated $\hat{z}$-directed electric field. The Gaussian beam at $x < 0$ is transformed into a Bessel beam at $x > 0$ with greater than 99% transmission. In Fig. 5.9(b) the simulated and desired values of $|E_z|$ are plotted at the input face of the Huygens' surface ($x = -1.67\lambda$), and at the focal plane ($x = 8.33\lambda$).

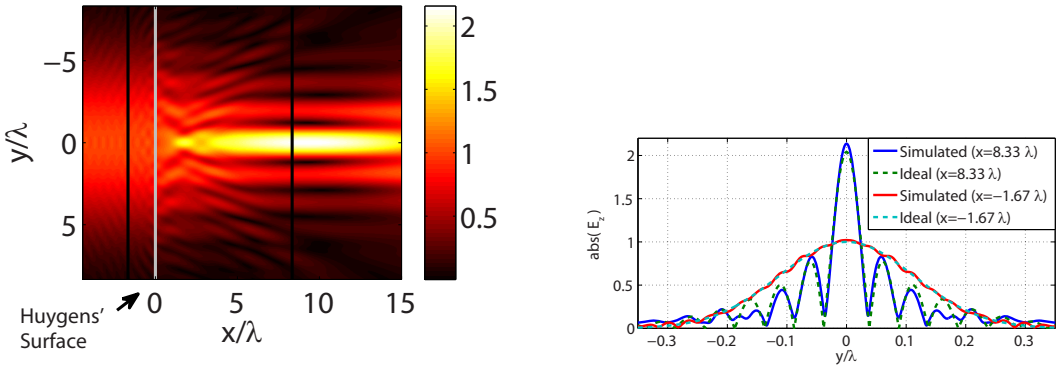

(a) (b)

Figure 5.9: **(a)** Electric field (E_z) magnitude of a two-dimensional Gaussian beam incident upon a Gaussian-to-Bessel beam transformer located at $x = 0$. **(b)** Simulated and computed electric field magnitude at the focal plane ($x = 8.33\lambda$) and at the input face of the Huygens's surface ($x = -1.67\lambda$).

5.7 Chapter Summary

The developed metamaterial Huygens' surfaces use both electric and magnetic polarization currents to manipulate electromagnetic wavefronts without reflection. These surfaces are composed of electrically small, polarizable particles which provide surface currents that satisfy the Surface Equivalence Principle between two regions. A design methodology was developed, and applied to demonstrate beam steering and shaping. A proof-of-concept Huygens' surface was experimentally demonstrated at microwave frequencies.

Metamaterial Huygens' surfaces could enable a myriad of novel devices. In the next chapter, surfaces possessing tensorial electric sheet admittances and magnetic sheet impedances with off-diagonal entries are shown to enable devices that manipulate the field profile, and allow polarization control such as linear-to-circular polarization conversion [169]. Further, in chapter 9 it is shown that metasurfaces of bianisotropic particles allow arbitrary polarization control and beamshaping. Such surfaces build on recent work showing that periodic metasurfaces exhibiting bianisotropy can perform any plane-wave polarization transformation [170]. Huygens surfaces may also find use in stealth applications. For example, two-dimensional arrays of electric and magnetic polarizable particles could be used to tailor reflected wavefronts. In addition, absorbers that are impedance matched to non-uniform wavefronts could be designed [171]. It is shown in chapter 8 that metamaterial Huygens' surfaces can also be extended to optical frequencies.

CHAPTER VI

Wavefront and Polarization Control using Cascaded Metallic Sheets

6.1 Chapter Introduction

In this chapter, we scale the concept of Huygens' surfaces up to millimeter-wave frequencies. In addition, polarization control is demonstrated. Millimeter-wave frequencies have become attractive for high bandwidth communication [51]. In particular, multi-gigabit data rates could enable emerging technologies such as wireless high-definition video, wireless local area networks, and "gigabit offices" [40, 172]. Another important application is point-to-point wireless communication, which promises to provide a lower cost alternative to fiber optic cables [52, 53]. Additionally, millimeter wavelengths offer high-resolution for imaging systems and radars in applications such as concealed weapons detection, automotive collision avoidance, missile guidance, and satellite tracking [173, 174].

All the above mentioned applications require antennas with high bandwidth, gain, and efficiency, while maintaining a low profile. At these frequencies, integrated antenna arrays suffer from excessive transmission-line losses. This has motivated systems that combine a low gain radiating element with a focusing lens. Dielectric lenses are viable options, but also bulky and expensive [172, 175, 176]. This has inspired the development of low profile metasurfaces that are capable of efficient phase and polarization control. Previously, these metasurfaces were often referred to as reflectarrays or transmitarrays for manipulation of a wavefront upon reflection and transmission, respectively.

Here, a beam-refracting Huygens' surface that also provides polarization control is presented at W-band frequencies. It is shown that it is possible to generate an arbitrary phase shift across a subwavelength thickness using three metallic sheets.

A cell design is presented that allows for independent control of the field polarized along the two orthogonal axes. The vias and complex networks that are commonly employed in traditional transmitarrays are not needed with the outlined design methodology [37,50]. This increases efficiency and reduces fabrication costs. Previous transmitarrays often achieved polarization control by placing a separately designed quarter-wave plate in front of the aperture [177]. In contrast, the beam-refracting surface developed here achieves polarization and phase control simultaneously with a single subwavelength thickness surface. This enables low-profile, high efficiency, beam shaping lenses that also incorporate polarization control.

It should be mentioned that it is often more common to design a focusing lens rather than a beam-refracting lens. However, it is more difficult to accurately characterize the fundamental performance of a focusing lens. Since the memory and time requirements for simulating entire focusing lenses are restrictive, approximations are required to characterize its performance. In contrast, a beam-refracting surface has a periodicity on the order of the wavelength, which allows simulation of the entire structure with a full wave electromagnetics solver. Additionally, the efficiency of a beam-refracting lens is easier to experimentally characterize since the feed does not present added loss such as spill-over and illumination taper. Finally, the numerical aperture of a focusing lens is limited by its ability to provide a steep phase progression at its edges. Therefore, a beam-refracting lens provides insight into the limitations of realizing focusing lenses.

6.2 Quarter-Wave Plate

To begin, polarization control is studied by considering a quarter-wave plate design. Quarter-wave plates have been extensively studied in the microwave engineering community. Some of the first reported quarter-wave plates cascaded three or four patterned sheets to realize large bandwidths on the order of 50% [62, 63, 178, 179]. However, the overall thickness of these designs was electrically large. More recently, single and double layer split-ring-resonators have been used [180, 181]. However, the bandwidth of these structures was approximately 10%. An improved design was presented in [182], where a reduced thickness and a large bandwidth were demonstrated.

Consider a plane wave propagating in the $\hat{x}$ direction, and normally incident upon a periodic quarter-wave plate in the yz plane. It is assumed that the quarter-wave plate is composed of three cascaded sheet admittances (patterned metallic sheets) as shown in Fig. 6.1(a). It should be noted that this geometry will be referred to

throughout the chapter. A necessary condition for achieving 100% transmission is that the quarter-wave plate must be symmetric, thus requiring the outer sheets to be identical. Each sheet admittance is anisotropic, diagonalized with eigenvectors in the $\hat{y}$ and $\hat{z}$ directions such that $\hat{y}$ and $\hat{z}$ polarized fields can be analyzed independent of each other. This scenario is usually modeled in terms of a circuit equivalent: free space is replaced with transmission lines and the sheet admittances with shunt loads. This enables the use of circuit based filter theory [183]. If it is assumed that all materials are lossless, the shunt loads become purely imaginary (reactive).

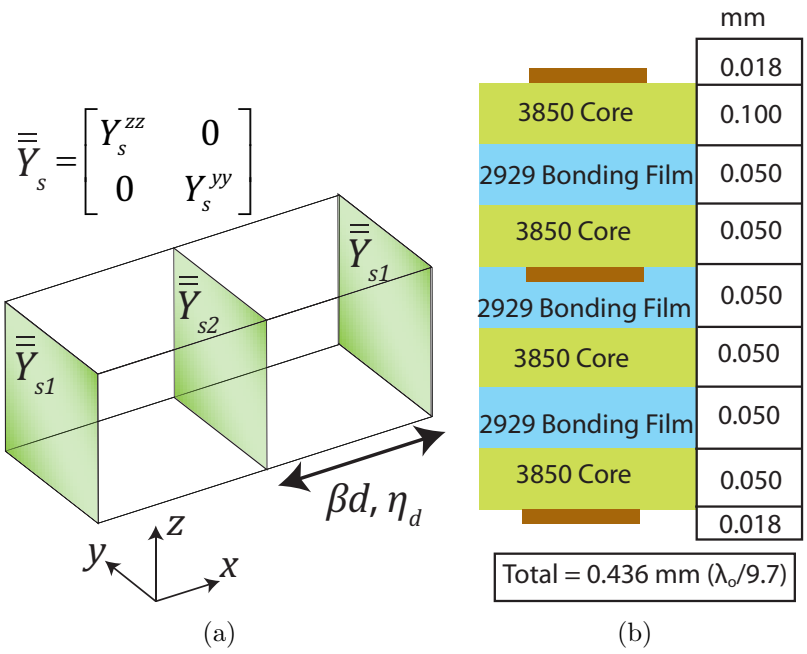

Figure 6.1: **(a)** Geometry of a generic unit cell that consists of three cascaded sheet admittances. In general each sheet admittance is anisotropic. **(b)** Material layers of the quarter-wave plate and beam-refracting Huygens' surface.

The unit cell shown in Fig. 6.2 was developed using a similar design procedure to the one presented in [182]. The quarter-wave plate consists of three cascaded patterned sheets, as shown in Fig. 6.1(b). The cell size is 1.1 mm x 1.1 mm ($\lambda_\circ$/3.5 x $\lambda_\circ$/3.5) with an overall thickness of 0.4 mm ($\lambda_\circ$/9.7). From the circuit model presented in Fig. 6.1(a), the necessary admittances of the outer and middle sheets are determined. In general, there are many admittance values that satisfy the condition of 90° phase difference between $\hat{y}$ and $\hat{z}$ polarizations while also maintaining high transmission. The solution that is chosen here consists of the outer sheets ($\overline{\overline{Y}}_{s1}$) being capacitive in the $\hat{y}$ direction and inductive in the $\hat{z}$ direction. Then simple heuristic guidelines are used to realize the necessary sheet admittances, while

also attempting to maximize the bandwidth over W-band frequencies, as suggested in [182]. To achieve an inductive response in the $\hat{z}$ direction, a central trace with dimensions 0.1 mm x 1.1 mm is used (see Fig. 6.2). Then, to increase the effective inductance further, the patches at the edges of the unit cell with dimensions 0.15 mm x 0.26 mm are added. These patches provide a capacitance in parallel with the central inductance. This increases the impedance below resonance. To achieve the capacitive response in the $\hat{y}$ direction, the rectangle with dimensions 0.79 mm x 0.2 mm is added to the center of the unit cell. The middle sheet ($\overline{\overline{Y}}_{s2}$) however is required to be inductive in the $\hat{y}$ direction and have a small capacitance in the $\hat{z}$ direction. Again, to realize the inductive response, a central trace with dimensions 1.1 mm x 0.1 mm is used in conjunction with capacitive patches (0.35 mm x 0.1 mm) at the edges of the unit cell. The required capacitance in the $\hat{z}$ direction is quite small. It is attained by the capacitive patches that have dimensions 0.35 mm x 0.1 mm.

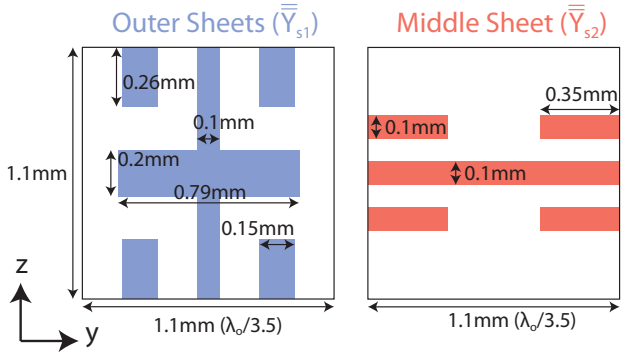

Figure 6.2: Dimensions of the outer and middle sheets of the designed quarter-wave plate.

This unit cell can be thought of as a building block for the Huygens' surface that will be developed in the next sections. When a plane wave traveling in the $\hat{x}$ direction is normally incident upon the quarter-wave plate, a 90° phase difference between $\hat{y}$ and $\hat{z}$ directed electric fields is achieved. Therefore, if the incident field is polarized along the $\hat{y} \pm \hat{z}$ directions such that the two polarizations are equally excited, the transmitted field will be circularly polarized.

The substrate was chosen to be the liquid crystal polymer, Rogers Ultralam 3850 ($\epsilon_r = 3.19$ and $\tan(\delta) = 0.0045$) with an 18 μm thick (1/2 oz.) copper cladding. The permittivity and loss tangent of the bonding film (Rogers 2929) were roughly the same as that of the Ultralam substrate. These materials were chosen because they have a low permittivity and loss, and are well characterized at mm-wave frequencies [184]. In addition, their low water absorption rate, low thermal expansion characteristics,

and flexibility make them extremely attractive for a broad range of applications [21]. Since the maximum substrate thickness that is commercially available is 100 μm, multiple layers needed to be stacked together to achieve the desired thickness of 400 μm, as shown in Fig. 6.1(b).

The quarter-wave plate was simulated with the full wave electromagnetic solver CST Microwave Studio. The simulated transmission coefficient and axial ratio are plotted in Fig. 6.3 for various angles of incidence along the xy plane. At normal incidence ($\phi = 0°$), the 3 dB axial ratio bandwidth is 40%, and the transmission coefficient is above -3 dB over this entire bandwidth. The performance of the quarter-wave plate is relatively insensitive to the angle of incidence. Only when the angle of incidence approaches $\phi = 40°$ does the performance begin to deteriorate. These results are quite similar to the design presented in [182], which represents the state of the art. The primary differences are we operate at frequencies that are four times higher, and chose to use materials that are compatible with commercial printed-circuit-board processes.

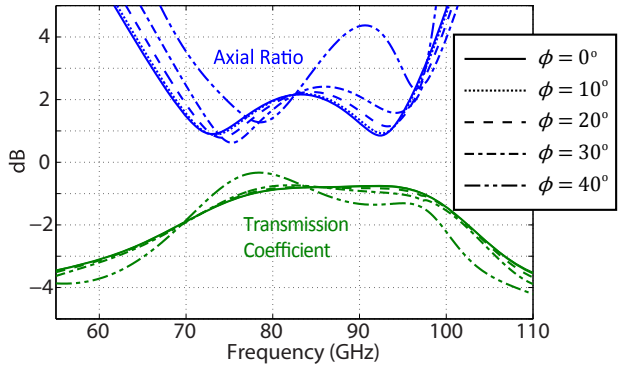

Figure 6.3: Simulated transmission coefficient and axial ratio of the transmitted field when illuminated with a linearly polarized plane wave with electric field oriented along $\hat{y}+\hat{z}$. Also shown is the performance at angles of incidence other than normal.

6.3 Cascaded Sheet Admittances

Only 90° phase coverage is necessary to realize quarter-wave plates. However, a full 360° phase coverage is desired for most applications. It has been shown that a three layer structure contains the minimum number of layers in which it is possible to provide perfect transmission and complete phase coverage [48]. A further increase in the number of layers would lead to increased bandwidth, fabrication complexity, and

cost. The reflection and transmission coefficients of the geometry shown in Fig. 6.1(a) can be related to the sheet admittances, using the transmission matrix approach [185]. First the $ABCD$ matrix that relates the field on either side of the cascaded sheets is found,

$$\begin{pmatrix} A & B \\ C & D \end{pmatrix} = \left[\begin{pmatrix} 1 & 0 \\ Y_{s1} & 1 \end{pmatrix} \begin{pmatrix} \cos(\beta d) & j\eta_d \sin(\beta d) \\ j\sin(\beta d)/\eta_d & \cos(\beta d) \end{pmatrix} \right.$$
$$\left. \cdot \begin{pmatrix} 1 & 0 \\ Y_{s2} & 1 \end{pmatrix} \begin{pmatrix} \cos(\beta d) & j\eta_d \sin(\beta d) \\ j\sin(\beta d)/\eta_d & \cos(\beta d) \end{pmatrix} \begin{pmatrix} 1 & 0 \\ Y_{s1} & 1 \end{pmatrix} \right] \tag{6.1}$$

The $ABCD$ matrix can then be related to the S-parameters of the structure,

$$\begin{pmatrix} S_{11} & S_{12} \\ S_{21} & S_{22} \end{pmatrix} = \begin{pmatrix} \frac{B/\eta_\circ - C\eta_\circ}{2A+B/\eta_\circ+C\eta_\circ} & \frac{2}{2A+B/\eta_\circ+C\eta_\circ} \\ \frac{2}{2A+B/\eta_\circ+C\eta_\circ} & \frac{B/\eta_\circ - C\eta_\circ}{2A+B/\eta_\circ+C\eta_\circ} \end{pmatrix} \tag{6.2}$$

Note that Eqn. (6.2) was simplified from that in [185], using the symmetry of the structure ($A = D$).

Alternatively, it is possible to relate the transmission matrix of the cascaded sheets to an image impedance and phase delay, which provides additional insight. The phase delay (ϕ) and image impedance (Z_i) of a reciprocal and symmetric structure are recalled in terms of the transmission matrix ($ABCD$) [185],

$$\cos(\phi) = A, \qquad Z_i = \frac{-jB}{D\,\tan(\phi)} \tag{6.3}$$

Then the $ABCD$ matrix from Eqn. (6.1) is inserted into Eqn. (6.3) to yield the phase delay and image impedance in terms of the sheet admittances (Y_{s1} and Y_{s2}), wave impedance in the substrate (η_d), wavenumber in the substrate (β), and separation between sheet admittances (d),

$$\begin{aligned} \sin^2\left(\frac{\phi}{2}\right) &= (-j\sin(2\beta d)/2)\left[\eta_d(Y_{s1}+Y_{s2}/2)\right. \\ &+ \left. j\tan(\beta d)(1+Y_{s1}Y_{s2}\eta_d^2/2)\right] \\ Z_i &= \frac{1}{(jY_{s1}+\cot(\beta d)/\eta_d)\,\tan(\phi/2)} \end{aligned} \tag{6.4}$$

From the image impedance and phase delay, the S-parameters of the cascaded sheets

can be solved [185],

$$\begin{aligned} S_{21} &= \frac{1}{\cos(\phi) + j\frac{\sin(\phi)}{2}(\frac{Z_i}{\eta_\circ} + \frac{\eta_\circ}{Z_i})} \\ S_{11} &= j\left(\frac{Z_i}{\eta_\circ} - \frac{\eta_\circ}{Z_i}\right)\frac{\sin(\phi)}{2}S_{21} \end{aligned} \tag{6.5}$$

Inserting Eqn. (6.4) into (6.5), the reflection and transmission coefficients can be written in terms of the sheet admittances.

Alternatively, it is possible to derive the sheet admittances in terms of the S-parameters. This is done by first solving for the phase delay and image impedance as a function of the S-parameters [186],

$$\begin{aligned} \cos(\phi) &= \frac{1 - S_{11}^2 + S_{21}^2}{2S_{21}} \\ Z_i &= \pm\eta_\circ\sqrt{\frac{(1+S_{11})^2 - S_{21}^2}{(1-S_{11})^2 - S_{21}^2}} \end{aligned} \tag{6.6}$$

Next, the sheet admittances from Eqn. (6.4) are solved for as a function of the image impedance (Z_i), phase delay (ϕ), wave impedance in the substrate (η_d), wavenumber in the substrate (β), and separation between sheet admittances (d),

$$\begin{aligned} Y_{s1} &= \frac{j}{\eta_d \tan(\beta d)} - \frac{j}{Z_i \tan(\phi/2)} \\ Y_{s2} &= j\left[-Z_i\sin(\phi/2) - Z_i\sin(3\phi/2)\right. \\ &+ \left. 2\eta_d\sin(2\beta d)\cos(\phi/2)\right]/(2\eta_d^2\cos(\phi/2)\sin^2(\beta d)) \end{aligned} \tag{6.7}$$

Inserting Eqn. (6.6) into (6.7), the sheet admittances can be expressed in terms of the reflection and transmission coefficients.

In Figs. 6.4 (a) and (b), the transmittance ($|S_{21}|^2$) and phase of the transmission coefficient are plotted as a function of Y_{s1} and Y_{s2}, assuming that the sheets in Fig. 6.1(a) are lossless. A dashed blue line is superimposed on the figures to outline points where the metasurface provides perfect transmission. Fig. 6.4(c) plots the transmitted phase as a function of the outer sheet admittances (Y_{s1}) along the dashed blue lines in Figs. 6.4 (a) and (b). It can be seen that the transmitted phase asymptotically approaches 360° coverage, while the magnitude maintains 100% transmittance.

Also shown in Fig. 6.4(c) is the relationship between the sheet admittance of the middle sheet (Y_{s2}) and outer sheets (Y_{s1}) that provides perfect transmission. In this analysis, it is assumed that all materials are lossless, the electrical length between each sheet is $\beta d = (2\pi)0.092$, and the wave impedance of the dielectric spacers is $\eta_d = (1/\sqrt{3.19})\eta_\circ = \sqrt{\mu_\circ/3.19\epsilon_\circ}$.

Note that as the magnitude of the outer sheet admittances is increased, the region of high transmission in Fig. 6.4(a) is reduced. Therefore, as the transmitted phase goes to 0°, the transmission bandwidth approaches 0%, since all reactive elements are frequency dispersive. To illustrate this point further, consider a cell that has an impedance of $Y_{s1}\eta_\circ = -5j$ and $Y_{s2}\eta_\circ = 2.8j$ (see Fig. 6.4). This cell has a transmittance of 100% and transmitted phase of −12°. However, if either admittance is perturbed slightly due to its frequency dispersion, the transmittance quickly drops off. In contrast, the cells operating closer to $Y_{s1}\eta_\circ = 0j$ and $Y_{s2}\eta_\circ = 0j$ have a much larger region of high transmittance, and therefore a larger transmission bandwidth.

A more physical, fields-based explanation can also demonstrate how complete phase control and high transmission are achieved with the cascaded sheet admittances shown in Fig. 6.1(a). Provided that the overall thickness of the cascaded sheet admittances is subwavelength, this structure can be treated as a single metasurface: a single boundary condition that supports both electric and magnetic surface currents [7]. In the previous chapter, it was shown that to maintain high transmission while generating complete phase coverage, both the electric and magnetic surface currents need to be independently controlled [187,188]. To demonstrate how this control is achieved here, let's first consider a quasi-static magnetic field interacting with the three sheet structure shown in Fig. 6.5. A $\hat{y}$-directed magnetic field generates circulating electric currents on the outer surfaces, thus creating an equivalent magnetic current [59]. However, the magnetic field will not interact with the middle sheet since the induced currents are canceled out due to symmetry considerations. Conversely, all three sheets will interact with a $\hat{z}$-directed electric field. Therefore, the outer sheets can be designed first, to realize any desired magnetic response. Then, the middle sheet can be designed to independently control the electric response, without affecting the magnetic response. This enables independent control over both the electric and magnetic surface currents, which in turn provides complete phase control.

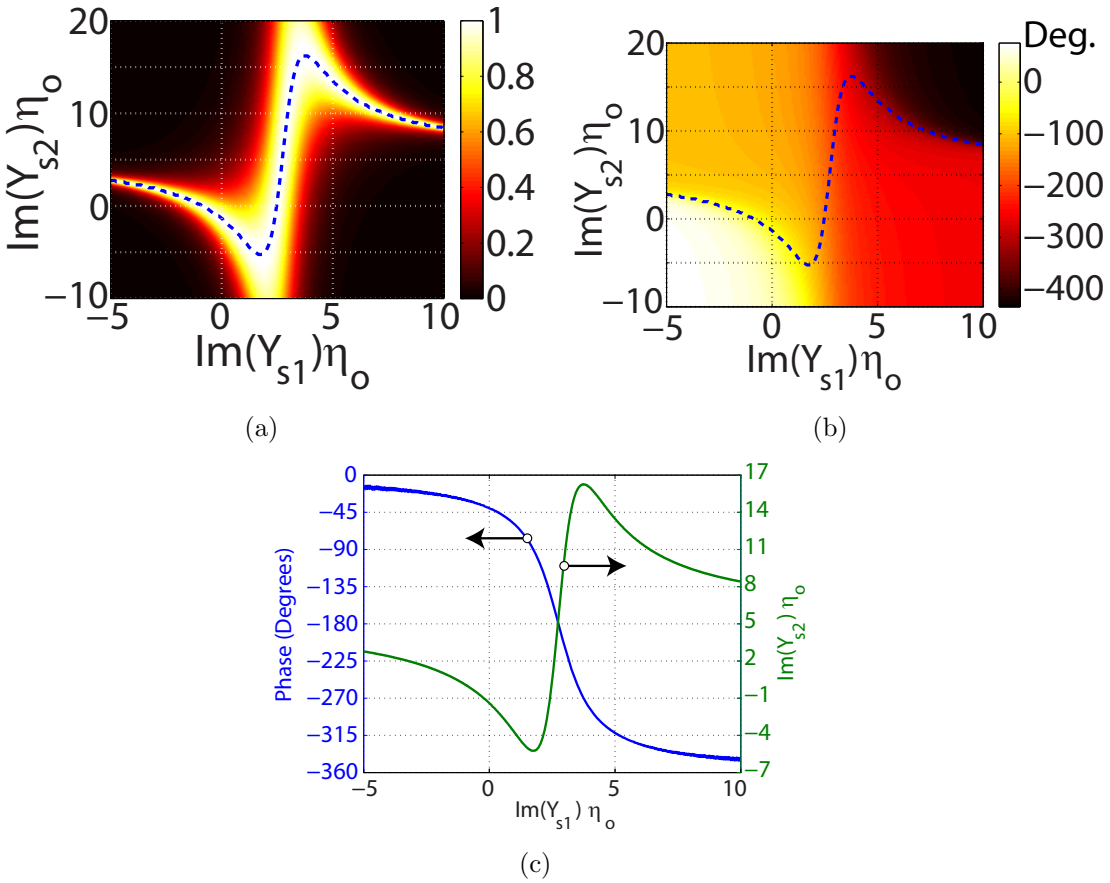

Figure 6.4: **(a)** Transmittance ($|S_{21}|^2$) as a function of the outer sheet admittances (Y_{s1}) and middle sheet admittance (Y_{s2}). **(b)** Transmitted phase as a function of the outer and middle sheet admittances. **(c)** Transmitted phase (left) and inner sheet admittance (right) as a function of the outer sheet admittance for points that satisfy perfect transmission (dashed blue line of (a) and (b)).

6.4 Cell Design

Arrays of capacitively loaded dipoles are used to realize the Huygens' surfaces' cascaded sheet admittances, as shown in Fig. 6.6. Using the insight gained from Figs. 6.4 (a) and (b), each unit cell is individually designed assuming infinite periodicity, which is known as the local periodicity approximation [35, 39, 64].

Each sheet admittance ($\overline{\overline{Y}}_{s1}$ and $\overline{\overline{Y}}_{s2}$) can be modeled as a series LC circuit, with independent control of the admittance for the $\hat{y}$ and $\hat{z}$ polarizations. The dimensions W_y and G_y primarily influence C and the dimension S_y primarily influences L, for a $\hat{y}$-polarized electric field. Similarly, W_z, G_z, and S_z influence L and C for a $\hat{z}$-polarized electric field. By tuning the resonance of the series LC circuit, the sheet admittance

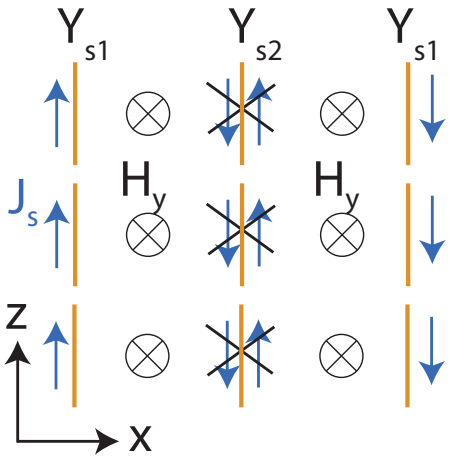

Figure 6.5: Induced currents on the three sheet admittances from a $\hat{y}$-directed, quasi-static magnetic field. There is no net current on the middle sheet due to symmetry. The sheet admittance of the outer sheets can control the magnetic response while the admittance of the middle sheet only controls the electric response.

can be made inductive or capacitive so that complete phase control is achievable. The minimum feature size was set to 75 μm so that standard PCB processes could be used for fabrication. The substrate was again chosen to be Rogers Ultralam 3850 ($\epsilon_r = 3.19$ and $\tan(\delta) = 0.0045$) with an 18 μm thick (1/2 oz.) copper cladding, as was previously shown in Fig. 6.1(b).

An iterative design approach is used to find the necessary design dimensions (W, G, and S) to achieve a desired phase shift while maintaining high transmission. First, the transmission coefficient is simulated for a unit cell whose dimensions are chosen arbitrarily. From the magnitude and phase of the transmission coefficient, the sheet admittances of the unit cell are estimated using Fig. 6.4. Then, the dimensions are changed to tune the sheet admittances closer to those that achieve high transmission and a desired phase shift. Generally, only a few iterations are necessary before the desired transmission coefficient is achieved. This process can be used to realize an arbitrary phase shift for both $\hat{y}$ and $\hat{z}$ polarizations.

The performance of a typical unit cell is shown in Fig. 6.7. This cell is designed to provide high transmission, a 105° phase delay for a $\hat{y}$-polarized electric field, and a 195° phase delay for a $\hat{z}$-polarized electric field, at 77 GHz. Reflection primarily accounts for the loss away from the center frequency.

In the next section, unit cells with varying dimensions will be distributed across a surface to generate a beam-refracting Huygens' surface. In non-periodic designs such

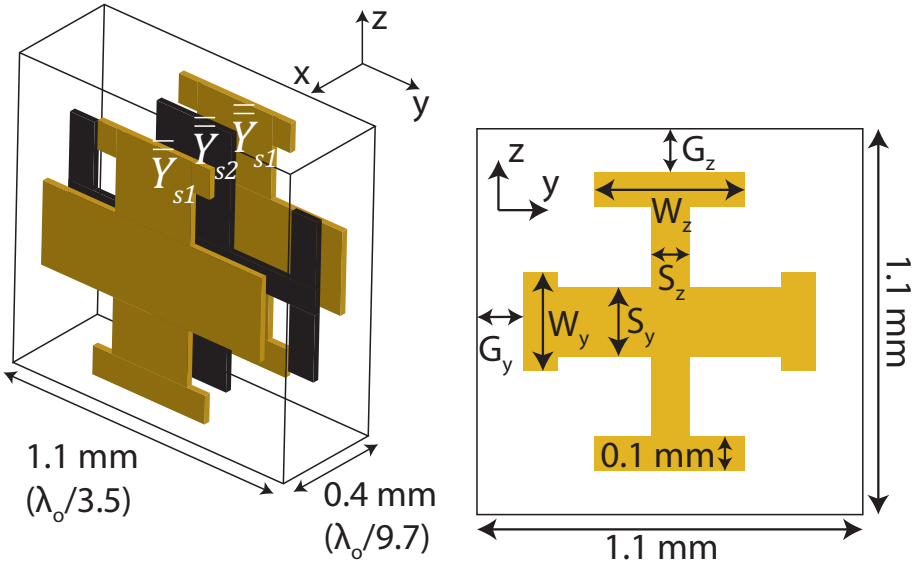

(a) (b)

Figure 6.6: **(a)** Perspective view of a typical unit cell that can provide complete phase control while maintaining high transmission. **(b)** Design dimensions of the outer ($\overline{\overline{Y}}_{s1}$) and middle ($\overline{\overline{Y}}_{s2}$) layers. With reference to Fig. 6.1(a), the dimensions S_z, G_z, and W_z primarily influence the Y_s^{zz} admittance, and the dimensions S_y, G_y, and W_y primarily influence the Y_s^{yy} admittance.

as this, there are two competing issues that must be weighed when designing each unit cell. For series LC resonators, bandwidth is enlarged with an increase in C, and corresponding decrease in L. This motivates maximizing the capacitance between neighboring cells. However, since two neighboring unit cells will be different, the assumption of infinite periodicity is somewhat inaccurate. This inaccuracy increases as the capacitance between cells is increased. In other words, increasing C creates a higher bandwidth, but more inaccuracy in the model. Therefore a compromise must be made between bandwidth and accuracy of the local periodicity approximation.

6.5 Beam-Refracting Huygens' Surface

Next, a metasurface that refracts a normally incident plane wave to an angle of $\phi_r = 45°$ and converts the polarization from linear to circular at 77 GHz is designed. This represents a steep phase progression compared to previous metasurfaces [36]. To realize a beam-refracting Huygens' surface with a discrete number of unit cells,

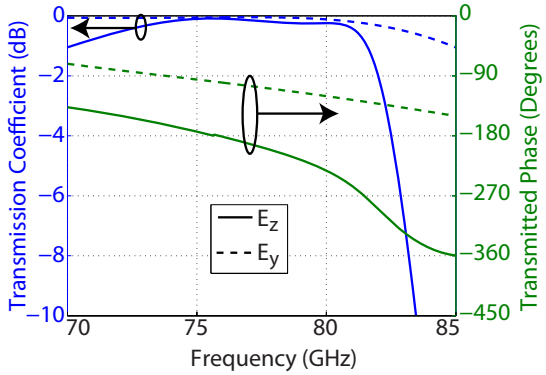

Figure 6.7: Frequency dependance of the transmitted amplitude and phase for a typical unit cell (Cell# 5 of the next section). Reflection primarily accounts for the loss away from the center frequency.

Floquet theory dictates that if the phase shift between each cell is given by [1],

$$\delta_n = 2\pi n/N + \delta_\circ \tag{6.8}$$

the angle of the refracted beam will satisfy,

$$\sin(\phi_r) = \left(\frac{\lambda_\circ}{Na}\right) - \sin(\phi_i) \tag{6.9}$$

Here, δ_n is the transmitted phase at cell n, N is the number of cells, $\delta_\circ$ is an arbitrary phase shift, and a is the cell size. The angles ϕ_i and ϕ_r represent the angles of the incident and refracted beams from normal, as shown in Fig. 6.8. A $\hat{z}$-directed electric field will be referred to as the transverse electric (TE) polarization and a $\hat{z}$-directed magnetic field will be referred to as the transverse magnetic (TM) polarization.

It should be noted that the refracted direction (ϕ_r) is a function the number of cells (N) as given by Eqn. (6.9). Here, the angle of refraction ($\phi_r = 45°$), incident angle ($\phi_i = 0°$), wavelength ($\lambda_\circ = 3.9$) mm, and cell size ($a = 1.1$) mm were all stipulated and then the necessary number of cells was solved for ($N = 5$).

As was previously mentioned, a tradeoff must be made between the bandwidth and the validity of the local periodicity approximation. This also led us to consider designing for a reduced phase coverage across the surface. By providing reduced phase coverage, both the bandwidth and model accuracy are improved since the variation in mutual coupling from cell-to-cell is decreased. On the other hand, if the phase coverage is reduced excessively, the efficiency decreases since more power scatters into undesired directions (Floquet harmonics). To illustrate this, consider the case

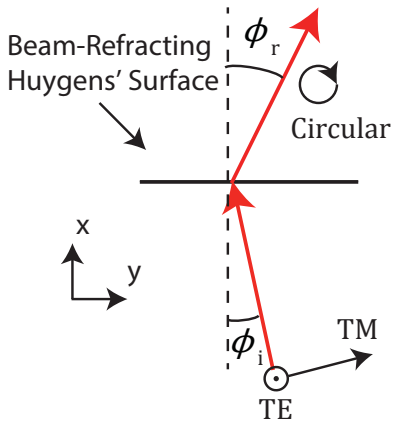

Figure 6.8: A linearly polarized plane wave is refracted by the Huygens' surface and its polarization is converted to circular.

where $N = 3$, $\delta_\circ = 0$, and $\phi_i = 0°$. If a theoretical beam-refracting surface has 100% transmission and the ideal phase shifts given by Eqn. (6.8) across it ($\delta_{1,2,3} = 120°, 240°, 360°$), 100% of the power will be refracted. However, if the phase of the third cell is reduced from 360° to 330° for example, only 94% of the incident power will be refracted since other Floquet harmonics will be excited as well [189]. From simulations, it was found that reducing the phase coverage to 279° from the ideal phase coverage of 306° resulted in a maximum efficiency of 74% at 77 GHz. The efficiency is defined here as the ratio of the power refracted into the desired direction to the incident power [187].

In this example, the ideal phase coverage is 306° due to the metasurface's discretization. Due to discretization, the phase difference between adjacent cells should be 72°, according to Eqn. (6.8). For Cell# 1, let us assume that the phase of the $\hat{z}$-polarized transmitted field is 0°, and the $\hat{y}$-polarized transmitted field is −90°. Since Cell# 5 is the furthest away from Cell# 1, it intuitively should have the largest transmitted phase. For Cell# 5, the phase is $-72° * 4 = -288°$ for the $\hat{z}$-polarized transmitted field and $-90° - 72° * 4 = -378°$ for the for the $\hat{y}$-polarized transmitted field. However, a phase of −378° is equivalent to a phase of −18°, due to phase wrapping. Therefore, we turn to Cell# 4 to see whether it affects the required phase coverage. For Cell# 4, the phase of the $\hat{y}$-polarized transmitted field is $-90 - 72° * 3 = -306°$, and therefore it dictates the maximum transmission phase for the metasurface. As a result, the required phase coverage is 306°.

One period of the optimized beam-refracting Huygens' surface is shown in Fig. 6.9,

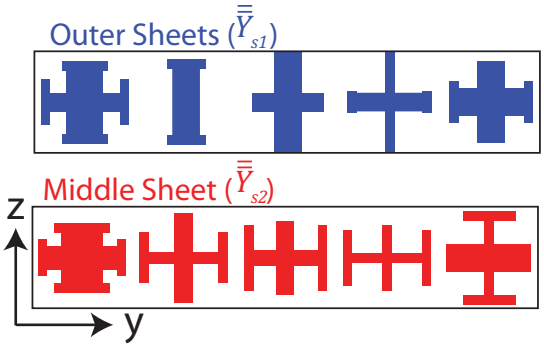

Figure 6.9: Designed geometry of the outer and middle sheets for the beam-refracting Huygens' surface.

and the dimensions of the patterns are listed in Tables 6.1 and 6.2. The transmitted power and phase at 77 GHz for each simulated cell is shown in Table 6.3. It can also be seen that each cell individually acts as a quarter-wave plate since the phase difference between the $\hat{y}$ and $\hat{z}$ polarizations is 90°. From the simulated reflection and transmission coefficients of each unit cell, the imaginary part of the sheet admittances in the equivalent circuit presented in Sections 6.2 and 6.3 were extracted, and they are listed in Table 6.4. The relationship between the outer and middle sheet admittances (Y_{s1} and Y_{s2}) extracted from simulation are shown in Fig. 6.10. For comparison purposes, the theoretical curve for perfect transmission from Fig. 6.4 is also shown. It can be seen that the simulated sheet admittances closely follow the theoretical curve, thus validating the circuit model and design. Note that the two cells with largest values of the sheet admittance do not follow the theoretical curve as closely. The admittance of these cells was reduced to increase bandwidth.

Table 6.1: Dimensions (μm) of the outer sheets ($\bar{\bar{Y}}_{s1}$) of the beam-refracting Huygens' surface

Cell#	G_{y1}	W_{y1}	S_{y1}	G_{z1}	W_{z1}	S_{z1}
1	150	500	200	210	500	400
2	400	300	300	170	420	300
3	320	200	200	0	300	300
4	190	240	200	0	100	100
5	200	450	300	220	300	300

The simulated performance of the Huygens' surface at normal incidence is presented in Fig. 6.11. Simulations assumed that a linearly polarized plane wave with electric field directed along $\hat{y} + \hat{z}$ was normally incident upon the metasurface. A time snapshot of the simulated co-polarized electric field is shown in Fig. 6.11(a).

Table 6.2: Dimensions (μm) of the middle sheet ($\overline{\overline{Y}}_{s2}$) of the beam-refracting Huygens' surface

Cell#	G_{y2}	W_{y2}	S_{y2}	G_{z2}	W_{z2}	S_{z2}
1	150	400	250	350	600	450
2	140	550	114	140	200	200
3	200	700	170	310	200	200
4	150	600	100	400	100	100
5	180	300	300	100	570	100

Table 6.3: Amplitude ($T_{y,z}$) and phase ($\phi_{y,z}$) of the transmission coefficient at 77 GHz of the various cells that comprise the beam-refracting Huygens' surface.

Cell#	T_y (dB)	T_z (dB)	ϕ_y (Deg.)	ϕ_z (Deg.)
1	-2.29	-0.81	-270	-180
2	-1.30	-1.33	-14	-251
3	-0.19	-0.78	-51	+9
4	-0.08	-0.27	-122	-33
5	-0.14	-0.04	-194	-105

The component of the electric field polarized along $\hat{y} + \hat{z}$ is shown for $x < 0$, and the left-handed circular component is shown for $x > 0$. If the incident field were polarized along $\hat{y} - \hat{z}$, the transmitted field would be right-handed circular instead. It can be seen that the linearly polarized plane wave from the bottom is efficiently refracted by the metasurface, and at the same time the polarization is converted to circular. This is better quantified in Fig. 6.11(b), which shows the frequency dependence of the axial ratio and transmission coefficient of the field in the refracted direction given by Eqn. (6.9). It should be noted that Floquet theory requires the refracted direction to scan with frequency, since Eqn. (6.9) is a function of the wavelength. Therefore, as the frequency is scanned from 70 GHz to 80 GHz, the angle of refraction varies from $\phi_r = 51^\circ$ to $\phi_r = 43^\circ$.

From simulation, it is possible to determine the loss mechanisms of the beam-refracting Huygens' surface, as shown in Fig. 6.12. First of all, a small percentage of the refracted power is converted to cross-polarized, right-handed circular polarization. In addition, Floquet theory stipulates that some of the power is also transmitted into the undesired $\phi_r = 0^\circ$ and $\phi_r = -45^\circ$ directions since a reduced phase coverage is used. Finally, some of the incident power is reflected and absorbed by the metasurface.

Since the cell size of the metasurface is subwavelength, it is expected that it will

Table 6.4: Imaginary parts of the normalized admittances of the outer and middle sheets at 77 GHz

Cell#	$\mathrm{Im}(Y_{s1}^{yy})\eta$	$\mathrm{Im}(Y_{s2}^{yy})\eta$	$\mathrm{Im}(Y_{s1}^{zz})\eta$	$\mathrm{Im}(Y_{s2}^{zz})\eta$
1	4.75	10.76	2.96	0.94
2	0.29	-3.75	3.92	11.17
3	1.02	-4.74	-6.48	3.10
4	2.24	-4.26	-2.72	1.84
5	2.91	7.27	1.98	-4.88

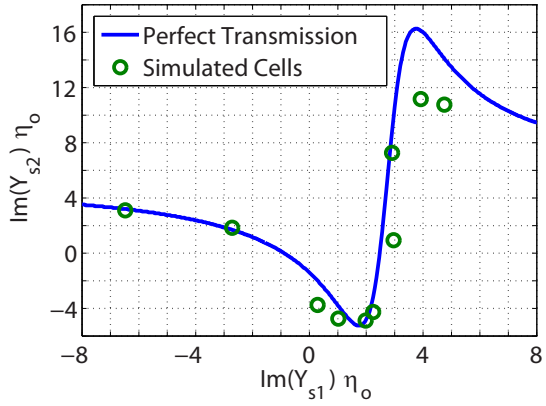

Figure 6.10: Sheet admittances extracted from simulation for each polarization (Y_s^{yy} and Y_s^{zz}) of the five unit cells comprising the beam-refracting Huygens' surface. Also shown is the relationship between the sheet admittances of the outer and middle sheets that correspond to perfect transmission (see Fig. 6.4).

be well behaved over a large range of incident angles [161]. As illustrated in Fig. 6.13, simulations show that the lens efficiently refracts the incident beam and converts the polarization from linear to circular for incident angles between $-10°$ to $70°$. The reason the performance is not symmetric with respect to incident angle is due to the additional $\left(\frac{\lambda_o}{Na}\right)$ term from Eqn. (6.9). This causes the refracted angle to approach $90°$ as the incident angle approaches $-18°$. However, if the incident angle is $+18°$ the refracted angle will be $23°$

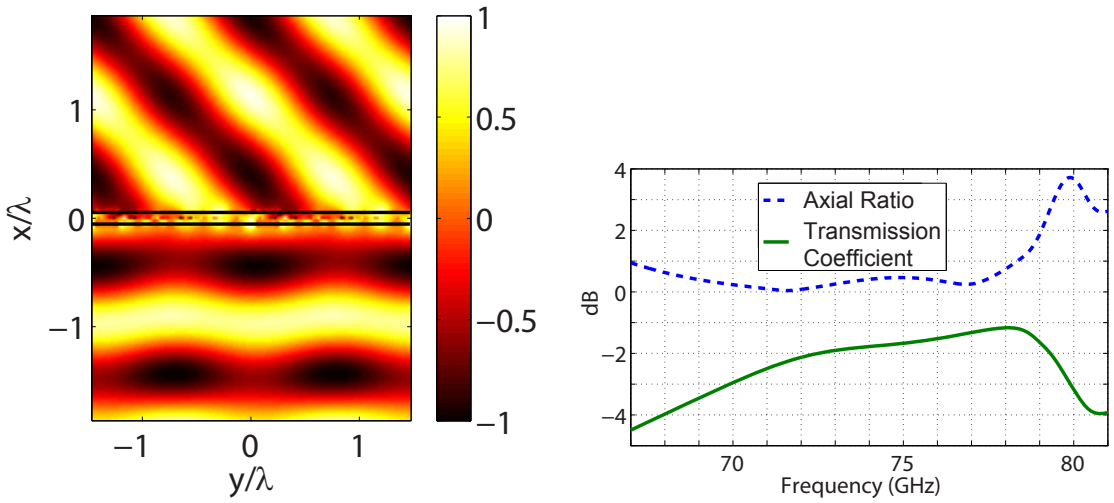

(a) (b)

Figure 6.11: Simulated performance of the metasurface at normal incidence. **(a)** Time snapshot of the co-polarized electric field of a linearly polarized plane wave incident upon the designed Huygens' surface at 77 GHz. The component of the electric field polarized along $\hat{y} + \hat{z}$ is shown for $x < 0$, and the left-handed circular component is shown for $x > 0$. **(b)** Frequency dependence of the axial ratio and transmission coefficient for the field transmitted in the refracted direction.

6.6 Measurements

6.6.1 Near Field Scanning System

Both the quarter-wave plate and beam-refracting Huygens' surface were fabricated using commercially available, printed-circuit-board processes with a minimum feature size of 75 μm. The sample sizes were 81.4 mm x 81.4 mm. To characterize the fabricated structures, the near-field scanning system shown in Fig. 6.14 was used [165]. A Gaussian-Optics-Antenna (Millitech GOA-10-R00004F) was connected to the transmitting port of a vector network analyzer (Agilent E8361A). The antenna illuminated the Huygens' surface at normal incidence with a focused Gaussian beam with a measured beam waist of 40 mm in diameter [164]. The incident field was linearly polarized with electric field oriented along the $\hat{y} + \hat{z}$ direction to equally excite the TE and TM polarizations. An open-ended WR-10 waveguide probe was connected to the receive port of the network analyzer to measure the transmitted, $\hat{y} + \hat{z}$ directed electric field. A scattering cone was used to minimize backscatter from the metallic structure supporting the waveguide probe [190]. Using a two-dimensional translation stage with 5 μm accuracy, the field was sampled over an 81 mm x 81 mm

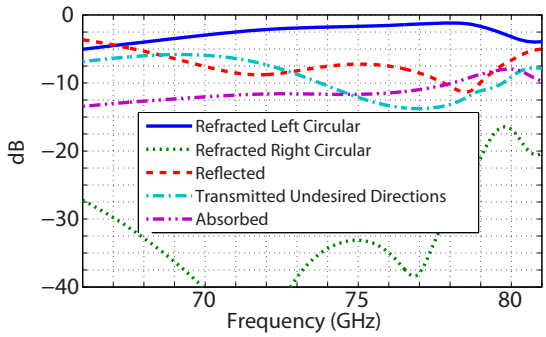

Figure 6.12: Simulated Floquet harmonics and loss mechanisms of the beam-refracting metasurface.

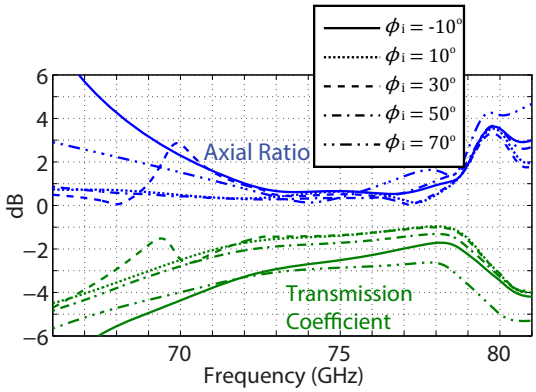

Figure 6.13: Axial ratio and transmission coefficient in the refracted direction when illuminated at angles away from normal incidence. Note that the refracted direction is a function of the incident angle as detailed in Eqn. (6.9).

area ($20.8\lambda_\circ$ x $20.8\lambda_\circ$) at the $x = 17$ mm ($4.4\lambda_\circ$) plane. The field was sampled every 1.35 mm ($\lambda_\circ/3.5$), which ensured that sampling errors were well below the noise floor. Next, an open-ended waveguide probe with a 90° twist was connected to the receive port of the network analyzer to measure the $\hat{y} - \hat{z}$ directed electric field. The transmitted field was again sampled, thus providing the transmitted amplitude and phase for two orthogonal polarizations. From these two measurements, the far-field radiation pattern was determined.

To ensure that the measurements were accurate, a number of precautions were taken. The diameter of the sample was twice the measured beam waist diameter of the incident Gaussian beam, which limited diffraction effects [164]. The field at the edge of the sampled area was approximately -30 dB below the peak value, which ensured that the majority of power was sampled. To reduce the effects of multiple reflections, time domain gating techniques were employed. To properly extract the

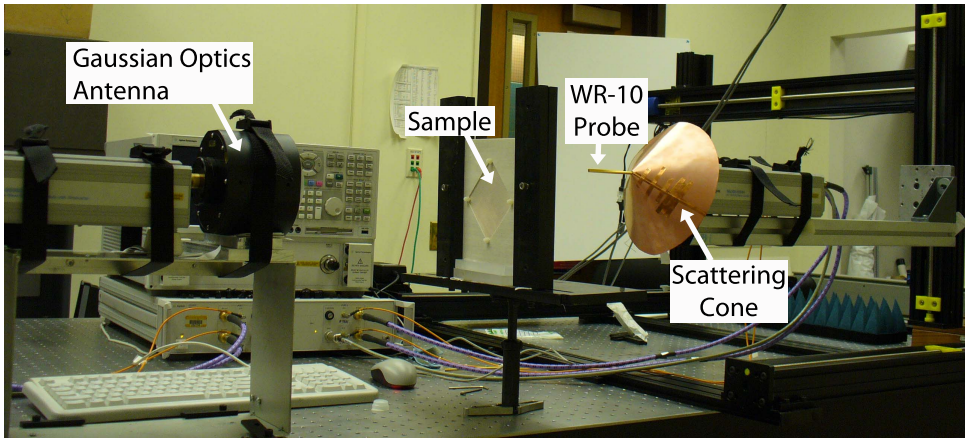

Figure 6.14: Experimental setup of the near field scanning system used to characterize the performance of the quarter-wave plate and Huygens' surface

far-field using a waveguide probe, the probe's radiation pattern was determined using full wave electromagnetic simulations, and probe correction was applied [165]. The system was calibrated by first measuring the far-field of the incident Gaussian beam, without the metasurface present. The metasurface was then placed at the beam waist of the Gaussian beam, and again the far-field measured. The far-field of the metasurface was then normalized by the peak amplitude of the incident beam's far-field. The transmission coefficient of the samples was characterized by taking the ratio of the field in the transmitted main beam to the field in the incident beam. The axial ratio was determined by noting its value in the direction with highest radiated field.

6.6.2 Quarter-Wave Plate Measurements

The quarter-wave plate presented in Section 6.2 was measured to demonstrate polarization conversion. A section of the fabricated quarter-wave plate is shown in Fig. 6.15(a). The measured axial ratio and transmission coefficient of the transmitted beam is plotted in Fig. 6.15(b). It can be seen that there is agreement between measurement and simulation. However, the measured axial ratio is higher than expected near 85 GHz. The axial ratio peaks at 3.7 dB, which corresponds to a 13.6 dB difference between the cross-polarization and co-polarization. Unfortunately, the near field scanning system only works between 70 GHz and 100 GHz, so the overall bandwidth of the quarter-wave plate could not be measured. The discrepancy between measurement and simulation can be attributed to fabrication errors.

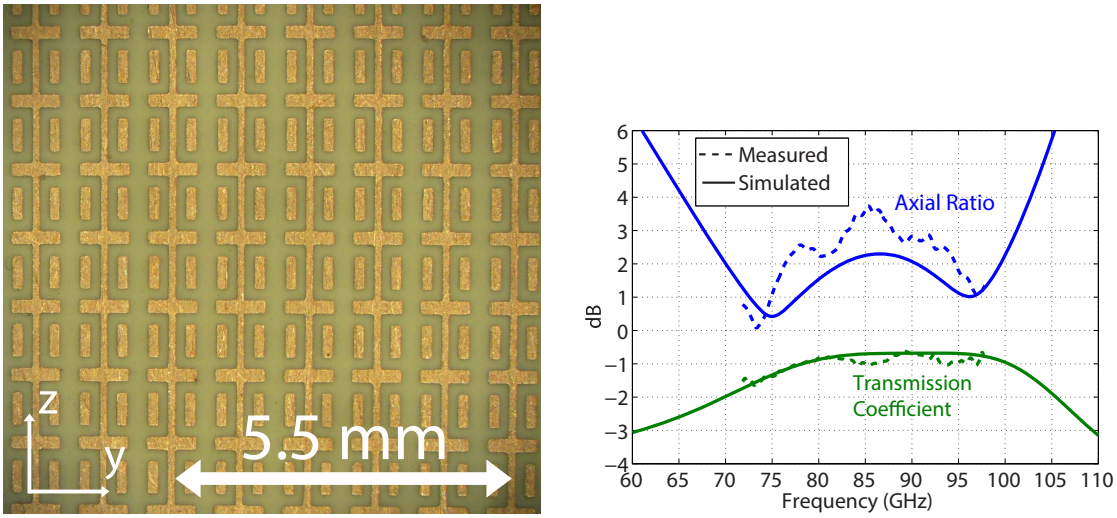

(a) (b)

Figure 6.15: Quarter-wave plate and its performance. **(a)** Section of the fabricated quarter-wave plate when viewed through an optical microscope. **(b)** Measured transmission coefficient and axial ratio of the transmitted field in the $\hat{x}$ direction.

6.6.3 Beam-Refracting Huygens' surface Measurements

Next, the beam-refracting Huygens' surface with polarization control was characterized. A section of the Huygens' surface is shown in Fig. 6.16. The dimensions of the metallic patterns on the outer sheets were measured with an optical microscope. It was found that on average, the fabricated gaps (G) were 10 μm larger and widths (W) were 15 μm smaller than designed. In addition, all the corners were rounded with an approximate radius of curvature of 50 μm. These fabrication errors caused the capacitance of each cell to be smaller than designed, which increased the operating frequency by 4.5 GHz.

Fig. 6.17(a) shows the total transmitted far-field. It can be seen that the metasurface efficiently refracts the normally incident beam to an angle $\phi = 42°$ at 82 GHz. As outlined in Fig. 6.17(b), the metasurface also provides a high polarization conversion from linear to circular by noting that the axial ratio in the direction of the main beam is 0.7 dB. The frequency dependence of the metasurface's performance is shown in Fig. 6.18. Fig. 6.18(a) plots the radiated field as a function of frequency and the angle of refraction (ϕ) in the $\theta = 90°$ plane. The blue dashed line superimposed on the figure plots the theoretical relationship between refracted angle and frequency given by Eqn. (6.9). On the other hand, Fig. 6.18(b) plots both the axial ratio and transmission coefficient into the refracted direction as a function of frequency. The

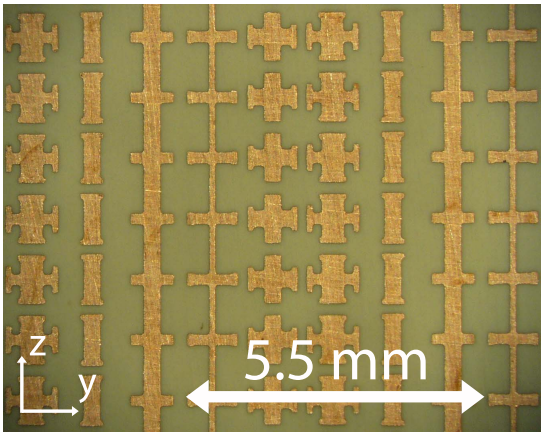

Figure 6.16: Section of the fabricated beam-refracting Huygens' surface when viewed through an optical microscope.

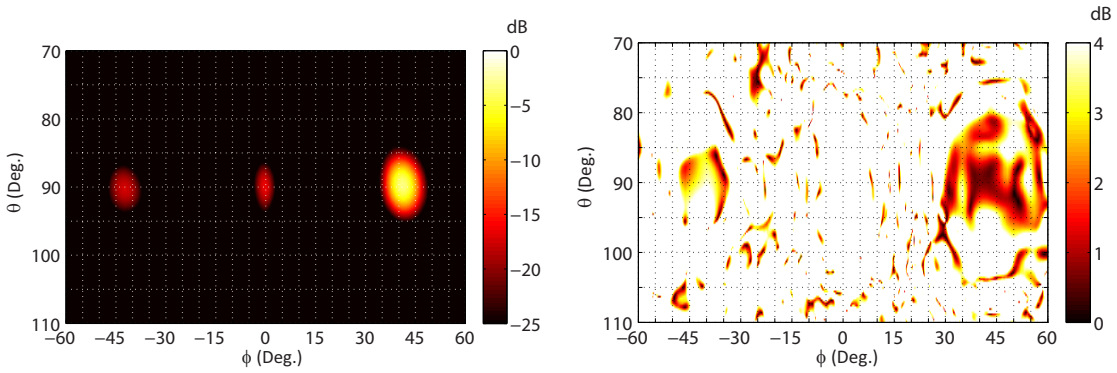

(a) (b)

Figure 6.17: Performance of the Huygens' surface at 82 GHz. **(a)** Far-field radiation pattern. **(b)** Axial ratio of the far-field.

transmission coefficient is above -3 dB from 71 GHz to 84.5 GHz, which suggests a bandwidth of 17%. The axial ratio is below 2.5 dB over this entire frequency range.

6.7 Chapter Summary

A Huygens' surface that provides wavefront and polarization control near 77 GHz was presented. A design methodology was developed that provides high transmission and complete phase control for both the TE and TM polarizations. First, a broadband, quarter-wave plate that solely converts the polarization from linear to circular was introduced. This was then extended to develop a metasurface that deflects a normally incident, linearly polarized plane wave to an angle of 45°, while also converting the polarization to circular. The results were experimentally verified, and a

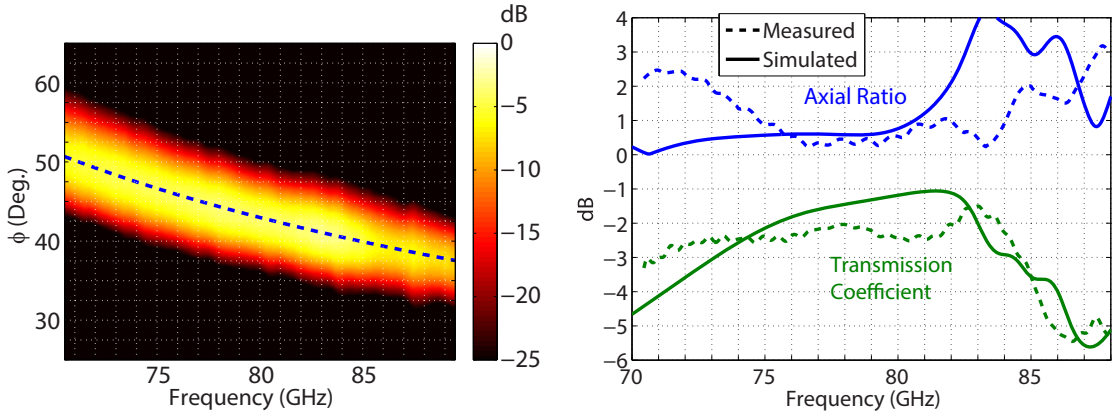

(a) (b)

Figure 6.18: Frequency dependance of the beam-refracting metasurface's performance. **(a)** Far-field radiation pattern as a function of frequency and ϕ in the plane $\theta = 90°$. The dashed blue line shows the theoretical dependance of the refracted angle vs. frequency given in Eqn. (6.9). **(b)** Axial ratio and transmission coefficient of the field transmitted into the refracted direction.

17% half-powered bandwidth was reported. In the next chapter, it is shown that this design process can be applied to develop novel lenses that simultaneously provide beam focusing and polarization control.

CHAPTER VII

Controlling Vector Bessel Beams with Metasurfaces

7.1 Chapter Introduction

In this chapter, it is first demonstrated that metasurfaces can simultaneously focus an incident wavefront and control its polarization [191]. Specifically, two metasurfaces are developed to convert linearly and circularly polarized Gaussian beams into vector Bessel beams: cylindrical vector beams with a Bessel profile. The unit cells of the two metasurface lenses are designed to act as anisotropic wave plates to convert the linearly-polarized and circular-polarized incident wavefronts to cylindrical polarizations (i.e. radial and azimuthal). The metasurfaces were fabricated using standard printed circuit board processes, and were experimentally characterized.

Next, the two metasurfaces are operated in a reciprocal manner to provide wavefront collimation. The metasurfaces are excited with a planar, leaky radial waveguide (Bessel beam launcher) that generates a radially polarized Bessel beam. The metasurfaces then collimate the radiation with minimal reflection loss, to realize high gain lens-antennas. The lens-antennas achieve an order of magnitude thickness reduction over previously reported lens-antennas since the metasurface lenses are directly integrated with the antenna feed (Bessel beam launcher) [191].

7.2 Gaussian-to-Bessel Metasurfaces

7.2.1 Motivation

Vector Bessel beams play a critical role in many optical systems [168]. These beams maintain a high intensity focus over a considerable distance for applications

such as particle trapping, tractor beams, near-field probes, laser machining, lithography, and optical data storage [192–194]. In addition, their azimuthal and radial polarizations are useful for the spectroscopy of magnetic dipole transitions in quantum dots [195]. Such beams also provide information about the orientation of a single molecule and are ideal sources for exciting surface plasmons in axially symmetric structures [61, 195]. Therefore, developing a simple means of transforming a commonplace Gaussian beam into a vector Bessel beam is highly desirable. However, this requires both polarization and phase control, which typically involves multiple lenses, spatial light modulators, dielectric waveplates, or other bulky components [61, 167, 168].

Here, two metasurfaces are introduced to efficiently convert normally incident Gaussian beams into Bessel beams. The first metasurface transforms x- and y-polarized Gaussian beams into transverse magnetic (TM or radially polarized) and transverse electric (TE or azimuthally polarized) polarized Bessel beams, respectively. The second metasurface transforms an incident left-handed-circularly polarized Gaussian beam into a transmitted TM-polarized Bessel beam, as shown in Fig. 7.1. Correspondingly, the two metasurfaces will be referred to as the linear-to-Bessel and the circular-to-Bessel metasurfaces. The unit cells comprising both metasurfaces utilize three anisotropic sheet admittances cascaded along the direction of propagation ($\hat{z}$). The cells are individually designed to realize a stipulated phase shift along their respective spatially-varying principle axes, while at the same time maintaining high transmission. Thus, the metasurfaces are low-loss and impedance-matched to free space to maximize efficiency.

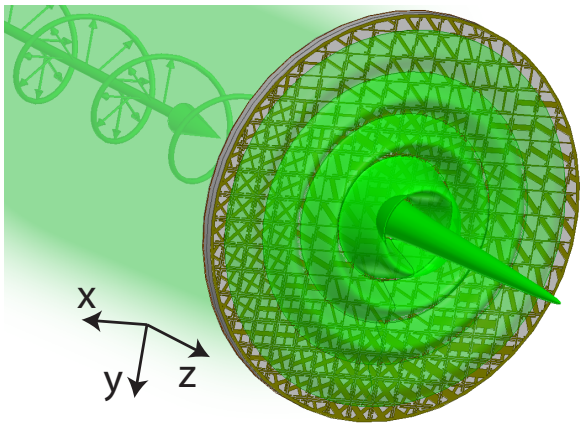

Figure 7.1: An inhomogeneous, anisotropic metasurface transforms a circularly polarized Gaussian beam into a vector Bessel beam with high efficiency.

7.2.2 Review of Vector Bessel Beams

Vector Bessel beams are axially symmetric beam solutions to Maxwell's equations [196, 197]. They can be written as,

$$\begin{aligned}\mathbf{E} &= e^{-jk_z z}\left(C_{\mathrm{TM}}J_0(k_\rho\rho)\hat{z} - C_{\mathrm{TE}}\frac{k\eta}{k_\rho}jJ_1(k_\rho\rho)\hat{\phi} + C_{\mathrm{TM}}\frac{k_z}{k_\rho}jJ_1(k_\rho\rho)\hat{\rho}\right)\\ \mathbf{H} &= e^{-jk_z z}\left(C_{\mathrm{TE}}J_0(k_\rho\rho)\hat{z} + C_{\mathrm{TM}}\frac{k}{\eta k_\rho}jJ_1(k_\rho\rho)\hat{\phi} + C_{\mathrm{TE}}\frac{k_z}{k_\rho}jJ_1(k_\rho\rho)\hat{\rho}\right)\end{aligned} \tag{7.1}$$

where C_{TM} and C_{TE} represent the coefficients of the TM (radially) and TE (azimuthally) polarized Bessel beams, respectively. A time-harmonic progression of $e^{j\omega t}$ and propagation in the $\hat{z}$ direction is assumed. In (7.1), k_ρ and k_z are the transverse and longitudinal wavenumbers, which satisfy the separation relation $k_z^2 + k_\rho^2 = k^2 = \omega^2\epsilon\mu$, and $J_0(k_\rho\rho)$ and $J_1(k_\rho\rho)$ are the zeroth and first order Bessel functions of the first kind. Non-paraxial Bessel beams with transverse wavenumbers of $k_\rho = 0.8k$ were chosen in this study. The Bessel beams under consideration are truncated with a Gaussian windowing function ($\exp(-\rho^2/w_0^2)$). Hence, these beams are often referred to as Bessel-Gauss beams.

7.2.3 Metasurface Design

It is well known how to transform linear or circular polarization to cylindrical polarization using the Jones matrices of spatially varying waveplates [61, 198, 199]. In short, each unit cell of the linear-to-Bessel metasurface acts as a half-wave-plate, and each unit cell of the circular-to-Bessel metasurface acts as a quarter-wave-plate. Such configurations allow the polarization to be transformed from linear and circular, respectively, to cylindrical. In addition, the metasurfaces must apply an inhomogeneous phase shift across their surfaces to transform the wavefront from a Gaussian profile to a Bessel profile. The necessary phase shift provided by each unit cell is determined by simply subtracting the phase of the desired wavefront (Bessel beam) from the phase of the incident wavefront (Gaussian beam). Fig. 7.2 shows the slow axis of each unit cell and the phase shift that should be imparted by the fast axis of the metasurface. For clarity only the middle portion of the metasurfaces are shown. Note that the circular-to-Bessel metasurface requires quarter-wave plates whose fast axis provides a full 2π phase coverage. This should not be confused with earlier metasurfaces that provided complete phase control for circularly polarized light by local changes in the polarization (Pancharatnam-Berry phase) [200].

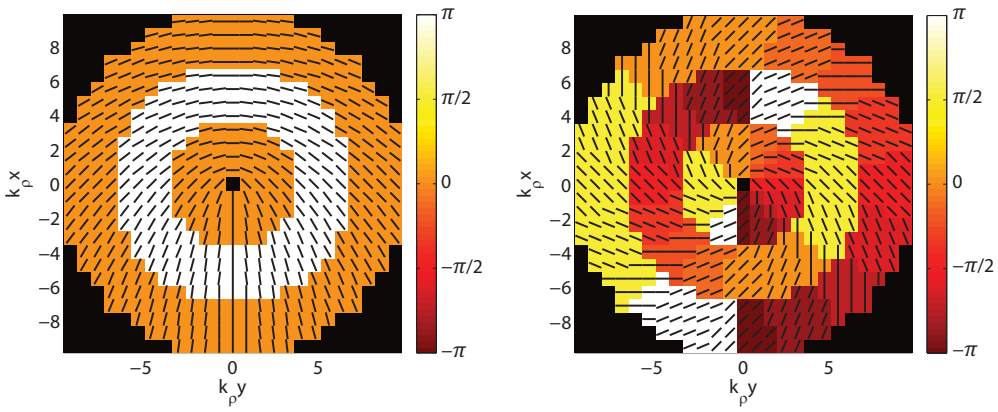

Figure 7.2: **(a)** Designed metasurface that converts a linearly polarized Gaussian beam into a vector Bessel beam. Each unit cell acts as a half-wave-plate. When the incident polarization of the Gaussian beam is oriented along $\hat{x}$ and $\hat{y}$, the transmitted Bessel beam is TM and TE polarized, respectively. **(b)** Designed metasurface that converts a circularly polarized Gaussian beam into a TM polarized bessel beam. Each unit cell acts as a quarter-wave plate. For both plots, the lines and color correspond to the orientation of the slow axis and the phase shift of the fast axis, respectively.

The geometry shown in Fig. 7.3(a) is employed to realize the unit cells of the metasurfaces. It consists of patterned metallic sheets (sheet admittances) cascaded in the direction of propagation. The metallic patterns are separated by Rogers 4003 substrates ($\epsilon_r = 3.55$, $\tan\delta = 0.0027$) that are 1.52 mm ($\lambda/19.7$) in thickness. A typical unit cell of the linear-to-Bessel metasurface is shown in Fig. 7.3(b). Each sheet admittance of a unit cell can be modelled as a parallel LC circuit. The inductance results from the metallic grid outlining the cell, and the capacitance from the top-hat loaded crossed-dipole at the center. Each sheet admittance can be controlled by adjusting the dimensions and orientation of the crossed-dipole relative to the x-axis. An additional advantage of this geometry is that the metallic grid outlining the unit cell reduces undesired coupling between neighboring unit cells, which is inherent to inhomogeneous designs such as this [201]. As a result it simplifies design. The average simulated transmittance of the fast and slow axes of all unit cells comprising the linear-to-Bessel metasurface are 0.93 and 0.84, respectively. The average simulated transmittance of the fast and slow axes of all unit cells comprising the circular-to-Bessel metasurface are 0.80 and 0.79, respectively. This high transmittance demonstrates that both metasurface designs exhibit low loss and are impedance

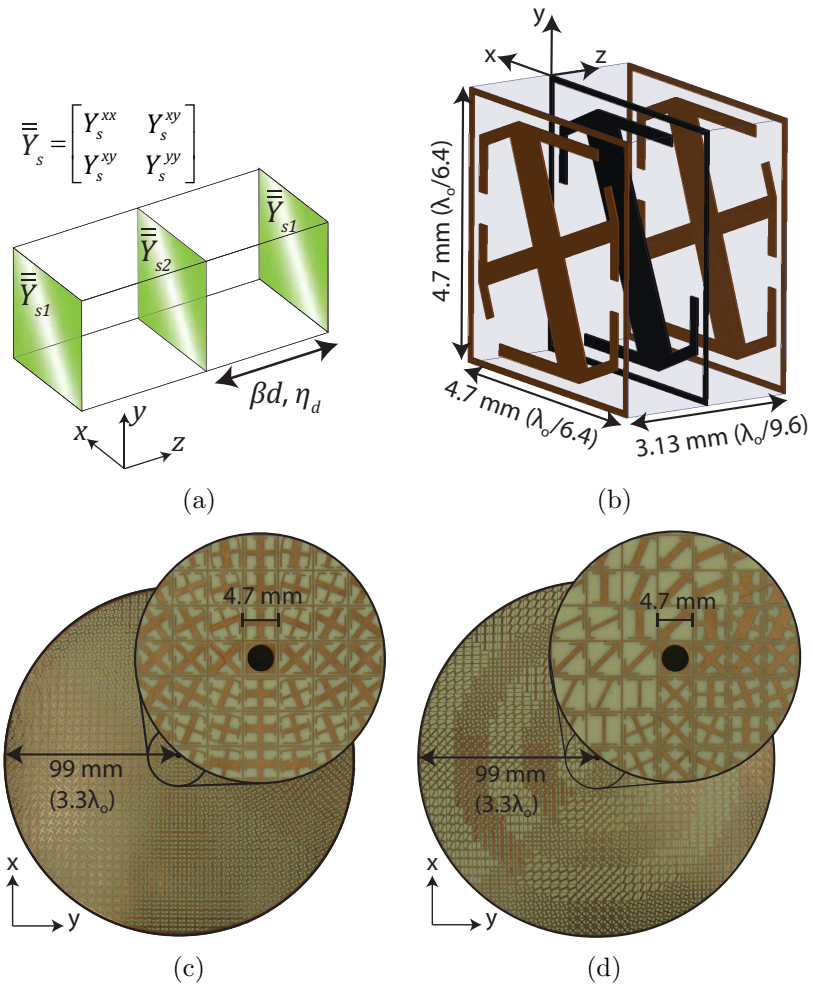

Figure 7.3: **(a)** Analytic model used to design each unit cell. **(b)** Schematic of a typical unit cell. This particular cell acts as a half wave plate with its fast axis oriented along $\phi = -\pi/8$. **(c)** Fabricated metasurface that converts a linearly polarized Gaussian beam into a vector Bessel beam. **(d)** Fabricated metasurface that converts a circularly-polarized Gaussian beam into a TM-polarized Bessel beam.

matched to free space.

7.2.4 Measurements

The metasurfaces were fabricated using standard printed-circuit-board processes. The top layers are shown in Figs. 7.3 (c) and (d). Both metasurfaces have an operating frequency of 9.9 GHz, a radius of 99 mm (3.3λ), and an overall thickness of 3.13 mm ($\lambda/9.6$). They were experimentally characterized by illuminating them with a Gaussian beam. The transmitted fields were scanned at a distance $z = 15$ mm from the surface. The normally incident Gaussian beam had a beam waist radius of $w_0 = 57$ mm (1.9λ). The experimental setup is identical to that described in [187].

First, the linear-to-Bessel metasurface was illuminated with x- and y-polarized electric fields, and the transmitted tangential magnetic field was measured, as shown in Figs. 7.4 (a) and (b). When illuminated with x- and y-polarization, the transmitted magnetic field is polarized along $\hat{\phi}$ and $\hat{\rho}$, respectively. Note that radially (TM) and azimuthally (TE) polarized Bessel beams have tangential magnetic fields that are polarized in the $\hat{\phi}$ and $\hat{\rho}$ directions, as given by (7.1). The non-diffracting property of the TM-polarized Bessel beam was also verified by measuring the longitudinal electric field, as shown in Fig. 7.4(c). It can be seen that the electric field closely resembles a zeroth order Bessel function, as expected.

Next, the circular-to-Bessel metasurface was characterized. As shown in Fig. 7.4 (d), a left-handed-circular polarization incident on the circular-to-Bessel metasurface results in a TM-polarized Bessel beam, as evidenced by the $\hat{\phi}$ directed magnetic field. In addition, Fig. 7.4(e) shows that the Bessel beam propagates a considerable distance from the metasurface located at the $z = 0$ plane. It should be noted that if the incident Gaussian beam were to travel in the $-\hat{z}$ direction rather than the $+\hat{z}$ direction, the circular-to-Bessel metasurface would instead convert right-handed-circular polarization into the TM polarization. Fig. 7.4(f) plots the profile of the transmitted wavefront for the cases where an x-polarized field is incident upon the linear-to-Bessel metasurface and a left-handed-circular polarized field is incident upon the circular-to-Bessel metasurface. In addition, an ideal Bessel-Gauss pattern ($J_0(k_\rho\rho)\exp(-\rho^2/w_0^2)$) is plotted as a reference.

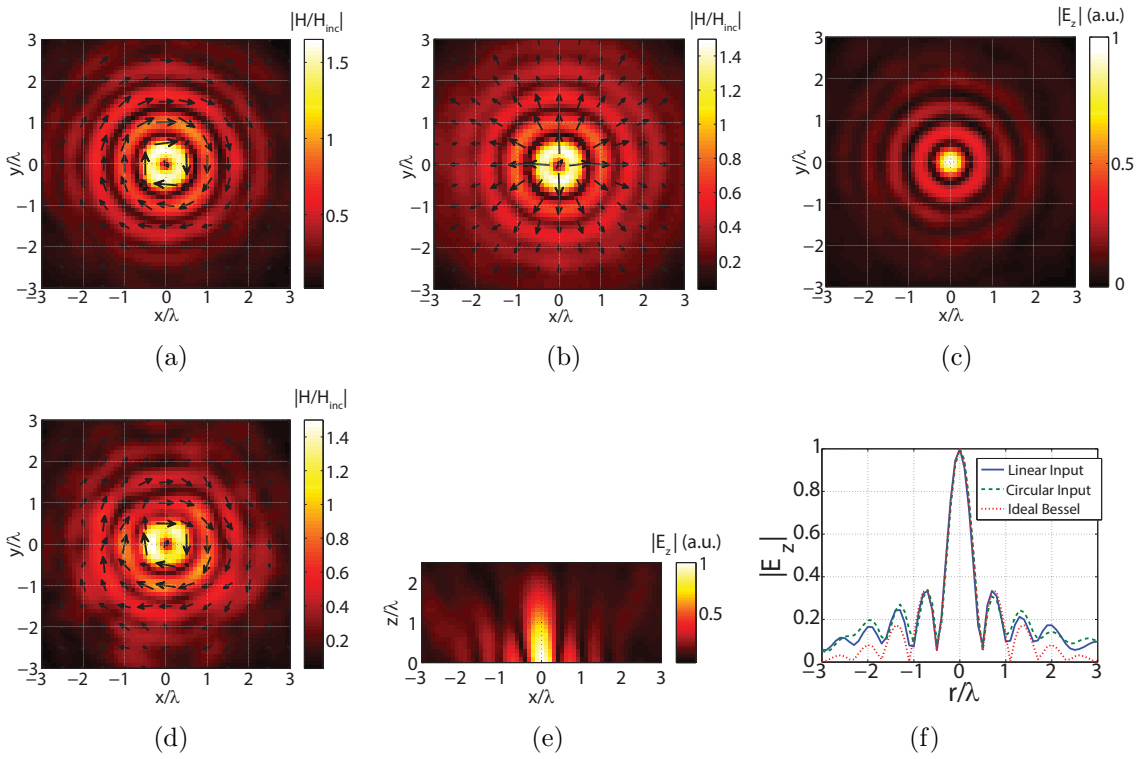

Figure 7.4: Measurements of the fabricated metasurfaces at the operating frequency of 9.9 GHz. For all plots, arrows point in the direction of the magnetic field, and the color corresponds to the absolute value of the magnetic or electric fields. **(a)** and **(b)** Transmitted magnetic field when x- and y-polarized Gaussian beams are incident on the linear-to-Bessel metasurface, respectively. **(c)** Transmitted z-directed electric field when an x-polarized Gaussian beam is incident upon the linear-to-Bessel metasurface. **(d)** and **(e)** Transmitted magnetic field in the xy-plane and z-directed electric field in the xz-plane, respectively, when a $\hat{z}$ propagating, left-handed-circularly polarized Gaussian beams is incident on the circular-to-Bessel metasurface. **(f)** Profile of the transmitted wavefront when x-polarized and left-handed-circular polarized Gaussian beams are incident upon the linear-to-Bessel and circular-to-Bessel metasrufaces, respectively. In addition, an ideal Gaussian truncated Bessel pattern is plotted as a reference.

7.3 Collimating Vector Bessel Beams

7.3.1 Motivation

In this section, the developed metasurfaces are operated in the reciprocal manner. A radially polarized Bessel beam is transformed into collimated, linearly and circularly polarized wavefronts, to realize high gain lens-antennas. High gain lens-antennas

are commonly employed for long range communication, radar, and radiometry [36]. These antennas utilize a lens to collimate the radiation from a low gain radiating element. Previously, dielectric lenses provided high efficiency and bandwidth, but they suffered from being heavy, bulky, and expensive [36, 202]. This motivated the development of ultra-thin metasurface lenses [36]. Although much effort has been spent on reducing the thickness of the collimating lens, the overall thickness of the lens-antenna combination has remained electrically large. To date, all lens-antennas have an overall thickness larger than the radius of the focusing element. This allows the fields from the feed to spread out to achieve a high aperture illumination efficiency (see Fig. 7.5). However, the large overall thickness of the system is limiting.

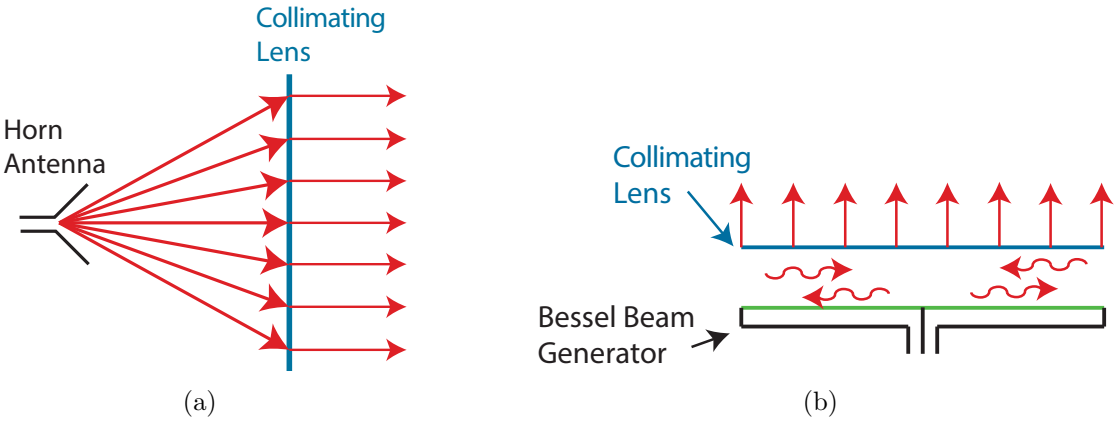

Figure 7.5: **(a)** Conventional lens-antenna collimates the radiation from a low gain horn antenna. This system is bulky since the overall thickness of the lens-antenna is larger than the radius of the lens. **(b)** Proposed lens-antenna collimates the radiation from a planar leaky-wave antenna (Bessel beam launcher). This proposed system is more compact since the lens can be placed directly above the antenna feed.

Alternatively, traveling-wave antennas can generate a high gain within a low profile. Some examples include partially reflecting surfaces [203], radial line slots [204], fast-wave structures [205], and modulated surface impedances [206]. However, they scan with frequency and their design process is completely different from lens-antennas. Radial line slot antennas have demonstrated high antenna efficiencies exceeding 80%. However, full-wave optimization techniques are required to account for undesired slot-to-slot coupling [207, 208]. Partially reflecting surface antennas are most similar to conventional lens-antennas since they also use a low gain radiating element that is collimated by the surface [203]. However, the surface of these antennas provides high reflection rather than high transmission, and they typically suffer from prohibitively narrow bandwidths since their bandwidth is inversely proportional

to the gain.

Here, an alternative approach to realizing high gain lens-antennas is reported. The lens-antenna utilizes a low profile vector Bessel beam launcher as its feed, and a metasurface lens collimates the radiation (see Fig. 7.6). The two metasurface lenses developed in the previous section transform the TM (radial) polarization radiated by the Bessel beam launcher into linear and circular polarizations, respectively. First, the Bessel beam launcher is reviewed. Then, calculations and measurements of the lens-antenna combination are reported.

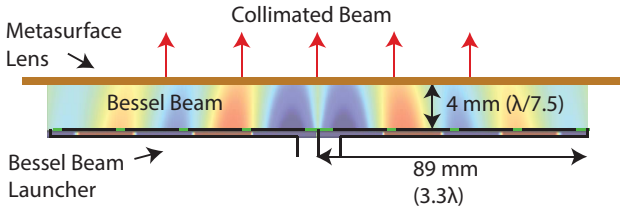

Figure 7.6: Schematic of the Bessel beam launcher and metasurface lens combination for realizing a high gain antenna. Dimensions are not to scale. A contour plot of the the simulated, tangential electric field between the Bessel beam launcher and metasurface lens is shown.

7.3.2 Antenna Feed: Vector Bessel Beam

The Bessel beam launcher reported in [209, 210] acts as the feed for the lens-antenna system. This feed is particularly attractive because it is low profile, and radiates a field with relatively uniform amplitude directly above its aperture. This enables a high aperture illumination efficiency for a small antenna-lens separation. In addition, the radiated field can be described by closed-form expressions. Therefore, designing the collimating lens is straightforward.

The launcher radiates a TM-polarized Bessel beam, which is an axially symmetric beam solution to Maxwell's equations [196, 197]. The radiated field can be written as,

$$\begin{aligned} \mathbf{E} &= e^{-jk_z z}\left(J_0(k_\rho \rho)\hat{z} - \frac{k_z}{k_\rho} j J_1(k_\rho \rho)\hat{\rho}\right) \\ \mathbf{H} &= e^{-jk_z z}\left(\frac{k}{\eta k_\rho} j J_1(k_\rho \rho)\hat{\phi}\right) \end{aligned} \tag{7.2}$$

The Bessel beam launcher consists of a coaxially fed, leaky-radial waveguide, as shown in Fig. 7.7. The waveguide has a deeply subwavelength thickness of 0.588 mm

($\lambda/50$) and a radius of 89 mm (3λ). The top of the Bessel beam launcher is a capacitive sheet admittance. The capacitance of the sheet, radius, and height of the Bessel beam launcher were designed to generate outward and inward propagating Hankel functions within the radial waveguide. The interference of these Hankel functions produces a propagating Bessel beam with $k_\rho = 0.8k$ at the operating frequency of 9.9 GHz. It should be noted that a quarter-wave transformer was added to the coaxial feed of the Bessel beam launcher to improve the impedance match to a 50 Ω load, which adds a considerable thickness to the launcher. In the future, alternative matching techniques could be utilized to avoid the added thickness.

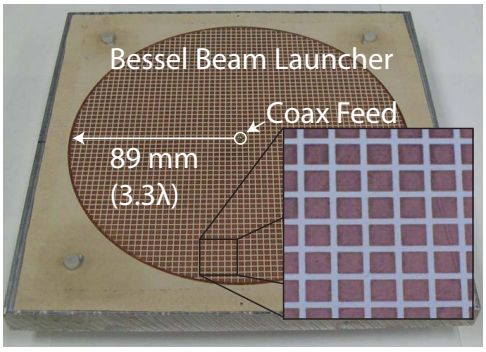

Figure 7.7: A Bessel beam launcher radiates a TM-polarized Bessel beam with $k_\rho = 0.8k$. The inset shows a zoomed in view of the capacitive sheet on top of the launcher.

7.3.3 Metasurface Lenses

Next, the planar Bessel beam launcher is integrated with the two developed metasurface lenses to realize low profile lens-antennas. The Bessel beam launcher radiates a TM-polarized Bessel beam just above its surface. The linear-to-Bessel and circular-to-Bessel metasurfaces are placed a subwavelength distance from the launcher to collimate the radiation and convert the polarization from radial to linear or circular, respectively (see Fig. 7.6). A 4 mm thick foam spacer composed of Rohacell 31 HF ($\epsilon_r = 1.046$, $\tan\delta = 0.0017$) is used to separate the metasurfaces from the Bessel beam launcher. The experimental setup of the Bessel beam launcher and metasurface lens combination is shown in Fig. 7.8.

The field radiated by the Bessel beam launcher (incident on the metasurface) is shown in Fig. 7.9(a). Here, we assume that the beam radiated by the Bessel beam launcher is equal to that of an ideal Bessel beam (see Eq. (7.2)). Fig. 7.9(b) plots the field transmitted by the linear polarizing lens. The transmitted field across the

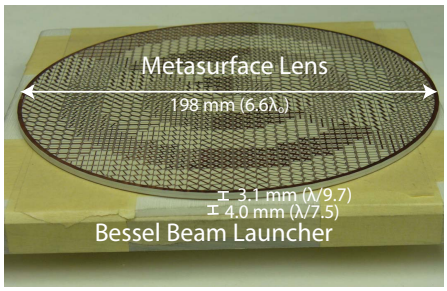

Figure 7.8: Experimental setup of the circular polarizing lens placed on top of the Bessel beam launcher. A 4 mm thick, Rohacell 31 HF foam spacer separates the Bessel beam launcher and the metasurface lens.

surface is calculated by simply multiplying the incident, transverse electric field at each point by the transmission coefficient of the corresponding unit cell. It can be seen that the metasurface efficiently rotates the spatially varying, radial polarization to a common direction ($\hat{x}$). In addition, the metasurface provides an inhomogeneous phase shift so that the transmitted phase is uniform (i.e. the transmitted electric field is real and positive).

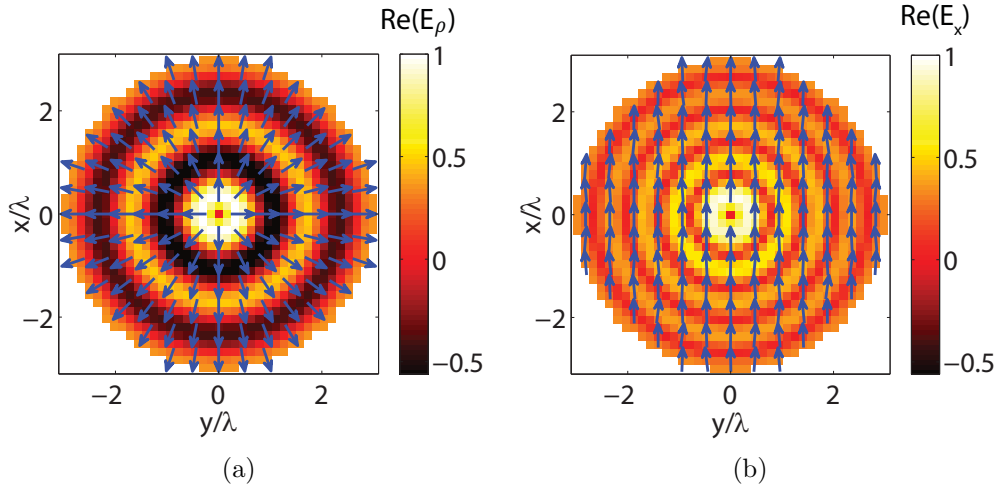

Figure 7.9: **(a)** Time snap-shot of the transverse electric field radiated by the Bessel beam launcher. The color corresponds to the radial component of the electric field, and the arrows plot the direction of the electric field vector in the xy plane. **(b)** Time snap-shot of the transverse electric field transmitted by the linear polarizing lens. The color corresponds to the $\hat{x}$ component of the electric field, and the arrows plot the direction of the electric field vector in the xy plane.

It should be emphasized that this design procedure is not only limited to collimating vector Bessel beams. In general a metasurface that provides polarization and

phase control can be placed in the near field of any simple radiator to generate a desired transmitted field profile. For example, the radiative near field of a $\hat{z}$ directed, Hertzian dipole has an electric field that is also radially polarized in the $z = 0.1\lambda$ plane. Therefore, a metasurface similar to the ones presented here could also collimate the radiation from a closely spaced dipole that is oriented perpendicular to the plane of the lens.

7.3.4 Calculated Performance

Simulating the entire Bessel beam launcher and metasurface lenses in a full-wave simulation was not feasible given the computational resources available. Therefore, Huygens' principle was applied to predict the overall performance of the lens-antenna [64]. First the Bessel beam launcher alone was simulated. This was done using the two-dimensional, axially symmetric solver in COMSOL. The capacitive sheet of the Bessel beam launcher was modelled as a homogenous sheet admittance boundary condition. This simulation predicted the reflection coefficient, loss of the Bessel beam launcher, and the field that is incident upon the metasurface lenses.

Huygens principle was then applied to model the metasurface lenses. Each unit cell of the metasurface lens was represented as a Huygens' source, which consists of crossed electric and magnetic hertzian dipoles [153]. It should be noted that this is somewhat of an approximation since it neglects undesired coupling between neighboring unit cells [201]. The magnitude and phase of each Huygens' source was determined by multiplying the incident field (Bessel beam) by the transmission coefficient of the designed unit cells. The incident field was determined from COMSOL simulations of the Bessel beam launcher. Once the phase and amplitude of each Huygens' source was determined, the far field from each cell was added to calculate the radiation pattern, directivity, and gain at each frequency.

7.3.5 Measurements

Measurements of the linearly and circularly polarized lens-antennas are shown in Figs. 7.10 and 7.11. In all plots, the calculated and measured performance is denoted by solid lines and dashed lines, respectively. It should be noted that at the operating frequency of the metasurface lenses (9.9 GHz) there is close agreement between measurement and calculation. The far-field radiation patterns, gain, and realized gain were measured in the University of Michigan, Radiation Laboratory's anechoic chamber. The gain was measured using the gain comparison method. The

realized gain is the antenna gain (G) multiplied by the reflection loss. From the gain, the antenna efficiency could be determined from $e_{ant} = G\lambda^2/(4\pi A)$, where A is the physical area of the metasurface lens. Characterizing the radiation efficiency and aperture illumination efficiency requires the antenna's directivity (D), which was measured using a near-field scanning system. The near-field scanning system provides the complete, three-dimensional radiation pattern above the lens-antenna, and thus was most accurate at estimating the directivity. The aperture illumination efficiency is defined as $e_{apt} = D\lambda^2/(4\pi A)$, and the radiation efficiency is defined as $e_{rad} = G/D$.

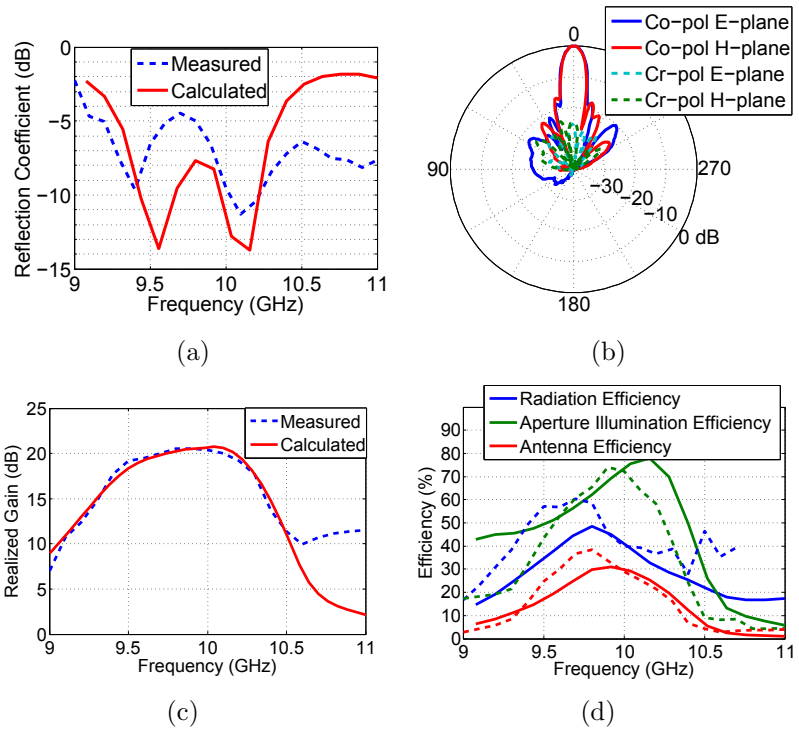

Figure 7.10: Measured and calculated performance of the linearly polarized lens-antenna. Measurements and calculations are denoted by dashed and solid lines, respectively. **(a)** Reflection coefficient of the lens-antenna. **(b)** Radiation pattern at the operating frequency of 9.9 GHz. **(c)** Frequency dependence of the realized gain. **(d)** Radiation efficiency, aperture illumination efficiency, and antenna efficiency.

The reflection coefficient of the linearly polarized lens-antenna is shown in Fig. 7.10(a). The measured reflection coefficient is larger than the calculated response below the operating frequency of 9.9 GHz. This is most likely due to reflections from the linear-to-Bessel metasurface, which are not accounted for in calculations. The measured radiation pattern is shown in Fig. 7.10(b). It can be seen that the main beam is symmetric and the sidelobes are low due to the cylindrical symmetry of the

lens-antenna. The measured and calculated realized gain is shown in Fig. 7.10(c). The peak gain was measured to be 22.1 dB. The half-power gain bandwidth was measured to be 8.1% and the ratio of the cross-polarized to co-polarized radiation is less than -20 dB in the broadside direction over this bandwidth. The radiation efficiency, aperture illumination efficiency, and the antenna efficiency are shown in Fig. 7.10(d), from 9 to 11 GHz.

The reflection coefficient of the circularly polarized lens-antenna is shown in Fig. 7.11(a). The measured radiation pattern is shown in Fig. 7.11(b). The measured and calculated realized gain is shown in Fig. 7.11(c). The peak gain was measured to be 20.4 dB. The half-power gain bandwidth was measured to be 7.6% and the axial ratio is less than 3 dB in the broadside direction over this bandwidth. The radiation efficiency, aperture illumination efficiency, and the antenna efficiency are shown in Fig. 7.11(d). Simulations show that the radiation efficiency is primarily limited by losses in the Bessel beam launcher, for both the linearly polarized and circularly polarized lens-antennas. In the future, the Bessel beam launcher can employ lower loss materials, which should significantly increase the radiation efficiency.

7.4 Chapter Summary

This work extends the capabilities of metasurfaces to enable increased control of a wavefront. This is demonstrated with two different metasurfaces that transform linearly and circularly polarized Gaussian beams to vector Bessel beams. In addition, the metasurfaces are operated in a reciprocal manner. They are combined with a planar Bessel beam launcher (leaky radial waveguide) to realize the first lens-antenna with a subwavelength overall thickness that achieves a high gain (exceeding 20 dB). In future work, lens-antennas can be further optimized by incorporating alternative leaky-wave or surface-wave feeding structures to replace the Bessel beam launcher. This would enable amplitude control as well as phase and polarization control. In addition, it should be emphasized that the same design procedure could be used to realize metasurfaces that control the radiative near field of any elementary source.

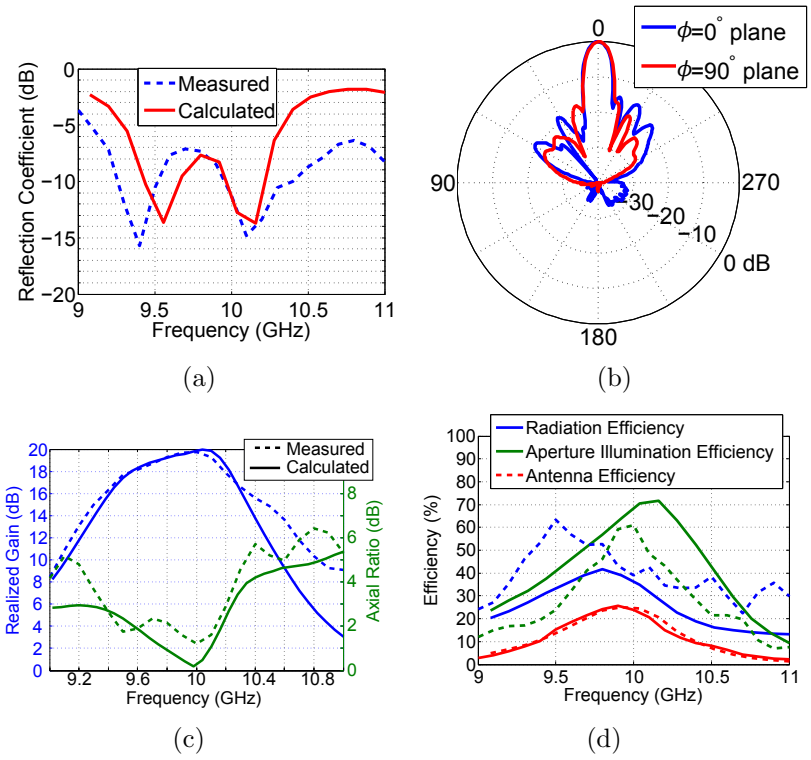

Figure 7.11: Measured and calculated performance of the circularly polarized lens-antenna. Measurements and calculations are denoted by dashed and solid lines, respectively. **(a)** Reflection coefficient of the lens-antenna. **(b)** Radiation pattern at the operating frequency of 9.9 GHz. **(c)** Frequency dependence of the realized gain. **(d)** Radiation efficiency, aperture illumination efficiency, and antenna efficiency.

CHAPTER VIII

Optical Huygens' Surfaces

8.1 Chapter Introduction

At optical frequencies, phase and polarization control are typically achieved with a combination of optically-thick wave plates and large dielectric lenses. An alternative technology is a spatial light modulator, which can achieve arbitrary phase shifts dynamically. However, these devices are bulky and have coarse pixel densities [211, 212]. More recently, metasurfaces exhibiting only an electric response have proved to be a viable option, but they exhibited efficiencies of only a few percent [54, 157, 158, 213–216]. In the previous chapters, it was shown that high performance metamaterial Huygens' surfaces can be realized if a magnetic response is added. However, these impedance-matched metasurfaces are far less common at optical frequencies [47, 217, 218].

In this chapter, a theoretical Huygens' surface that both focuses light and controls its polarization at a wavelength of 2 μm is first demonstrated. The metasurface is realized with a grid of spatially-varying, unit cells that are each ($\lambda_\circ/2.5$ x $\lambda_\circ/2.5$) in size. It is shown that cascading four patterned sheets dramatically improves the efficiency over the more common single sheet designs. The magnetic response is generated by circulating, longitudinal electric currents supported by the cascaded metallic sheets. Simulations demonstrate that the proposed structure achieves large phase coverage while maintaining high transmission. In addition, by utilizing anisotropic sheets, extreme birefringence can be achieved. A planar lens that both focuses light and converts its polarization from linear to circular is developed.

Next, the first experimental metamaterial Huygens' surface at optical frequencies is demonstrated. To simplify fabrication, the experimental Huygens' surface consists of three, rather than four, patterned metallic sheets. The metasurface is designed to refract normally incident light to an angle of 35° from normal at the design wavelength

of 1.5 μm. Simulations show that the surface exhibits a high efficiency of 30%, and an order of magnitude improvement in the extinction ratio over previously reported metasurfaces. The metamaterial Huygens' surface is then fabricated by sequentially patterning three gold (Au) sheets using standard electron beam lithography and liftoff processes, while employing SU-8 dielectric spacers between them. Measurements are performed using a spectroscopic ellipsometer, and the performance significantly exceeds previously reported metasurfaces. In addition, this work presents the first experimental demonstration of an isotropic metasurface that is capable of providing wavefront control for arbitrarily polarized light.

8.2 Theoretical Metasurface for Complete Phase Control

8.2.1 Four Sheet Design

To begin, let's consider a plane wave normally incident upon a periodic metasurface in the xy plane. We first assume the metasurface is composed of a single, metallic sheet with a subwavelength pattern. It has been shown that this structure can be modeled by a well defined sheet admittance boundary condition given by [7],

$$\vec{J}_{t,av}\Big|_S = \overline{\overline{Y}}_s \cdot \vec{E}_{t,av}\Big|_S \tag{8.1}$$

The expressions $\vec{J}_{t,av}|_S$ and $\vec{E}_{t,av}|_S$ represent the average surface current and electric field tangential to the surface S. In general, $\overline{\overline{Y}}_s$ is a tensorial quantity, assumed here to be diagonalized with eigenvectors in the x and y directions.

It was shown in chapter 6 that it is theoretically possible to obtain a symmetric structure with perfect transmission and complete phase coverage with only three layers. However, since the metasurface is required to operate next to a stop-band to achieve phase delays near 0°, the achievable bandwidth is limited. Therefore, a four layer design will be investigated first, as shown in Figure 8.1(a). In Figure 8.1(b), the magnitude and phase of the transmission coefficient are plotted as a function of Y_s, assuming that the sheets are lossless for the time being (Y_s is purely imaginary). It can be seen that the transmitted phase spans an entire 360° region, while the magnitude maintains a transmittance greater than 60%. To simplify the analysis, it is assumed that all 4 sheets are identical, the electrical length between each layer is $\beta d = \pi/2$, and the wave impedance of the dielectric spacers is $\eta_d = (2/3)\eta_\circ = \sqrt{\mu_\circ/2.25\epsilon_\circ}$.

It should be noted that if each sheet is allowed to be different, the transmittance could be 100% for every desired phase shift, as shown in chapter 6. However, chapter

6 assumed low-loss materials were utilized, and arbitrary metallic patterns could be fabricated with high accuracy. Neither of these assumptions are valid at optical frequencies. Therefore, we limit ourselves to the simplified case for the time being.

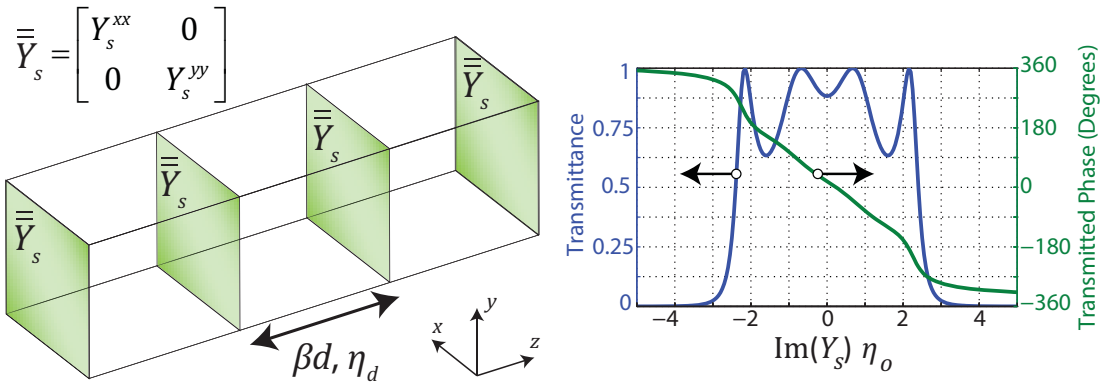

(a) (b)

Figure 8.1: **(a)** Generic structure that consists of four cascaded metasurfaces (electric sheet admittances) separated by dielectric layers. In general, the sheet admittances are anisotropic such that x and y polarized light can be controlled independently. **(b)** Transmitted power and phase as a function of the normalized sheet admittance for $\beta d = \pi/2$ and $\eta_d = (2/3)\eta_\circ = \sqrt{\mu_\circ/2.25\epsilon_\circ}$.

To realize the necessary sheet admittances, the geometry shown in Figure 8.2 is employed. It consists of four Au layers patterned on a SiO_2 substrate. The substrate is modeled as a lossless dielectric with an index of refraction of 1.5. The permittivity of the Au near an operating wavelength of 2 μm is described by a Drude model with plasma frequency $f_p = 2180$ THz and collision frequency $f_c = 20$ THz.

Each of the four sheet admittances can be modeled as a parallel LC circuit. The inductance is created by both electron inertia and the wire grid outlining each unit cell. The capacitance is created by the central patch. This structure is similar to the well-known fishnet structure [219], with the primary difference being that the capacitive patches do not touch the wire grid. This increases inductance and reduces capacitance, which in turn enhances the bandwidth near resonance. By adjusting the dimensions of the patch and wires (s_x, s_y, w_x, w_y), the admittance can be sufficiently controlled to provide complete phase coverage. Realizing anisotropic sheet admittances is also straightforward since the inductance and capacitance in the x and y directions can be independently controlled. This is equivalent to extreme birefringence in optical crystals since arbitrary phase shifts between the two axes are achievable within a subwavelength thickness. The minimum feature size for this structure is set

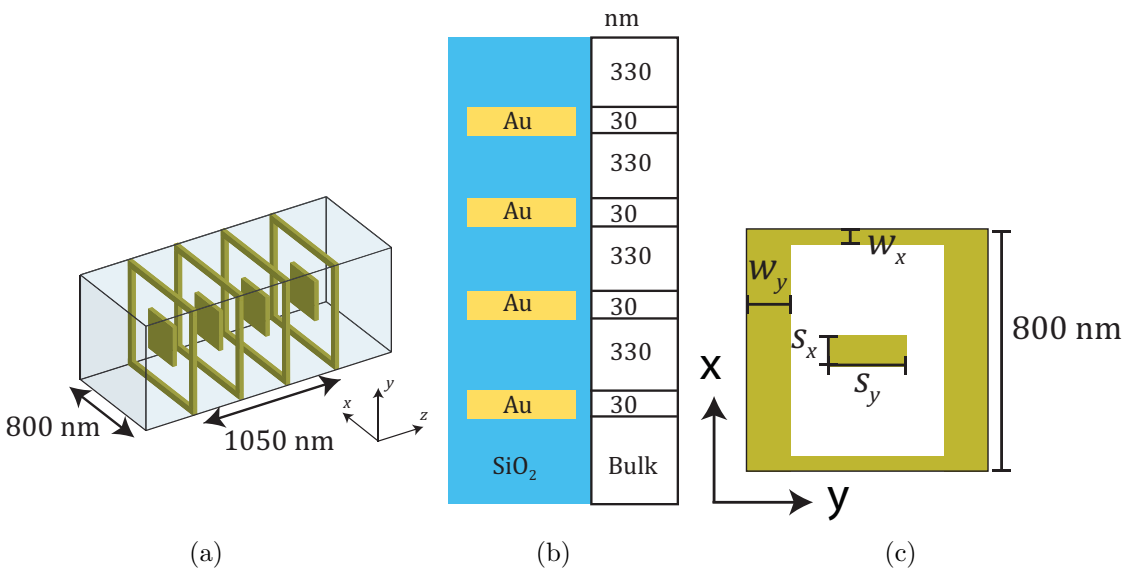

Figure 8.2: **(a)** Perspective view of a typical unit cell. This particular cell is isotropic. **(b)** Side view of each cell. The dimensions are not to scale. **(c)** Top view of a generic unit cell. By adjusting the parameters s_x, s_y, w_x, and w_y, the transmitted phase of both polarizations can be independently controlled.

to 90 nm.

8.2.2 Comparison to Fishnet Structure

The proposed geometry exhibits a larger bandwidth than the well-known fishnet structure [60, 219]. To illustrate this, consider the unit cells shown in Figures 8.3(a) and 8.3(b). For the polarization shown, Figure 8.3(a) has an identical operation as the geometry presented in Figure 8.2 (c), whereas Figure 8.3(b) is the fishnet geometry. Both structures are similar since they can be modeled as parallel LC circuits. The dimension 'w' primarily affects the inductance and 'd' primarily affects the capacitance. Both geometries can also be made to resonate at the same frequency. However, the geometry shown in Figure 8.3(a) has a larger inductance and correspondingly smaller capacitance than the geometry shown in Figure 8.3(b).

Let both geometries have a resonant frequency of $\omega_\circ = 1/\sqrt{L_1C_1} = 1/\sqrt{L_2C_2}$, where $L_1 > L_2$ and $C_1 < C_2$. The impedance of this structure is given by its parallel combination, $Z = (1/(j\omega L) + j\omega C + 1/R)^{-1}$. The resistance (R) models the metallic loss and is assumed to be equal for both geometries. The impedance bandwidth is inversely proportional to its frequency derivative at resonance,

$$\frac{dZ}{d\omega} = \frac{jLR^2(1+\omega^2LC)}{R-\omega^2RLC+j\omega L} \tag{8.2}$$

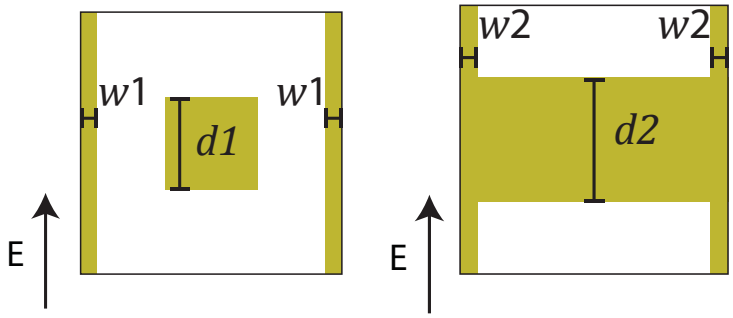

(a) (b)

Figure 8.3: **(a)** Proposed geometry that has an identical operation as the geometry presented in Figure 8.2 (c) for the polarization shown. **(b)** Fishnet geometry. The fishnet geometry has a larger capacitance and correspondingly smaller inductance than the proposed geometry.

Operating near resonance, $\omega = \omega_\circ$, $C = 1/(\omega_\circ^2 L)$, it can be seen that the frequency derivative is inversely proportional to the inductance,

$$\left.\frac{dZ}{d\omega}\right|_{\omega=\omega_\circ} = \frac{-j2R^2}{L\omega_\circ^2} \tag{8.3}$$

Thus, to achieve a maximal bandwidth, the inductance should be maximized and the capacitance should be minimized. However, it should be noted that this analysis is only accurate when the spacing between metallic sheets along the z axis is large enough that evanescent coupling can be neglected. When realizing bulk negative index metamaterials, the spacing between metallic sheets is usually reduced from the 360 nm spacing used here, and there is significant evanescent coupling between the sheets [60].

8.2.3 Four Sheet Unit Cell Simulations

The unit cell shown in Figure 8.2 was simulated for many values of its free parameters (s_x, s_y, w_x, w_y). By interpolating between the swept points, the transmitted phases that can be achieved were determined, as shown in Figure 8.4(a). The x and y axes of Figure 8.4(a) correspond to the transmitted phase of x and y polarized light, respectively. The color represents the average of the transmittance for the two polarizations. The black areas correspond to regions where it is not possible to achieve the desired transmitted phase due to either low transmittance or requiring feature sizes below 90 nm. Figure 8.4(b) shows the dimensions of the cascaded unit cells

that act as quarter wave plates (dashed green lines of 8.4(a)). It can be seen that the proposed metasurface provides high transmission and complete phase control for both polarizations.

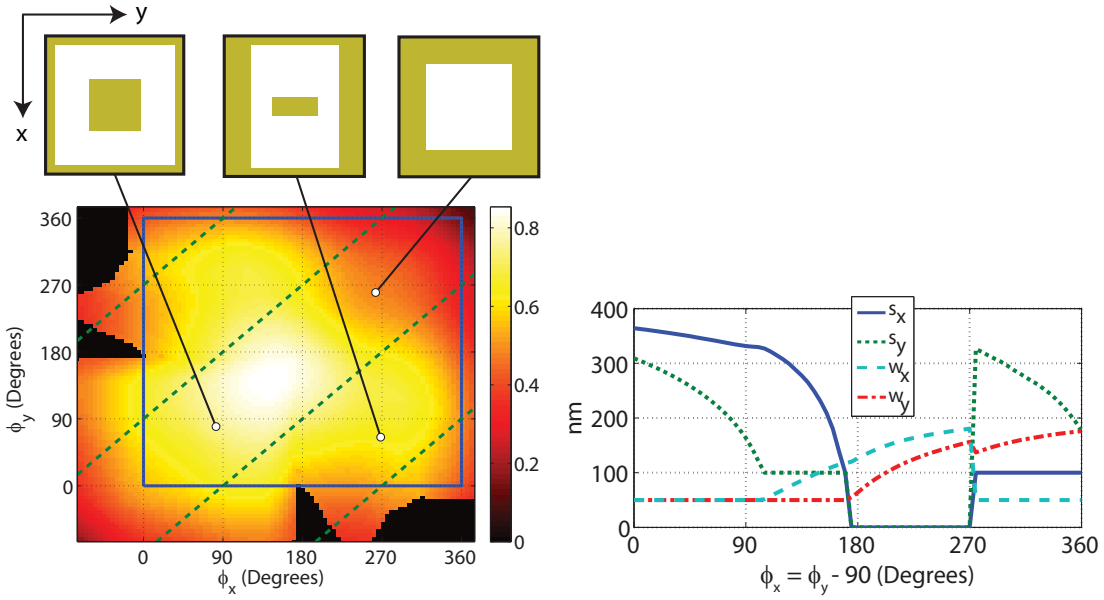

(a) (b)

Figure 8.4: **(a)** The transmitted phases that can be achieved by the cascaded metasurfaces shown in Figure 8.2. The x and y axes denote the transmitted phase of x and y polarized light, respectively. The color represents the average of the transmittance for the two polarizations. Black areas correspond to regions where it is not possible to achieve the desired transmitted phase. The blue box outlines a region with complete control of the transmitted phase for both polarizations. The dashed green lines correspond to cells that act as a quarter-wave plate. Also shown are three different unit cells that achieve the corresponding phases shifts. **(b)** Dimensions of the cascaded unit cells (s_x, s_y, w_x, w_y) that act as quarter-wave plates.

8.2.4 Calculations of Focusing and Polarization Control

Let's consider a metasurface lens that both focuses and controls the polarization of a normally incident plane wave. It is assumed that the incident wave is linearly polarized at 45° relative to the x-axis so that the x and y components of the metasurface are equally excited. If the unit cells are restricted to act as quarter-wave-plates (dashed green lines of Figure 8.4(a)), each cell will convert the polarization from linear to circular. In addition, a quadratic phase with a focal length of 400 μm is realized across a 160 μm diameter lens (NA=0.20). This is accomplished by spatially

distributing the unit cells across the lens to achieve the desired transmitted phase at each point, as shown in Figure 8.5(a). This effectively amounts to combining a parabolic lens and quarter-wave plate into a single, low profile device. If the polarization of the incident light was different, the lens would still focus the light to a spot, but it would convert the polarization to elliptical in general. Since an ideal phase distribution can be generated across the surface, the lens does not suffer from spherical aberration, coma, and astigmatism [157].

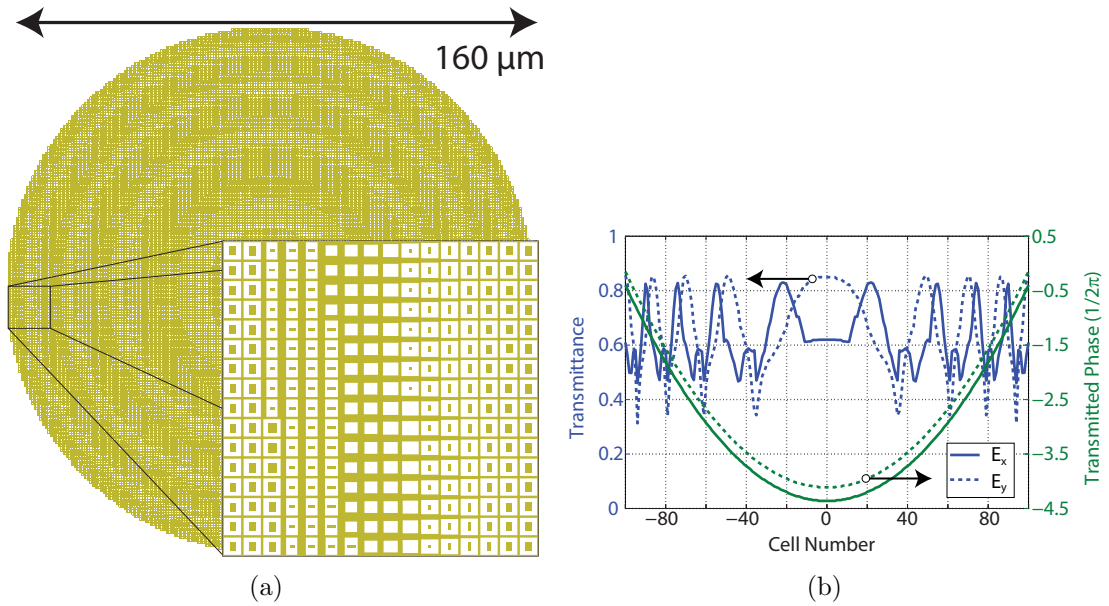

(a) (b)

Figure 8.5: **(a)** Zoomed in view of a section of the designed metasurface. **(b)** Transmitted power and phase along the diameter of the lens for x and y polarized light.

Given the computational resources available, it was not feasible to simulate the entire array using a full wave electromagnetics solver. Therefore, Love's equivalence principle is employed to validate the design [152]. Each unit cell is approximated as a crossed electric and magnetic, infinitesimal dipole (Huygens' source) with phase and amplitude given by its simulated transmission coefficient. This method has proven accurate at modeling previous lens designs, and accounts for any amplitude variation across the lens [47, 220]. Figure 8.5(b) shows the magnitude and phase of the x and y directed Huygens' sources across the diameter of the lens. When these sources are radiated, the intensity at the focal plane can be found, as shown in Figure 8.6(a). The magnitude is normalized by the peak intensity of an ideal lens that provides 100% transmittance and ideal parabolic phase. The simulated lens has a peak intensity that is 62% of the ideal lens. Wherever the normalized intensity is above 1% of

the peak value, the axial ratio (AR) is less than 1 dB, as shown in Figure 8.6(b). This indicates a pure circular polarization. The axial ratio is defined here as $AR = 20\ \log_{10}(E_{max}/E_{min})$, where E_{max} and E_{min} are the major and minor axes of the polarization ellipse, respectively. Note that although the phase distribution across the lens is ideal, there is variation in the amplitude. This causes some abberation in the focal plane.

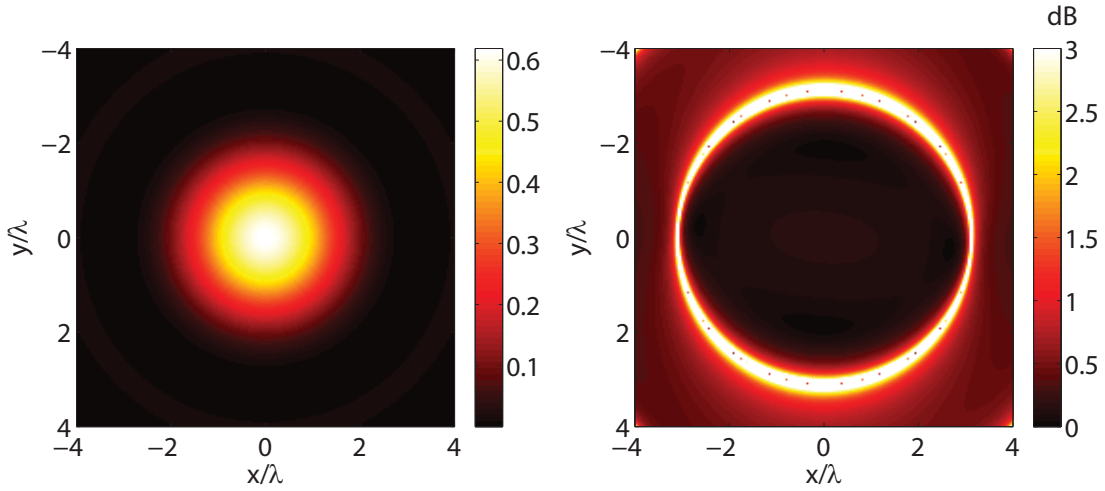

(a) (b)

Figure 8.6: **(a)** Intensity at the focal plane normalized by the peak intensity of an ideal lens with 100% transmittance and ideal phase. **(b)** Axial ratio (AR) at the focal plane. $AR < 1$ dB wherever the normalized intensity is above 1% of the peak value, thus indicating a pure circular polarization.

8.3 Experimental Validation

Next, the design process is experimentally verified by again considering the example of beam refraction as shown in Fig. 8.7. To simplify fabrication, the experimental Huygens' surface consists of three, rather than four, patterned metallic sheets. In addition, the experimental Huygens' surface is isotropic.

8.3.1 Three Sheet Unit Cell Design

The isotropic unit cell of the experimental Huygens' surface consists of three 30 nm thick Au sheets patterned on a SiO_2 substrate, as shown in Fig. 8.8. The Au sheets are separated by 200 nm thick SU-8 dielectric spacers to realize an overall thickness of 430 nm ($\lambda_\circ/3.5$). The SiO_2 substrate is modeled as a lossless, infinite half space

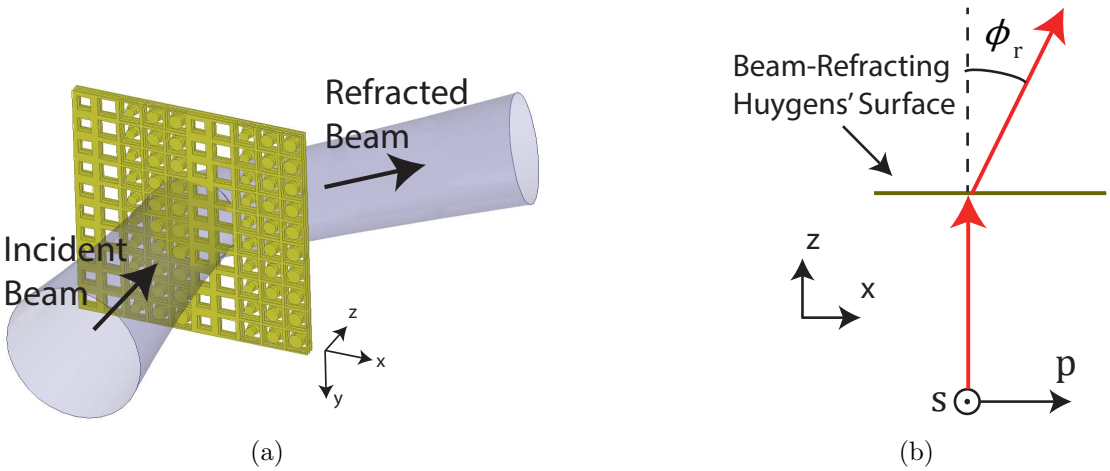

Figure 8.7: **(a)** Perspective view of an optically thin, isotropic metamaterial Huygens' surface that efficiently refracts a normally incident beam at telecommunication wavelengths. **(b)** Top view of the beam-refracting metamaterial Huygens' surface.

with an index of refraction of $n_{\mathrm{SiO_2}} = 1.45$. The index of refraction of the SU-8 is $n_{\text{SU-8}} = 1.57$. Near the operating wavelength of 1.5 μm, the relative permittivity of Au is described by the Drude model $\epsilon_{\mathrm{Au}} = \epsilon_\infty - \omega_p^2/(\omega^2 + j\omega\omega_c)$, with $\epsilon_\infty = 9.0$, the plasma frequency is $\omega_p = 1.363\text{x}10^{16}$ rad/s (8.97 eV), and the collision frequency is $\omega_c = 3.60\text{x}10^{14}$ rad/s (0.24 eV). This collision frequency assumes a loss that is over three times that of the previous section. This increased loss takes into account thin film surface scattering and grain boundary effects [221].

As in the previous section, each of the three sheet admittances can be modeled as a parallel LC circuit (see Figure 8.8(c)). The inductance arises from both electron inertia and the wire grid outlining each unit cell. The capacitance is created by the central disk. In other words, increasing 'w' decreases the imaginary part of the sheet admittance, whereas increasing 'd' increases the imaginary part of the sheet admittance. The central disc is circular rather than square, which eases fabrication tolerances. Once the sheet admittances are realized, their cascaded response can be calculated using the transfer matrix approach described earlier. In Figure 8.9, the transmittance, transmitted phase, and reflectance are plotted as a function of the outer sheet admittances ($Y_{s1} = Y_{s3}$). From the analytic model that includes losses, it was found that enforcing the condition $Y_{s1} = Y_{s3} = Y_{s2}/1.5$, provides a good trade-off between maximizing transmission bandwidth and phase coverage, while minimizing loss and reflection. It should be noted that transmittance and phase coverage increase with reduced metallic loss.

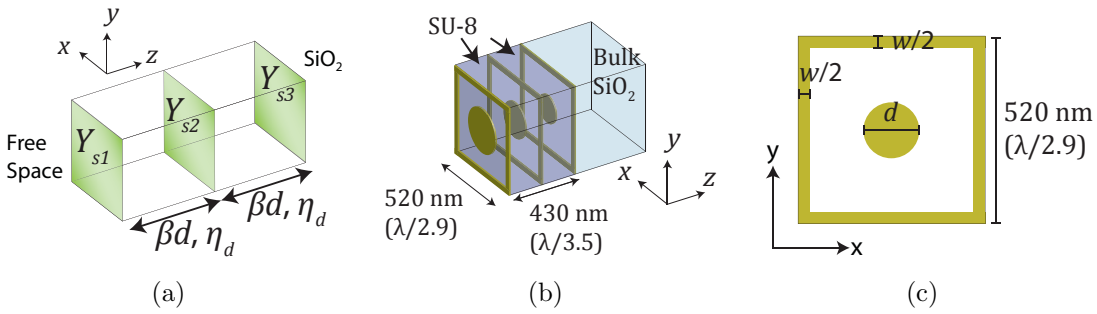

Figure 8.8: Experimental unit cell design. **(a)** Analytic model of a unit cell consisting of three metallic sheets cascaded in the direction of propagation. **(b)** Perspective view of a typical unit cell. **(c)** Top view of each of the three sheet admittances. The imaginary part of the sheet admittance increases with increasing 'd,' whereas the imaginary part of the sheet admittance decreases with increasing 'w'. It can be seen that the cell is isotropic. Therefore, there is no scattered power in the cross-polarized field component.

The imaginary part of the sheet admittance is primarily responsible for controlling the phase delay through a unit cell, and the real part accounts for the loss. For an accurate model of the cascaded sheet admittances, the relationship between the real and imaginary parts of the sheet admittance must be determined. From simulations of the geometry shown in Figure 8.8(c), it was found that the real part of the sheet admittance increases nearly monotonically with the magnitude of the imaginary part of the sheet admittance, as shown in Figure 8.10. This relationship between the real and imaginary parts of the sheet admittance is incorporated in the analytic model presented in Figure 8.9.

8.3.2 Beam Refraction Simulations

Table 8.1: Designed dimensions (nm) of each sheet admittance. The subscripts 1, 2, and 3 denote the dimensions of the first, second, and third layers, respectively.

Cell#	w_1	d_1	w_2	d_2	w_3	d_3
1	166	0	212	0	206	0
2	78	0	110	0	110	0
3	60	278	60	210	60	214
4	60	324	60	298	60	270
5	60	364	60	306	60	296

A beam-refracting metamaterial Huygens' surface is then realized by stipulating

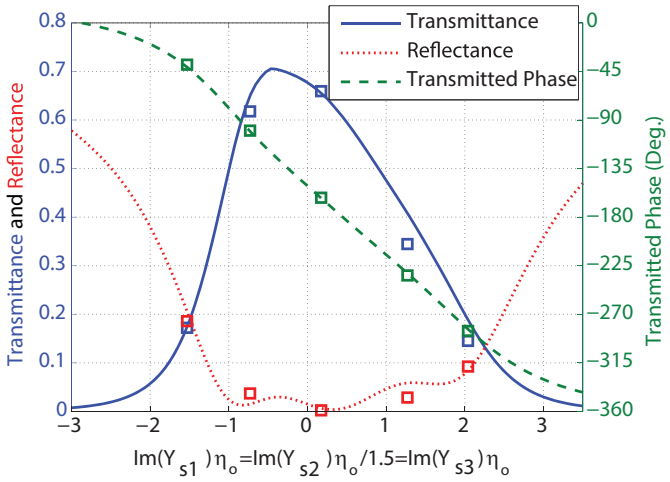

Figure 8.9: Transmittance, transmitted phase, and reflectance as a function of the imaginary part of the outer sheet admittances ($Y_{s1} = Y_{s3}$) at a wavelength of 1.5 μm. Light is incident from the SiO_2 substrate side. The squares indicate the simulated reflection and transmission coefficients of the five unit cells shown in Figure 8.11(a). It is assumed the middle sheet admittance is 1.5 times the outer sheet admittances ($Y_{s1} = Y_{s3} = Y_{s2}/1.5$), which limits reflection loss. The loss of the sheet admittance is estimated from simulations of the unit cell shown in 8.8(b).

a linear phase gradient across the surface. This example was again chosen because its performance is straightforward to characterize in experiment [158]. Figure 8.11(a) shows a section of the designed Huygens' surface that refracts normally incident light to an angle of 35.2° at a wavelength of 1.5 μm. The exact dimensions are supplied in Table 8.1. Each supercell contains five unit cells whose simulated performance is shown in Figure 8.9. Simulations were performed using the full-wave solver, CST Microwave Studio. It can be seen that there is a good agreement between the simulated data points and the analytic model. Figure 8.11 shows the wavelength dependence of the transmittance and transmitted phase shift of the five unit cells. It should be noted that the achievable phase coverage was reduced due to Au loss. If the minimum transmittance of each unit cell is stipulated to be 0.15, the achievable phase coverage is limited to 260° rather than the ideal 360°. In addition, the transmittances of each unit cell are not identical. Both the reduced phase coverage and nonidentical transmittance creates aberration in the transmitted field. For periodic structures such as beam-refracting surfaces, these aberrations can be easily quantified using well-known Floquet theory [189]. In short, the transmitted field can be decomposed into propagating Floquet harmonics. For example, transmission into the $n = 0$ harmonic corresponds to light that is transmitted in the normal direction ($\phi_r = 0°$), whereas

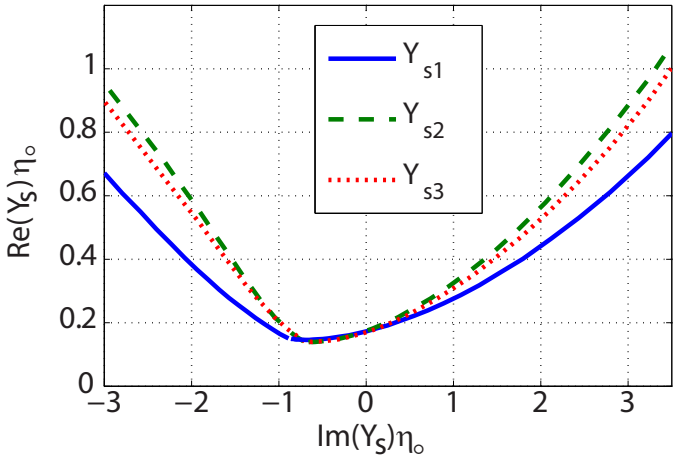

Figure 8.10: Relationship between the real and imaginary parts of each sheet admittance.

the $n = 1$ harmonic corresponds the refracted direction ($\phi_r = 35.2°$). The goal here is to maximize the power in the $n = 1$ harmonic, while minimizing the power in other harmonics.

The simulated performance of the designed metamaterial Huygens' surface is shown in Figure 8.12. Figure 8.12(a) shows a time snapshot of the steady-state electric field when a plane wave is normally incident from the SiO_2 substrate at a wavelength of 1.5 μm. It can be seen that the Huygens' surface efficiently refracts the incident light to ($\phi_r = 35.2°$). The ripple in the field is from power that is scattered into undesired Floquet harmonics. In Figure 8.12(b), the transmittance is plotted as a function of the refracted angle and wavelength. This shows the angular dependence of the various Floquet harmonics. It can be seen that the majority of the transmitted power is in the $n = 1$ harmonic. As the operating wavelength varies from 1.2 μm to 2 μm, the refracted angle of this harmonic scans from ($\phi_r = 27.5°$) to ($\phi_r = 50.3°$). The power that is refracted is better quantified in Figure 8.13, which plots the transmittance and reflectance versus wavelength. In this plot, the s- and p-refracted curves correspond to the transmittance of the two polarizations into the $n = 1$ Floquet harmonic. Also shown are two of the loss mechanisms of the Huygens' surface, which include reflection and transmission into undesired Floquet harmonics (for example, $n = -2$, $n = -1$, $n = 0$, $n = 2$ harmonics). Virtually no power (<-60 dB) is scattered into cross-polarized light. The power that is lost due to Au absorption is 1 - (refracted) - (reflected) - (transmitted undesired), which is approximately 60% at the wavelength of 1.5 μm. The metamaterial Huygens' surface is isotropic since the s- and p-polarized curves coincide over much of the operating wavelengths. The

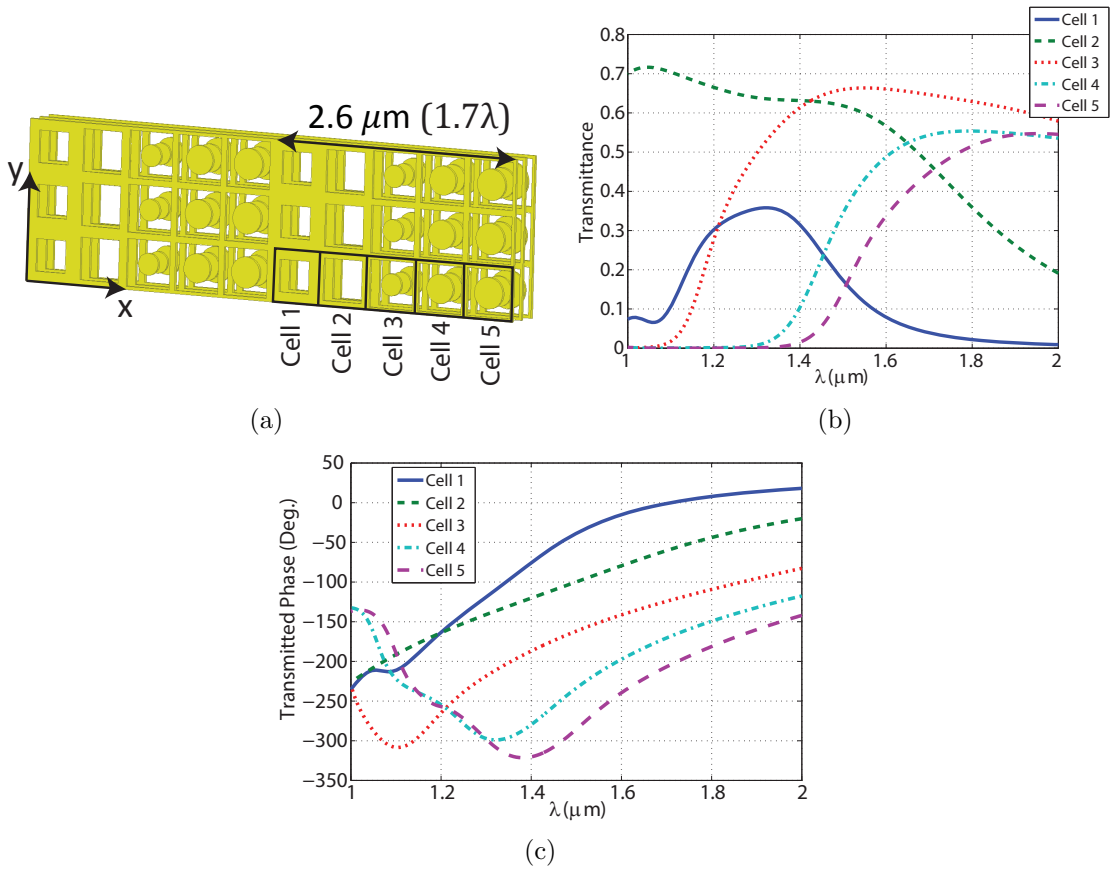

Figure 8.11: Designed beam-refracting Huygens' surface. **(a)** Perspective view of the metamaterial Huygens' surface when viewed from the bulk SiO_2 side. All dimensions are to scale. The five unit cells comprising the surface are outlined. **(b,c)** Simulated wavelength dependence of the transmittance and transmitted phase shift of each unit cell comprising the designed metamaterial Huygens' surface.

difference between the two polarizations is most likely due to the coupling between spatially varying unit cells since this is not accounted for in the analytic model. It should also be noted that the response is broadband. The refracted field maintains a transmittance that is greater than half its peak value over a bandwidth of 1.33 μm to 1.95 μm (38%) for both polarizations. Two important performance metrics are the peak efficiency (transmittance in the refracted direction) and extinction ratio (ratio of the refracted transmittance to normal transmittance) [49]. Simulations demonstrate a peak efficiency and extinction ratio of 32.6% and 11.6 dB, respectively, for s-polarized light and 30.4% and 10.3 dB, respectively, for p-polarized light.

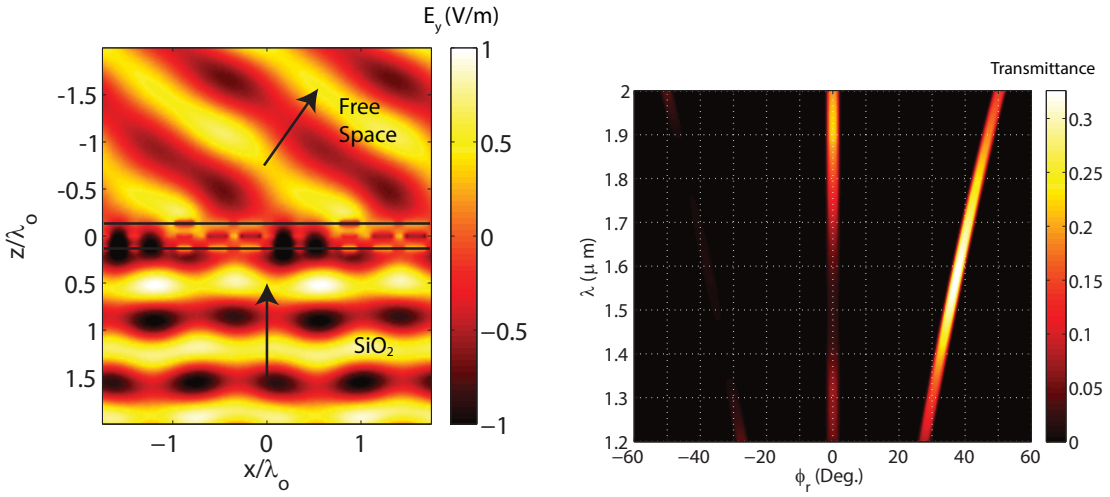

(a) (b)

Figure 8.12: Simulated beam-refracting metamaterial Huygens' surface. **(a)** Time snapshot of the steady-state, y-polarized electric field when a plane wave is normally incident from the bottom at a wavelength of 1.5 μm. The incident electric field has an amplitude of 1 V/m. **(b)** Transmittance as a function of wavelength and transmitted angle for s-polarized light. At the design wavelength of 1.5 μm, the transmittance of the $n = 1$ Floquet harmonic ($\phi_r = 35.2°$) is much larger than the $n = -1$ ($\phi_r = -35.2°$) and $n = 0$ ($\phi_r = 0°$) harmonics.

8.3.3 Fabrication

The metasurface was fabricated and measured at Purdue University by Naresh Emani, and Amr Shaltout, who are in Alexandra Boltasseva's and Vladimir Shalaev's research groups [222]. The fabrication process is shown in Figure 8.14(a) [12]. The design is fabricated on a 500 μm thick SiO_2 substrate. First, the bottom sheet admittance (Y_{s3}) is fabricated by patterning a 2 nm Ti adhesion layer and 28 nm Au layer using standard electron beam lithography and liftoff. Next, a 200 nm thick, SU-8 dielectric layer is spin coated onto the wafer, which naturally planarizes the surface for the following layer (measured roughness < 5 nm). This process is repeated until three Au layers are patterned to achieve the unit cell shown in Figure 8.8(b). The patterned area is 500 μm x 500 μm. Scanning electron microscope (SEM) pictures of the fabricated metamaterial Huygens' surface are shown in Figure 8.14. As measured from SEM pictures, the fabricated dimensions of each layer are shown in Table 8.2, and are 30 nm different from the design dimensions.

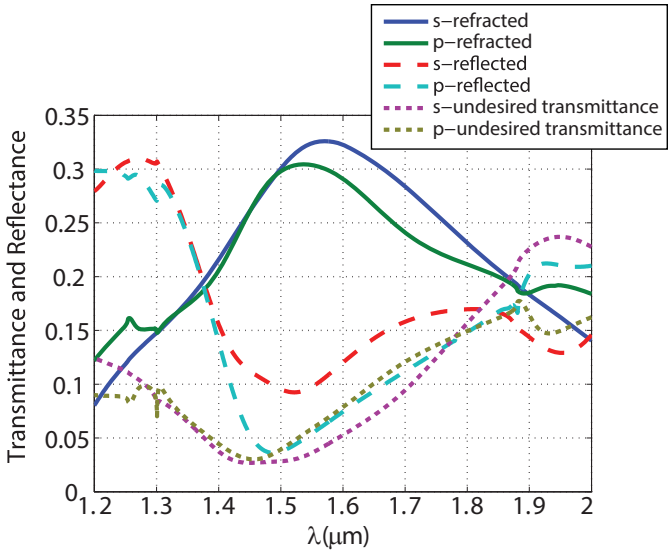

Figure 8.13: Transmittance and reflectance versus wavelength for both polarizations. s- and p-refracted denotes the transmittance of light that is refracted into the $n = 1$ harmonic for the s- and p-polarizations, respectively. s- and p-reflected denotes the total reflectance. s- and p-undesired transmittance denotes the total transmittance that is not in the $n = 1$ harmonic. Virtually no power (<-60 dB) is scattered into cross-polarized light.

8.3.4 Measurements

The fabricated sample is measured using the transmission module of an ellipsometer (V-VASE, J. A. Woollam Co.) A monochromator scans the wavelength of a normally incident light source, and the transmitted power is measured at each refracted angle. Unlike in the simulations of Figure 8.12, the incident light in measurements propagates in the $+z$ direction, which simplifies the alignment procedure. This has minimal effect on the transmittance but does increase the reflectance. Simulations suggest that when the incident light propagates in the $+z$ direction, the refracted transmittance is at most 3% different from when the incident light propagates in the z direction. The measured transmittance in the refracted direction and normal direction are shown in Figure 8.15 for s-polarized and p-polarized light, respectively. As mentioned, SEM pictures show that the dimensions of the fabricated surface are off by 30 nm, which causes the discrepancy between the measured performance and the simulations presented in Figure 8.12. To demonstrate that the difference between the fabricated and designed dimensions is the cause of error between measurement and simulation, the fabricated dimensions are also simulated, which is shown in Figure 8.15. It can be seen that the re-simulated and measured performance agree for the

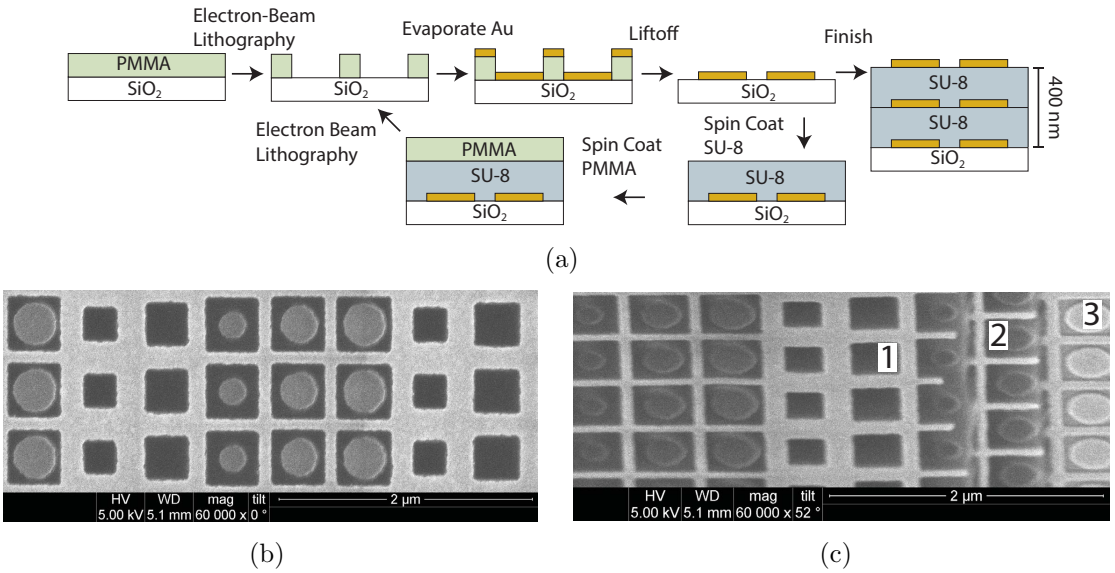

Figure 8.14: Fabrication of the metamaterial Huygens' surface. **(a)** Fabrication process involves sequential patterning of each 2 nm/28 nm thick Ti/Au layer using standard electron-beam lithography and liftoff, followed by spin coating of a 200 nm thick SU-8 dielectric layer. Three metallic layers are patterned using the process resulting in an overall thickness of 430 nm. **(b)** Scanning electron microscope (SEM) picture of a section of the metamaterial Huygens' surface. **(c)** Perspective view of the edge of the Huygens' surface, such that all three layers can be seen.

refracted power. However, the power that is transmitted into the normal direction is still roughly 5% larger in measurement than simulation, but the trends are the same. The difference between simulation and measurement can be attributed to additional fabrication and measurement errors. If the fabricated sample is not centered on the incident beam for the ellipsometry measurements, a small percentage of the power is not captured by the metamaterial Huygens' surface. In addition, there is some uncertainty when modeling the surface roughness and loss of the Au, which introduces error into the simulations. Despite the various sources of error, these measurements achieve a peak efficiency and extinction ratio of 19.9% and 2.93 dB, respectively, for s-polarized light, and 18.0% and 3.05 dB, respectively, for p-polarized light. This is an improvement of a factor of 3 in efficiency and a factor of 4 in extinction ratio over the state of the art V-antenna [69]. In addition, the response is isotropic, which enables control of an arbitrary incident polarization. However, it should be noted that this increased performance does come at the expense of an increased thickness and a multilayer fabrication process.

Table 8.2: Fabricated dimensions (nm) of each sheet admittance measured with SEM pictures. It can be seen that the fabricated dimensions are 30 nm different from the design dimensions, which reduced the measured performance.

Cell#	w_1	d_1	w_2	d_2	w_3	d_3
1	255	0	255	0	270	0
2	140	0	140	0	190	0
3	93	200	93	200	110	220
4	93	290	93	290	110	325
5	93	340	93	340	110	355

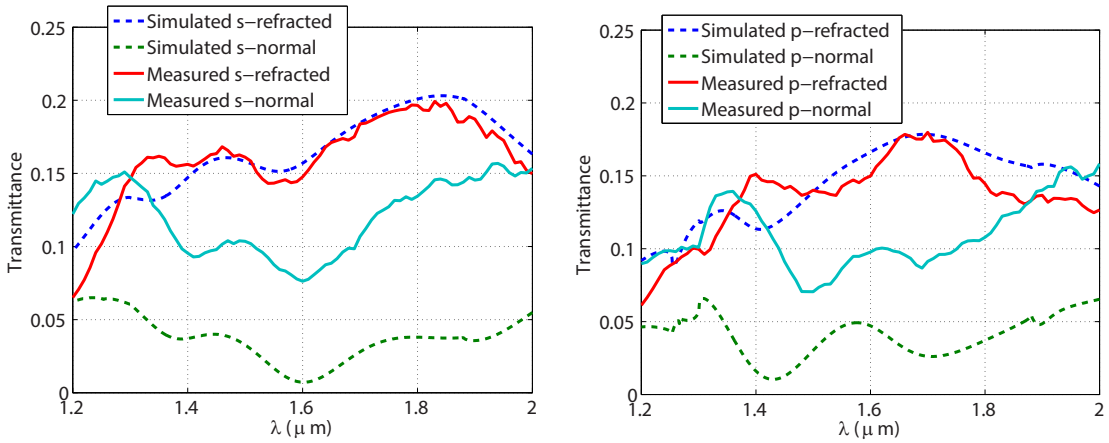

(a) (b)

Figure 8.15: Transmittance measurement results. **(a)** Transmittance of s-polarized light into the refracted and normal directions versus wavelength. **(b)** Transmittance of p-polarized light into the refracted and normal directions versus wavelength. For both (a,b), the simulation values account for the fabricated dimensions of the Au patterns, which are off by roughly 30 nm from the design values based on SEM pictures.

8.4 Chapter Summary

In summary, an efficient metasurface with complete control over the transmitted phase of x and y polarized light was presented. Since both polarizations of light can be independently controlled, arbitrary waveplates can be generated. A lens that both focuses light and converts the polarization from linear to circular is demonstrated. This lens has a simulated peak intensity that is 62% of an ideal lens (i.e. a lens with 100% transmission and parabolic phase gradient) of the same dimensions. This phase and polarization control can find applications in the design of novel lenses that manipulate both the profile and polarization of light.

Next, a low profile metamaterial Huygens' surface was experimentally demonstrated for the first time at optical wavelengths. In addition, the surface exhibits an isotropic response and large extinction ratio. In future work, the fabrication process can be further optimized so that the fabricated dimensions are closer to the design. In addition, large area soft lithography processes, such as nanoimprint lithography, can be used to dramatically reduce the cost of metasurfaces. This work can find numerous applications such as low profile lenses [157], computer-generated-holography [218], nondestructive evaluation [223], and stealth technologies [151]. In addition, novel types of beams such as Airy beams [224], Bessel beams [167], and vortex beams [54] can be generated.

CHAPTER IX

Bianisotropic Metasurfaces for Optimal Polarization Control: Analysis and Synthesis

9.1 Chapter Introduction

In the previous chapters, it was shown that adding a magnetic response to metasurfaces can dramatically increase their efficiency [55, 187, 225]. Here, electric and magnetic anisotropy and magnetoelectric coupling are also systematically incorporated into metasurface design to allow for complete control of an electromagnetic wavefront's polarization and phase. To date, many structures have been reported that exhibit novel polarization effects such as asymmetric transmission [**?**,65,226,227], and giant optical activity [66, 170]. However, the performance of most devices has been suboptimal since systematic design methodologies for realizing these low symmetry structures has been limited [170]. Designs typically employ a resonant geometry that exhibits the necessary mirror and rotational symmetry such that a desired bianisotropic response is observed rather than attempting to provide optimal performance [67]. Additionally, the principle of operation is often device specific, and its generalization to other designs is not straightforward.

Previously reported analyses modeled bianisotropic metasurfaces as coupled electric and magnetic dipoles [228]. In [170], the interaction of neighboring particles is also considered. However, the model is rather complex since the polarizabilities relate the induced dipole moment to the incident field rather than the average field [170]. Alternatively, it is possible to model a metasurface as a thin bianisotropic slab [229]. However, the scattering parameters cannot be solved for in closed form unless some simplifying approximations are made [**?**]. Further, the interpretation is not strictly appropriate since the thickness of a metasurface is ill-defined [230].

In this chapter, methods to both analyze and design bianisotropic metasurfaces are

presented. First, bianisotropic metasurfaces are analyzed using closed-form expressions that relate the reflection and transmission coefficients (scattering parameters) to constituent surface parameters. This is an alternative approach to that used in [170], and provides additional physical intuition. Here, the constituent surface parameters relate the induced dipole moments to the average field quantities as in standard homogenization techniques for bulk materials. Next, a method to systematically design bianisotropic structures is introduced. It is shown that cascading anisotropic, patterned metallic sheets can provide significant control over the constituent surface parameters. A transfer matrix approach is used to directly solve for the scattering parameters (S-parameters) of the structure, enabling devices with optimal performance: polarization purity and high transmission. It should be emphasized that the main claim is that the performance, rather than the implementation, is optimal. Finally, the ability to realize a wide range of constituent surface parameters is demonstrated with four different devices: a polarization rotator, an asymmetric circular polarizer, an asymmetric linear polarizer, and a symmetric circular polarizer.

9.2 Analysis: Relating S-parameters to Constituent Surface Parameters

Let us consider two regions of space (Regions 1 and 2) with wave impedances given by $\eta_1 = \sqrt{\mu_1/\epsilon_1}$ and $\eta_2 = \sqrt{\mu_2/\epsilon_2}$, respectively. The two regions of space are separated by an arbitrary metasurface along the $z = 0$ plane, as shown in Fig. 9.1. The metasurface is illuminated by normally incident plane. The scattering parameters (S-parameters) are equal to the ratio of the scattered electric field to the incident electric field. In general, $\mathbf{S}_{nm} = \begin{pmatrix} S_{nm}^{xx} & S_{nm}^{xy} \\ S_{nm}^{yx} & S_{nm}^{yy} \end{pmatrix}$ is a 2x2 matrix relating the field scattered into Region n when a plane wave is normally incident from Region m. For example, S_{21}^{yx} represents the y-polarized field transmitted into Region 2 when an x-polarized plane wave is incident from Region 1. The parameters $\mathbf{S}_{11}$ and $\mathbf{S}_{22}$ are the reflection coefficients when viewed from Regions 1 and 2 respectively, and $\mathbf{S}_{21}$ and $\mathbf{S}_{12}$ are the transmission coefficients when viewed from Regions 1 and 2, respectively. The transmission coefficient is often referred to as the Jones matrix [67].

An arbitrary metasurface can be modeled as a two-dimensional array of polarizable particles [155]. Each particle is characterized by its quasi-static electric and magnetic polarizabilities ($\boldsymbol{\alpha}_{e,m}$), defined as the ratio of the dipole moment to the local field. When these particles are closely spaced across a two-dimensional surface, a surface

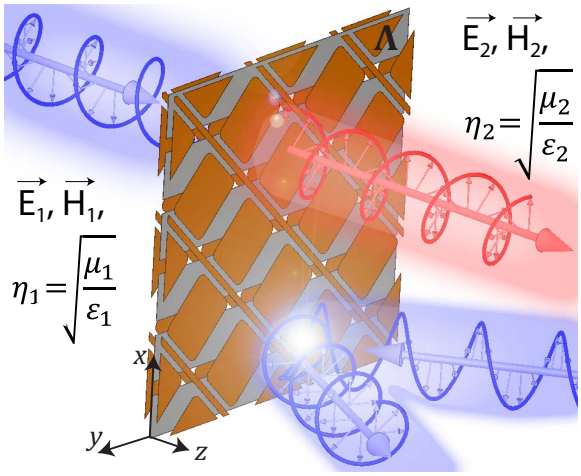

Figure 9.1: Bianisotropic metasurfaces exhibiting electric, magnetic, and magnetoelectric responses can achieve complete control of the polarization of an electromagnetic wavefront. This artistic rendering shows the example of an asymmetric circular polarizer converting right-handed-circularly polarized light from Region 1 to left-handed-circularly-polarized light in Region 2. However, right-handed-circularly polarized light is completely reflected when incident from Region 2.

polarizability ($\boldsymbol{\alpha}^s_{e,m}$) that accounts for coupling between particles can be defined [155]. They represent the effective polarizability per unit area,

$$\begin{pmatrix} \mathbf{p}^s \\ \mathbf{m}^s \end{pmatrix} = \begin{pmatrix} \boldsymbol{\alpha}^s_{ee} & \boldsymbol{\alpha}^s_{em} \\ \boldsymbol{\alpha}^s_{me} & \boldsymbol{\alpha}^s_{mm} \end{pmatrix} \begin{pmatrix} \mathbf{E} \\ \mathbf{H} \end{pmatrix} \tag{9.1}$$

Here, $\mathbf{p}^s = [p^s_x \quad p^s_y]^T$ and $\mathbf{m}^s = [m^s_x \quad m^s_y]^T$ represent the electric and magnetic dipole moments, while $\mathbf{E} = [E_x \quad E_y]^T$ and $\mathbf{H} = [H_x \quad H_y]^T$ represent the average field tangential to the surface.

A time-harmonic progression of $e^{j\omega t}$ is assumed, where ω is the radial frequency and t is time. We then define an electric sheet admittance tensor ($\mathbf{Y} = j\omega\boldsymbol{\alpha}^s_{ee}$), magnetic sheet impedance tensor ($\mathbf{Z} = j\omega\boldsymbol{\alpha}^s_{mm}$), and dimensionless magnetoelectric coupling tensors ($\boldsymbol{\chi} = j\omega\boldsymbol{\alpha}^s_{em}, \boldsymbol{\Upsilon} = j\omega\boldsymbol{\alpha}^s_{me}$) in terms of the surface polarizabilities. Multiplying both sides of (9.1) by $j\omega$ and noting that a time-varying dipole moment can be equated to a surface current, the electric and magnetic surface currents established on the metasurface can be related to the average, tangential electric and magnetic fields,

$$\begin{pmatrix} \mathbf{J}^s \\ \mathbf{M}^s \end{pmatrix} = \begin{pmatrix} \mathbf{Y} & \boldsymbol{\chi} \\ \boldsymbol{\Upsilon} & \mathbf{Z} \end{pmatrix} \begin{pmatrix} \mathbf{E} \\ \mathbf{H} \end{pmatrix} = \boldsymbol{\Lambda} \begin{pmatrix} \mathbf{E} \\ \mathbf{H} \end{pmatrix} \tag{9.2}$$

The variables $\mathbf{Y}$, $\boldsymbol{\chi}$, $\boldsymbol{\Upsilon}$, and $\mathbf{Z}$ are all 2x2 tensors that relate the x and y field components to the x and y current density components: $\mathbf{Y} = \begin{pmatrix} Y_{xx} & Y_{xy} \\ Y_{yx} & Y_{yy} \end{pmatrix}$, $\boldsymbol{\chi} = \begin{pmatrix} \chi_{xx} & \chi_{xy} \\ \chi_{yx} & \chi_{yy} \end{pmatrix}$, $\boldsymbol{\Upsilon} = \begin{pmatrix} \Upsilon_{xx} & \Upsilon_{xy} \\ \Upsilon_{yx} & \Upsilon_{yy} \end{pmatrix}$, $\mathbf{Z} = \begin{pmatrix} Z_{xx} & Z_{xy} \\ Z_{yx} & Z_{yy} \end{pmatrix}$. Intuitively, $\mathbf{Y}$ and $\mathbf{Z}$ are the two dimensional equivalent of electric and magnetic material susceptibilities, respectively [7]. Similarly, $\boldsymbol{\chi}$ and $\boldsymbol{\Upsilon}$ are the two dimensional equivalent of the magetoelectric material parameters. If the metasurface is reciprocal, $\mathbf{Y} = \mathbf{Y}^T$, $\boldsymbol{\Upsilon} = -\boldsymbol{\chi}^T$, and $\mathbf{Z} = \mathbf{Z}^T$ [231]. In addition, if it is lossless, $\mathbf{Y}$ and $\mathbf{Z}$ are purely imaginary, whereas $\boldsymbol{\Upsilon}$ and $\boldsymbol{\chi}$ are purely real [231].

Next, relations between the S-parameters and the constituent parameters are derived. The boundary condition given by (9.2) is explicitly written in terms of the tangential field in Regions 1 and 2,

$$\mathbf{Y}\left(\frac{\mathbf{E}_1+\mathbf{E}_2}{2}\right)+\boldsymbol{\chi}\left(\frac{\mathbf{H}_1+\mathbf{H}_2}{2}\right) = \hat{n}\times(\mathbf{H}_2-\mathbf{H}_1) = \mathbf{n}(\mathbf{H}_2-\mathbf{H}_1) \tag{9.3}$$

$$\boldsymbol{\Upsilon}\left(\frac{\mathbf{E}_1+\mathbf{E}_2}{2}\right)+\mathbf{Z}\left(\frac{\mathbf{H}_1+\mathbf{H}_2}{2}\right) = -\hat{n}\times(\mathbf{E}_2-\mathbf{E}_1) = -\mathbf{n}(\mathbf{E}_2-\mathbf{E}_1) \tag{9.4}$$

Consider an x-polarized plane wave, normally incident on the bianisotropic metasurface from Region 1. The field in Region 1 is expressed as $\mathbf{E}_1^+ = \mathbf{I}_x + \mathbf{S}_{11}^x$ and $\mathbf{H}_1^+ = \eta_1^{-1}\mathbf{n}(\mathbf{I}_x - \mathbf{S}_{11}^x)$. The field in Region 2 is written as $\mathbf{E}_2^+ = \mathbf{S}_{21}^x$ and $\mathbf{H}_2^+ = \eta_2^{-1}\mathbf{n}\mathbf{S}_{21}^x$. Here, the + sign indicates the excitation is incident from Region 1 (traveling in the $+z$ direction), $\mathbf{I}_x = (1 \quad 0)^T$, $\mathbf{S}_{11}^x = (S_{11}^{xx} \quad S_{11}^{yx})^T$, $\mathbf{S}_{21}^x = (S_{21}^{xx} \quad S_{21}^{yx})^T$, and $\mathbf{n} = \begin{pmatrix} 0 & -1 \\ 1 & 0 \end{pmatrix}$. Substituting these expressions for $\mathbf{E}^+$ and $\mathbf{H}^+$ into (9.3) and (9.4), the S-parameters are related to the constituent surface parameters,

$$\frac{\mathbf{Y}}{2}(\mathbf{I}_x+\mathbf{S}_{11}^x+\mathbf{S}_{21}^x) \quad + \quad \frac{\boldsymbol{\chi}\mathbf{n}}{2}\left(\frac{\mathbf{I}_x}{\eta_1}-\frac{\mathbf{S}_{11}^x}{\eta_1}+\frac{\mathbf{S}_{21}^x}{\eta_2}\right) = -\left(\frac{-\mathbf{I}_x}{\eta_1}+\frac{\mathbf{S}_{11}^x}{\eta_1}+\frac{\mathbf{S}_{21}^x}{\eta_2}\right) \tag{9.5}$$

$$\frac{\boldsymbol{\Upsilon}}{2}(\mathbf{I}_x+\mathbf{S}_{11}^x+\mathbf{S}_{21}^x) \quad + \quad \frac{\mathbf{Z}\mathbf{n}}{2}\left(\frac{\mathbf{I}_x}{\eta_1}-\frac{\mathbf{S}_{11}^x}{\eta_1}+\frac{\mathbf{S}_{21}^x}{\eta_2}\right) = -\mathbf{n}(-\mathbf{I}_x-\mathbf{S}_{11}^x+\mathbf{S}_{21}^x) \tag{9.6}$$

This linear system of equations is solved in closed form,

$$\begin{pmatrix} \mathbf{S}_{11}^x \\ \mathbf{S}_{21}^x \end{pmatrix} = \begin{pmatrix} \frac{\mathbf{Y}}{2}-\frac{\boldsymbol{\chi}\mathbf{n}}{2\eta_1}+\frac{\mathbf{I}}{\eta_1} & \frac{\mathbf{Y}}{2}+\frac{\boldsymbol{\chi}\mathbf{n}}{2\eta_2}+\frac{\mathbf{I}}{\eta_2} \\ -\frac{\mathbf{Z}\mathbf{n}}{2\eta_1}+\frac{\boldsymbol{\Upsilon}}{2}-\mathbf{n} & \frac{\mathbf{Z}\mathbf{n}}{2\eta_2}+\frac{\boldsymbol{\Upsilon}}{2}+\mathbf{n} \end{pmatrix}^{-1} \begin{pmatrix} -\frac{\mathbf{Y}\mathbf{I}_x}{2}-\frac{\boldsymbol{\chi}\mathbf{n}\mathbf{I}_x}{2\eta_1}+\frac{\mathbf{I}_x}{\eta_1} \\ -\frac{\mathbf{Z}\mathbf{n}\mathbf{I}_x}{2\eta_1}-\frac{\boldsymbol{\Upsilon}\mathbf{I}_x}{2}+\mathbf{n}\mathbf{I}_x \end{pmatrix} \tag{9.7}$$

where $\mathbf{I} = \begin{pmatrix} 1 & 0 \\ 0 & 1 \end{pmatrix}$ is the identity matrix. Similarly, $\mathbf{S}_{11}^{y}$ and $\mathbf{S}_{21}^{y}$ are solved by replacing $\mathbf{I}_x = (1 \quad 0)^T$ with $\mathbf{I}_y = (0 \quad 1)^T$.

The variables, $\mathbf{S}_{12}$ and $\mathbf{S}_{22}$ are also solved using the boundary conditions (9.3) and (9.4). A normally incident x-polarized plane wave excitation is stipulated in Region 2. The field in Region 2 is then expressed as $\mathbf{E}_2^- = \mathbf{I}_x + \mathbf{S}_{22}^x$, and $\mathbf{H}_2^- = \eta_2^{-1}\mathbf{n}(-\mathbf{I}_x + \mathbf{S}_{22}^x)$. The field in Region 1 is written as $\mathbf{E}_1^- = \mathbf{S}_{12}^x$ and $\mathbf{H}_1^- = -\eta_1^{-1}\mathbf{n}\mathbf{S}_{12}^x$. As before, the $-$ sign indicates the excitation is incident from Region 2, $\mathbf{S}_{12}^x = (S_{12}^{xx} \quad S_{12}^{yx})^T$, and $\mathbf{S}_{22}^x = (S_{22}^{xx} \quad S_{22}^{yx})^T$. The expressions for $\mathbf{E}^-$ and $\mathbf{H}^-$ are then substituted into (9.3) and (9.4),

$$\frac{\mathbf{\Upsilon}}{2}(\mathbf{I}_x + \mathbf{S}_{12}^x + \mathbf{S}_{22}^x) + \frac{\boldsymbol{\chi}\mathbf{n}}{2}\left(-\frac{\mathbf{I}_x}{\eta_2} - \frac{\mathbf{S}_{12}^x}{\eta_1} + \frac{\mathbf{S}_{22}^x}{\eta_2}\right) = -\left(\frac{-\mathbf{I}_x}{\eta_2} + \frac{\mathbf{S}_{12}^x}{\eta_1} + \frac{\mathbf{S}_{22}^x}{\eta_2}\right) \tag{9.8}$$

$$\frac{\mathbf{\Upsilon}}{2}(\mathbf{I}_x + \mathbf{S}_{12}^x + \mathbf{S}_{22}^x) + \frac{\mathbf{Z}\mathbf{n}}{2}\left(-\frac{\mathbf{I}_x}{\eta_2} - \frac{\mathbf{S}_{12}^x}{\eta_1} + \frac{\mathbf{S}_{22}^x}{\eta_2}\right) = -\mathbf{n}(\mathbf{I}_x - \mathbf{S}_{12}^x + \mathbf{S}_{22}^x) \tag{9.9}$$

Again, there are two equations and two unknowns that can be solved,

$$\begin{pmatrix} \mathbf{S}_{12}^x \\ \mathbf{S}_{22}^x \end{pmatrix} = \begin{pmatrix} \frac{\mathbf{Y}}{2} - \frac{\boldsymbol{\chi}\mathbf{n}}{2\eta_1} + \frac{\mathbf{I}}{\eta_1} & \frac{\mathbf{Y}}{2} + \frac{\boldsymbol{\chi}\mathbf{n}}{2\eta_2} + \frac{\mathbf{I}}{\eta_2} \\ -\frac{\mathbf{Z}\mathbf{n}}{2\eta_1} + \frac{\mathbf{\Upsilon}}{2} - \mathbf{n} & \frac{\mathbf{Z}\mathbf{n}}{2\eta_2} + \frac{\mathbf{\Upsilon}}{2} + \mathbf{n} \end{pmatrix}^{-1} \begin{pmatrix} -\frac{\mathbf{Y}\mathbf{I}_x}{2} + \frac{\boldsymbol{\chi}\mathbf{n}\mathbf{I}_x}{2\eta_2} + \frac{\mathbf{I}_x}{\eta_2} \\ \frac{\mathbf{Z}\mathbf{n}\mathbf{I}_x}{2\eta_2} - \frac{\mathbf{\Upsilon}\mathbf{I}_x}{2} - \mathbf{n}\mathbf{I}_x \end{pmatrix} \tag{9.10}$$

The expressions $\mathbf{S}_{12}^y$ and $\mathbf{S}_{22}^y$ are solved by replacing $\mathbf{I}_x$ with $\mathbf{I}_y$. Therefore, all the S-parameters are written concisely as,

$$\begin{aligned} \begin{pmatrix} \mathbf{S}_{11} & \mathbf{S}_{12} \\ \mathbf{S}_{21} & \mathbf{S}_{22} \end{pmatrix} = &\begin{pmatrix} \frac{\mathbf{Y}}{2} - \frac{\boldsymbol{\chi}\mathbf{n}}{2\eta_1} + \frac{\mathbf{I}}{\eta_1} & \frac{\mathbf{Y}}{2} + \frac{\boldsymbol{\chi}\mathbf{n}}{2\eta_2} + \frac{\mathbf{I}}{\eta_2} \\ -\frac{\mathbf{Z}\mathbf{n}}{2\eta_1} + \frac{\mathbf{\Upsilon}}{2} - \mathbf{n} & \frac{\mathbf{Z}\mathbf{n}}{2\eta_2} + \frac{\mathbf{\Upsilon}}{2} + \mathbf{n} \end{pmatrix}^{-1} \\ &\cdot \begin{pmatrix} -\frac{\mathbf{Y}}{2} - \frac{\boldsymbol{\chi}\mathbf{n}}{2\eta_1} + \frac{\mathbf{I}}{\eta_1} & -\frac{\mathbf{Y}}{2} + \frac{\boldsymbol{\chi}\mathbf{n}}{2\eta_2} + \frac{\mathbf{I}}{\eta_2} \\ -\frac{\mathbf{Z}\mathbf{n}}{2\eta_1} - \frac{\mathbf{\Upsilon}}{2} + \mathbf{n} & \frac{\mathbf{Z}\mathbf{n}}{2\eta_2} - \frac{\mathbf{\Upsilon}}{2} - \mathbf{n} \end{pmatrix} \end{aligned} \tag{9.11}$$

Alternatively, the constituent surface parameters can be written in terms of the S-parameters. In total, there are four illuminations (x-polarized and y-polarized from the front and back of the metasurface). These illuminations are inserted into (9.3) and (9.4),

$$\begin{pmatrix} \mathbf{Y} & \boldsymbol{\chi} \\ \mathbf{\Upsilon} & \mathbf{Z} \end{pmatrix} \begin{pmatrix} \frac{\mathbf{E}_1^+ + \mathbf{E}_2^+}{2} & \frac{\mathbf{E}_1^- + \mathbf{E}_2^-}{2} \\ \frac{\mathbf{H}_1^+ + \mathbf{H}_2^+}{2} & \frac{\mathbf{H}_1^- + \mathbf{H}_2^-}{2} \end{pmatrix} = \begin{pmatrix} \mathbf{n}(\mathbf{H}_2^+ - \mathbf{H}_1^+) & \mathbf{n}(\mathbf{H}_2^- - \mathbf{H}_1^-) \\ -\mathbf{n}(\mathbf{E}_2^+ - \mathbf{E}_1^+) & -\mathbf{n}(\mathbf{E}_2^- - \mathbf{E}_1^-) \end{pmatrix} \tag{9.12}$$

Substituting the expressions for $\mathbf{E}_{1,2}^{+,-}$ and $\mathbf{H}_{1,2}^{+,-}$, and bringing the average field values to the right-hand side of the equation, the constituent surface parameters can be solved for,

$$\begin{pmatrix} \mathbf{Y} & \boldsymbol{\chi} \\ \boldsymbol{\Upsilon} & \mathbf{Z} \end{pmatrix} = 2 \begin{pmatrix} \frac{\mathbf{I}}{\eta_1} - \frac{\mathbf{S}_{11}}{\eta_1} - \frac{\mathbf{S}_{21}}{\eta_2} & \frac{\mathbf{I}}{\eta_2} - \frac{\mathbf{S}_{12}}{\eta_1} - \frac{\mathbf{S}_{22}}{\eta_2} \\ \mathbf{n} + \mathbf{n}\mathbf{S}_{11} - \mathbf{n}\mathbf{S}_{21} & -\mathbf{n} + \mathbf{n}\mathbf{S}_{12} - \mathbf{n}\mathbf{S}_{22} \end{pmatrix} \cdot \begin{pmatrix} \mathbf{I} + \mathbf{S}_{11} + \mathbf{S}_{21} & \mathbf{I} + \mathbf{S}_{12} + \mathbf{S}_{22} \\ \frac{\mathbf{n}}{\eta_1} - \frac{\mathbf{n}\mathbf{S}_{11}}{\eta_1} + \frac{\mathbf{n}\mathbf{S}_{21}}{\eta_2} & -\frac{\mathbf{n}}{\eta_2} - \frac{\mathbf{n}\mathbf{S}_{12}}{\eta_1} + \frac{\mathbf{n}\mathbf{S}_{22}}{\eta_2} \end{pmatrix}^{-1} \tag{9.13}$$

Similar to material parameter extraction procedures for bulk metamaterials [186], (9.11) and (9.13) provide a powerful framework to design and analyze metasurfaces that realize arbitrary polarization, phase, and amplitude transformations.

9.3 Synthesis

9.3.1 Relating S-parameters to Cascaded Sheet Admittances

Next, a geometry is proposed that can achieve a wide range of constituent surface parameters. The geometry consists of cascaded metallic sheets (electric sheet admittances) separated by subwavelength dielectric spacers, as shown in Fig. 9.2. It should be emphasized that this cascaded structure can be modeled using the constitutive surface parameters derived in the previous section, provided that its overall thickness is subwavelength. This geometry is attractive because it allows for straightforward design and fabrication from microwave to optical wavelengths [12,35,222]. Inspiration for this geometry is derived from recent work showing that the diagonal elements of the electric and magnetic surface susceptibility tensors can be completely controlled with cascaded sheets [55]. Recent work has also shown that polarization controlling devices, such as quarter-wave plates, half-wave plates, and circular polarizers, can be realized by cascading anisotropic sheets [64, 201, 232].

Following an approach similar to that in [233], the reflection and transmission properties of the cascaded sheet admittances are solved. The transfer matrix approach is taken (**ABCD** matrix), which reduces the analysis to matrix multiplication once the transfer matrix of the sheet admittances and dielectric substrate are derived.

The transfer matrix (**ABCD** matrix) of an arbitrary structure relates the total field in Regions 1 and 2,

$$\begin{pmatrix} \mathbf{E}_1 \\ \mathbf{H}_1 \end{pmatrix} = \begin{pmatrix} \mathbf{A} & \mathbf{B} \\ \mathbf{C} & \mathbf{D} \end{pmatrix} \begin{pmatrix} \mathbf{E}_2 \\ \mathbf{H}_2 \end{pmatrix} \tag{9.14}$$

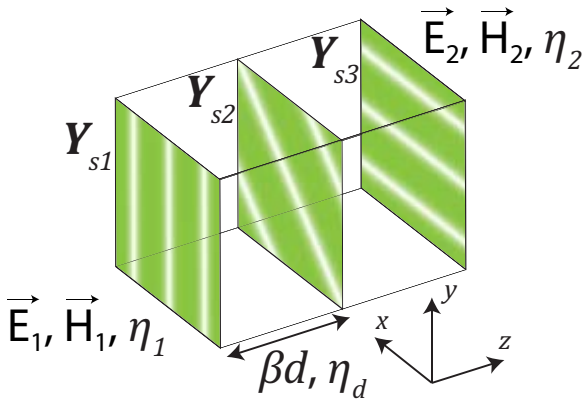

Figure 9.2: Anisotropic sheet admittances cascaded in the direction of propagation can realize a wide range of constituent surface parameters. Provided the overall thickness of the cascaded sheets is subwavelength, they can be modeled as a single bianisotropic metasurface.

As before, we define, $\mathbf{E}_{1,2} = [E^x_{1,2} \quad E^y_{1,2}]^T$, $\mathbf{H}_{1,2} = [H^x_{1,2} \quad H^y_{1,2}]^T$, $\mathbf{A} = \begin{pmatrix} A_{xx} & A_{xy} \\ A_{yx} & A_{yy} \end{pmatrix}$, $\mathbf{B} = \begin{pmatrix} B_{xx} & B_{xy} \\ B_{yx} & B_{yy} \end{pmatrix}$, $\mathbf{C} = \begin{pmatrix} C_{xx} & C_{xy} \\ C_{yx} & C_{yy} \end{pmatrix}$, and $\mathbf{D} = \begin{pmatrix} D_{xx} & D_{xy} \\ D_{yx} & D_{yy} \end{pmatrix}$.

The **ABCD** matrix of an electric sheet admittance $\mathbf{Y}_s$ is then derived. First, it is noted that the boundary condition of an electric sheet admittance can be written as,

$$\hat{n} \times (\mathbf{H}_2 - \mathbf{H}_1) = \mathbf{n}\,(\mathbf{H}_2 - \mathbf{H}_1) = \mathbf{Y}_s\mathbf{E}_1 = \mathbf{Y}_s\mathbf{E}_2 \tag{9.15}$$

Two separate conditions are then stipulated to provide two linearly independent equations: Condition A ($\mathbf{E}_2 = \mathbf{I}$, and $\mathbf{H}_2 = \mathbf{0}$) and Condition B ($\mathbf{E}_2 = \mathbf{0}$, $\mathbf{H}_2 = \mathbf{I}$). Thus we have,

$$\begin{pmatrix} \mathbf{E}_1^A & \mathbf{E}_1^B \\ \mathbf{H}_1^A & \mathbf{H}_1^B \end{pmatrix} = \begin{pmatrix} \mathbf{A} & \mathbf{B} \\ \mathbf{C} & \mathbf{D} \end{pmatrix} \begin{pmatrix} \mathbf{E}_2^A & \mathbf{E}_2^B \\ \mathbf{H}_2^A & \mathbf{H}_2^B \end{pmatrix} = \begin{pmatrix} \mathbf{A} & \mathbf{B} \\ \mathbf{C} & \mathbf{D} \end{pmatrix} \tag{9.16}$$

Enforcing the boundary condition of an electric sheet admittance under the two separate conditions, the field in Region 1 is solved. This provides the **ABCD** matrix of an electric sheet admittance,

$$\begin{pmatrix} \mathbf{A} & \mathbf{B} \\ \mathbf{C} & \mathbf{D} \end{pmatrix} = \begin{pmatrix} \mathbf{I} & \mathbf{0} \\ \mathbf{n}\mathbf{Y}_s & \mathbf{I} \end{pmatrix} \tag{9.17}$$

It should be noted that $-\mathbf{nn} = \mathbf{I}$.

The **ABCD** matrix of a dielectric substrate with wave impedance η_d and thickness βd is then derived. First consider Condition A ($\mathbf{E}_2 = \mathbf{I}$, and $\mathbf{H}_2 = \mathbf{0}$). This is

equivalent to the case where a plane wave is incident from Region 1 with an incident electric field of $\mathbf{I}/2$. In addition, Region 1 must have a wave impedance of η_d, and Region 2 an infinite wave impedance (perfect magnetic conductor). Thus the field in Region 1 can be written as,

$$\begin{aligned} \mathbf{E}_1^A &= \mathbf{I}\frac{e^{j\beta d}+e^{-j\beta d}}{2} = \mathbf{I}\cos(\beta d) \\ \mathbf{H}_1^A &= \mathbf{n}\frac{e^{j\beta d}-e^{-j\beta d}}{2\eta_d} = \mathbf{n}j\eta_d^{-1}\sin(\beta d) \end{aligned} \tag{9.18}$$

Similarly, Condition B ($\mathbf{E}_2 = \mathbf{0}$, $\mathbf{H}_2 = \mathbf{I}$) is equivalent to the case where a plane wave is incident from Region 1 with an incident magnetic field of $\mathbf{I}/2$. In addition, Region 1 has a wave impedance of η_d, and Region 2 is replaced with a perfect electric conductor,

$$\begin{aligned} \mathbf{E}_1^B &= -\mathbf{n}\eta_d\frac{e^{j\beta d}-e^{-j\beta d}}{2} = -\mathbf{n}j\eta_d\sin(\beta d) \\ \mathbf{H}_1^B &= \mathbf{I}\frac{e^{j\beta d}+e^{-j\beta d}}{2} = \mathbf{I}\cos(\beta d) \end{aligned} \tag{9.19}$$

Thus the **ABCD** matrix of a dielectric substrate can be written as,

$$\begin{pmatrix} \mathbf{A} & \mathbf{B} \\ \mathbf{C} & \mathbf{D} \end{pmatrix} = \begin{pmatrix} \cos(\beta d)\mathbf{I} & -j\sin(\beta d)\eta_d\mathbf{n} \\ j\sin(\beta d)\eta_d^{-1}\mathbf{n} & \cos(\beta d)\mathbf{I} \end{pmatrix} \tag{9.20}$$

When three electric sheet admittances are separated by dielectric spacers, the **ABCD** matrix of the entire structure becomes,

$$\begin{aligned} \begin{pmatrix} \mathbf{A} & \mathbf{B} \\ \mathbf{C} & \mathbf{D} \end{pmatrix} = \Bigg[&\begin{pmatrix} \mathbf{I} & \mathbf{0} \\ \mathbf{n}\mathbf{Y}_{s1} & \mathbf{I} \end{pmatrix} \begin{pmatrix} \cos(\beta d)\mathbf{I} & -j\sin(\beta d)\eta_d\mathbf{n} \\ j\sin(\beta d)\eta_d^{-1}\mathbf{n} & \cos(\beta d)\mathbf{I} \end{pmatrix} \\ \cdot &\begin{pmatrix} \mathbf{I} & \mathbf{0} \\ \mathbf{n}\mathbf{Y}_{s2} & \mathbf{I} \end{pmatrix} \begin{pmatrix} \cos(\beta d)\mathbf{I} & -j\sin(\beta d)\eta_d\mathbf{n} \\ j\sin(\beta d)\eta_d^{-1}\mathbf{n} & \cos(\beta d)\mathbf{I} \end{pmatrix} \begin{pmatrix} \mathbf{I} & \mathbf{0} \\ \mathbf{n}\mathbf{Y}_{s3} & \mathbf{I} \end{pmatrix} \Bigg] \end{aligned} \tag{9.21}$$

Next, the **ABCD** matrix entries of an arbitrary structure can be related to its S-parameters. The total field in Regions 1 and 2 can be written as,

$$\begin{pmatrix} \mathbf{I}+\mathbf{S}_{11} & \mathbf{S}_{12} \\ \frac{\mathbf{n}}{\eta_1}(\mathbf{I}-\mathbf{S}_{11}) & -\frac{\mathbf{n}}{\eta_1}\mathbf{S}_{12} \end{pmatrix} = \begin{pmatrix} \mathbf{A} & \mathbf{B} \\ \mathbf{C} & \mathbf{D} \end{pmatrix} \begin{pmatrix} \mathbf{S}_{21} & \mathbf{I}+\mathbf{S}_{22} \\ \frac{\mathbf{n}}{\eta_2}\mathbf{S}_{21} & \frac{\mathbf{n}}{\eta_2}(-\mathbf{I}+\mathbf{S}_{22}) \end{pmatrix} \tag{9.22}$$

Then, the **ABCD** matrix of an arbitrary structure is written in terms of the S-

parameters by solving (9.22),

$$\begin{pmatrix} \mathbf{A} & \mathbf{B} \\ \mathbf{C} & \mathbf{D} \end{pmatrix} = \begin{pmatrix} \mathbf{I}+\mathbf{S}_{11} & \mathbf{S}_{12} \\ \frac{\mathbf{n}}{\eta_1}(\mathbf{I}-\mathbf{S}_{11}) & -\frac{\mathbf{n}}{\eta_1}\mathbf{S}_{12} \end{pmatrix} \begin{pmatrix} \mathbf{S}_{21} & \mathbf{I}+\mathbf{S}_{22} \\ \frac{\mathbf{n}}{\eta_2}\mathbf{S}_{21} & \frac{\mathbf{n}}{\eta_2}(-\mathbf{I}+\mathbf{S}_{22}) \end{pmatrix}^{-1} \tag{9.23}$$

Alternatively, the S-parameters can be written in terms of the **ABCD** matrix by solving (9.22),

$$\begin{pmatrix} \mathbf{S}_{11} & \mathbf{S}_{12} \\ \mathbf{S}_{21} & \mathbf{S}_{22} \end{pmatrix} = \begin{pmatrix} -\mathbf{I} & \frac{\mathbf{Bn}}{\eta_2}+\mathbf{A} \\ \frac{\mathbf{n}}{\eta_1} & \frac{\mathbf{Dn}}{\eta_2}+\mathbf{C} \end{pmatrix}^{-1} \begin{pmatrix} \mathbf{I} & \frac{\mathbf{Bn}}{\eta_2}-\mathbf{A} \\ \frac{\mathbf{n}}{\eta_1} & \frac{\mathbf{Dn}}{\eta_2}-\mathbf{C} \end{pmatrix} \tag{9.24}$$

9.3.2 Finding and Realizing the Sheet Admittances

Analytically solving for the S-parameters of a given structure is straightforward. For example, the S-parameters of three cascaded sheet admittances can be found by inserting (9.21) into (9.24). However, we are looking to solve the inverse problem: stipulating the S-parameters and solving for the necessary sheet admittances. Since the necessary sheet admittances have not been solved analytically, a numerical solver was employed. The *fmincon* function provided by Matlab's optimization toolbox was used to perform a gradient descent method. The specific cost function that was minimized was $|S_{21}^{xx}-T^{xx}|^2+|S_{21}^{xy}-T^{xy}|^2+|S_{21}^{yx}-T^{yx}|^2+|S_{21}^{yy}-T^{yy}|^2$, where $\mathbf{S}_{21}$ is the transmission coefficient of the cascaded sheet admittances, and $\mathbf{T}$ is the desired transmission coefficient. Since this is a nonlinear problem, the gradient descent method may only return a local minimum rather than the global minimum, depending on the initial starting point. Nevertheless, the optimizer typically converged to the global minimum with less than 10 randomly seeded initial starting points. Once the required sheet admittances are known, their physical realization is straightforward using frequency-selective surface theory [57]. Typically, each sheet consists of patterned metal on a dielectric substrate. At optical frequencies, dielectric patterning also becomes an attractive option [55, 234].

9.4 Bianisotropic Metasurface Examples

To demonstrate the versatility of the design process, four devices exhibiting novel polarization transformations are presented: a polarization rotator, an asymmetric circular polarizer, an asymmetric linear polarizer, and a symmetric circular polarizer. Each structure requires significantly different constituent surface parameters.

It should be emphasized that the reported structures operate fundamentally different from devices that achieve polarization control through cascading Jones matrices. The structures reported here rely on the interference of multiple reflections between the sheets to achieve various phase discontinuities and novel polarization effects, while also maintaining a subwavelength profile. In contrast, simply cascading the Jones matrices of wave-plates and linear polarizers does not take advantage of the multiple reflections between sheets, and therefore the resulting devices are significantly bulkier [68].

9.4.1 Polarization Rotator at Microwave Frequencies

Chiral materials with a strong rotary power are commonly used in analytical chemistry, biology, and crystallography for identifying the spatial structure of molecules [235]. Chirality can also provide an alternative route to achieve negative refraction [236]. A particularly interesting structure that exhibits a strong chiral response is the polarization rotator, which rotates an incident linear polarization by 90° upon transmission. Previously, polarization rotation was accomplished with an isotropic helical structure [170]. However, the three-dimensional geometry requires metallized via holes, which become prohibitively difficult to fabricate at higher frequencies, especially optical frequencies. In addition, the structure exhibited a large insertion loss (S_{21}=-5 dB) at the 10 GHz operating frequency. Alternatively, bilayered metamaterials that utilize two sheet admittances (patterned metallic surfaces) separated by an electrically thin dielectric can also act as polarization rotators [66, 235]. These works demonstrated that complex helical patterns are not required to achieve significant chirality. In [235], it was shown that such bilayered metamaterials can have orders of magnitude larger rotary powers than naturally occurring gyrotropic crystals in the visible spectrum. The rotary power was later increased by optimizing the patterns on each sheet [66]. However, the design process was not straightforward, which led to a narrow bandwidth and low transmission coefficient (-5 dB) at the operating frequency. Here, a systematic method for designing polarization rotators is presented, resulting in optimal performance.

A polarization rotator with a reflection coefficient equal to zero and transmission coefficient equal to,

$$\mathbf{S}_{21} = e^{j\phi} \begin{pmatrix} 0 & -1 \\ 1 & 0 \end{pmatrix} \tag{9.25}$$

is considered [66, 170]. In other words, any linearly-polarized incident plane wave

traveling in the $+z$ direction will undergo a clockwise polarization rotation of 90° upon transmission, when viewed from Region 1. By inserting (9.25) into (9.13), the ideal constituent parameters of such a device are,

$$\mathbf{\Lambda} = \begin{pmatrix} \frac{-2j\,\tan(\phi)}{\eta_\circ} & 0 & -2\,\sec(\phi) & 0 \\ 0 & \frac{-2j\,\tan(\phi)}{\eta_\circ} & 0 & -2\,\sec(\phi) \\ 2\,\sec(\phi) & 0 & -2j\eta_\circ\,\tan(\phi) & 0 \\ 0 & 2\,\sec(\phi) & 0 & -2j\eta_\circ\,\tan(\phi) \end{pmatrix} \tag{9.26}$$

The metasurface is isotropic and chiral.

When realizing polarization transformations, the absolute phase delay (ϕ) generated by the metasurface is typically not important for most applications. Therefore, the phase delay can be viewed as a free parameter that can be adjusted to increase the bandwidth and reduce the loss of the metasurface.

The polarization rotator considered here consists of four patterned metallic sheets. The fourth sheet allows added bandwidth. To analyze this structure, (9.21) is modified to account for the fourth sheet,

$$\begin{aligned} \begin{pmatrix} \mathbf{A} & \mathbf{B} \\ \mathbf{C} & \mathbf{D} \end{pmatrix} = \Bigg[& \begin{pmatrix} \mathbf{I} & \mathbf{0} \\ \mathbf{n}\mathbf{Y}_{s1} & \mathbf{I} \end{pmatrix} \begin{pmatrix} \cos(\beta d_1)\mathbf{I} & -j\sin(\beta d_1)\eta_d\mathbf{n} \\ j\sin(\beta d_1)\eta_d^{-1}\mathbf{n} & \cos(\beta d_1)\mathbf{I} \end{pmatrix} \\ \cdot & \begin{pmatrix} \mathbf{I} & \mathbf{0} \\ \mathbf{n}\mathbf{Y}_{s2} & \mathbf{I} \end{pmatrix} \begin{pmatrix} \cos(\beta d_2)\mathbf{I} & -j\sin(\beta d_2)\eta_d\mathbf{n} \\ j\sin(\beta d_2)\eta_d^{-1}\mathbf{n} & \cos(\beta d_2)\mathbf{I} \end{pmatrix} \begin{pmatrix} \mathbf{I} & \mathbf{0} \\ \mathbf{n}\mathbf{Y}_{s3} & \mathbf{I} \end{pmatrix} \\ & \begin{pmatrix} \cos(\beta d_1)\mathbf{I} & -j\sin(\beta d_1)\eta_d\mathbf{n} \\ j\sin(\beta d_1)\eta_d^{-1}\mathbf{n} & \cos(\beta d_1)\mathbf{I} \end{pmatrix} \begin{pmatrix} \mathbf{I} & \mathbf{0} \\ \mathbf{n}\mathbf{Y}_{s4} & \mathbf{I} \end{pmatrix} \Bigg] \end{aligned} \tag{9.27}$$

It should be noted that due to the adhesive layers used in fabrication, the middle dielectric spacer (d_2) is a different thickness than the outer dielectric spacers (d_1).

The necessary cascaded sheet admittances that realize a polarization rotator are numerically found by inserting (9.25) into (9.24), and combining the result with (9.27). If the operating frequency equals 10 GHz, $\phi = -40°$, $\eta_1 = \eta_2 = \eta_\circ$, $\eta_d = \eta_\circ/1.88$, $\beta d_1 = 2\pi/10.48$, and $\beta d_2 = 2\pi/9.54$, the required sheet admittances are $\mathbf{Y}_{s1} = \frac{j}{\eta_\circ}\begin{pmatrix} 0.92 & -1.39 \\ -1.39 & 2.14 \end{pmatrix}$, $\mathbf{Y}_{s2} = \frac{j}{\eta_\circ}\begin{pmatrix} 5.21 & -8.07 \\ -8.07 & 5.21 \end{pmatrix}$, $\mathbf{Y}_{s3} = \frac{j}{\eta_\circ}\begin{pmatrix} 7.88 & -1.17 \\ -1.17 & 2.50 \end{pmatrix}$, and $\mathbf{Y}_{s4} = \frac{j}{\eta_\circ}\begin{pmatrix} 5.67 & 0 \\ 0 & -2.63 \end{pmatrix}$. It was found that a transmitted phase of $\phi = -40°$ maximized the bandwidth.

The metallic patterns that realize the desired sheet admittances of the polarization rotator are shown in Fig. 9.3. Each sheet has a periodicity of 3.7 mm x 3.7 mm ($\lambda_\circ/8.11$ x $\lambda_\circ/8.11$). It can be seen that the sheet admittance of the first sheet ($\mathbf{Y}_{s1}$) has a small capacitance along $0.838\hat{x}+0.545\hat{y}$ and a larger capacitance along $0.547\hat{x}-0.837\hat{y}$, which are its principle axes. The large capacitance along the $0.547\hat{x}-0.837\hat{y}$ direction is realized with interdigitated capacitors. For the second sheet ($\mathbf{Y}_{s2}$), the sheet admittance is inductive along the $(\hat{x}+\hat{y})/\sqrt{2}$ direction and capacitive along the $(\hat{x}-\hat{y})/\sqrt{2}$ direction. For the third sheet ($\mathbf{Y}_{s3}$), the sheet admittance is capacitive along both principle axes, $0.204\hat{x}+0.979\hat{y}$ and $0.979\hat{x}-0.205\hat{y}$. The fourth sheet is similar to the second in that it is inductive along one principle axis ($\hat{y}$) and capacitive along the other ($\hat{x}$).

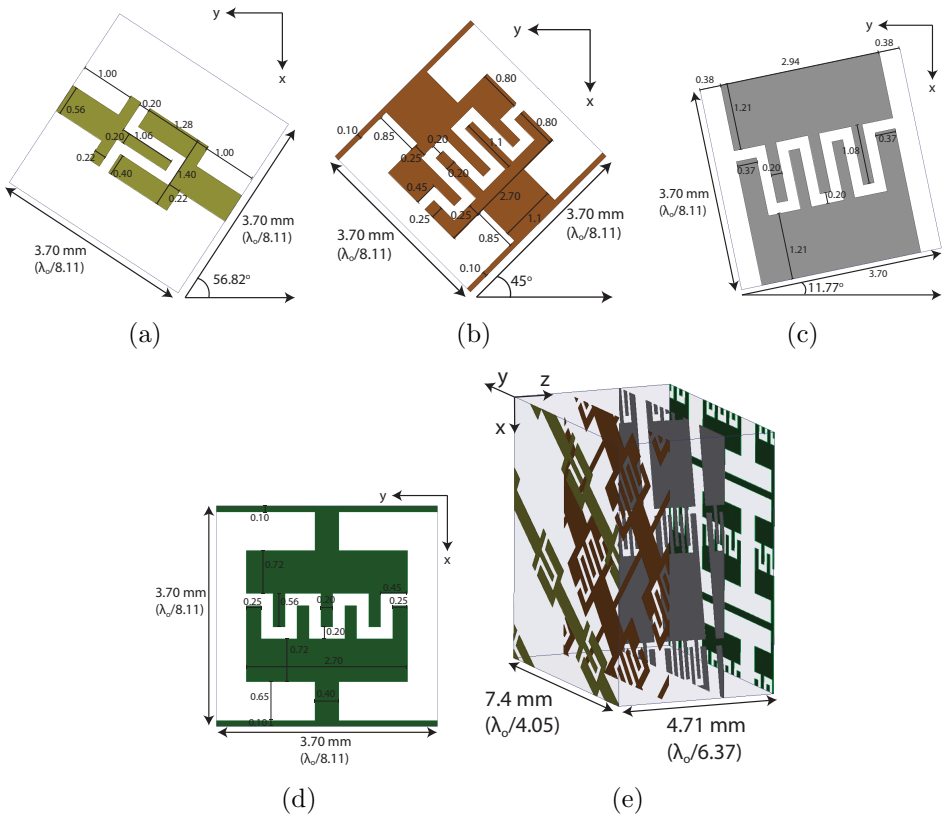

Figure 9.3: Dimensions of the polarization rotator. **(a)-(d)** Dimensions (mm) of the first, second, third, and fourth sheets, respectively. **(e)** Perspective view of a section of the polarization rotator.

The bianisotropic metasurface was fabricated by patterning four metallic sheets on 1.52 mm thick, Rogers 4003 substrates ($\epsilon_r = 3.55$, $\tan\delta = 0.0027$). A section of the developed polarization rotator is shown in Fig. 9.4(a), while the bottom sheet of the fabricated structure is shown in Fig. 9.4(b). The simulated and measured perfor-

mance is shown in Fig. 9.4(c). There is a 2% frequency shift between measurement and simulation due to fabrication tolerances. For comparison purposes, a 0.2 GHz frequency shift was added to the measured data in Fig. 9.4(c).

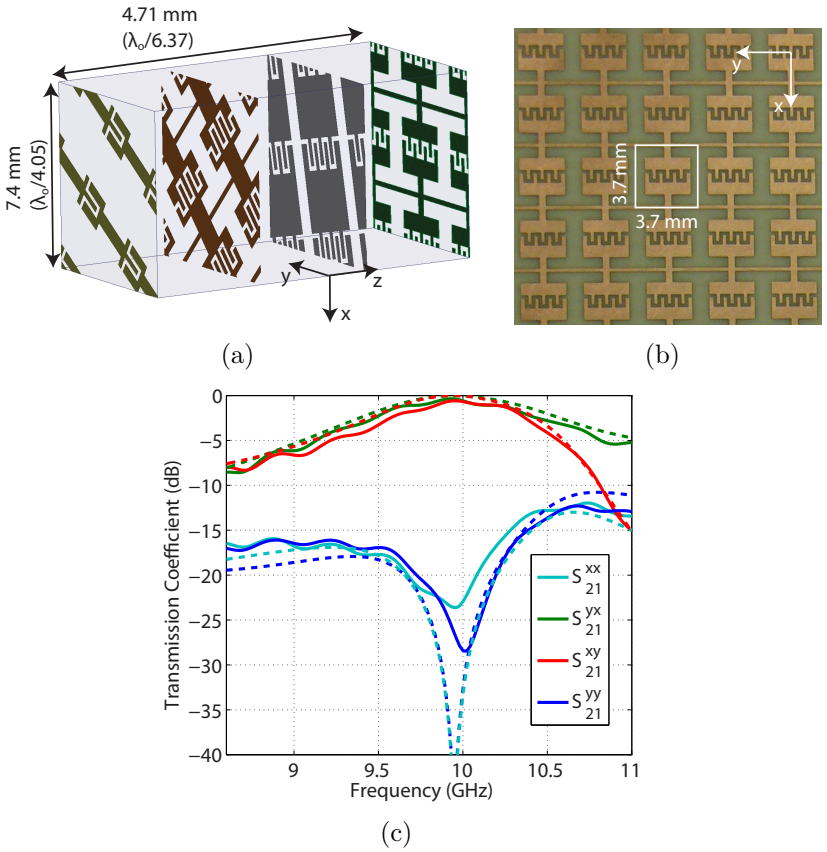

Figure 9.4: Metasurface exhibiting polarization rotation near 10 GHz. **(a)** Schematic of the unit cell. For clarity, the z-axis is scaled by a factor of 3 so that all four sheets are visible. **(b)** Bottom sheet ($\mathbf{Y}_{s4}$) of the fabricated polarization rotator. **(c)** Transmission coefficient for an incident plane wave traveling in the $+z$ direction. Measured data is denoted by solid lines, whereas simulated is denoted by dashed lines. For clarity, the measured data is frequency shifted by +0.20 GHz in the plot.

It is also important to note that (9.26) dictates that a polarization rotator must be isotropic. The isotropic response of the fabricated structure was verified by rotating the incident linear polarization by an angle θ about the z-axis. As shown in Figs. 9.5 (a)-(d) and Fig. 9.6, the cross-polarized transmission is near 0 dB and co-polarized transmission is near or below -20 dB, for all angles θ around 10 GHz. A slight frequency shift of 2% can be seen between the measured (Figs. 9.5 (a) and (c)) and simulated (Figs. 9.5 (b) and (d)) transmission coefficients. This is in contrast to the more common half-wave plate, which only achieves high cross-polarization (rotated

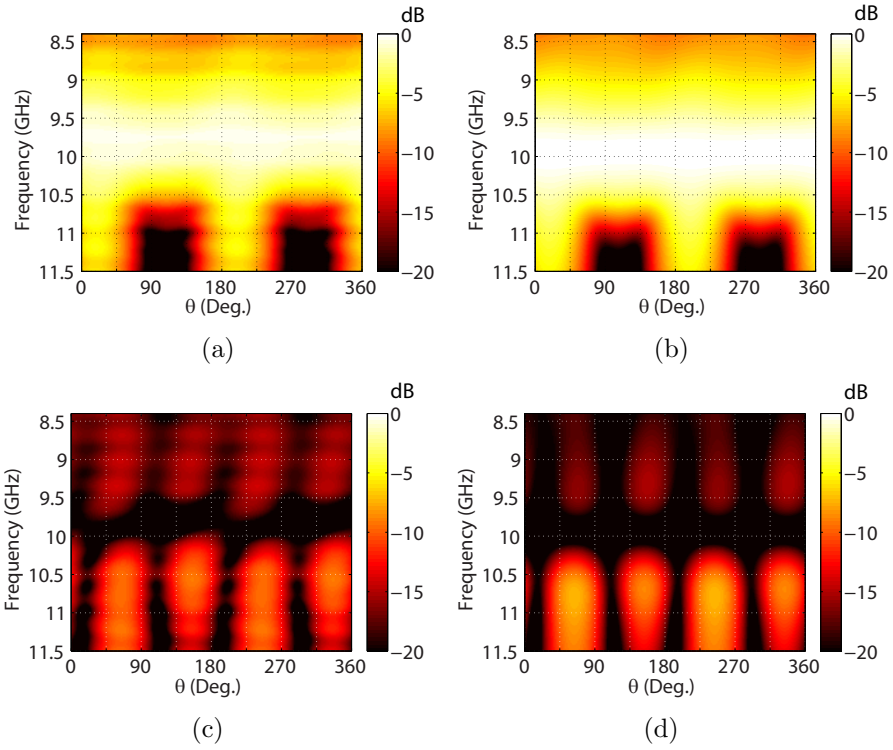

Figure 9.5: Additional performance metrics of the polarization rotator. **(a)** Measured cross-polarized transmission (S_{21}^{yx}) as a function of frequency and input linear polarization. The angle θ refers to the angle between the x and y axes of the input linear polarization. **(b)** Simulated cross-polarized transmission (S_{21}^{yx}) as a function of frequency and input linear polarization. It can be seen that the cross-polarized transmission coefficient is near 0 dB, independent of θ. **(c)** Measured co-polarized transmission (S_{21}^{xx}) as a function of frequency and input linear polarization. **(d)** Simulated co-polarized transmission (S_{21}^{xx}) as a function of frequency and input linear polarization.

field) when the incident field is polarized 45° relative to its crystal axis. The fractional bandwidth of this structure was measured to be 8.7%. The bandwidth is defined as the frequency range over which the cross-polarized transmission coefficient is greater than -3 dB and a co-polarized transmission coefficient is less than -10 dB, independent of the incident linear polarization. The simulated metasurface is well matched at the operating frequency, as shown in Fig. 9.7.

It should be noted that the polarization rotator is the only structure presented here that utilizes four patterned sheets. Initially, three sheets were used to realize a polarization rotator. However, the simulated bandwidth was narrow (0.6%) and the loss was high (S_{21}=-1.7 dB). This led to a structure that was extremely sensitive to fabrication tolerances. Therefore, a fourth layer was added to provide additional

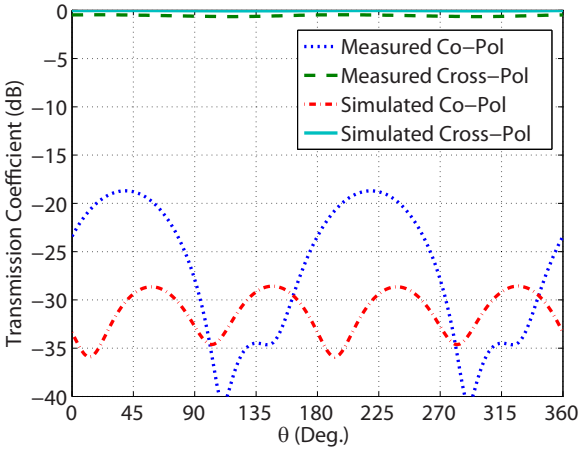

Figure 9.6: Co-polarized and cross-polarized transmission as a function of the input linear polarization at the measured (9.78 GHz) and simulated (10.00 GHz) operating frequencies.

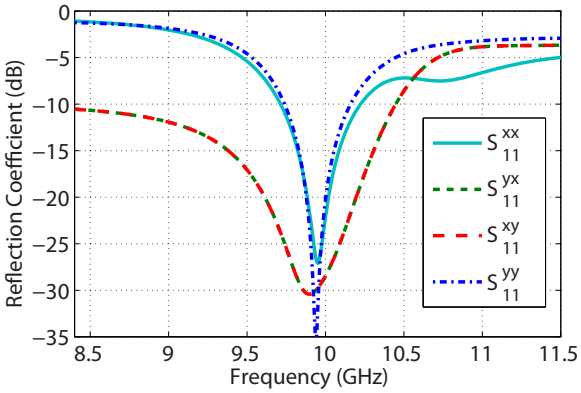

Figure 9.7: Simulated reflection coefficient of the polarization rotator.

degrees of freedom that were exploited to increase bandwidth and reduce loss.

Unlike the other metasurfaces presented here, the sheet admittances comprising the polarization rotator are not periodic with respect to a single coordinate system. Thus Fig. 9.4(a) is not a unit cell of the structure, but rather a section of the structure. Since the polarization rotator cannot be discretized into a single unit cell, its performance cannot be verified using a full-wave simulation with periodic boundary conditions [237]. Instead, the simulated responses shown in Fig. 9.5 is found by simulating each sheet admittance individually, and calculating the overall cascaded response analytically. Specifically, each sheet admittance is extracted from full wave simulations, and their values are inserted into (9.27) to find the overall **ABCD** matrix of the entire structure. The S-parameters are then evaluated by inserting the **ABCD** matrix into (9.24). In contrast, all the other structures presented here (e.g. asymmet-

ric circular polarizer, asymmetric linear polarizer, symmetric circular polarizer) can be discretized into periodic unit cells, and their performances were simulated using Ansys HFSS.

The constituent surface parameters of the polarization rotator can be determined from simulation by inserting the S-parameters of the structure into (9.13). They are shown in Fig. 9.8. The plot shows that at the operating frequency of 10 GHz, $Y_{xy}\eta_\circ = Z_{xy}/\eta_\circ = 2$, and $\chi_{xy} = \chi_{yx} = -2.8$. In addition, all the off diagonal constituent parameters are zero (e.g. $Y_{xy} = Z_{xy} = \chi_{xy} = \chi_{yx} = 0$). This is consistent with the ideal values of the constituent surface parameters (Eq. (9.26)) when $\phi = -45°$. The terms leading to loss (Re($\mathbf{Y}$), Re($\mathbf{Z}$), Im($\boldsymbol{\chi}$)) are low and are not plotted. All other terms that are not plotted can be inferred from the fact that the structure is reciprocal.

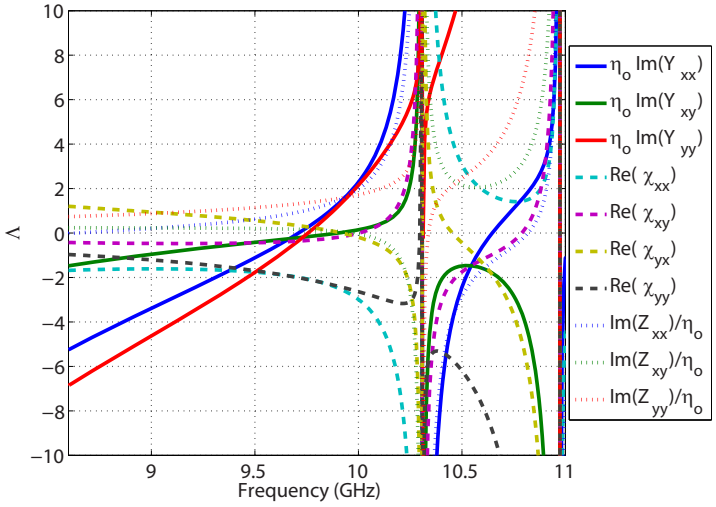

Figure 9.8: Constituent surface parameters of the simulated polarization rotator. The terms leading to loss (Re($\mathbf{Y}$), Re($\mathbf{Z}$), Im($\boldsymbol{\chi}$)) are low and are not plotted. All other terms that are not plotted can be inferred by noting that the structure is reciprocal.

9.4.2 Asymmetric Circular Polarizer at mm-wave Frequencies

Additional control over the constituent surface parameters is demonstrated with a metasurface that provides asymmetric transmission for circularly polarized waves at millimeter-wave frequencies. This effect exhibits some similarity to Faraday rotation, but requires no magnetic field or nonreciprocal materials [65]. It should be emphasized that this structure is reciprocal. In addition, this metasurface acts as a circular polarizer since it transmits circular polarization of one handedness and reflects the

other. Demonstrating this effect at millimeter-wave frequencies is particularly useful for a number of reasons. Millimeter wavelengths are long enough to easily propagate through visibly opaque media, while short enough to realize large operating bandwidths and millimeter resolution [52]. This enables high resolution radar and imaging systems, as well as high bandwidth communication. In particular, 77 GHz is relevant to automotive radar systems [238].

To date, the most common method to realize asymmetric circular transmission is with a purely electric response: printing two-dimensional chiral patterns on a single sheet [65]. In such a scheme, the asymmetric response is significant only when the eigenvectors of the sheet admittance are complex, which requires high loss. Therefore, the efficiency of these structures is fundamentally limited. The asymmetric response is often defined as the difference between the transmittance of a given handedness of circular polarization, propagating in the $+z$ and $-z$ directions. It is typically low for single sheets geometries (not exceeding 0.25) [226]. Alternatively, it was recently shown that a bi-layered metasurface realized by cascading two-dimensional chiral patterns can achieve a larger asymmetric response of 0.6 [226]. However, the design procedure and physical description were vague, and the transmittance and asymmetric response were still too low for most applications. In contrast, the metasurface presented here achieves a near-optimal asymmetric response of 0.99 at the design frequency. In addition, a thorough analysis and systematic design procedure is outlined.

The metasurface converts right-handed-circular to left-handed-circular when traveling in the $+z$ direction. It exhibits the following transmission coefficient,

$$\mathbf{S}_{21} = \frac{e^{j\phi}}{2}\begin{pmatrix} 1 & j \\ j & -1 \end{pmatrix} \tag{9.28}$$

However, when propagating in the $-z$ direction, the same metasurface converts left-handed-circular to right-handed-circular. Therefore it exhibits asymmetric transmission for circularly polarized waves. It should be noted that this does not violate reciprocity since $\mathbf{S}_{21} = \mathbf{S}_{12}^T$. Hence, the performance of the structure can be analyzed by only considering plane waves incident from Region 1. The constituent surface

parameters of the metasurface are given by,

$$\mathbf{\Lambda} = \begin{pmatrix} \frac{-2j\,\tan(\phi/2)}{\eta_\circ} & 0 & 0 & 0 \\ 0 & \frac{2j\,\cot(\phi/2)}{\eta_\circ} & 0 & 0 \\ 0 & 0 & -2j\eta_\circ\,\tan(\phi) & 2j\eta_\circ\,\sec(\phi) \\ 0 & 0 & 2j\eta_\circ\,\sec(\phi) & -2j\eta_\circ\,\tan(\phi) \end{pmatrix} \tag{9.29}$$

As was previously noted, asymmetric transmission does not require three-dimensional chirality ($\boldsymbol{\chi} = \boldsymbol{\Upsilon} = 0$) [65,67]. However, the principle axes of the electric and magnetic responses should be rotated with respect to each other since $Y_{xy} = 0$ and $Z_{xy} \neq 0$.

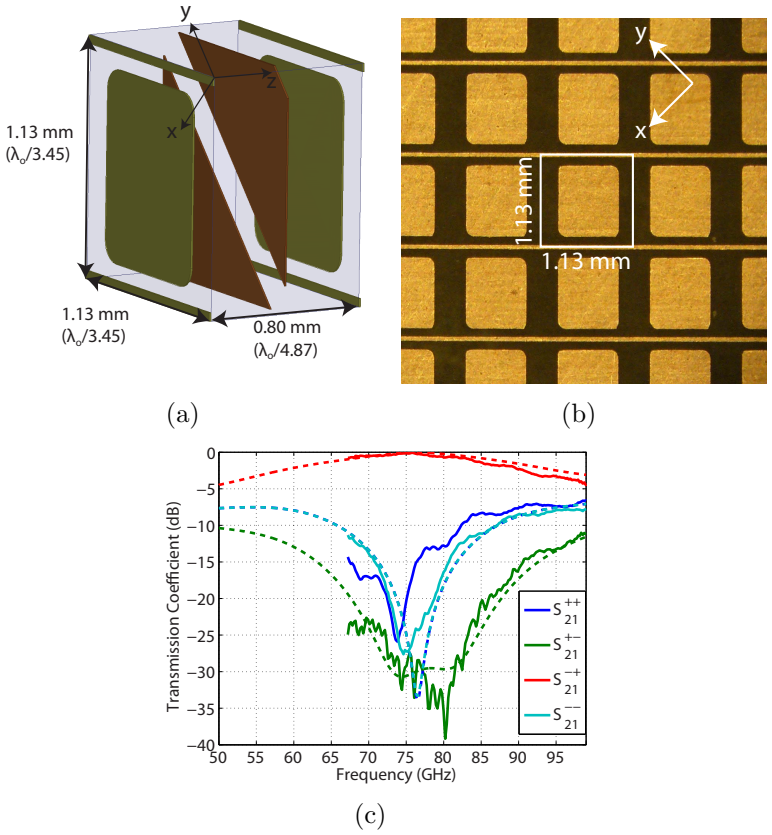

Figure 9.9: Metasurface exhibiting asymmetric circular transmission at millimeter-wave frequencies. **(a)** Schematic of the unit cell. **(b)** Top sheet ($\mathbf{Y}_{s1}$) of the fabricated asymmetric circular polarizer. **(c)** Transmission coefficient for an incident plane wave traveling in the $+z$ direction, where the superscript '+' denotes right-handed-circular and '-' denotes left-handed-circular. Measured data is denoted by solid lines, whereas simulated is denoted by dashed lines.

The asymmetric circular polarizer has the following properties: $\phi = 175°$, $\beta d = 2\pi/6.37$, $\eta_d = \eta_\circ/1.483$, and $\eta_1 = \eta_2 = \eta_\circ$. The necessary sheet admittances were then

numerically solved for, $\mathbf{Y}_{s1} = \frac{j}{\eta_\circ}\begin{pmatrix} 1.01 & -1.00 \\ -1.00 & 1.01 \end{pmatrix}$, $\mathbf{Y}_{s2} = \frac{j}{\eta_\circ}\begin{pmatrix} 2.19 & 0 \\ 0 & -200 \end{pmatrix}$, and $\mathbf{Y}_{s3} = \frac{j}{\eta_\circ}\begin{pmatrix} 1.01 & -1.00 \\ -1.00 & 1.01 \end{pmatrix}$. To realize the sheet admittances, copper was patterned on 380 μm thick, Rogers 5880 Duroid substrates ($\epsilon_r = 2.2$, $\tan\delta = 0.0009$). For an operating frequency of 77 GHz, the designed unit cell is shown in Fig. 9.9(a), while the top sheet of the fabricated structure is shown in Fig. 9.9(b). The simulated and measured transmission coefficients are shown in Fig. 9.9(c). The surface exhibits near perfect conversion of right-handed-circular into left handed circular when propagating in the $+z$ direction. In addition the measured asymmetric response is broadband: S_{21}^{++}, S_{21}^{+-}, and S_{21}^{--} are below -10 dB, and S_{21}^{-+} is above -0.8 dB, over a bandwidth of 20%. The superscript '+' denotes right-handed-circular polarization and '-' denotes left-handed-circular polarization.

The detailed metallic patterns of the sheets comprising the asymmetric circular polarizer are shown in Fig. 9.10. The structure is reflection symmetric along the $z = 0$ plane ($\mathbf{Y}_{s1} = \mathbf{Y}_{s3}$), which causes all magnetoelectric coupling terms to reduce to zero [67]. All three sheets are capacitive along one principle axis and inductive along the other. It should be noted that although the second sheet looks very similar to a wire grid polarizer, there are important differences. Wire grid polarizers are generally designed to minimize the inductance along the y axis, while also minimizing the capacitance along the x axis to provide high reflection and transmission, respectively. Here, the cell size and patterned copper are chosen to realize a specific capacitance ($Y_{s2}^{xx} = 2.19j/\eta_\circ$) along the x axis, in order to achieve an optimal performance at the design frequency.

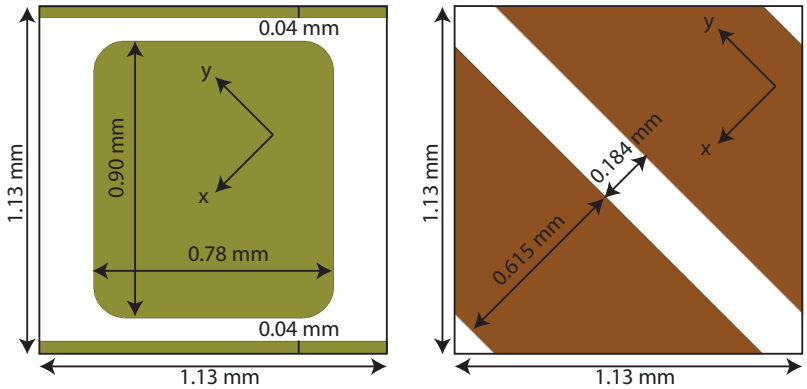

Figure 9.10: Dimensions of the asymmetric circular polarizer. **(a)** Dimensions of the first and third sheets. **(b)** Dimensions of the second sheet.

It should be noted that the constituent surface parameters of the ideal asymmetric circular polarizer (Eq. (9.29)) are a function of the stipulated reflection coefficients in addition to the transmission coefficient. Eq. (9.29) assumes the reflection coefficients are equal to,

$$\mathbf{S}_{11} = \mathbf{S}_{22} = \frac{e^{j\phi}}{2}\begin{pmatrix} 1 & -j \\ -j & -1 \end{pmatrix} \tag{9.30}$$

In other words, when left-handed-circular is incident in the $+z$ direction, all of the power is reflected to left-handed-circular [68]. Similarly, when right-handed-circular is incident in the $-z$ direction, all of the power is reflected to right-handed-circular.

As was mentioned, when left-handed-circular is incident in the $+z$ direction, all of the power is ideally reflected to left-handed-circular [68]. Similarly, when right-handed-circular is incident in the $-z$ direction, all of the power is reflected to right-handed-circular. The reflection coefficients of the simulated asymmetric circular polarizer are shown in Fig. 9.11.

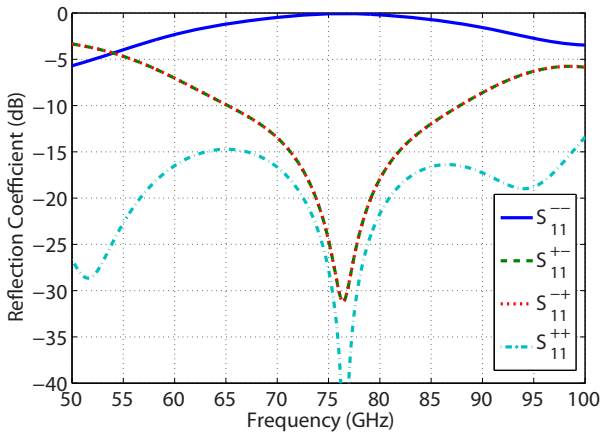

Figure 9.11: Reflection coefficient of the asymmetric circular polarizer.

The constituent parameters of the asymmetric circular polarizer are shown in Fig. 9.12. It can be seen that all magnetoelectric coupling terms are zero since the structure is reflection symmetric about the $z = 0$ plane. At the design frequency of 77 GHz, the principle axes of the electric susceptibility are aligned along the $\hat{x}$ and $\hat{y}$ axes since $Y_{xy} = 0$, and the principle axes of the magnetic susceptibility are aligned along $(\hat{x} + \hat{y})/\sqrt{2}$ and $(\hat{x} - \hat{y})/\sqrt{2}$, since $Z_{xx} = Z_{yy}$ and $Z_{xy} \neq 0$. In other words, the principle axes of the electric and magnetic response are rotated by 45° from each other to achieve an optimal performance. It should be noted that, some degree of asymmetric transmission is present whenever the principle axes of the electric and magnetic susceptibilities are not aligned. This can be shown using (9.11).

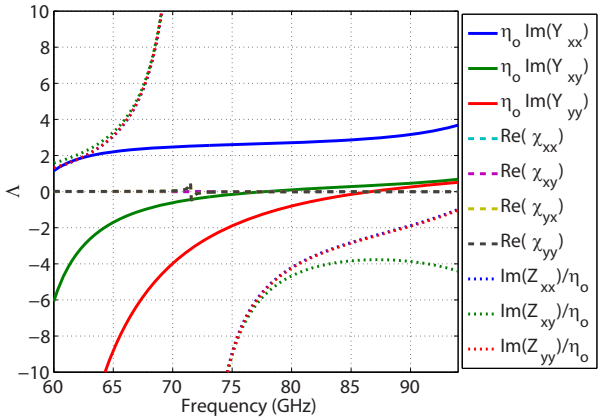

Figure 9.12: Constituent surface parameters of the simulated asymmetric circular polarizer. The terms leading to loss (Re($\mathbf{Y}$), Re($\mathbf{Z}$), Im($\boldsymbol{\chi}$)) are low and are not plotted. All other terms that are not plotted can be inferred by noting that the structure is reciprocal.

9.4.3 Asymmetric Circular Polarizer at Optical Frequencies

Next we demonstrate that the asymmetric circular polarizer can be scaled to optical frequencies. The designed unit cell is shown in Figure 9.13, while exact dimensions are shown in Fig. 9.14

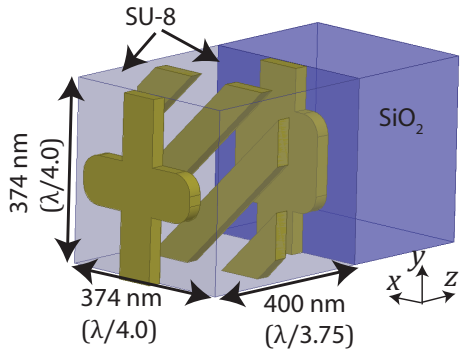

Figure 9.13: Perspective view of the designed asymmetric circular polarizer that operates at optical frequencies.

As in the previous chapter, the SiO_2 substrate is modeled as a lossless, infinite half space with an index of refraction of $n_{SiO_2} = 1.45$. The index of refraction of the SU-8 is $n_{\text{SU-8}} = 1.57$. The relative permittivity of Au at near-infrared wavelengths is described by the Drude model $\epsilon_{\text{Au}} = \epsilon_\infty - \omega_p^2/(\omega^2 + j\omega\omega_c)$, with $\epsilon_\infty = 9.0$, the plasma frequency is $\omega_p = 1.363\text{x}10^{16}$ rad/s (8.97 eV), and the collision frequency is $\omega_c = 3.60\text{x}10^{14}$ rad/s (0.24 eV). This collision frequency assumes a loss that is over

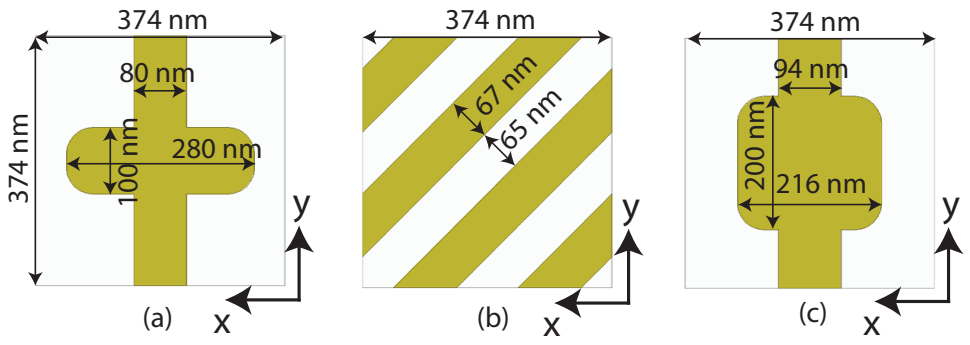

Figure 9.14: Designed dimensions of the first, second, and third sheets.

three times that of bulk Au [239], to take into account thin film surface scattering and grain boundary effects [221].

At the design wavelength of 1.5 μm, the metallic patterns shown in Figure 9.13 realize simulated sheet admittances of $\mathbf{Y}_{s1} = \frac{1}{\eta_\circ}\begin{pmatrix} 0.24+1.36j & 0 \\ 0 & 0.36-1.85j \end{pmatrix}$, $\mathbf{Y}_{s2} = \frac{1}{\eta_\circ}\begin{pmatrix} 1.01-2.87j & -0.98+3.67j \\ -0.98+3.67j & 1.01-2.87j \end{pmatrix}$, and $\mathbf{Y}_{s3} = \frac{1}{\eta_\circ}\begin{pmatrix} 0.17+1.67j & 0 \\ 0 & 0.54-2.28j \end{pmatrix}$, for the first, second, and third patterned Au sheets, respectively. All three sheets are inductive along one principle axis and capacitive along the orthogonal axis. In other words, each sheet has a continuous metallic trace along one principle axis and small gaps along the orthogonal axis. Using full-wave electromagnetic simulations, the width of each metallic trace and the size of the gap were designed such that the inductance and capacitance approached the ideal values that were numerically computed using the analytic model. It should be noted that if material losses are neglected, the sheet admittances are purely imaginary. In this lossless case, the structure can provide 100% polarization conversion from RHCP to LHCP [240]. However, all metals exhibit loss at near-infrared wavelengths. This causes the sheet admittances to become complex, where the real part represents absorption in the metal. The loss reduced the efficiency of the metasurface to 53%.

The metasurface was fabricated by Cheng Zhang in L. Jay Guo's research group at the University of Michigan [241]. The metasurface is fabricated on a 500 μm thick fused silica substrate using the process shown in Figure 9.15(a) [12, 222]. First, the bottom sheet admittance ($\mathbf{Y}_{s3}$) is fabricated by patterning a 2 nm Ti adhesion layer and 28 nm Au layer using electron beam lithography and liftoff. Next, a 200 nm thick, SU-8 dielectric layer is spin coated onto the wafer, which naturally planarizes the surface for the following layer. This process is repeated until three Au layers

are patterned to achieve the unit cell shown in Figure 9.13. The patterned area is 250 μm x 250 μm. Scanning electron microscope (SEM) pictures of the three Au layers comprising the fabricated metasurface are shown in Figures 9.15(b)-(d). In the future, large area soft lithography processes, such as nanoimprint lithography, can be employed to dramatically reduce the fabrication cost [242].

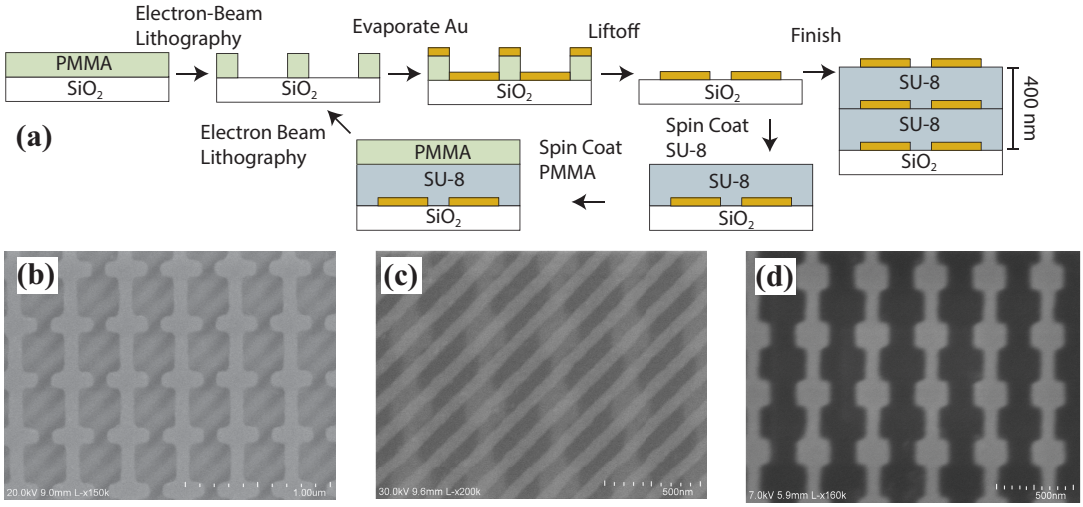

Figure 9.15: Fabrication of the asymmetric circular polarizer. **(a)** Fabrication process involves sequential patterning of each 2 nm/28 nm thick Ti/Au layer using electron-beam lithography and liftoff, followed by spin coating of a 200 nm thick SU-8 dielectric layer. Three metallic layers are patterned using the process, resulting in an overall thickness of 430 nm. **(b)** Scanning electron microscope (SEM) picture of the first Au sheet ($\mathbf{Y}_{s1}$). The second sheet can be seen below the first, although it is less clear. **(c)** SEM picture of the second Au sheet ($\mathbf{Y}_{s2}$). The third sheet can be seen below it. **(d)** SEM picture of the third Au sheet ($\mathbf{Y}_{s3}$).

Following fabrication, the metasurface was experimentally characterized. The output of a 1.5 μm tunable laser (Newport TLB 6326) was sent through a linear polarizer, followed by a quarter-wave plate, and then focused upon the metasurface. The transmitted power was collected by another quarter-wave plate, followed by a linear polarizer, and then received by a power meter. Rotating the quarter-wave plates allowed for characterization of the metasurfaces Jones matrix. The measured and simulated transmittance is plotted in Figure 9.16, and show close agreement. At the operating wavelength of 1.5 μm, the fabricated metasurface provides a high transmittance of 50% for left-handed-circular polarization when right-handed-circular polarization is incident. In addition, all other elements of the Jones matrix in the circular polarization basis are below 2.5%, which suggests an extinction ratio of 20:1.

The extinction ratio is defined as the ratio of transmittance from RHCP to LHCP (S_{21}^{-+}) relative to the maximum transmittance of RHCP to RHCP (S_{21}^{++}), LHCP to LHCP (S_{21}^{--}), and LHCP to RHCP (S_{21}^{+-}). These experimental results represent an order of magnitude improvement in the extinction ratio over the state-of-the-art optical structures providing asymmetric transmission for both linear and circular polarizations [243–246]. This extinction ratio is comparable to that of the Au helix metamaterial, which acts as a symmetric circular polarizer [247]. However, the Au helix operates at longer wavelengths (3.5 μm to 7.5 μm), requires a complex fabrication process (3D laser writing and gold plating), and its design cannot be extended to alternative polarization controlling devices. In contrast, the design and fabrication procedures presented here can realize a large range of bianisotropic metasurfaces such as symmetric circular polarizers, polarization rotators, and asymmetric linear polarizers by simply fabricating different metallic patterns [240].

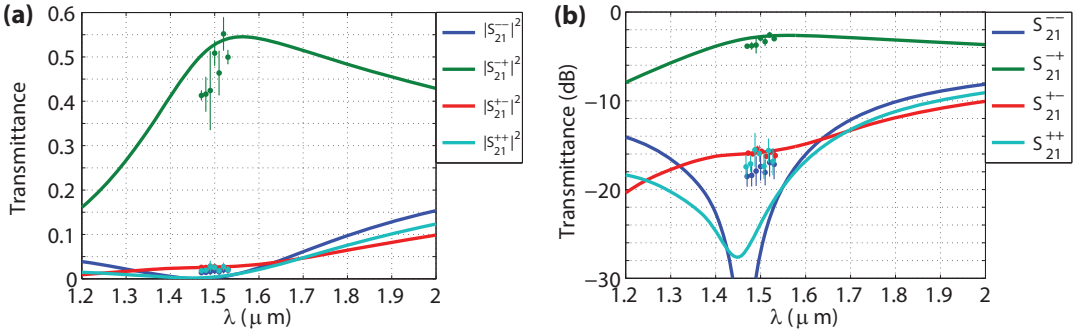

Figure 9.16: Measured and simulated Jones matrix of the metasurface on linear **(a)** and logarithmic **(b)** scales. Solid lines correspond to simulation whereas circles correspond to measurements. Error bars denote one standard deviation in the measured data. It can be seen that the metasurface provides high transmission of 50% for the left-handed-circular when right-handed-circular is incident. In addition, all other elements of the Jones matrix in the circular polarization basis are below 2.5% at the operating wavelength of 1.5 μm.

Figure 9.16 shows that the simulated response is quite broadband. However, the bandwidth of the available laser source limited measurements to the wavelength range of 1.47 μm to 1.53 μm. Simulations indicate that when right-handed-circular is incident, 37% of the power is absorbed in the Au patterns while 10% is reflected, thus resulting in a 53% efficiency (see. Figure 9.17). Alternatively, when left-handed-circular is incident, 37% of the power is absorbed and 60% of the power is reflected.

The metasurface also has a robust angular tolerance due to the subwavelength cell

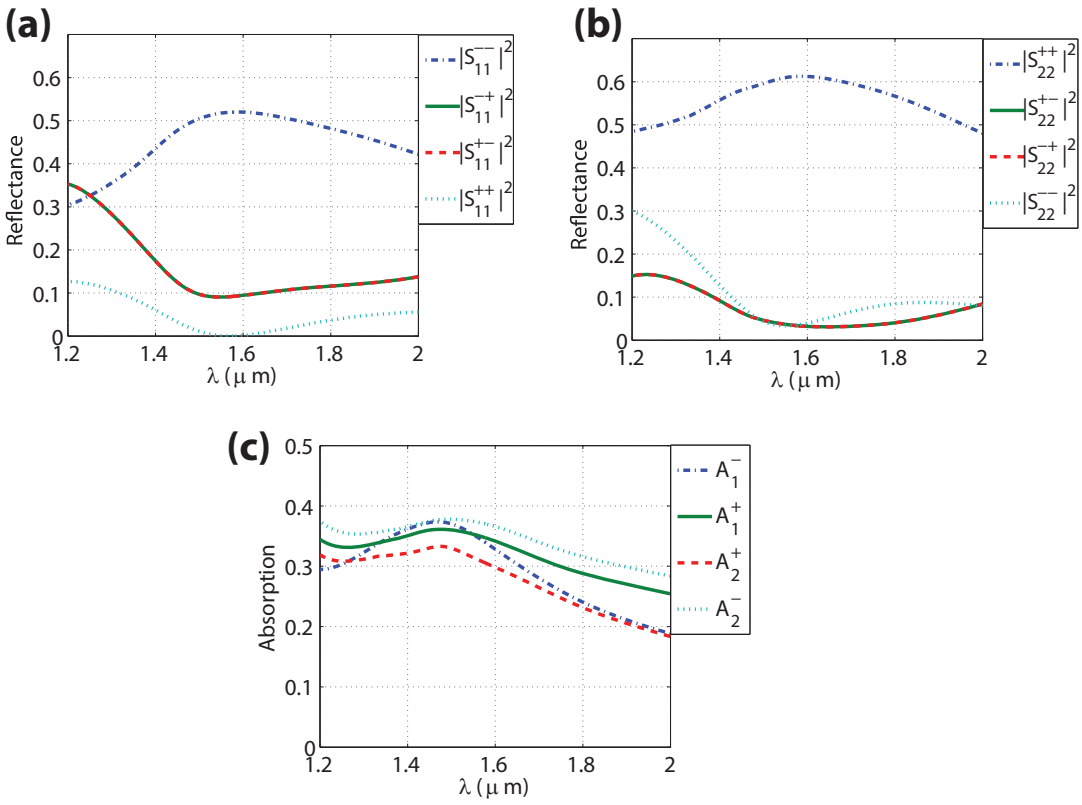

Figure 9.17: **(a),(b)** Simulated reflection coefficients from Regions 1 and 2, respectively. **(c)** Simulated dissipation in the Au patterns when left and right handed circular polarization is incident from Region 1 ($A_1^{(-,+)}$) and Region 2 ($A_2^{(-,+)}$), respectively.

size, as shown in Figure 9.18 [35]. Only when the incident angle exceeds 40° does the performance begin to deteriorate, which is useful for many applications [248, 249]. It should also be noted that the angle of incidence is always identical to the angle of the transmitted wave for periodic metasurfaces with cell sizes less than $\lambda/2$, as is the case here.

9.4.4 Asymmetric linear polarizer at mm-wave frequencies

Asymmetric transmission for linearly-polarized waves requires geometries that do not exhibit mirror or rotational symmetry [67]. These metasurfaces can be used to increase the polarization diversity of microwave and optical devices. Previously, devices exhibiting asymmetric linear transmission were realized with two and three layered chiral meta-atoms [245, 246, 250] or asymmetric helical geometries [228]. Although a near-optimal polarization purity was achieved, the response was narrowband [246]. A more straightforward design procedure based on Fabry-Perot resonances was re-

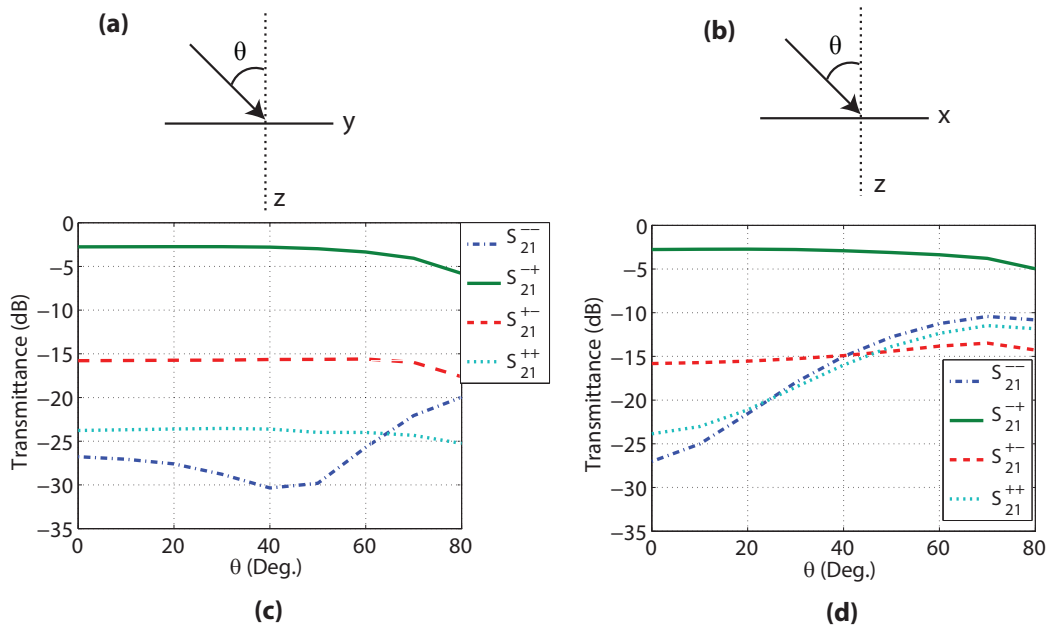

Figure 9.18: **(a),(b)** An incident plane wave impinges upon the metasurface at various angles of θ along the yz and xz planes, respectively. **(c),(d)** Simulated transmittance of the metasurface at the operating wavelength of 1.5 μm at various angles of θ along the yz and xz planes, respectively.

ported in [45]. This approach led to an enhanced bandwidth, but at the expense of an increased electrical thickness.

Here, an analytic approach is used to systematically design arbitrarily thin metasurfaces. The asymmetric linear polarizer considered here has the following transmission coefficient,

$$\mathbf{S}_{21} = e^{j\phi} \begin{pmatrix} 0 & 0 \\ 1 & 0 \end{pmatrix} \tag{9.31}$$

When an x-polarized plane wave is incident from Region 1, it is transmitted as a y-polarized plane wave in Region 2. However, if an x-polarized plane wave is incident from Region 2, all the power is reflected. Hence, the structure exhibits asymmetric transmission for linear polarization. Assuming the undesired polarization is completely reflected,

$$\mathbf{S}_{11} = e^{j\phi} \begin{pmatrix} 0 & 0 \\ 0 & -1 \end{pmatrix}, \quad \mathbf{S}_{22} = e^{j\phi} \begin{pmatrix} -1 & 0 \\ 0 & 0 \end{pmatrix} \tag{9.32}$$

this metasurface has the constituent surface parameters given by,

$$\boldsymbol{\Lambda} = \begin{pmatrix} 4j\eta_\circ^{-1}\cot(\phi) & -4j\eta_\circ^{-1}\csc(\phi) & 0 & -2 \\ -4j\eta_\circ^{-1}\csc(\phi) & 4j\eta_\circ^{-1}\cot(\phi) & -2 & 0 \\ 0 & 2 & 0 & 0 \\ 2 & 0 & 0 & 0 \end{pmatrix} \tag{9.33}$$

It can be seen that both an anisotropic electric susceptibility and an anisotropic magnetoelectric response are required. Again, the necessary sheet admittances are solved by inserting (9.31) and (9.32) into (9.24), and combining the result with (9.21). Setting $\phi = 135°$, $\beta d = 2\pi/6.37$, $\eta_d = \eta_\circ/1.483$, and $\eta_1 = \eta_2 = \eta_\circ$, the necessary sheet admittances are $\mathbf{Y}_{s1} = \frac{j}{\eta_\circ}\begin{pmatrix} 0.88 & 0 \\ 0 & -77.0 \end{pmatrix}$, $\mathbf{Y}_{s2} = \frac{j}{\eta_\circ}\begin{pmatrix} -0.70 & 4.15 \\ 4.15 & -0.70 \end{pmatrix}$, and $\mathbf{Y}_{s3} = \frac{j}{\eta_\circ}\begin{pmatrix} -77.0 & 0 \\ 0 & 0.88 \end{pmatrix}$.

A unit cell of this metasurface is shown in Fig. 9.19(a). The simulated cross-polarized and co-polarized transmission coefficients are shown in Fig. 9.19(b). Although the structure is designed for an operating frequency of 77 GHz, the performance is quite broadband. A 1 dB transmission bandwidth of 2.43:1 for the desired polarization is achieved. The rejection of the unwanted polarization is greater than 30 dB in this band. S_{11}^{yy} is greater than -0.01 dB, and all other S-parameters are less than -30 dB over the entire operating bandwidth, and are not shown.

The metallic patterns that realize the desired sheet admittances of the asymmetric linear polarizer are shown in Fig. 9.20. It can be seen that the sheet admittance of the first layer ($\mathbf{Y}_{s1}$) is capacitive along $\hat{x}$ and inductive along $\hat{y}$. The second sheet is inductive along the $(\hat{x}-\hat{y})/\sqrt{2}$ direction and capacitive along the $(\hat{x}+\hat{y})/\sqrt{2}$ direction. The third sheet is identical to the first, except rotated by 90°.

The constituent surface parameters of the metasurface providing asymmetric linear transmission are shown in Fig. 9.21. They were determined from simulation by inserting the S-parameters of the structure into (9.13). It can be seen that over the entire frequency range, the magnetic susceptibility is near zero and the crystal axes of the electric susceptibility are located in the $(\hat{x}+\hat{y})/\sqrt{2}$ and $(\hat{x}-\hat{y})/\sqrt{2}$ directions. In addition, the magnetoelectric term is $\boldsymbol{\chi} = \begin{pmatrix} 0 & -2 \\ -2 & 0 \end{pmatrix}$, which is consistent with (9.33). Note that $Y_{xx} = Y_{yy}$ for all plotted frequencies.

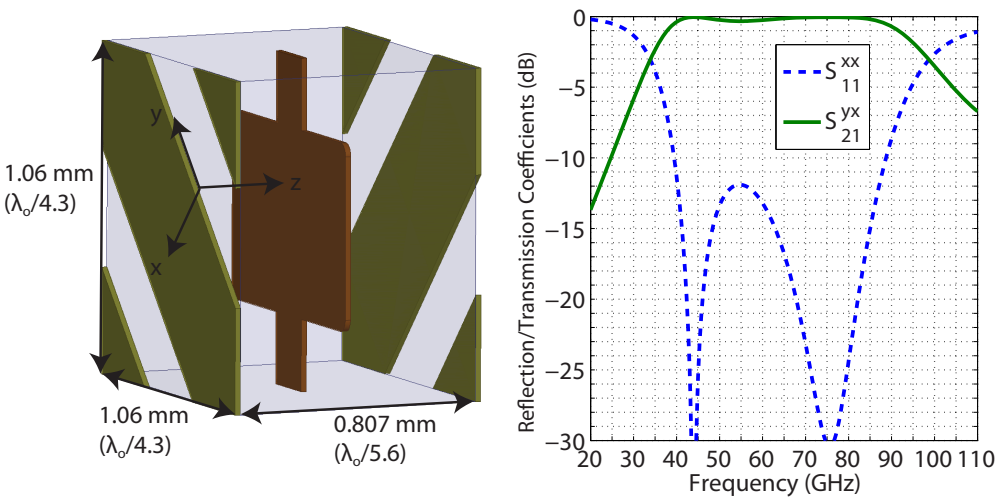

(a) (b)

Figure 9.19: Metasurface exhibiting asymmetric linear transmission. **(a)** Schematic of the unit cell. **(b)** Simulated co-polarized reflection coefficient (S_{11}^{xx}) and cross-polarized transmission coefficient (S_{21}^{yx}) for an incident plane wave traveling in the $+z$ direction. S_{11}^{yy} is greater than -0.01 dB, and all other S-parameters are less than -30 dB over the entire frequency range, and are not shown.

9.4.5 Symmetric Circular Polarizer at Optical Frequencies

As a final demonstration of the versatility of the design process, a symmetric circular polarizer is demonstrated at optical frequencies. Analogous to conventional linear polarizers, these structures transmit one handedness of circular polarization but reflect the other, independent of the propagation direction ($+\hat{z}$ or $-\hat{z}$). At optical frequencies, circular polarizers are attractive for color displays, microscopy, and photography [251]. These devices are most commonly realized by combining quarter-wave plates and linear polarizers [68]. However, this leads to bulky structures that do not lend themselves to optical integration. Recently, helical structures have demonstrated a reduced thickness and much broader bandwidth [247, 251]. However, they require a restrictively difficult fabrication process. This motivated cascading patterned metallic sheets with rotated principle axes [232].

The symmetric circular polarizer considered here transmits right-handed-circularly polarized light but reflects the left-handed-circular polarization, regardless of the propagation direction. The transmission coefficient is given by,

$$\mathbf{S}_{21} = \frac{e^{j\phi}}{2}\begin{pmatrix} 1 & j \\ -j & 1 \end{pmatrix} \tag{9.34}$$

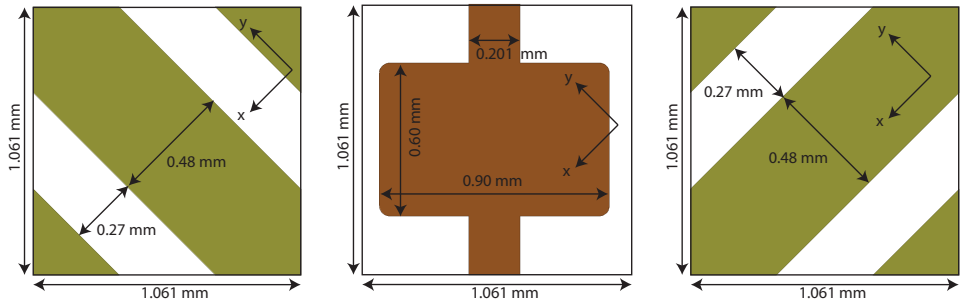

Figure 9.20: **(a)-(c)**Dimensions first, second and third sheets of the asymmetric linear polarizer, respectively.

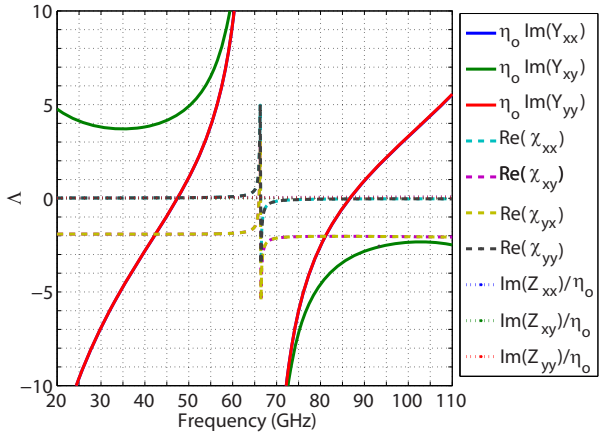

Figure 9.21: Constituent surface parameters of the simulated asymmetric linear polarizer. Note that $Y_{xx} = Y_{yy}$ for all plotted frequencies. The terms leading to loss (Re($\mathbf{Y}$), Re($\mathbf{Z}$), Im($\boldsymbol{\chi}$)) are low and are not plotted. All other terms that are not plotted can be inferred by noting that the structure is reciprocal.

and the constituent surface parameters are given by,

$$\boldsymbol{\Lambda} = \begin{pmatrix} \frac{-2j\,\tan(\phi/2)}{\eta_\circ} & 0 & 0 & 0 \\ 0 & \frac{2j\,\cot(\phi)}{\eta_\circ} & 0 & -2\,\csc(\phi) \\ 0 & 0 & -2j\eta_\circ\,\tan(\phi/2) & 0 \\ 0 & 2\,\csc(\phi) & 0 & 2j\eta_\circ\,\cot(\phi) \end{pmatrix} \tag{9.35}$$

This metasurface exhibits anisotropic electric and magnetic susceptibilities, as well as anisotropic magnetoelectric coupling. Eq. (9.35) assumes that both Regions 1 and

2 are composed of free space and that the reflection coefficients are given by,

$$\mathbf{S}_{11} = \frac{e^{j\phi}}{2}\begin{pmatrix} 1 & -j \\ -j & -1 \end{pmatrix}, \quad \mathbf{S}_{22} = \frac{e^{j\phi}}{2}\begin{pmatrix} 1 & j \\ j & -1 \end{pmatrix} \tag{9.36}$$

In other words, left-handed-circularly polarized light is completely reflected into left-handed-circular polarization from both the front and the back of the metasurface, whereas right-handed-circularly polarized light has zero reflection.

Again looking to (9.24) and (9.21), and setting $\phi = 170°$, $\beta d = 2\pi/4.77$, $\eta_d = \eta_\circ/1.572$, $\eta_1 = \eta_\circ$, and $\eta_2 = \eta_\circ/1.444$, the necessary sheet admittances to realize a symmetric circular polarizer become, $\mathbf{Y}_{s1} = \frac{j}{\eta_\circ}\begin{pmatrix} 0.34 & -1.11 \\ -1.11 & 0.34 \end{pmatrix}$, $\mathbf{Y}_{s2} = \frac{j}{\eta_\circ}\begin{pmatrix} 1.10 & 0 \\ 0 & -9.00 \end{pmatrix}$, and $\mathbf{Y}_{s3} = \frac{j}{\eta_\circ}\begin{pmatrix} 0.57 & 1.57 \\ 1.57 & 0.57 \end{pmatrix}$. When solving for the cascaded sheet admittances, an upper bound on the maximum value of the sheet admittances was imposed due to limitations in achieving extremely small feature sizes at optical frequencies. The magnitude of the sheets were required to be less than $9.0/\eta_\circ$. The designed unit cell is shown in Fig. 9.22(a). The simulated transmission coefficient is shown in Fig. 9.22(b). The superscript '+' denotes right-handed-circular polarization and '-' denotes left-handed-circular polarization. It can be seen that at the design frequency of 1.5 μm, the metasurface achieves low loss for right-handed-circularly polarized light, and provides greater than 15 dB of rejection for left-handed-circularly polarized light. For completeness, the transmittance is also plotted on a linear scale in Fig. 9.22(c), so that its performance can be easily compared to earlier reported structures [232, 247].

The metallic patterns that realize the desired sheet admittances of the symmetric circular polarizer are shown in Fig. 9.23. All corners are rounded with a radius of curvature of 40 nm to resemble a fabricated structure. As in the previous metasurfaces, each sheet admittance is individually designed such that its imaginary part is identical to the desired sheet admittances. However, the analytic model assumes the sheets are lossless, which is somewhat of an approximation. Therefore, the performance can be improved further by using the optimizer provided by Ansys HFSS. The dimensions are varied to minimize the real part of the admittance while also approaching an ideal imaginary part. The optimization process is relatively quick since the initial structure represents a good starting point. The dimensions shown in Fig. 9.23 correspond to the optimized structure. Each sheet is capacitive along one principle axis and inductive along the other.

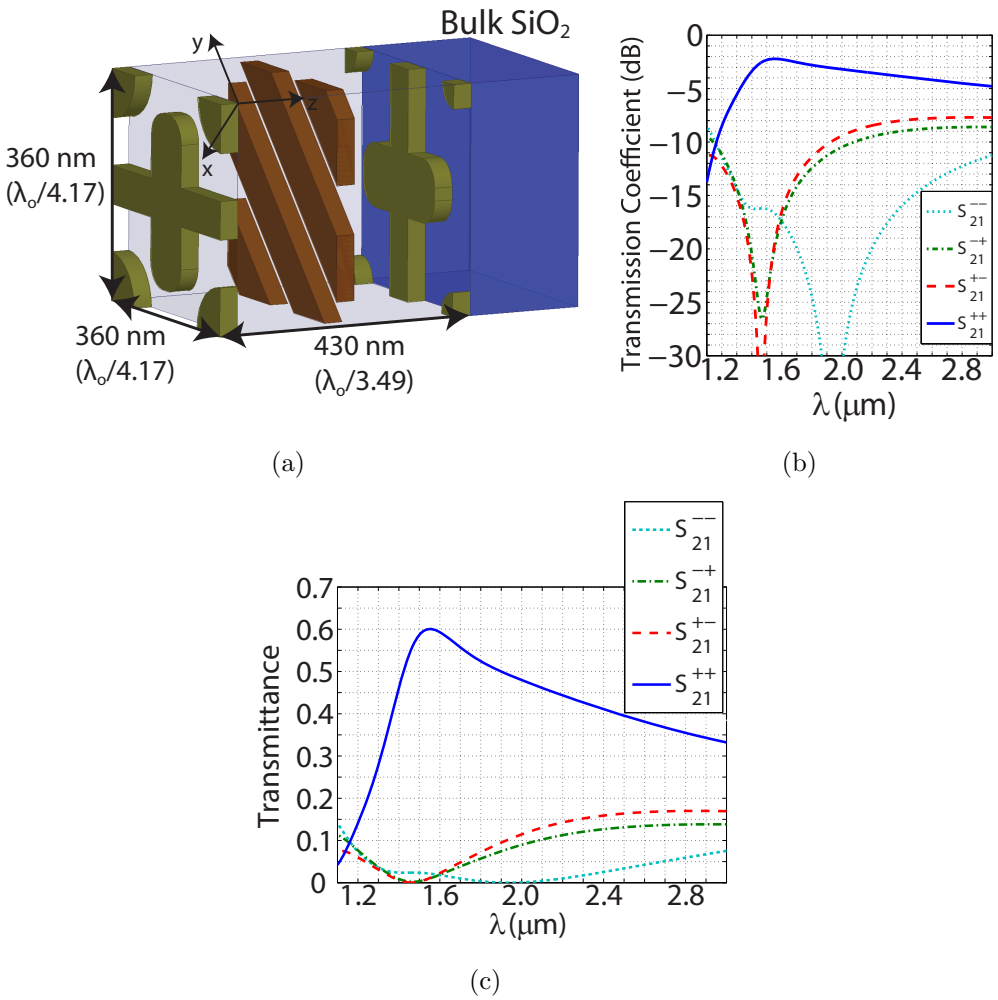

Figure 9.22: Symmetric circular polarizer at near-infrared wavelengths. The surface is designed to operate at a wavelength of 1.5 μm. **(a)** Schematic of the unit cell. **(b)** Transmission coefficient, where the superscript '+' denotes right-handed-circular and '-' denotes left-handed-circular. **(c)** Transmittance ($|\mathbf{S}_{21}|^2$) on a linear scale.

This metasurface is impedance matched for right-handed-circularly polarized light at the design frequency. This is confirmed by the reflection coefficients shown in Fig. 9.24. The power absorbed by the metasurface can be calculated by subtracting the incident power from the transmitted and reflected power $1 - |S_{11}|^2 - |S_{21}|^2$, which is $\sim$40%.

The constituent surface parameters of the symmetric circular polarizer can be determined from simulation by inserting the S-parameters of the structure into (9.13). They are shown in Figs. 9.25 (a) and (b). The terms representing loss (Re($\mathbf{Y}$), Re($\mathbf{Z}$), Re($\boldsymbol{\chi}$)) cannot be neglected. It can be seen that at the operating wavelength of 1.5

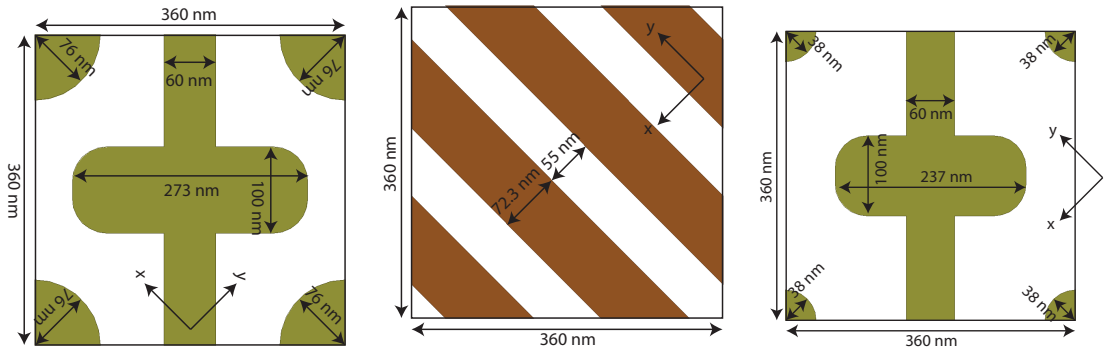

Figure 9.23: **(a)-(c)** Dimensions of the first, second, and third sheets of the symmetric circular polarizer, respectively.

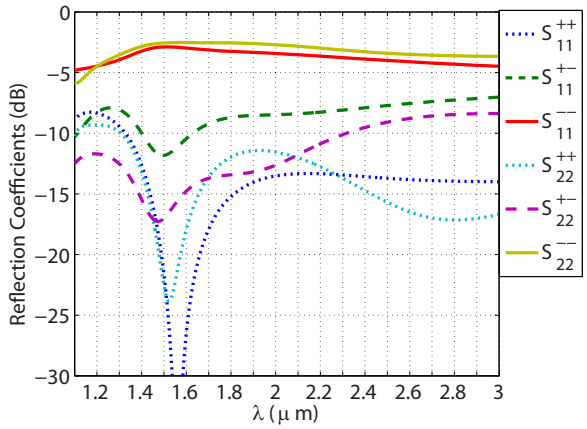

Figure 9.24: Symmetric circular polarizer at near-infrared wavelengths. Reflection coefficient.

μm, Re(χ_{yy}) is much larger than the other magnetoelectric terms. In addition Im(Y_{xx}) $\sim$ Im(Z_{xx}) and Im(Y_{yy}) $\sim$ Im(Z_{yy}), which are all necessary conditions for symmetric circular polarization, as given by (9.35). Although (9.35) assumes that $\eta_1 = \eta_2$, which is not the case here, it is still valuable at providing physical insight since the wave impedance of SiO_2 is similar to that of free space.

The performance of this structure exceeds that of previous metasurfaces in a few respects. At the operating frequency, the structure presented here achieves a polarization rejection of 15 dB. This is comparable to the rejection levels of the Au helix metamaterial [247], which achieved a larger bandwidth at the expense of significantly increased fabrication complexity and overall thickness. This polarization rejection is also an order of magnitude higher than the previous three layer structure that cascaded identical electric dipoles with a rotation between the sheets [232].

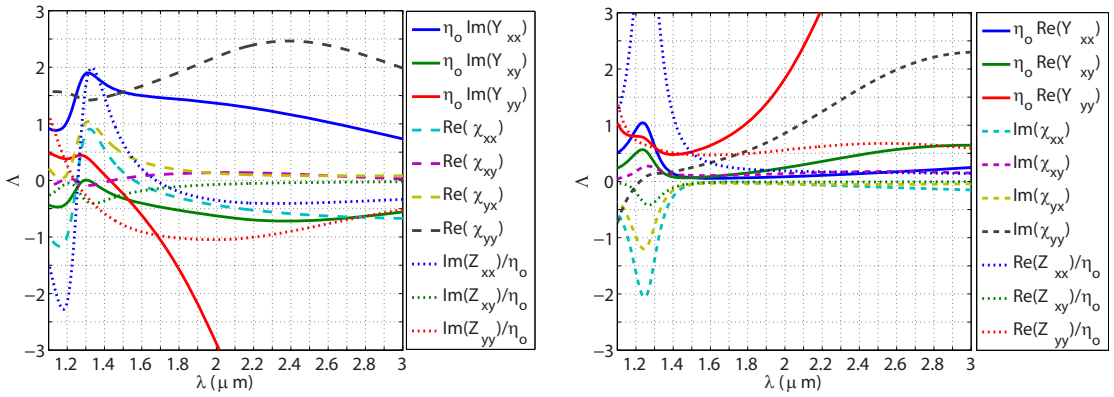

(a) (b)

Figure 9.25: **(a)** Constituent surface parameters of the symmetric circular polarizer. **(b)** The terms leading to loss (Re($\mathbf{Y}$), Re($\mathbf{Z}$), Im($\boldsymbol{\chi}$)). All other terms that are not plotted can be inferred by noting that the structure is reciprocal.

9.4.6 Symmetric Circular Polarizer at mm-wave Frequencies

Next, a symmetric circular polarizer was also developed at 77 GHz. Most reflectarray antennas are linearly polarized. These antennas could also be made to operate with circularly polarized radiation by incorporating symmetric circular polarizers. This would be beneficial for applications such as satellite communication, remote sensing, and radar [68, 252]. Conventional circular polarizers at microwave frequencies are realized with a helical geometry [68,253–255]. However, these designs suffer from a complex fabrication process that is prohibitive at higher frequencies. This motivated two and three layer structures that can be fabricated using standard printed-circuit-board processes [252, 256]. However, these designs suffered from a narrow bandwidth, relatively low extinction ratio, and high insertion loss.

Using the same design procedure as before, it can be shown that the necessary sheets of this structure are identical to those of the metasurface providing asymmetric circular transmission, except the first sheet is rotated by 90°. The transmission coefficient for the desired polarization is near unity, while the rejection of the undesired polarization is greater than 30 dB at the design frequency (see Fig. 9.26(b)). In addition, the constituent surface parameters are very close to the ideal values that achieve a symmetric polarizer at the design frequency of 77 GHz. This can be verified by looking to (9.35) and letting the transmitted phase be $\phi = -103°$, and then comparing the result with Fig. 9.26(c).

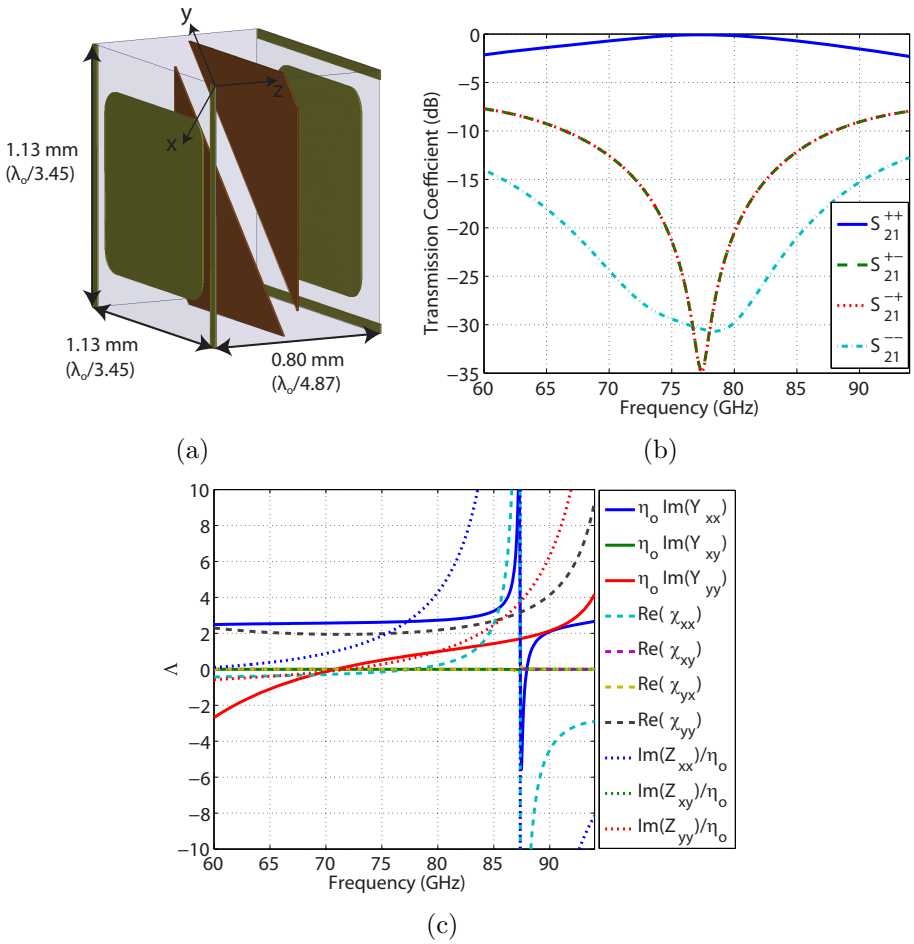

Figure 9.26: Symmetric circular polarizer at mm-wave frequencies. **(a)** Perspective view of the symmetric circular polarizer. **(b)** Transmission coefficient, where the superscript '+' denotes right-handed-circular and '-' denotes left-handed-circular. **(c)** Constituent surface parameters.

9.5 Chapter Summary

Closed-form expressions are derived that relate the reflection and transmission coefficients of a general bianisotropic metasurface to its constituent surface parameters. In addition, a systematic method to design bianisotropic metasurfaces is reported. Specifically, it is analytically shown that cascading anisotropic, patterned metallic sheets provides control of the electric, magnetic, and magnetoelectric responses. This geometry is particularly attractive because it allows for straightforward design and fabrication from microwave to optical wavelengths. Four different polarization controlling devices are reported. In the future, three-dimensional metamaterials can also benefit from this work [236]. By cascading the unit cell in the propagation direction ($\hat{z}$-direction), a bulk bianisotropic response is attainable [150].

CHAPTER X

Conclusion

10.1 Summary

Significant advances in the small antennas and metasurfaces were reported in this thesis. First, a novel fabrication process was developed to mass produce small antennas with near optimal performance. The small antennas were fabricated using a direct transfer patterning process that allows one to stamp a desired metallic pattern onto an arbitrarly contoured substrate. The small antennas that were fabricated operated around 1 GHz and had quality factors approaching the fundamental limits set out by Chu and Wheeler. In the future, this same fabrication process can potentially be used in other areas such as high gain antennas, conformal antenna arrays, RFIDs, and metamaterials.

Next, a physically intuitive method to analyze small antennas was introduced. By considering the frequency dependent polarizability of an arbitrary geometry, a circuit model was derived that predicts the radiation quality factor (Q), radiation efficiency (η_{rad}), and bandwidth. This circuit model will aid in the design of small antennas. In addition, analyzing a particle's frequency dependent polarizability provides intuition for its response when distributed along a two-dimensional array (i.e. metasurface). Next, the directivity of a conventional small antenna was doubled by utilizing a geometry that generates equal electric and magnetic dipole moments to realize a Huygens' source. Closed-form expressions were derived that accurately modeled the directivity and bandwidth of these Huygens' sources.

It was then shown that placing Huygens' sources along a two-dimensional array provides efficient wavefront control without reflection. These metasurfaces are termed as Huygens' surfaces because they control electromagnetic wavefronts in the same manner that was envisioned by Christiaan Huygens in 1690. In contrast, the majority of previously reported metasurafes used only an electric response which necessarily

suffered from significant polarization and reflection losses. It was experimentally shown that Huygens' surfaces can achieve a high efficiency of 86% at microwave frequencies.

The initially proposed Hugyens' surface utilized split-ring-resonators to achieve its magnetic response, which is difficult to fabricate. Therefore, an alternative geometry was proposed that consists of cascaded metallic sheets. It was shown that this structure also exhibits electric and magnetic responses, but is much simpler to fabricate than split-ring-resonators. In addition, polarization control is straightforward with the proposed geometry. Using cascaded metallic sheets, a beam refracting surface was developed that also converts the polarization from linear to circular. Next, more extreme examples of wavefront and polarization control were investigated by developing metasurfaces that converted normally incident Gaussian beams into vector Bessel beams. These metasurfaces represent the state-of-the-art in terms of the extent to which they provide both extreme wavefront control and high efficiency.

The cascaded metallic sheet geometry was scaled to near-infrared wavelengths to realize the first Huygens' surface that controls light. It was theoretically shown that by utilizing anisotropic sheets, the unit cells of a metasurface can generate arbitrary phase shifts along the x and y axes, independent of each other. A beam refracting Huygens' surface with an isotropic response was designed and fabricated. This metasurface achieved a peak efficiency of 18% and extinction ratio of 3 dB, which represented the state-of-the-art in terms of wavefront control by a metasurface at optical frequencies.

Finally, magneto-electric coupling (i.e. chirality) was systematically added to metasurfaces to enable complete control of a wavefront. Such metasurfaces provide the utmost in field control, since they allow coupling between electric and magnetic fields. Since these metasurfaces exhibit electric, magnetic, magnetoelectric responses we refer to them as bianisotropic metasurfaces. Systematic methods to analyze and design these metasurfaces were developed. It was shown that cascading anisotropic, patterned metallic sheets allows for significant control of their bianisotropic responses. These metasurfaces were experimentally verified at microwave, mm-wave, and optical frequencies, which highlighted their versatility.

10.2 Future Directions

In this thesis, it was shown that anisotropic metasurfaces can be designed to convert a normally incident beam into any desired wavefront. In the future, a myriad

of useful beams can be generated by simply illuminating a metasurface with a Gaussian beam. For example, Gaussian-to-Bessel beam transformers were demonstrated at microwave frequencies in chapter 7. These metasurfaces could also be straightforwardly scaled to the optical regime using the techniques presented in chapter 8. In addition, a bianisotropic response could be added to allow for additional polarization control [240]. For example, it was shown that the linear-to-Bessel metasurface generates radial polarization when illuminated with x-polarization, and azimuthal polarization when illuminated with y-polarization. In contrast, it can be shown that the circular-to-Bessel metasurface requires an additional chiral response in order to achieve the same effect with incident right-handed circular and left-handed circular polarizations. Alternatively, a bianisotropic metasurface could be developed that converts an incident x-polarized Gaussian beam into a tractor beam (i.e. nonparaxial vector Bessel beam with both TE and TM polarizations) to pull small particles towards the laser source [257]. In addition, the same metasurface could convert an incident y-polarized Gaussian beam into a linearly polarized Bessel beam, which pushes small particles away from the source laser. Thus, by varying the polarization of the incident Gaussian beam, a single bianisotropic metasurface can produce near-optimal beams for arbitrarily manipulating and sorting small particles, which may find many applications in chemistry and biology [258].

In addition to arbitrary polarization and phase control of the transmission coefficient, bianisotropic metasurfaces can also control the amplitude, phase, and polarization of the reflection coefficient. Therefore, we can envision metasurfaces that simultaneously control transmitted and reflected fields. For example, Fig. 10.1 shows a bianisotropic metasurface that focuses half the incident light to a radially polarized point, while also reflecting half the light off to an anomalous direction.

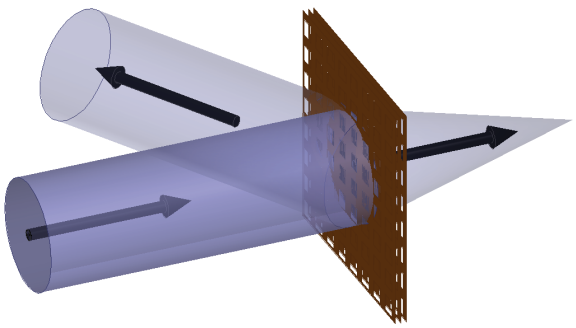

Figure 10.1: A metasurface focuses half the incident light to a radially polarized point, while reflecting half the light off to an anomalous direction.

Bianisotropic metasurfaces could also be combined with a metallic ground plane

to realize a wave guiding structure, as shown in Fig. 10.2. By controlling the phase and amplitude of the reflection coefficient, the propagation constant and leakage rate can be completely controlled. Setting the leakage rate to 0, implies the metasurface and ground plane combination supports surface waves that do not radiate into free space [259]. This is analogous to a dielectric slab supporting total internal reflection. Having a nonzero leakage rate allows the metasurface and ground plane combination to slowly radiate as the wave propagates. The angle of emission is determined by the propagation constant within the wave guiding structure. To first order, the amplitude of the metasurfaces reflection coefficient controls the leakage rate, while the phase controls the propagation constant/angle of emission. If the metasurfaces are inhomogeneous, this should permit waves with different tangential wavevectors and polarizations to be supported on either side of the metasurface. These metasurfaces will, in turn, allow the generation of arbitrary modes within an optical cavity, while also independently shaping the beam radiated from the cavity. This should allow for the realization of cavities with arbitrary Q factors that radiate tailored beams of arbitrary polarization. For instance, cavities that can generate unconventional beams such as optical vortex beams, Bessel beams, and Airy beams could be envisioned.

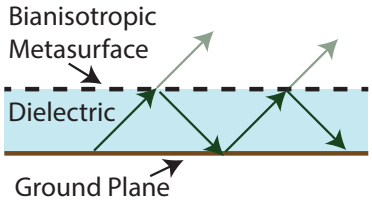

Figure 10.2: A bianisotropic metasurface combined with a ground plane supports guided modes with arbitrary propagation constants and leakage rates.

In this thesis, all the reported optical metasurfaces were fabricated using electron-beam lithography, which is an expensive process. This fabrication process is generally only used for developing proof-of-concept devices since any commercial devices using this process would be far too expensive for most consumer applications. Electron-beam lithography is a direct write process, which means that every trace is individually drawn. In the future, large area soft lithography processes, such as nanoimprint lithography, could be used to dramatically reduce the cost of optical metasurfaces [242]. Nanoimprint lithography uses a hard mold to mechanically pattern nanometer feature sizes into a soft material. Using this process, large areas could be rapidly fabricated by simply 'stamping' the desired pattern. This would allow optical metasurfaces to be transitioned from interesting devices to commercial

products.

10.3 Contributions

The work in this thesis has been published in the following peer-reviewed journals, conference proceedings, conference summaries, and patents. It was also cited in popular literature several times.

10.3.1 Journal Papers

1. **C. Pfeiffer** and A. Grbic, "Bianisotropic Metasurfaces for Optimal Polarization Control: Analysis and Synthesis," *Phys. Rev. Applied*, vol. 2, no. 4, pp. 044011, 2014

2. **C. Pfeiffer** and A. Grbic, "Controlling Vector Bessel Beams with Metasurfaces," *Phys. Rev. Applied*, vol. 2, no. 4, pp. 044012, 2014

3. **C. Pfeiffer**, C. Zheng, V. Ray, L. J. Guo, and A. Grbic, "High performance bianisotropic metasurfaces: asymmetric transmission of light," *Phys. Rev. Lett.*, vol. 113, no. 2, pp. 023902, 2014

4. **C. Pfeiffer**, N. K. Emani, A. M. Shaltout, A. Boltasseva, V. M. Shalaev, and A. Grbic, "Efficient light bending with isotropic metamaterial Huygens surfaces," *Nano Lett.*, vol. 14, no. 5, pp. 2491, 2014

5. **C. Pfeiffer** and A. Grbic, "Millimeter-wave transmitarrays for wavefront and polarization control," *IEEE Trans. Microwave Theory Techniques*, vol. 61, no. 12, pp. 4407, 2013

6. **C. Pfeiffer** and A. Grbic, "Cascaded metasurfaces for complete phase and polarization control," *Appl. Phys. Lett.*, vol. 102, no. 23, pp. 231116, 2013

7. **C. Pfeiffer** and A. Grbic, "Metamaterial Huygens' surfaces: tailoring wave fronts with reflectionless sheets," *Phys. Rev. Lett.*, vol. 110, no. 19, pp. 197401, 2013

8. **C. Pfeiffer** and A. Grbic, "A circuit model for electrically small antennas," *IEEE Trans. Antenn. Propag.*, vol. 60, no. 4, pp. 1671, 2012

9. **C. Pfeiffer**, X. Xu, S. R. Forrest, and A. Grbic, "Direct transfer patterning of electrically small antennas onto three-dimensionally contoured substrates," *Advanced Materials*, vol. 24, no. 9, pp. 1166, 2012

10. S. M. Rudolph, **C. Pfeiffer**, and A. Grbic, "Design and free-space measurements of broadband, low-loss negative-permeability and negative-index media," *IEEE Trans. Antenn. Propag.*, vol. 59, no. 8, pp. 2989, 2011

10.3.2 Conference Proceedings

1. **C. Pfeiffer** and A. Grbic, "Analysis and synthesis of bianisotropic metasurfaces," *IEEE Antennas and Propagation Society International Symposium (APSURSI)*, Memphis, TN, July 6-11, 2014

2. **C. Pfeiffer** and A. Grbic, "Metasurfaces for phase and polarization control," *National Aerospace and Electronics Conference (NAECON)*, Dayton, OH, June 25-27, 2014 (Invited Paper)

3. **C. Pfeiffer**, N. K. Emani, A. M. Shaltout, A. Boltasseva, V. M. Shalaev, and A. Grbic, "Experimental Huygens' surface for NIR wavelengths," *Conference on Lasers and Electro-Optics (CLEO)*, San Jose, CA, June 8-13, 2014

4. **C. Pfeiffer** and A. Grbic, "A refracting metasurface that converts linear to circular polarization," *Meta*, Singapore, May 20-23, 2014 (Invited Paper)

5. **C. Pfeiffer** and A. Grbic, "Metamaterial Huygens' surfaces from microwave to optical frequencies," *European Conference on Antennas and Propagation (EuCAP)*, The Hague, Netherlands, April 6-11, 2014

6. **C. Pfeiffer** and A. Grbic, "Manipulating wavefronts with metamaterial huygens surfaces," *International Congress on Advanced Electromagnetic Materials in Microwaves and Optics (Metamaterials 2013)*, Bordeaux, France, Sept. 16-19, 2013

7. **C. Pfeiffer** and A. Grbic, "Metamaterial Huygens' surfaces," *IEEE International Microwave Symposium (IMS)*, Seattle, WA, June 2-7, 2013

8. A. Grbic, G. Gok, M. F. Imani, A. M. Patel, **C. Pfeiffer** and M. Ettorre, "Metamaterial surfaces for near and far-field applications," *European Conference on Antennas and Propagation (EuCAP)*, Gothenburg, Sweden, April 8-12, 2013 (Invited Paper)

9. **C. Pfeiffer** and A. Grbic, "Realizing Huygens sources through spherical sheet impedances," *IEEE Antennas and Propagation Society International Symposium (APSURSI)*, Chicago, IL, July 8-14, 2012

10. **C. Pfeiffer** and A. Grbic, "Novel methods to analyze and fabricate electrically small antennas," *IEEE Antennas and Propagation Society International Symposium (APSURSI)*, Spokane, WA, July 3-8, 2011

11. **C. Pfeiffer** and A. Grbic, "Equivalent circuits for electrically small antennas," *European Conference on Antennas and Propagation (EuCAP)*, Rome, Italy, April 11-15, 2011

12. **C. Pfeiffer**, X. Xu, S. R. Forrest, and A. Grbic, "A printed spherical helix antenna," *International Symposium on Antenna Technology and Applied Electromagnetics (ANTEM)*, Ottawa, Canada, 2010

10.3.3 Conference Summaries

1. Anthony Grbic and **C. Pfeiffer**, "Metamaterial Huygens' surfaces," *Winter Colloquium on the Physics of Quantum Electronics (PQE)*, Snowbird, UT, January 5-9, 2014 (Invited Paper)

2. **C. Pfeiffer** and A. Grbic, "Beam shaping with metamaterial Huygens' surfaces," *USNC/URSI National Radio Science Meeting (APSURSI)*, Lake Buena Vista, FL, July 7-12, 2013

3. S. M. Rudolph, **C. Pfeiffer**, and A. Grbic, "Broadband negative-refractive-index media: analytical modeling and free space measurements," *URSI General Assembly*, Chicago, IL, August 7-16, 2008

10.3.4 Patents

A. Grbic, **C. Pfeiffer**, X. Xu, and S. R. Forrest, "Antenna Fabrication with Three-Dimensional Contoured Substrates," US8745853 B2, June 2014.

10.3.5 Citations in Popular Literature

1. S. Chang, "Tailor-made surface swaps light polarization," Physics Today, July 2014, http://scitation.aip.org/content/aip/magazine/physicstoday/news/10.1063/PT.5.7087

2. A. Alu, "Viewpoint: Wave-Shaping Surfaces," Physics, 6, 53, May 2013. DOI: 0.1103/Physics.6.53, http://physics.aps.org/articles/v6/53

3. Nature Research Highlights: Materials, "Printing Tiny Coil Antennas," Nature, 482, 134, February 9, 2012, http://www.nature.com/nature/journal/v482/n7384/full/482134c.html

4. Innovation on MSNBC.com, "Mass Production Ahead for Smallest Possible Wi-Fi Antenna," July 7 2011, http://www.nbcnews.com/id/43675715/ns/technology_and_science-innovation/t/mass-production-ahead-smallest-possible-wi-fi-antenna

BIBLIOGRAPHY

BIBLIOGRAPHY

[1] S. Tretyakov, *Analytical modeling in applied electromagnetics*. Artech House, 2003.

[2] R. A. Shelby, D. R. Smith, and S. Schultz, "Experimental verification of a negative index of refraction," *Science*, vol. 292, no. 5514, pp. 77–79, 2001.

[3] J. B. Pendry, D. Schurig, and D. R. Smith, "Controlling electromagnetic fields," *Science*, vol. 312, no. 5781, pp. 1780–1782, 2006.

[4] H. N. Krishnamoorthy, Z. Jacob, E. Narimanov, I. Kretzschmar, and V. M. Menon, "Topological transitions in metamaterials," *Science*, vol. 336, no. 6078, pp. 205–209, 2012.

[5] V. M. Shalaev, "Optical negative-index metamaterials," *Nat. Photonics*, vol. 1, no. 1, pp. 41–48, 2007.

[6] D. Smith, J. Pendry, and M. Wiltshire, "Metamaterials and negative refractive index," *Science*, vol. 305, no. 5685, pp. 788–792, 2004.

[7] C. Holloway, E. Kuester, J. Gordon, J. O'Hara, J. Booth, and D. Smith, "An overview of the theory and applications of metasurfaces: The two-dimensional equivalents of metamaterials," *Antenn. and Propag. Mag., IEEE*, vol. 54, no. 2, pp. 10–35, 2012.

[8] A. V. Kildishev, A. Boltasseva, and V. M. Shalaev, "Planar photonics with metasurfaces," *Science*, vol. 339, no. 6125, 2013.

[9] J. B. Pendry, "Negative refraction makes a perfect lens," *Phys. Rev. Lett.*, vol. 85, no. 18, p. 3966, 2000.

[10] A. Grbic, L. Jiang, and R. Merlin, "Near-field plates: subdiffraction focusing with patterned surfaces," *Science*, vol. 320, no. 5875, pp. 511–513, 2008.

[11] R. Merlin, "Radiationless electromagnetic interference: evanescent-field lenses and perfect focusing," *Science*, vol. 317, no. 5840, pp. 927–929, 2007.

[12] N. Liu, H. Guo, L. Fu, S. Kaiser, H. Schweizer, and H. Giessen, "Three-dimensional photonic metamaterials at optical frequencies," *Nature Mat.*, vol. 7, no. 1, pp. 31–37, 2007.

[13] N. Engheta, "Circuits with light at nanoscales: optical nanocircuits inspired by metamaterials," *Science*, vol. 317, no. 5845, pp. 1698–1702, 2007.

[14] S. R. Best and D. L. Hanna, "A performance comparison of fundamental small-antenna designs," *IEEE Antennas and Propagation Magazine*, vol. 52, no. 1, pp. 47–70, 2010.

[15] A. Erentok and R. W. Ziolkowski, "Metamaterial-inspired efficient electrically small antennas," *IEEE Transactions on Antennas and Propagation*, vol. 56, no. 3, pp. 691–707, 2008.

[16] C. A. Balanis, *Antenna theory: analysis and design*. John Wiley & Sons, 2012.

[17] S. R. Best, "A discussion on the properties of electrically small self-resonant wire antennas," *IEEE Antennas and Propagation Magazine*, vol. 46, no. 6, pp. 9–22, 2004.

[18] ——, "The radiation properties of electrically small folded spherical helix antennas," *IEEE Transactions on Antennas and Propagation*, vol. 52, no. 4, pp. 953–960, 2004.

[19] O. S. Kim, "Low-q electrically small spherical magnetic dipole antennas," *IEEE Transactions on Antennas and Propagation*, vol. 58, no. 7, pp. 2210–2217, 2010.

[20] J. J. Adams, E. B. Duoss, T. F. Malkowski, M. J. Motala, B. Y. Ahn, R. G. Nuzzo, J. T. Bernhard, and J. A. Lewis, "Conformal printing of electrically small antennas on three-dimensional surfaces," *Advanced Materials*, vol. 23, no. 11, pp. 1335–1340, 2011.

[21] R. Vyas, A. Rida, S. Bhattacharya, and M. M. Tentzeris, "Liquid crystal polymer (lcp): the ultimate solution for low-cost rf flexible electronics and antennas," in *Antennas and Propagation Society International Symposium, 2007 IEEE*. IEEE, 2007, pp. 1729–1732.

[22] A. D. Yaghjian and S. R. Best, "Impedance, bandwidth, and q of antennas," *IEEE Transactions on Antennas and Propagation*, vol. 53, no. 4, pp. 1298–1324, 2005.

[23] H. W. Bode, *Network Analysis and Feedback Amplifier Design*. D. Van Nostrand Co., New York, NY, 1945.

[24] R. M. Fano, "Theoretical limitations on the broadband matching of arbitrary impedances," *Journal of the Franklin Institute*, vol. 249, no. 1, pp. 57–83, 1950.

[25] S. E. Sussman-Fort and R. M. Rudish, "Non-foster impedance matching of electrically-small antennas," *IEEE Transactions on Antennas and Propagation*, vol. 57, no. 8, pp. 2230–2241, 2009.

[26] N. Zhu and R. W. Ziolkowski, "Design and measurements of an electrically small, broad bandwidth, non-foster circuit-augmented protractor antenna," *Applied Physics Letters*, vol. 101, no. 2, pp. 024 107–024 107, 2012.

[27] C. R. White, J. S. Colburn, and R. G. Nagele, "A non-foster vhf monopole antenna," *IEEE Antennas and Wireless Propagation Letters*, vol. 11, pp. 584–587, 2012.

[28] J. T. Aberle, "Two-port representation of an antenna with application to non-foster matching networks," *IEEE Transactions on Antennas and Propagation*, vol. 56, no. 5, pp. 1218–1222, 2008.

[29] L. J. Chu, "Physical limitations of omni-directional antennas," *Journal of Applied Physics*, vol. 19, pp. 1163–1175, December 1948.

[30] H. A. Wheeler, "The radiansphere around a small antenna," *Proceedings of the IRE*, vol. 47, no. 8, pp. 1325–1331, 1959.

[31] J. L. Volakis, C.-C. Chen, and K. Fujimoto, *Small antennas: miniaturization techniques & applications.* McGraw-Hill, 2010.

[32] J. Peng and R. W. Ziolkowski, "Metamaterial-inspired, electrically small Huygens sources," *IEEE Antennas and Wireless Propagation Letters*, vol. 9, pp. 501–505, May 2010.

[33] C. Huygens, *Traité de la Lumière.* Leyden, 1690. Translated into English by S. P. Thompson, London, 1912, reprinted by The University of Chicago Press.

[34] D. Berry, R. Malech, and W. Kennedy, "The reflectarray antenna," *IEEE Trans. Antenn. Propag.*, vol. 11, no. 6, pp. 645–651, 1963.

[35] M. A. Al-Joumayly and N. Behdad, "Wideband planar microwave lenses using sub-wavelength spatial phase shifters," *IEEE Trans. on Antenn. and Propag.*, vol. 59, no. 12, pp. 4542–4552, 2011.

[36] N. Gagnon, A. Petosa, and D. A. McNamara, "Research and development on phase-shifting surfaces (PSSs)," *IEEE Antenn. and Propag. Mag.*, vol. 55, no. 2, pp. 29–48, 2013.

[37] A. Abbaspour-Tamijani, K. Sarabandi, and G. M. Rebeiz, "Antenna-filter-antenna arrays as a class of bandpass frequency-selective surfaces," *IEEE Trans. on Microwave Theory and Tech.*, vol. 52, no. 8, pp. 1781–1789, 2004.

[38] D. Pozar and T. Metzler, "Analysis of a reflectarray antenna using microstrip patches of variable size," *Electronics Lett.*, vol. 29, no. 8, pp. 657–658, 1993.

[39] D. M. Pozar, S. D. Targonski, and H. Syrigos, "Design of millimeter wave microstrip reflectarrays," *IEEE Trans. on Antenn. and Propag.*, vol. 45, no. 2, pp. 287–296, 1997.

[40] H. Kaouach, L. Dussopt, J. Lanteri, T. Koleck, and R. Sauleau, "Wideband low-loss linear and circular polarization transmit-arrays in V-band," *IEEE Trans. on Antenn. and Propag.*, vol. 59, no. 7, pp. 2513–2523, 2011.

[41] J. Y. Lau and S. V. Hum, "A planar reconfigurable aperture with lens and reflectarray modes of operation," *IEEE Trans. on Microwave Theory and Tech.*, vol. 58, no. 12, pp. 3547–3555, 2010.

[42] L. Boccia, I. Russo, G. Amendola, and G. Di Massa, "Multilayer antenna-filter antenna for beam-steering transmit-array applications," *IEEE Trans. on Microwave Theory and Tech.*, vol. 60, no. 7, pp. 2287–2300, 2012.

[43] C.-C. Cheng and A. Abbaspour-Tamijani, "Study of 2-bit antenna–filter–antenna elements for reconfigurable millimeter-wave lens arrays," *IEEE Trans. on Microwave Theory and Tech.*, vol. 54, no. 12, pp. 4498–4506, 2006.

[44] Z. Popovic and A. Mortazawi, "Quasi-optical transmit/receive front ends," *IEEE Trans. on Microwave Theory and Tech.*, vol. 46, no. 11, pp. 1964–1975, 1998.

[45] N. K. Grady, J. E. Heyes, D. R. Chowdhury, Y. Zeng, M. T. Reiten, A. K. Azad, A. J. Taylor, D. A. Dalvit, and H.-T. Chen, "Terahertz metamaterials for linear polarization conversion and anomalous refraction," *Science*, vol. 340, no. 6138, pp. 1304–1307, 2013.

[46] N. Yu, P. Genevet, F. Aieta, M. Kats, R. Blanchard, G. Aoust, J. Tetienne, Z. Gaburro, and F. Capasso, "Flat optics: Controlling wavefronts with optical antenna metasurfaces," *IEEE Journal of Selected Topics in Quantum Electronics*, vol. 19, no. 3, p. 4700423, 2013.

[47] B. Memarzadeh and H. Mosallaei, "Array of planar plasmonic scatterers functioning as light concentrator," *Optics Lett.*, vol. 36, no. 13, pp. 2569–2571, 2011.

[48] F. Monticone, N. M. Estakhri, and A. Alù, "Manipulating the nanoscale optical transmission with a meta-transmitarray," *Phys. Rev. Lett.*, vol. 110, p. 203903, 2013.

[49] X. Ni, S. Ishii, A. V. Kildishev, and V. M. Shalaev, "Ultra-thin, planar, Babinet-inverted plasmonic metalenses," *Light: Science & Applications*, vol. 2, no. 4, p. e72, 2013.

[50] A. Abbaspour-Tamijani, K. Sarabandi, and G. Rebeiz, "A millimetre-wave bandpass filter-lens array," *Microwaves, Antenn. & Propag., IET*, vol. 1, no. 2, pp. 388–395, 2007.

[51] A. Niknejad, "Siliconization of 60 GHz," *IEEE Microwave Mag.*, vol. 11, no. 1, pp. 78–85, 2010.

[52] J. Wells, "Faster than fiber: The future of multi-G/s wireless," *IEEE Microwave Mag.*, vol. 10, no. 3, pp. 104–112, 2009.

[53] T. Kosugi, A. Hirata, T. Nagatsuma, and Y. Kado, "MM-wave long-range wireless systems," *IEEE Microwave Mag.*, vol. 10, no. 2, pp. 68–76, 2009.

[54] N. Yu, P. Genevet, M. Kats, F. Aieta, J. Tetienne, F. Capasso, and Z. Gaburro, "Light propagation with phase discontinuities: generalized laws of reflection and refraction," *Science*, vol. 334, no. 6054, pp. 333–337, 2011.

[55] F. Monticone, N. M. Estakhri, and A. Alù, "Full control of nanoscale optical transmission with a composite metascreen," *Phys. Rev. Lett.*, vol. 110, no. 20, p. 203903, 2013.

[56] S. Schelkunoff, "Some equivalence theorems of electromagnetics and their application to radiation problems," *Bell Syst. Tech. J*, vol. 15, no. 1, 1936.

[57] B. A. Munk, *Frequency selective surfaces: theory and design.* John Wiley & Sons, New York, NY, 2005.

[58] D. Smith, W. Padilla, D. Vier, S. Nemat-Nasser, and S. Schultz, "Composite medium with simultaneously negative permeability and permittivity," *Phys. Rev. Lett.*, vol. 84, no. 18, pp. 4184–4187, 2000.

[59] V. M. Shalaev, W. Cai, U. K. Chettiar, H.-K. Yuan, A. K. Sarychev, V. P. Drachev, and A. V. Kildishev, "Negative index of refraction in optical metamaterials," *Opt. Lett.*, vol. 30, no. 24, pp. 3356–3358, 2005.

[60] J. Valentine, S. Zhang, T. Zentgraf, E. Ulin-Avila, D. A. Genov, G. Bartal, and X. Zhang, "Three-dimensional optical metamaterial with a negative refractive index," *Nature*, vol. 455, no. 7211, pp. 376–379, 2008.

[61] Q. Zhan, "Cylindrical vector beams: from mathematical concepts to applications," *Advances in Optics and Photonics*, vol. 1, no. 1, pp. 1–57, 2009.

[62] D. Lerner, "A wave polarization converter for circular polarization," *IEEE Trans. on Antenn. and Propag.*, vol. 13, no. 1, pp. 3–7, 1965.

[63] L. Young, L. Robinson, and C. Hacking, "Meander-line polarizer," *IEEE Trans. on Antenn. and Propag.*, vol. 21, no. 3, pp. 376–378, 1973.

[64] C. Pfeiffer and A. Grbic, "Cascaded metasurfaces for complete phase and polarization control," *Appl. Phys. Lett.*, vol. 102, p. 231116, 2013.

[65] V. Fedotov, P. Mladyonov, S. Prosvirnin, A. Rogacheva, Y. Chen, and N. Zheludev, "Asymmetric propagation of electromagnetic waves through a planar chiral structure," *Phys. Rev. Lett.*, vol. 97, no. 16, p. 167401, 2006.

[66] Y. Ye and S. He, "90° polarization rotator using a bilayered chiral metamaterial with giant optical activity," *Appl. Phys. Lett.*, vol. 96, no. 20, pp. 203 501–203 501, 2010.

[67] C. Menzel, C. Rockstuhl, and F. Lederer, "Advanced jones calculus for the classification of periodic metamaterials," *Phys. Rev. A*, vol. 82, no. 5, p. 053811, 2010.

[68] J. E. Roy and L. Shafai, "Reciprocal circular-polarization-selective surface," *IEEE Antenn. and Propag. Mag.*, vol. 38, no. 6, pp. 18–33, 1996.

[69] J. Liu, A. M. Shaltout, X. Ni, V. M. Shalaev, and A. V. Kildishev, "Experimental validation of a new bianisotropic parameter retrieval technique using plasmonic metasurfaces made of v-shape antennas," in *SPIE NanoScience+ Engineering*. International Society for Optics and Photonics, 2013, pp. 88 060F–88 060F.

[70] H. R. Stuart and C. Tran, "Small spherical antennas using arrays of electromagnetically coupled planar elements," *IEEE Antennas and Wireless Propagation Letters*, vol. 6, pp. 7–10, 2007.

[71] S. R. Best, "On the performance properties of the koch fractal and other bent wire monopoles," *IEEE Transactions on Antennas and Propagation*, vol. 51, no. 6, pp. 1292–1300, 2003.

[72] D.-Y. Shin, Y. Lee, and C. H. Kim, "Performance characterization of screen printed radio frequency identification antennas with silver nanopaste," *Thin Solid Films*, vol. 517, no. 21, pp. 6112–6118, 2009.

[73] X. Xu, M. Davanco, X. Qi, and S. R. Forrest, "Direct transfer patterning on three dimensionally deformed surfaces at micrometer resolutions and its application to hemispherical focal plane detector arrays," *Organic Electronics*, vol. 9, no. 6, pp. 1122–1127, 2008.

[74] R. Pelster, "A novel analytic method for the broadband determination of electromagnetic impedances and material parameters," *IEEE Transactions on Microwave Theory and Techniques*, vol. 43, no. 7, pp. 1494–1501, 1995.

[75] G. S. Ferguson, M. K. Chaudhury, G. B. Sigal, and G. M. Whitesides, "Contact adhesion of thin gold films on elastomeric supports: Cold welding under ambient conditions," *Science*, vol. 253, pp. 776–778, 1991.

[76] C. Kim and S. R. Forrest, "Fabrication of organic light-emitting devices by low-pressure cold welding," *Advanced Materials*, vol. 15, no. 6, pp. 541–545, 2003.

[77] C. Kim, P. E. Burrows, and S. R. Forrest, "Micropatterning of organic electronic devices by cold-welding," *Science*, vol. 288, no. 5467, pp. 831–833, 2000.

[78] C. Kim, M. Shtein, and S. R. Forrest, "Nanolithography based on patterned metal transfer and its application to organic electronic devices," *Applied Physics Letters*, vol. 80, no. 21, pp. 4051–4053, 2002.

[79] N. Bowden, S. Brittain, A. G. Evans, J. W. Hutchinson, and G. M. Whitesides, "Spontaneous formation of ordered structures in thin films of metals supported on an elastomeric polymer," *Nature*, vol. 393, no. 6681, pp. 146–149, 1998.

[80] D. M. De Leeuw, P. A. Kraakman, P. F. G. Bongaerts, C. M. J. Mutsaers, and D. B. M. Klaassen, "Electroplating of conductive polymers for the metallization of insulators," *Synthetic Metals*, vol. 66, no. 3, pp. 263–273, 1994.

[81] M. P. Seah, "Pure element sputtering yields using 500–1000 ev argon ions," *Thin Solid Films*, vol. 81, no. 3, pp. 279–287, 1981.

[82] W. E. McKinzie III, "A modified wheeler cap method for measuring antenna efficiency," in *IEEE Antennas and Propagation Society International Symposium*, vol. 1. IEEE, 1997, pp. 542–545.

[83] H. L. Thal, "New radiation limits for spherical wire antennas," *IEEE Transactions on Antennas and Propagation*, vol. 54, no. 10, pp. 2757–2763, 2006.

[84] S. R. Best and A. D. Yaghjian, "The lower bounds on q for lossy electric and magnetic dipole antennas," *Antennas and Wireless Propagation Letters, IEEE*, vol. 3, no. 1, pp. 314–316, 2004.

[85] J. S. McLean, "A re-examination of the fundamental limits on the radiation Q of electrically small antennas," *IEEE Transactions on Antennas and Propagation*, vol. 44, no. 5, pp. 672–676, May 1996.

[86] R. C. Hansen and R. E. Collin, "A new Chu formula for Q," *IEEE Antennas and Propagation Magazine*, vol. 51, no. 5, pp. 38– 41, October 2009.

[87] H. L. Thal, "New radiation Q limits for spherical wire atennas," *IEEE Transactions on Antennas and Propagation*, vol. 54, no. 10, pp. 2757– 2763, October 2006.

[88] A. D. Yaghjian and H. R. Stuart, "Lower bounds on the Q of electrically small dipole antennas," *IEEE Transactions on Antennas and Propagation*, vol. 58, no. 10, pp. 3114–3121, October 2010.

[89] M. Gustafsson, C. Sohl, and G. Kristensson, "Illustrations of new physical bounds on linearly polarized antennas," *IEEE Transactions on Antennas and Propagation*, vol. 57, no. 5, pp. 1319–1327, May 2009.

[90] H. R. Stuart, "Electrically small antenna elements using negative permittivity resonators," *IEEE Transactions on Antennas and Propagation*, vol. 54, no. 6, pp. 1644–1653, June 2006.

[91] S. Tretyakov, *Analyitcal modelling in applied electromagnetics*. Massechusetts: Artech House Inc., 2003.

[92] J. D. Jackson, *Classical electrodynamics, 2nd ed.* New York: Wiley, 1975.

[93] S. R. Best, "On the performance properties of Koch fractal and other bent wire monopoles," *IEEE Transactions on Antennas and Propagation*, vol. 51, no. 6, pp. 1292–1300, June 2003.

[94] A. D. Yaghjian and S. R. Best, "Impedance, bandwidth, and Q of antennas," *IEEE Transactions on Antennas and Propagation*, vol. 53, no. 4, pp. 1298–1324, April 2005.

[95] L. D. Landau and E. M. Lifshitz, *Electrodynamics of continuous media*. Massechusetts: Addison-Wesley Reading, 1960.

[96] H. R. Stuart, "Bandwidth limitations in small antennas composed of negative permittivity materials and metamaterials," *XXIX General Assembly of the International Union of Radio Science (URSI)*, Chicago, IL, August 7-16, 2008.

[97] N. Engheta, A. Salandrino, and A. Alu, "Circuit elements at optical frequencies: nanoinductors, nanocapacitors, and nanoresistors," *Physical Review Letters*, vol. 95, no. 5, p. 95504 (4 pages), August 2005.

[98] R. W. Ziolkowski and A. D. Kipple, "Application of double negative materials to increase the power radiated by electrically small antennas," *IEEE Transactions on Antennas and Propagation*, vol. 51, no. 10, pp. 2626–2640, October 2003.

[99] R. D. Averitt, S. L. Westcott, and N. J. Halas, "Linear optical properties of gold nanoshells," *Journal of the Optical Society of America B*, vol. 16, no. 10, pp. 1824–1832, 1999.

[100] P. M. Hansen and R. Adams, "The minimum value for the quality factor of an electrically small antenna in spheroidal coordinates," *IEEE Antennas and Propagation Society International Symposium*, Toronto, ON, July 11-17, 2010.

[101] ——, "Minimum raditaion Q for spheroids-extension to cylinder, comparsion to spherical formulas and practical antennas," *IEEE Antennas and Propagation Society International Symposium*, Toronto, ON, July 11-17, 2010.

[102] C. F. Bohren and D. R. Huffman, *Absorption and scattering of light by small particles*. New York: Wiley, 1983.

[103] A. Ahmadi, S. Saadat, and H. Mosallaei, "Resonance and Q performance of ellipsoidal ENG subwavelength radiators," *IEEE Transactions on Antennas and Propagation*, vol. 59, no. 3, pp. 706–713, March 2011.

[104] I. Alexeff, T. Anderson, S. Parameswaran, E. P. Pradeep, J. Hulloli, P. Hulloli, "Experimental and theoretical results with plasma antennas," *IEEE Transactions on Plasma Science*, vol. 34, no. 2, pp. 166–172, April 2006.

[105] J. P. Rayner, A. P. Whichello, A. D. Cheetham, "Physical characteristics of plasma antennas," *IEEE Transactions on Plasma Science*, vol. 32, no. 1, pp. 269–281, February 2004.

[106] D. Sievenpiper, M. Sickmiller, and E. Yablonovitch, "3D wire mesh photonic crystals," *Phyical Review Letters*, vol. 76, pp. 2480–2483, 1996.

[107] J. B. Pendry, A. J. Holden, W. J. Stewart, and I. Youngs, "Extremely low frequency plasmons in metallic mesostructures," *Physical Review Letters*, vol. 76, pp. 4773–4776, 1996.

[108] R. F. Harrington, *Time-harmonic electromagnetic fields*. New York: Wiley-IEEE Press, 2001.

[109] T. P. Crummey, R. Farshadnia, P. J. Fleming, A. C. W. Grace, and S. D. Hancock, "An optimization toolbox for MATLAB," *International Conference on Control*, Edinburgh, UK, March 25-28 1991.

[110] G. Thiele, P. Detweiler, and R. Penno, "On the lower bound of the radiation q for electrically small antennas," *IEEE Transactions on Antennas and Propagation*, vol. 51, no. 6, pp. 1263–1269, 2003.

[111] H. R. Stuart, "Eigenmode analysis of small multielement spherical antennas," *IEEE Transactions on Antennas and Propagation*, vol. 56, no. 9, pp. 2841–2851, September 2008.

[112] B. A. Munk, *Frequency selective surfaces: theory and design*. New York: John Wiley & Sons, 2000.

[113] A. Alu, "Mantle cloak: invisibility induced by a surface," *Physical Review B*, vol. 80, no. 24, p. 245115 (5 pages), 2009.

[114] S. R. Best, "The radiation properties of electrically small folded spherical helix antennas," *IEEE Transactions on Antennas and Propagation*, vol. 52, no. 4, pp. 953–960, April 2004.

[115] O. S. Kim, O. Breinbjerg and A. D. Yaghjian, "Electrically small magnetic dipole antennas with quality factors approaching the Chu lower bound," *IEEE Transactions on Antennas and Propagation*, vol. 58, no. 6, pp. 1898–1906, June 2010.

[116] S. R. Best, "A discussion on the quality factor of impedance matched electrically small antennas," *IEEE Transactions on Antennas and Propagation*, vol. 53, no. 1, pp. 502–508, January 2005.

[117] A. D. Yaghjian, T. H. O'Donnell, E. E. Altshuler, S. R. Best, "Electrically small supergain endfire arrays," *Radio Science*, vol. 43, May 2008, RS3002.

[118] O. S. Kim, "Minimum Q circularly polarized electrically small spherical antennas," *IEEE International Symposium on Antennas and Propagation*, Spokane, WA, USA, July 3-9 2011.

[119] S. R. Best, "Low Q electrically small linear and elliptical polarized spherical dipole antennas," *IEEE Transactions on Antennas and Propagation*, vol. 53, no. 3, pp. 1047–1053, March 2005.

[120] J. Peng, R. W. Ziolkowski, "Multi-frequency, linear and circular polarized, metamaterial-inspired, near-field resonant parasitic antennas," *IEEE Transactions on Antennas and Propagation*, vol. 59, no. 5, pp. 1446–1459, May 2011.

[121] P. Jin and R. W. Ziolkowski, "Low Q, electrically small, efficient near field resonant parasitic antennas," *IEEE Transactions on Antennas and Propagation*, vol. 57, no. 9, pp. 2548–2563, September 2009.

[122] O. Kim, A. Erentok, and O. Breinbjerg, "Resonant excitation of a truncated metamaterial cylindrical shell by a thin wire monopole," in *EuCAP 2009. 3rd European Conference on Antennas and Propagation.* IEEE, 2009, pp. 3155–3157.

[123] O. Kim and O. Breinbjerg, "Miniaturised self-resonant split-ring resonator antenna," *Electronics letters*, vol. 45, no. 4, pp. 196–197, 2009.

[124] ——, "Decreasing the radiation quality factor of magnetic dipole antennas by a magnetic-coated metal core," in *ICECom, 2010 Conference Proceedings.* IEEE, 2010, pp. 1–3.

[125] R. W. Ziolkowski and A. Erentok, "Metamaterial-based efficient electrically small antennas," *IEEE Transactions on Antennas and Propagation*, vol. 54, no. 7, pp. 2113–2130, July 2006.

[126] H. Stuart and A. Yaghjian, "Approaching the lower bounds on q for electrically small electric-dipole antennas using high permeability shells," *IEEE Transactions on Antennas and Propagation*, vol. 58, no. 12, pp. 3865–3872, December 2010.

[127] R. F. Harrington, "Effect of antenna size on gain, bandwidth, and efficiency," *Journal of Reseach of the National Bureau of Standards*, vol. 64D, pp. 1–12, 1960.

[128] J. L. Volakis, C.C. Chen, and K. Fujimoto, *Small antennas: miniaturization techniques and applications.* McGraw-Hill, 2010.

[129] Y. Geyi, "Physical limitations of antenna," *IEEE Transactions on Antennas and Propagation*, vol. 51, pp. 2116–2123, August 2003.

[130] G. Vandenbosch, "Simple procedure to derive lower bounds for radiation q of electrically small devices of arbitrary topology," *IEEE Transactions on Antennas and Propagation*, vol. 59, no. 6, pp. 2217–2225, 2011.

[131] M. Gustafsson, M. Cismasu, and B. Jonsson, "Physical bounds and optimal currents on antennas," *IEEE Transactions on Antennas and Propagation*, vol. 60, no. 6, pp. 2672–2681, 2012.

[132] D. H. Kwon, "On the radiation q and the gain of crossed electric and magnetic dipole moments," *IEEE Transactions on Antennas and Propagation*, vol. 53, pp. 1681–1687, May 2005.

[133] ——, "Radiation q and gain of tm and te sources in phase-delayed rotated configurations," *IEEE Transactions on Antennas and Propagation*, vol. 56, pp. 2783–2786, August 2008.

[134] D. M. Pozar, "New results for minimum q, maximum gain, and polarization properties of electrically small antennas," *EuCAP 2009*, pp. 23–27, Berlin, Germany, March 2009.

[135] H. L. Thal, "New gain and q bounds for coupled tm-te modes," *IEEE Transactions on Antennas and Propagation*, vol. 57, pp. 1879–1885, July 2009.

[136] S. Best, "Progress in the design and realization of an electrically small huygens source," in *Antenna Technology (iWAT), 2010 International Workshop on*, 2010, pp. 1–4.

[137] T. Niemi, P. Alitalo, A. Karilainen, and S. Tretyakov, "Electrically small huygens source antenna for linear polarisation," *IET Microwaves, Antennas & Propagation*, vol. 6, no. 7, pp. 735–739, 2012.

[138] A. Yaghjian, "Increasing the supergain of electrically small antennas using metamaterials," in *Antennas and Propagation, 2009. EuCAP 2009. 3rd European Conference on*, 2009, pp. 858–860.

[139] C. Pfeiffer and A. Grbic, "Realizing huygens sources through spherical sheet impedances," in *IEEE Antennas and Propagation Society International Symposium (APS-URSI)*. IEEE, 2012, pp. 1–2.

[140] K. Alici and E. Ozbay, "Electrically small split ring resonator antennas," *Journal of applied physics*, vol. 101, p. 083104, 2007.

[141] H. R. Stuart, "An electromagnetic comparison of the tapered spherical helix and the negative permittivity sphere," *IEEE Antennas and Propagation Society International Symposium*, pp. 3472–3475, June 2007.

[142] S. Ghadarghadr, A. Ahmadi, and H. Mosallaei, "Negative permeability-based electrically small antennas," *Antennas and Wireless Propagation Letters, IEEE*, vol. 7, pp. 13–17, 2008.

[143] C. Pfeiffer, A. Grbic, X. Xu, and S. Forrest, "Novel methods to analyze and fabricate electrically small antennas," in *Antennas and Propagation (APSURSI), 2011 IEEE International Symposium on*, 2011, pp. 761–764.

[144] C. Pfeiffer and A. Grbic, "A circuit model for electrically small antennas," *IEEE Transactions on Antennas and Propagation*, vol. 60, no. 4, pp. 1671–1683, 2012.

[145] H. Stuart, S. Best, and A. Yaghjian, "Limitations in relating quality factor to bandwidth in a double resonance small antenna," *IEEE Antennas and Wireless Propagation Letters*, vol. 6, pp. 460–463, 2007.

[146] H. A. Wheeler, "The spherical coil as an inductor, shield, or antenna," *Proceedings of the IRE*, vol. 46, pp. 1595–1602, September 1958.

[147] C. Pfeiffer, X. Xu, S. R. Forrest, and A. Grbic, "Direct transfer patterning of electrically small antennas onto three-dimensionally contoured substrates," *Advanced Materials*, vol. 24, no. 9, pp. 1166–1170, 2012.

[148] C. Holloway, E. Kuester, and D. Novotny, "Waveguides composed of metafilms/metasurfaces: The two-dimensional equivalent of metamaterials," *IEEE Antenn. and Wireless Propag. Lett.*, vol. 8, pp. 525–529, 2009.

[149] J. Gordon, C. Holloway, and A. Dienstfrey, "A physical explanation of angle-independent reflection and transmission properties of metafilms/metasurfaces," *IEEE Antenn. and Wireless Propag. Lett.*, vol. 8, pp. 1127–1130, 2009.

[150] C. Fietz and G. Shvets, "Homogenization theory for simple metamaterials modeled as one-dimensional arrays of thin polarizable sheets," *Phys. Rev. B*, vol. 82, no. 20, p. 205128, 2010.

[151] Y. Avitzour, Y. A. Urzhumov, and G. Shvets, "Wide-angle infrared absorber based on a negative-index plasmonic metamaterial," *Phys. Rev. B*, vol. 79, no. 4, p. 045131, 2009.

[152] A. Love, "The integration of the equations of propagation of electric waves. series a," *Philosophical Trans. of the Royal Society of London*, vol. 197, pp. 1–45, 1901.

[153] P. Jin and R. Ziolkowski, "Metamaterial-inspired, electrically small huygens sources," *IEEE Antenn. and Wireless Propag. Lett.*, vol. 9, pp. 501–505, 2010.

[154] A. Karilainen and S. Tretyakov, "Circularly polarized receiving antenna incorporating two helices to achieve low backscattering," *IEEE Trans. on Antenn. and Propag.*, vol. 60, no. 7, pp. 3471–3475, 2012.

[155] E. Kuester, M. Mohamed, M. Piket-May, and C. Holloway, "Averaged transition conditions for electromagnetic fields at a metafilm," *IEEE Trans. on Antenn. and Propag.*, vol. 51, no. 10, pp. 2641–2651, 2003.

[156] C. Holloway, M. Mohamed, E. Kuester, and A. Dienstfrey, "Reflection and transmission properties of a metafilm: With an application to a controllable surface composed of resonant particles," *IEEE Trans. on Electromagnetic Compatibility*, vol. 47, no. 4, pp. 853–865, 2005.

[157] F. Aieta, P. Genevet, M. Kats, N. Yu, R. Blanchard, Z. Gaburro, and F. Capasso, "Aberration-free ultra-thin flat lenses and axicons at telecom wavelengths based on plasmonic metasurfaces," *Nano Lett.*, 2012.

[158] X. Ni, N. Emani, A. Kildishev, A. Boltasseva, and V. Shalaev, "Broadband light bending with plasmonic nanoantennas," *Science*, vol. 335, no. 6067, pp. 427–427, 2012.

[159] M. Al-Joumayly and N. Behdad, "A generalized method for synthesizing low-profile, band-pass frequency selective surfaces with non-resonant constituting elements," *IEEE Trans. on Antenn. and Propag.*, vol. 58, no. 12, pp. 4033–4041, 2010.

[160] D. Pozar, "Flat lens antenna concept using aperture coupled microstrip patches," *Electronics Lett.*, vol. 32, no. 23, pp. 2109–2111, 1996.

[161] K. Sarabandi and N. Behdad, "A frequency selective surface with miniaturized elements," *IEEE Trans. on Antenn. and Propag.*, vol. 55, no. 5, pp. 1239–1245, 2007.

[162] C. Ryan, M. Chaharmir, J. Shaker, J. Bray, Y. Antar, and A. Ittipiboon, "A wideband transmitarray using dual-resonant double square rings," *IEEE Trans. on Antenn. and Propag.*, vol. 58, no. 5, pp. 1486–1493, 2010.

[163] B. A. Munk, "Frequency selective surfaces," *New York*, 2000.

[164] P. Goldsmith, "Quasi-optical techniques," *Proc. of the IEEE*, vol. 80, no. 11, pp. 1729–1747, 1992.

[165] A. Yaghjian, "An overview of near-field antenna measurements," *IEEE Trans. on Antenn. and Propag.*, vol. 34, no. 1, pp. 30–45, 1986.

[166] S. Rudolph, C. Pfeiffer, and A. Grbic, "Design and free-space measurements of broadband, low-loss negative-permeability and negative-index media," *IEEE Trans. on Antenn. and Propag.*, vol. 59, no. 8, pp. 2989–2997, 2011.

[167] J. Durnin, J. Miceli, and J. Eberly, "Diffraction-free beams," *Phys. Rev. Lett.*, vol. 58, no. 15, pp. 1499–1501, 1987.

[168] D. McGloin and K. Dholakia, "Bessel beams: diffraction in a new light," *Contemp. Physics*, vol. 46, no. 1, pp. 15–28, 2005.

[169] N. Yu, F. Aieta, P. Genevet, M. A. Kats, Z. Gaburro, and F. Capasso, "A broadband, background-free quarter-wave plate based on plasmonic metasurfaces," *Nano Lett.*, vol. 12, no. 12, pp. 6328–6333, 2012.

[170] T. Niemi, A. Karilainen, and S. Tretyakov, "Synthesis of polarization transformers," *IEEE Trans. on Antenn. and Propag.*, vol. 61, no. 6, pp. 3102–3111, 2013.

[171] R. Alaee, C. Menzel, C. Rockstuhl, and F. Lederer, "Perfect absorbers on curved surfaces and their potential applications," *Optics Express*, vol. 20, no. 16, pp. 18 370–18 376, 2012.

[172] N. T. Nguyen, R. Sauleau, and L. Le Coq, "Reduced-size double-shell lens antenna with flat-top radiation pattern for indoor communications at millimeter waves," *IEEE Trans. on Antenn. and Propag.*, vol. 59, no. 6, pp. 2424–2429, 2011.

[173] D. M. Sheen, D. L. McMakin, and T. E. Hall, "Three-dimensional millimeter-wave imaging for concealed weapon detection," *IEEE Trans. on Microwave Theory and Tech.*, vol. 49, no. 9, pp. 1581–1592, 2001.

[174] S. Raman, N. S. Barker, and G. M. Rebeiz, "A W-band dielectric-lens-based integrated monopulse radar receiver," *IEEE Trans. on Microwave Theory and Tech.*, vol. 46, no. 12, pp. 2308–2316, 1998.

[175] B. Schoenlinner, X. Wu, J. P. Ebling, G. V. Eleftheriades, and G. M. Rebeiz, "Wide-scan spherical-lens antennas for automotive radars," *IEEE Trans. on Microwave Theory and Tech.*, vol. 50, no. 9, pp. 2166–2175, 2002.

[176] X. Wu, G. V. Eleftheriades, and T. E. van Deventer-Perkins, "Design and characterization of single-and multiple-beam mm-wave circularly polarized substrate lens antennas for wireless communications," *IEEE Trans. on Microwave Theory and Tech.*, vol. 49, no. 3, pp. 431–441, 2001.

[177] E. Arnaud, R. Chantalat, M. Koubeissi, T. Monediere, E. Rodes, and M. Thevenot, "Global design of an ebg antenna and meander-line polarizer for circular polarization," *IEEE Antenn. Wireless Propag. Lett.*, vol. 9, pp. 215–218, 2010.

[178] R.-S. Chu and K.-M. Lee, "Analytical method of a multilayered meander-line polarizer plate with normal and oblique plane-wave incidence," *IEEE Trans. on Antenn. and Propag.*, vol. 35, no. 6, pp. 652–661, 1987.

[179] A. K. Bhattacharyya and T. J. Chwalek, "Analysis of multilayered meander line polarizer," *Int. J. of Microwave and Millimeter-Wave Computer-Aided Eng.*, vol. 7, no. 6, pp. 442–454, 1997.

[180] M. Euler, V. Fusco, R. Cahill, and R. Dickie, "Comparison of frequency-selective screen-based linear to circular split-ring polarisation convertors," *IET Microwaves, Antenn. & Propag.*, vol. 4, no. 11, pp. 1764–1772, 2010.

[181] ——, "325 GHz single layer sub-millimeter wave fss based split slot ring linear to circular polarization convertor," *IEEE Trans. on Antenn. and Propag.*, vol. 58, no. 7, pp. 2457–2459, 2010.

[182] M. Joyal and J. Laurin, "Analysis and design of thin circular polarizers based on meander lines," *IEEE Trans. on Antenn. and Propag.*, vol. 60, no. 6, pp. 3007–3011, 2012.

[183] A. I. Zverev, *Handbook of filter synthesis*. Wiley, 1967, vol. 47.

[184] D. C. Thompson, O. Tantot, H. Jallageas, G. E. Ponchak, M. M. Tentzeris, and J. Papapolymerou, "Characterization of liquid crystal polymer (LCP) material and transmission lines on LCP substrates from 30 to 110 GHz," *IEEE Trans. on Microwave Theory and Tech.*, vol. 52, no. 4, pp. 1343–1352, 2004.

[185] D. M. Pozar, *Microwave engineering*. Wiley. com, 2009.

[186] D. Smith, S. Schultz, P. Markoš, and C. Soukoulis, "Determination of effective permittivity and permeability of metamaterials from reflection and transmission coefficients," *Phys. Rev. B*, vol. 65, no. 19, p. 195104, 2002.

[187] C. Pfeiffer and A. Grbic, "Metamaterial huygens' surfaces: Tailoring wave fronts with reflectionless sheets," *Phys. Rev. Lett.*, vol. 110, no. 19, p. 197401, 2013.

[188] ——, "Metamaterial Huygens' surfaces." IEEE Int. Microwave Symp., Seattle, WA, June 2-7, 2013.

[189] S. Larouche and D. R. Smith, "Reconciliation of generalized refraction with diffraction theory," *Optics Lett.*, vol. 37, no. 12, pp. 2391–2393, 2012.

[190] S. Gregson, J. McCormick, and C. Parini, *Principles of planar near-field antenna measurements*. Institution of Engineering and Technology, London, 2007, vol. 53.

[191] C. Pfeiffer and A. Grbic, "Controlling vector bessel beams with metasurfaces," *Physical Review Applied*, vol. 2, no. 4, p. 044012, 2014.

[192] A. Novitsky, C.-W. Qiu, and H. Wang, "Single gradientless light beam drags particles as tractor beams," *Phys. Rev. Lett.*, vol. 107, no. 20, p. 203601, 2011.

[193] F. O. Fahrbach, P. Simon, and A. Rohrbach, "Microscopy with self-reconstructing beams," *Nature Phot.*, vol. 4, no. 11, pp. 780–785, 2010.

[194] M. Duocastella and C. B. Arnold, "Bessel and annular beams for materials processing," *Laser & Photonics Reviews*, vol. 6, no. 5, pp. 607–621, 2012.

[195] R. Dorn, S. Quabis, and G. Leuchs, "Sharper focus for a radially polarized light beam," *Phys. Rev. Lett.*, vol. 91, no. 23, p. 233901, 2003.

[196] J. Durnin, "Exact solutions for nondiffracting beams. i. the scalar theory," *JOSA A*, vol. 4, no. 4, pp. 651–654, 1987.

[197] S. R. Mishra, "A vector wave analysis of a bessel beam," *Optics Commun.*, vol. 85, no. 2, pp. 159–161, 1991.

[198] M. Beresna, M. Gecevičius, P. G. Kazansky, and T. Gertus, "Radially polarized optical vortex converter created by femtosecond laser nanostructuring of glass," *Appl. Phys. Lett.*, vol. 98, no. 20, p. 201101, 2011.

[199] G. Machavariani, Y. Lumer, I. Moshe, A. Meir, and S. Jackel, "Spatially-variable retardation plate for efficient generation of radially-and azimuthally-polarized beams," *Optics Commun.*, vol. 281, no. 4, pp. 732–738, 2008.

[200] L. Huang, X. Chen, H. Muhlenbernd, G. Li, B. Bai, Q. Tan, G. Jin, T. Zentgraf, and S. Zhang, "Dispersionless phase discontinuities for controlling light propagation," *Nano Lett.*, vol. 12, no. 11, pp. 5750–5755, 2012.

[201] C. Pfeiffer and A. Grbic, "Millimeter-wave transmitarrays for wavefront and polarization control," *IEEE Trans. Microwave Theory and Techniques*, 2013.

[202] A. Neto, "UWB, non dispersive radiation from the planarly fed leaky lens antenna-part 1: Theory and design," *IEEE Trans. on Antenn. and Propag.*, vol. 58, no. 7, pp. 2238–2247, 2010.

[203] A. Feresidis and J. Vardaxoglou, "High gain planar antenna using optimised partially reflective surfaces," *IEE Proceedings-Microwaves, Antennas and Propagation*, vol. 148, no. 6, pp. 345–350, 2001.

[204] M. Ando, K. Sakurai, N. Goto, K. Arimura, and Y. Ito, "A radial line slot antenna for 12 ghz satellite tv reception," *IEEE Trans. on Antenn. and Propag.*, vol. 33, no. 12, pp. 1347–1353, 1985.

[205] A. A. Oliner and D. R. Jackson, "Leaky-wave antennas," *Ch. 11 of Antenna Engineering Handbook*, vol. 4, 2007.

[206] G. Minatti, F. Caminita, M. Casaletti, and S. Maci, "Spiral leaky-wave antennas based on modulated surface impedance," *IEEE Trans. on Antenn. and Propag.*, vol. 59, no. 12, pp. 4436–4444, 2011.

[207] J. I. Herranz-Herruzo, A. Valero-Nogueira, and M. Ferrando-Bataller, "Optimization technique for linearly polarized radial-line slot-array antennas using the multiple sweep method of moments," *IEEE Trans. on Antenn. and Propag.*, vol. 52, no. 4, pp. 1015–1023, 2004.

[208] A. Akiyama, T. Yamamoto, M. Ando, and N. Goto, "Numerical optimisation of slot parameters for a concentric array radial line slot antenna," *IEE Proceedings-Microwaves, Antenn. and Propag.*, vol. 145, no. 2, pp. 141–145, 1998.

[209] M. Ettorre and A. Grbic, "Generation of propagating bessel beams using leaky-wave modes," *IEEE Trans. on Antenn. and Propag.*, vol. 60, no. 8, pp. 3605–3613, 2012.

[210] M. Ettorre, S. M. Rudolph, and A. Grbic, "Generation of propagating bessel beams using leaky-wave modes: Experimental validation," *IEEE Trans. on Antenn. and Propag.*, vol. 60, no. 6, pp. 2645–2653, 2012.

[211] J. E. Curtis, B. A. Koss, and D. G. Grier, "Dynamic holographic optical tweezers," *Opt. Commun.*, vol. 207, no. 1, pp. 169–175, 2002.

[212] E. R. Dufresne, G. C. Spalding, M. T. Dearing, S. A. Sheets, and D. G. Grier, "Computer-generated holographic optical tweezer arrays," *Rev. of Sci. Instruments*, vol. 72, no. 3, pp. 1810–1816, 2001.

[213] M. Kang, T. Feng, H.-T. Wang, and J. Li, "Wave front engineering from an array of thin aperture antennas," *Opt. Express*, vol. 20, no. 14, pp. 15 882–15 890, 2012.

[214] X. M. Goh, L. Lin, and A. Roberts, "Plasmonic lenses for wavefront control applications using two-dimensional nanometric cross-shaped aperture arrays," *JOSA B*, vol. 28, no. 3, pp. 547–553, 2011.

[215] A. Pors, M. G. Nielsen, G. D. Valle, M. Willatzen, O. Albrektsen, and S. I. Bozhevolnyi, "Plasmonic metamaterial wave retarders in reflection by orthogonally oriented detuned electrical dipoles," *Opt. Lett.*, vol. 36, no. 9, pp. 1626–1628, 2011.

[216] L. Verslegers, P. B. Catrysse, Z. Yu, J. S. White, E. S. Barnard, M. L. Brongersma, and S. Fan, "Planar lenses based on nanoscale slit arrays in a metallic film," *Nano Lett.*, vol. 9, no. 1, pp. 235–238, 2008.

[217] B. Walther, C. Helgert, C. Rockstuhl, and T. Pertsch, "Diffractive optical elements based on plasmonic metamaterials," *Applied Phys. Lett.*, vol. 98, no. 19, p. 191101, 2011.

[218] S. Larouche, Y.-J. Tsai, T. Tyler, N. M. Jokerst, and D. R. Smith, "Infrared metamaterial phase holograms," *Nature Mat.*, vol. 11, pp. 450–454, 2012.

[219] S. Zhang, W. Fan, K. Malloy, S. Brueck, N. Panoiu, and R. Osgood, "Near-infrared double negative metamaterials," *Opt. Exp.*, vol. 13, no. 13, pp. 4922–4930, 2005.

[220] M. Li, M. A. Al-Joumayly, and N. Behdad, "Broadband true-time-delay microwave lenses based on miniaturized element frequency selective surfaces," *IEEE Trans. on Antenn. and Propag.*, vol. 61, no. 3, pp. 1166–1179, 2013.

[221] K.-P. Chen, V. P. Drachev, J. D. Borneman, A. V. Kildishev, and V. M. Shalaev, "Drude relaxation rate in grained gold nanoantennas," *Nano Lett.*, vol. 10, no. 3, pp. 916–922, 2010.

[222] C. Pfeiffer, N. K. Emani, A. M. Shaltout, A. Boltasseva, V. M. Shalaev, and A. Grbic, "Efficient light bending with isotropic metamaterial huygens' surfaces," *Nano Lett.*, vol. 14, no. 5, pp. 2491–2497, 2014.

[223] T. A. Planchon, L. Gao, D. E. Milkie, M. W. Davidson, J. A. Galbraith, C. G. Galbraith, and E. Betzig, "Rapid three-dimensional isotropic imaging of living cells using bessel beam plane illumination," *Nature Methods*, vol. 8, no. 5, pp. 417–423, 2011.

[224] P. Zhang, Y. Hu, T. Li, D. Cannan, X. Yin, R. Morandotti, Z. Chen, and X. Zhang, "Nonparaxial mathieu and weber accelerating beams," *Phys. Rev. Lett.*, vol. 109, no. 19, p. 193901, 2012.

[225] M. Selvanayagam and G. V. Eleftheriades, "Discontinuous electromagnetic fields using orthogonal electric and magnetic currents for wavefront manipulation," *Optics Exp.*, vol. 21, no. 12, pp. 14 409–14 429, 2013.

[226] L. Wu, Z. Yang, Y. Cheng, M. Zhao, R. Gong, Y. Zheng, J. Duan, and X. Yuan, "Giant asymmetric transmission of circular polarization in layer-by-layer chiral metamaterials," *Appl. Phys. Lett.*, vol. 103, no. 2, pp. 021 903–021 903, 2013.

[227] A. B. Khanikaev, S. H. Mousavi, G. Shvets, and Y. S. Kivshar, "One-way extraordinary optical transmission and nonreciprocal spoof plasmons," *Phys. Rev. Lett*, vol. 105, no. 12, p. 126804, 2010.

[228] S. Zhang, F. Liu, T. Zentgraf, and J. Li, "Interference-induced asymmetric transmission through a monolayer of anisotropic chiral metamolecules," *Phys. Rev. A*, vol. 88, no. 2, p. 023823, 2013.

[229] A. Shaltout, V. Shalaev, and A. Kildishev, "Homogenization of bi-anisotropic metasurfaces," *Optics Exp.*, vol. 21, no. 19, pp. 21 941–21 950, 2013.

[230] C. L. Holloway, E. F. Kuester, and A. Dienstfrey, "Characterizing metasurfaces/metafilms: The connection between surface susceptibilities and effective material properties," *IEEE Antenn. and Wireless Propag. Lett.*, vol. 10, pp. 1507–1511, 2011.

[231] J. A. Kong, "Theorems of bianisotropic media," *Proc. of the IEEE*, vol. 60, no. 9, pp. 1036–1046, 1972.

[232] Y. Zhao, M. Belkin, and A. Alù, "Twisted optical metamaterials for planarized ultrathin broadband circular polarizers," *Nature Comm.*, vol. 3, p. 870, 2012.

[233] Y. Zhao, N. Engheta, and A. Alù, "Homogenization of plasmonic metasurfaces modeled as transmission-line loads," *Metamaterials*, vol. 5, no. 2, pp. 90–96, 2011.

[234] C. Wu, N. Arju, G. Kelp, J. A. Fan, J. Dominguez, E. Gonzales, E. Tutuc, I. Brener, and G. Shvets, "Spectrally selective chiral silicon metasurfaces based on infrared fano resonances," *Nat. Commun.*, vol. 5, p. 3892, 2014.

[235] A. V. Rogacheva, V. A. Fedotov, A. S. Schwanecke, and N. I. Zheludev, "Giant gyrotropy due to electromagnetic-field coupling in a bilayered chiral structure," *Phys. Rev. Lett.*, vol. 97, no. 17, p. 177401, 2006.

[236] J. Pendry, "A chiral route to negative refraction," *Science*, vol. 306, no. 5700, pp. 1353–1355, 2004.

[237] J. Ma, R. Mittra, and N. T. Huang, "Analysis of multiple fss screens of unequal periodicity using an efficient cascading technique," *IEEE Trans. on Antenn. and Propag.*, vol. 53, no. 4, pp. 1401–1414, 2005.

[238] M. Schneider, "Automotive radar–status and trends," in *German microwave conference*, 2005, pp. 144–147.

[239] P. B. Johnson and R.-W. Christy, "Optical constants of the noble metals," *Phy. Rev. B*, vol. 6, no. 12, p. 4370, 1972.

[240] C. Pfeiffer and A. Grbic, "Bianisotropic metasurfaces for optimal polarization control: Analysis and synthesis," *Physical Review Applied*, vol. 2, no. 4, p. 044011, 2014.

[241] C. Pfeiffer, C. Zhang, V. Ray, L. J. Guo, and A. Grbic, "High performance bianisotropic metasurfaces: Asymmetric transmission of light," *Physical Review Letters*, vol. 113, no. 2, p. 023902, 2014.

[242] L. J. Guo, "Nanoimprint lithography: methods and material requirements," *Advanced Mater.*, vol. 19, no. 4, pp. 495–513, 2007.

[243] A. S. Schwanecke, V. A. Fedotov, V. V. Khardikov, S. L. Prosvirnin, Y. Chen, and N. I. Zheludev, "Nanostructured metal film with asymmetric optical transmission," *Nano Lett.*, vol. 8, no. 9, pp. 2940–2943, 2008.

[244] V. A. Fedotov, A. S. Schwanecke, N. I. Zheludev, V. V. Khardikov, and S. L. Prosvirnin, "Asymmetric transmission of light and enantiomerically sensitive plasmon resonance in planar chiral nanostructures," *Nano Lett.*, vol. 7, no. 7, pp. 1996–1999, 2007.

[245] C. Menzel, C. Helgert, C. Rockstuhl, E. B. Kley, A. Tünnermann, T. Pertsch, and F. Lederer, "Asymmetric transmission of linearly polarized light at optical metamaterials," *Phys. Rev. Lett.*, vol. 104, no. 25, p. 253902, 2010.

[246] M. Mutlu, A. E. Akosman, A. E. Serebryannikov, and E. Ozbay, "Diodelike asymmetric transmission of linearly polarized waves using magnetoelectric coupling and electromagnetic wave tunneling," *Phys. Rev. Lett.*, vol. 108, no. 21, p. 213905, 2012.

[247] J. K. Gansel, M. Thiel, M. S. Rill, M. Decker, K. Bade, V. Saile, G. von Freymann, S. Linden, and M. Wegener, "Gold helix photonic metamaterial as broadband circular polarizer," *Science*, vol. 325, no. 5947, pp. 1513–1515, 2009.

[248] Y. J. Shin, Y.-K. Wu, K.-T. Lee, J. G. Ok, and L. J. Guo, "Fabrication and encapsulation of a short-period wire grid polarizer with improved viewing angle by the angled-evaporation method," *Advanced Optical Mater.*, vol. 1, no. 11, pp. 863–868, 2013.

[249] Y.-K. R. Wu, A. E. Hollowell, C. Zhang, and L. J. Guo, "Angle-insensitive structural colours based on metallic nanocavities and coloured pixels beyond the diffraction limit," *Scientific Reports*, vol. 3, p. 1194, 2013.

[250] C. Huang, Y. Feng, J. Zhao, Z. Wang, and T. Jiang, "Asymmetric electromagnetic wave transmission of linear polarization via polarization conversion through chiral metamaterial structures," *Phys. Rev. B*, vol. 85, no. 19, p. 195131, 2012.

[251] Z. Y. Yang, M. Zhao, P. X. Lu, and Y. F. Lu, "Ultrabroadband optical circular polarizers consisting of double-helical nanowire structures," *Optics Lett.*, vol. 35, no. 15, pp. 2588–2590, 2010.

[252] I.-Y. Tarn and S.-J. Chung, "A new advance in circular polarization selective surface-a three layered cpss without vertical conductive segments," *IEEE Trans. on Antenn. and Propag.*, vol. 55, no. 2, pp. 460–467, 2007.

[253] R. Pierrot, "Éléments résonants en polarization circulaire et réflecteur semi-transparent composé de ces éléments," *French Republic Patent #89.609, No.1.512.598, December 30, 1966.*

[254] G. A. Morin, "A simple circular polarization selective surface (cpss)," in *IEEE Antennas and Propagation Society International Symposium, 1990.* IEEE, 1990, pp. 100–103.

[255] W. V. Tilston, T. Tralman, and S. M. Khanna, "A polarization selective surface for circular polarization," in *IEEE Antennas and Propagation Society International Symposium, 1988.* IEEE, 1988, pp. 762–765.

[256] Y. Ye, X. Li, F. Zhuang, and S. Chang, "Homogeneous circular polarizers using a bilayered chiral metamaterial," *Appl. Phys. Lett.*, vol. 99, no. 3, pp. 031 111–031 111, 2011.

[257] A. Novitsky, C.-W. Qiu, and A. Lavrinenko, "Material-independent and size-independent tractor beams for dipole objects," *Phys. Rev. Lett.*, vol. 109, no. 2, p. 023902, 2012.

[258] O. Brzobohatỳ, V. Karásek, M. Šiler, L. Chvátal, T. Čižmár, and P. Zemánek, "Experimental demonstration of optical transport, sorting and self-arrangement using a tractor beam," *Nature Photonics*, vol. 7, no. 2, pp. 123–127, 2013.

[259] C. Pfeiffer and A. Grbic, "A printed, broadband luneburg lens antenna," *Antennas and Propagation, IEEE Transactions on*, vol. 58, no. 9, pp. 3055–3059, 2010.